Vibrational properties of glasses at the transition from microscopic to macroscopic regime

Beatrice Ruta

THESE

Pour obtenir le grade de

DOCTEUR de L'UNIVERSITE de GRENOBLE

Spécialité: Physique de la matiere condensée et du rayonnement

Arrêté ministériel: 7 août 2006

Présentée et soutenue publiquement par

Beatrice Ruta

le 28 Septembre 2010

Les propriétés vibrationnelles des verres: un étude expérimental dans la region de transition entre le régime microscopique et macroscopique

Thèse dirigée par Giulio Monaco

devant le jury composé de:

Hubert Renevier	President
Aleksandar Matic	Rapporteur
Alain Mermet	Rapporteur
Pierangelo Rolla	Examinateur
Marie Plazanet	Examinateur

Thèse préparée au sein du laboratoire:
European Synchrotron Radiation Facility - Grenoble
dans l'Ecole Doctorale de Physique du Grenoble

Vibrational properties of glasses at the transition from microscopic to macroscopic regime

by

Beatrice Ruta

27/09/2010

Declaration of Authorship

I, Beatrice Ruta, declare that this thesis titled, 'Vibrational properties of glasses at the transition from microscopic to macroscopic regime' and the work presented in it are my own. I confirm that:

- This work was done wholly or mainly while in candidature for a research degree at this University.
- Where any part of this thesis has previously been submitted for a degree or any other qualification at this University or any other institution, this has been clearly stated.
- Where I have consulted the published work of others, this is always clearly attributed.
- Where I have quoted from the work of others, the source is always given. With the exception of such quotations, this thesis is entirely my own work.
- I have acknowledged all main sources of help.
- Where the thesis is based on work done by myself jointly with others, I have made clear exactly what was done by others and what I have contributed myself.

Signed: _____

Date: _____

“Cacahué!”

Acknowledgements

I am indebted to many people who nicely and patiently followed every step of this work during these three years, teaching me a lot and supporting me. I would like to start thanking all the ID16 group at the ESRF. First of all my supervisor, Giulio Monaco, who offered me the big opportunity to perform my Ph.D. at the ESRF on such an interesting and challenging project. His passion and his talent in his work is definitely something that I will keep as an example.
I wish to thank Giacomo Baldi and Valentina Giordano for sharing with me several beamtimes and for supporting me also with interesting ideas, that always resulted to be helpful in solving problems arising during the various stages of this project.
I deeply thank Daniele Fioretto and Filippo Scarponi for the pleasant and fruitful collaborations. In particular for the discussions and for their fast and always precise answer to any questions.
I sincerely thank Stéphane Rols for giving me the possibility to perform the neutron measurements and for the encouragement in the article preparation. Thank to Laura Orsingher for the patience and help in the neutron data analysis.
I thank Spyros Yannopoulos for the preparation of pure sulfur and for all the discussions. I wish to thank also Roberto Verbeni and Christian Henriquet for the big help in designing and setting-up the experimental apparatus for all the experiments, Alexander Chumakov for the support and the discussions and Kristine Niss, Christiane Alba-Simionesco and Cécile Dalle-Ferrier for suggesting me the very interesting case of sorbitol.
A special acknowledgment to Simo Huotari, Tuomas Pylkkanen and Laura Simonelli for the strong support during these three years. Finally I wish to thank Giancarlo Ruocco, who gave me the possibility to come to work at the ESRF during my master Thesis.

Contents

List of Figures

List of Tables

Introdution (français)

Une des questions les plus ambitieuses dans la Physique de la Matière Condensée concerne la compréhension des propriétés vibrationnelles des verres. Malgré l'absence d'ordre à longue distance, cette classe de systèmes est caractérisée par des comportements universels qui se distinguent fortement de ceux de leur cristaux correspondants. En particulier, une anomalie présente de la densité d'états vibrationnels (VDOS), $g(E)$, à des énergies de quelques meV a suscité beaucoup d'intérêt en raison de sa présence universelle dans les verres [1]. Cette anomalie apparaît sous la forme d'un pic large, appelé boson peak (BP), dans la densité réduite des états, $g(E)/E^2$, par rapport à la prévision du continuum élastique de Debye, dans une région d'énergies où le modèle de Debye fonctionne encore assez bien pour les correspondants cristaux.
Bien que le BP a été découvert plus de 40 ans, aucun accord n'existe sur son origine physique et il reste encore l'objet d'un nombre croissant d'études théoriques et expérimentales. Selon un accord général le BP est une manifestation du désordre, mais la question de savoir si le BP est lié à un comportement particulier des excitations acoustiques présent dans la région d'énergies correspondante ou à l'existence de certains modes supplémentaires, spécifiques de l'état vitreux, est encore sans réponse. L'absence d'un cadre théorique clair pour servir de référence et la difficulté de démêler les effets spécifiques d'un système par rapport aux comportements universels, aussi bien dans les résultats expérimentaux que dans les simulations numériques, ralentit les progrès dans ce domaine.
Les propriétés vibrationnelles des verres semblent également être liées aux propriétés visqueuses des correspondants liquides surfondus au dessus de la température de la transition vitreuse, T_g, qui sont saisies à travers la valeur de la fragilité cinétique. Ce paramètre a été introduit pour la première fois par C.A. Angell, et il décrit avec quelle vitesse le temps de relaxation structurel, ou la viscosité, augmente lorsque la température diminue à l'approche de T_g [2]. Selon cette définition, il est possible de classer les systèmes formant des verres comme "fort" et "fragile". Les systèmes présentant un comportement super-Arrhenius de la viscosité à l'approche de T_g sont appelés fragiles, tandis que ceux affichant une comportement d'Arrhénius sont appelés forts.
A titre d'exemple des corrélations proposées entre les propriétés vibrationnelles et visqueuses, Scopigno *et al.* ont proposé, il y a quelques années, une corrélation

entre la fragilité cinétique et le facteur de nonergodicité de l'état vitreux [3]. Cette dernière quantité représente la limite à longs temps de la fonction de corrélation densité-densité normalisée au facteur de structure statique dans l'état vitreux.
La dépendance en température de ce facteur dans la limite de grandes longueurs d'onde permet d'obtenir un paramètre α qui est en corrélation avec la fragilité cinétique des liquides surfondus pour un certain nombre de différents systèmes. Après ce travail des nombreux progrès ont été fait pour la compréhension de cette corrélation même si il semble qu'elle est mieux satisfaite dans les systèmes forts et intermédiaires plutôt que dans les systèmes fragiles [4].
D'autres relations ont été proposées entre les propriétés vibrationnelles et visqueuses des verres et l'idée de base d'un lien entre les propriétés élastiques des verres et la fragilité des liquides correspondants reste au moins valable qualitativement, même si aucune des corrélations proposées ne semble valoir pour tous les verres à un niveau quantitatif [4–6].
Cette thèse présente une analyse détaillée des propriétés vibrationnelles de deux verres fragiles, sorbitol et soufre polymère, au moyen de la diffusion inélastique de la lumière (BLS), des rayons x (IXS) et de neutrons (INS). L'utilisation combinée de ces différentes techniques est une *conditio sine qua non* pour une investigation correcte sur la nature du BP et de sa relation avec les propriétés élastiques des verres et avec la fragilité des liquides correspondants.
Le principal échantillon étudié dans cette thèse, le sorbitol, est un système fragile caractérisé par une organisation spatiale des molécules induites par des liaisons hydrogène. Le caractère fragile du sorbitol et la valeur élevée de la position du maximum du BP rendent le sorbitol un très bon candidat pour une étude détaillée des propriétés acoustiques dans la région du BP, en utilisant IXS, car elles compensent en partie les difficultés dues à la résolution en énergie limitée de la technique. La relation entre BP et les propriétés élastiques a été étudiée suivant deux approches différentes: d'un côté la dépendance en température du BP a été comparé à celle des propriétés élastiques mesurées à basse fréquence (GHz) avec BLS; de l'autre côté, une étude précise de la dépendance en température des excitations acoustiques ayant des énergies comparables à celles de la position du BP a été réalisée. Dans le cas de l'autre échantillon étudié dans cette thèse - soufre polymère - seulement la dépendance en température de la dynamique vibrationnelle à basse et haute fréquence (THz) a été étudiée.
Dans les deux systèmes la dépendance en température des courbes de dispersion acoustique à haute fréquence peut être décrite avec une bonne approximation dans un cadre quasi-harmonique, et l'atténuation acoustique correspondante est définitivement d'origine non dynamique. En outre, dans le cas du sorbitol, la dépendance en température du BP est entièrement décrite par les transformations correspondantes du continuum élastique et sa forme peut être reproduite quantitativement par les courbes de dispersion et par l'atténuation acoustique à haute fréquence, ce qui suggère une forte relation entre les propriétés acoustiques dans la région mésoscopique et le BP. Enfin, les informations collectées sur les modes

acoustiques du soufre et du sorbitol dans une large gamme de fréquence - dans la gamme de fréquences du GHz au moyen de BLS et dans le THz au moyen de IXS - nous permettent aussi de tester la validité de certaines des corrélations proposées entre les propriétés visqueuses des liquides surfondus et les propriétés vibrationnelles des verres. Les deux systèmes étudiés ici se révelent être un défi pour les corrélations proposées et nous permettent de mieux comprendre le sens de ces corrélations.

La thèse a été établie selon le schéma suivant:

- Le premier chapitre est consacré à un résume des principaux concepts concernant la phénoménologie de la transition vitreuse. Après avoir présenté quelques comportements universels des liquides surfondus, le reste du chapitre rapporte une brève description de l'état vitreux, avec une attention particulière aux propriétés thermodynamiques et de transport.

- Dans le deuxième chapitre les principales caractéristiques de la dynamique vibrationnelle dans des verres à l'échelle nanométrique sont mentionnées. Le BP est ici introduit avec quelques-uns entre les différents modèles rapportés dans la littérature pour expliquer son origine. Une vue d'ensemble sur les corrélations entre les propriétés élastiques des verres et le BP est ensuite discutée. Enfin, la dernière partie du chapitre présente un bref résumé de certaines des relations proposées entre la dynamique lente dans la phase liquide surfondu et la dynamique rapide des verres.

- Le troisième chapitre présente l'étude des fluctuations de la densité du sorbitol et du soufre mesurées au moyen de BLS. Après un bref rappel des principes de base de la spectroscopie BLS nous introduisons les deux échantillons étudiés dans cette thèse . Les propriétés élastiques de ces systèmes dans la gamme de fréquences de GHz sont ensuite discutées en référence aussi à quelques-unes des corrélations proposées avec les propriétés des correspondants liquides visqueux.

- Le quatrième chapitre est consacré à l'étude de la dynamique à haute fréquence du verre de sorbitol. Les principes de base de la spectroscopie IXS sont rappelés. Nous retrouvons des anomalies élastiques dans la courbe de dispersion du sorbitol à l'échelle nanométrique. Une étude de la dépendance en température de ces anomalies montre qu'elles peuvent être traitées dans une approche quasi-harmonique, en accord avec les données à basse fréquence discutées dans le troisième chapitre. La relation entre le paramètre de non-ergodicité et la fragilité cinétique pour le cas du sorbitol est ensuite discutée.

- Dans le cinquième chapitre nous discutons la relation entre le BP et les propriétés élastiques du sorbitol. Le BP a été mesuré l'aide d'un spectromètre de

diffusion inélastique des neutrons de type “temps de vol”, dont les principes de base sont signalés au début du chapitre. Les modifications du BP avec la température sont complètement dictées par les transformations correspondantes du milieu élastique macroscopique. En outre, le BP peut être quantitativement décrit par la dépendance en fréquence de la vitesse du son et atténuation mesurées à haute fréquence. Enfin nous présentons une comparaison avec un modèle théorique récent pour le BP.

- Le sixième chapitre décrit la dynamique vibrationnelle à haute fréquence d'un verre polymère de soufre. Les mesures IXS ont été réalisées au cours de mon mémoire de maîtrise en 2006 et sont ici mises en relation d'un côté avec les résultats à basse fréquence mesurés au cours de mon travail de thèse et rapportés dans le troisième chapitre, et de l'autre avec les informations sur la VDOS et sur la fragilité du matériel. La dynamique à haute fréquence du soufre ne présente aucun signe des anomalies élastiques trouvées dans le cas du sorbitol ou d'autres systèmes. Cette incongruité apparente peut être expliquée en regardant le BP du soufre, qui est situé à l'extérieur de la fenêtre d'énergies qui peut être sondée par IXS.

- Dans le septième chapitre nous résumons les principaux résultats de ce travail de thèse. En particulier une comparaison avec d'autres systèmes montre comment la présence des anomalies élastiques à l'échelle nanométrique semble être une caractéristique universelle des verres et elle est fortement liée au BP. La dernière partie du chapitre présente un résumé des résultats sur les corrélations entre la fragilité des liquides visqueux et les propriétés élastiques des verres.

Enfin dans les conclusions nous signalons une vue d'ensemble sur les résultats de cette thèse avec quelques idées sur les perspectives futures de ce type d'études.

Introduction

One of the most challenging issues in Solid State Physics concerns the understanding of the vibrational properties of glasses. Despite of the lack of long range order, this class of systems is characterized by some universal behaviors that strongly differ from those of their crystalline counterparts. In particular, an anomaly present in the vibrational density of states (VDOS), $g(E)$, at energies of few meV has attracted much interest due to its universal occurrence in glasses [1]. This anomaly is best evidenced as a broad bump, known as boson peak (BP), appearing in the reduced density of states $g(E)/E^2$ over the Debye, elastic continuum prediction in an energy range where the Debye model still works reasonably well for the corresponding crystals.

Albeit the BP was first discovered more than 40 years ago, no agreement exists on its physical origin and it still remains the subject of an increasing number of theoretical and experimental works. There is a general agreement that the boson peak is a manifestation of disorder, but the question of whether this peak is related to a peculiar behavior of the acoustic excitations present in the corresponding energy range or to the existence of some additional modes, specific of the glassy state, is still unanswered. The absence of a clear theoretical frame to serve as a reference and the difficulty of disentangling system specific effects from universal behaviors in both experimental and numerical simulation results makes in fact slow the progress in the field.

The vibrational properties of glasses seem also to be related to the viscous properties of the corresponding deeply undercooled melts above the glass transition temperature, T_g, which are grasped by the value of the kinetic fragility. This parameter was introduced for the first time by C. A. Angell, and describes how fast the structural relaxation time, or the viscosity, increases with decreasing temperature on approaching T_g [2]. Following this definition, it is possible to classify glass formers as "strong" and "fragile". The systems showing a super-Arrhenius behavior of the viscosity on approaching T_g are called fragile, while those displaying an Arrhenius behavior are called strong.

As an example of the correlations proposed between vibrational and viscous properties, Scopigno *et al.* proposed some years ago a correlation between the kinetic fragility and the nonergodicity factor in the glassy state [3]. The latter quantity represents the long time limit of the density-density correlator in the glassy state.

From the temperature dependence of this factor in the long-wavelength limit, it is possible to extract a parameter α that correlates with the kinetic fragility in the supercooled liquid for a number of different systems. After this work, a significant progress in the understanding of this correlation has been achieved, though it seems that it holds better for strong and intermediate glass-formers than for fragile systems [4].
Other relations have been proposed as well between vibrational and viscous properties of glasses and the basic idea of a connection between elastic properties of glasses and the fragility of the corresponding liquids remains at least qualitatively valid, even though none of the proposed correlations seems to hold for all glasses at a quantitative level [4–6].
This Thesis reports a detailed analysis of the vibrational properties of two fragile glasses, sorbitol and polymeric sulfur, by means of inelastic light (BLS), x-ray (IXS) and neutron (INS) scattering spectroscopies. The combined use of these different techniques has been found to be a *condicio sine qua non* for a correct investigation of the nature of the BP and of its relation with the elastic properties of glasses and with the fragility of the corresponding melts.
The sample mostly studied in this Thesis, sorbitol, is a fragile glass-former characterized by a spatial organization of the molecules induced by hydrogen bonds. Its very fragile character together with a quite high boson peak position, make sorbitol a very good candidate for a detailed investigation of the acoustic properties in the boson peak region using IXS, since they partly counterweight the difficulties deriving from the limited energy resolution of the technique. The relation between BP and elastic properties has been investigated following two different approaches: from one side the temperature dependence of the boson peak has been compared to that of the elastic properties measured at low frequency (GHz) with BLS; on the other side, an accurate study of the temperature dependence of the acoustic excitations at energies comparable to the boson peak position has been performed as well. In the case of the other sample investigated in this Thesis - polymeric sulfur - only the temperature dependence of the vibrational dynamics at low and high frequencies (THz) has been studied.
In both systems the temperature dependence of the high frequency acoustic dispersion curves is found to be described to a good approximation within a quasi-harmonic picture, and the corresponding acoustic damping is definitively non dynamic in origin. Moreover, in the case of sorbitol, the BP scales with the elastic continuum and its shape can be quantitatively reproduced by the high frequency dispersion curves and sound attenuation, suggesting a strong connection between acoustic properties in the mesoscopic range and boson peak.
Finally, the collected information on the acoustic modes of sulfur and sorbitol in a wide frequency range - in the GHz frequency range by means of BLS and in the THz one by means of IXS - allows us also to test the validity of some of the proposed correlations between viscous properties of supercooled liquids and vibrational properties of glasses. The two systems studied here come out to be

a challenge for the proposed correlations, and allow us to better understand the meaning of these correlations.

The Thesis has been set out according the following scheme:

- The first Chapter is devoted to a review of the main concepts regarding the phenomenology of the glass transition. After presenting some of the universal behaviors of supercooled liquids, the rest of the Chapter reports a brief description of the glassy state, with particular attention to thermodynamic and transport properties.

- In the second Chapter the main characteristics of the vibrational dynamics in glasses at the nanometer length scale are reported. The boson peak is here introduced, together with some of the different models reported in literature to explain its origin. An overview on the correlations between elastic properties of glasses and boson peak is then discussed. Finally, the last part of the Chapter reports a brief summary of some of the proposed relations between the slow dynamics in the supercooled liquid phase and the fast dynamics of glasses.

- The third Chapter presents the BLS investigation of the density fluctuations in glassy sorbitol and sulfur. After a brief summary of the basic principles of BLS spectroscopy, a presentation of the two samples studied in this Thesis is reported. The elastic properties of these systems in the GHz frequency range are then discussed also with reference to some of the proposed correlations to the properties of the corresponding viscous melt.

- The fourth Chapter is dedicated to the study of the high frequency dynamics of the glass of sorbitol. The basic principles of the IXS spectroscopy are recalled. Peculiar anomalies are found in the dispersion curve of sorbitol at the nanometer length scale. A temperature dependent study of these anomalies shows that they can be treated within a quasi-harmonic approach, in agreement with the low frequency data discussed in the third Chapter. The relation between the nonergodicity factor and the kinetic fragility for the case of sorbitol is then discussed.

- In the fifth Chapter the relation between boson peak and elastic properties of sorbitol is discussed. The boson peak has been measured using an inelastic neutron time of flight spectrometer, whose basic principles are reported at the beginning of the Chapter. The changes of the BP with temperature are found to be completely dictated by the corresponding transformation of the macroscopic elastic medium. Moreover the boson peak can be quantitatively described by the measured frequency dependence of the high frequency sound velocity and attenuation. Finally a comparison to a recent theoretical model for the BP is presented.

- The sixth Chapter is dedicated to the high frequency vibrational dynamics of polymeric glassy sulfur. The data have been collected during my master Thesis in 2006 and are here discussed in relation to the low frequency results measured during my PhD work and reported in the third Chapter and to both the BP and the fragility of the system. The high frequency dynamics of sulfur does not display any signature of the elastic anomalies found in sorbitol and in other systems. This apparent incongruity can be explained looking at the BP of sulfur, which is located at energies outside the window which can be probed by IXS.

- In the seventh Chapter the main results of this Thesis work are summarized. In particular a comparison with other systems shows how the presence of elastic anomalies on the nanometer length scale seems to be a universal feature of glasses and is strictly related to the boson peak. The last part of the Chapter is instead dedicated to update our evaluation of some correlations proposed between the vibrational properties of glasses and the kinetic fragility of liquids.

Finally a general view of the results of this Thesis is reported in the Conclusions together with some ideas on the future perspectives of this kind of studies.

Résumé du chapitre 1

La compréhension fine de l'état vitreux est encore une des questiones fondamentales de la physique de la matière condensée aujourd'hui. La transition vitreuse présente, en fait, une phénoménologie assez semblable pour des systèmes extrêmement variés, malgré la présence du désordre structurel.
La façon la plus courante pour produire un verre consiste à refroidir un liquide suffisament rapidament pour éviter la cristallisation à sa température de fusion T_m. Dans ces conditions, en dessous de T_m, le liquide est alors dans un état métastable appelé liquide surfondu. Si l'on diminue encore la température du système, sa viscosité augmente très fortement et la dynamique du système ralentie jusqu'à l'arrêt à la température de transition vitreuse T_g. En dessous de cette température, le système est hors d'équilibre dans un état appelé état vitreux.
Les principaux aspects de cette phase de liquide surfondu sont présentés dans la première partie du chapitre. Dans le reste du chapitre, les aspects généraux de l'état vitreux sont présentés en se référant plus particulièrement au comportement particulier des propriétés thermiques du verre telles que la capacitè thermique et la conductivitè thermique. En effet, toutes ces quantités physiques, á basse température se comportent de manière inattendue si on les compare à celles des cristaux issus de la thèorie de Debye.

Chapter 1

Phenomenology of glasses

Glasses are known and used by man since the Stone Age. The first manufactured products appear to date back to the 2nd millennium BC in the Old Kingdom Egypt and in the Eastern Mesopotamia. Despite of millenniums of history, this class of materials persists fascinating men's life due to the continuous discoveries of new properties and applications.
In general a glass can be viewed as a liquid in which a huge slowing down of the diffusive motion of the particles has destroyed its ability to flow on experimental time scales, thus remaining frozen in a metastable state. The most common way to produce a glass consists on cooling a liquid fast enough to avoid crystallization. The glassy state can be obtained also through different less conventional routes like: i) condensation of gas at low temperature; ii) application of hydrostatic pressure; iii) chemical reactions, such as polymerization or condensation of chemically reacted vapors. Therefore, the possibility to obtain a glass is not strictly related to the material itself, but it rather depends on the available time allowed to a system to solidify into a disordered structure [7, 8]. For this reason the glassy state can be considered as the "*fourth state*" of conventional matter: a glass is solid as in crystalline state, but without long range order as in the liquid state [9].
The presence of coexisting liquid and solid properties, led to the formulation of several different "glass" definitions. For the US National Research Council a glass is "an amorphous material which exhibits the glass transition, this being defined as that phenomenon in which a solid amorphous phase exhibits, by changing the temperature, a more or less abrupt change in the derivative thermodynamic properties, such as heat capacity or thermal expansivity, from crystal-like to liquid-like values". The region over which the change of slope occurs is termed the "glass transition temperature T_g".
The behavior of glass forming systems is broadly recognized as being rich in phenomenology both in the supercooled and in the glassy state. Despite of the large efforts done in the last decades, many aspects remain poorly understood and the understanding of the glassy state is still considered as one of the most challenging topics in condensed matter.

1.1 The glass transition

When a liquid is cooled below its melting temperature T_m two distinct processes can take place: either crystallization or vitrification. The occurrence of these solid phases can be checked by looking at the temperature dependence of extensive thermodynamic variables such as volume, entropy or enthalpy at constant pressure. Figure 1.1 shows a schematic drawing of a liquid's volume or enthalpy during cooling. The crystallization process corresponds to an abrupt jump in volume or enthalpy at the melting temperature, while the glass formation is characterized by a smoother decreasing behavior. In fact if the liquid is cooled below T_m rapidly enough so that detectable nucleation and crystal growth cannot occur, it falls out of equilibrium and becomes supercooled. Upon further cooling the viscosity of the liquid increases until the system becomes solid-like around T_g.

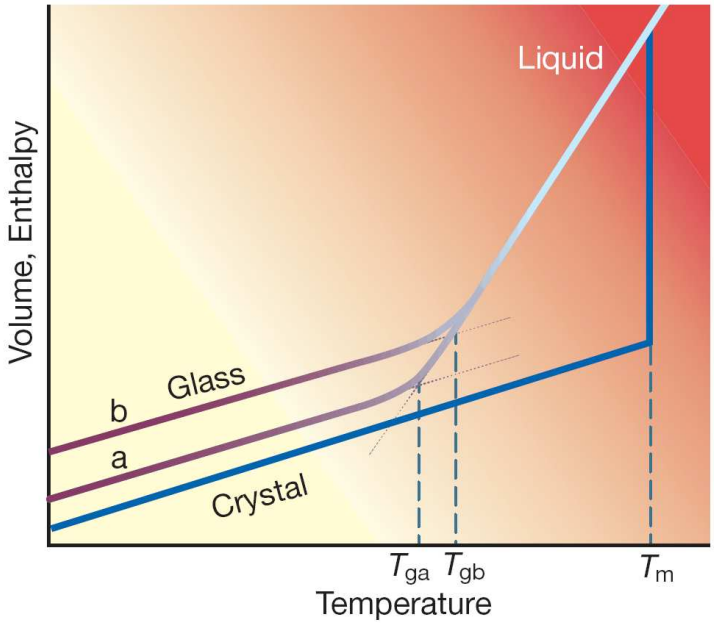

FIGURE 1.1: Volume or enthalpy temperature dependence at constant pressure. The glassy state is characterized by a gradual change in slope in the region around T_g, while crystallization is signed by an abrupt decrease at T_m. T_{ga} and T_{gb} represent the effect on the glass transition of a slower or faster cooling rate, respectively [10].

The change in slope of thermodynamic variables implies a discontinuity in the corresponding derivative variables, such as thermal expansion coefficient α_T or heat capacity C_P. Figure 1.2 reports the temperature dependence of C_P for different glass forming systems. On crossing the glass transition temperature from the liquid side, the heat capacity of the system drops abruptly in a narrow temperature range.

At first sight the vitrification would seem similar to a second-order phase transition. In fact, following the Ehrenfest criterion, the order of a phase transition is defined by the lowest order derivative of the Gibbs energy, G, showing a discontinuity at the phase transition temperature. In the case of crystals, the solidification

process corresponds to a jump in the volume $V = (\partial G/\partial P)_T$ (first order phase transition), while in glasses the discontinuity takes place in the heat capacity $C_p = -T(\partial^2 G/\partial T^2)_P$.

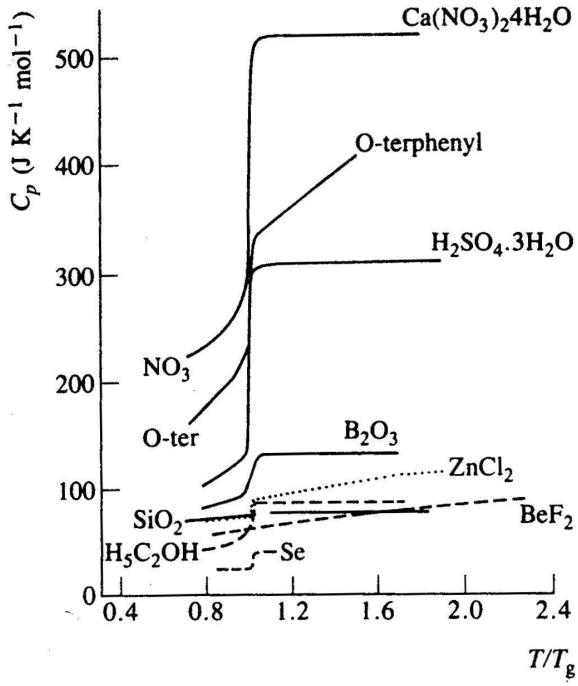

FIGURE 1.2: Heat capacity C_P as a function of the reduced temperature T/T_g for different glass forming liquids. The glass transition corresponds to a discontinuity in the C_P temperature dependence [11].

For glasses, actually this classification scheme is not appropriate, being the glass transition dependent on the thermal history and the cooling rate. Indeed, whether or not a given liquid crystallizes during cooling before T_g is reached, is strictly a kinetic problem involving the rate of nucleation and growth of the crystal on the one hand, and the rate at which the thermal energy can be extracted from the cooling liquid on the other [12]. The slower the cooling rate of the liquid, the larger is the supercooled region and thus, the lower is the glass transition temperature. This behavior is described by the two lines "a" and "b" in Figure 1.1: a slower cooling rate implies a lower solidification temperature T_{ga}.
The value of T_g depends as well on the time scale of the experiment used to observe the process. As shown in Figure 1.1, the liquid and glassy phases are not really distinct; the glass is solid in the sense that the characteristic time scale of diffusivity becomes so large to appear infinite with respect to any experimental time. The slowing down of the diffusive motion of supercooled liquids is expressed through the relaxation time τ_α, that represents, generally speaking, the characteristic time on which the slowest measurable process relaxes to equilibrium. More specifically, the supercooled phase, thus the region where $T_m > T > T_g$, is characterized by more than one relaxation with a "fast" one ($\sim 10^{-12}$s) related to vibrations of the particles around the disordered instantaneous positions, and the "slow" structural one related to the cooperative rearrangements of the disordered structure around which the fast vibrations take place [11].

Cooling down from the liquid phase, the system falls out of equilibrium: the slow liquid degrees of freedom are no more able to explore the whole phase space and the relaxation time of the under-cooled melt, or the viscosity proportional to it through the Maxwell relation $\eta = G_\infty \tau_\alpha$[1], suddenly grows by several orders of magnitude in a relatively small temperature interval between T_m and T_g [7]. From these considerations, it naturally follows that the material will behave as a liquid or solid depending on the time necessary to the system to relax into a new equilibrium configuration with respect to the experimental time scale. This assertion represents a clear signature of the kinetic nature of the glass transition. In particular, the vitrification takes place when the structural relaxation time, called also α-relaxation, becomes comparable with the time necessary to perform a measurement. For experimental times $\tau_{exp} > \tau_\alpha$ the material will appear liquid-like, while for $\tau_{exp} < \tau_\alpha$ it behaves as if it were solid-like. In this way it is possible to define T_g as the temperature where τ_α corresponds to a time scale of ~ 1000 s, or where the viscosity reaches a value of 10^{13} poise[2].
As said above, the properties of a glass depend on the process by which it is formed. However, the dependence of T_g on the cooling rate is weak (in some systems T_g changes by 3/5 °C when the cooling rate changes by an order of magnitude), and the transformation range is narrow, so that T_g becomes an important material characteristic [10]. In general, the glass transition temperature is measured by means of differential scanning calorimetry (DSC). This technique allows performing a thermal analysis of the system by monitoring the enthalpy variations on varying the temperature across T_g. In this way it is possible to collect information on the heat capacity, being $C_p = (\partial H/\partial T)_P$. T_g is usually defined as the temperature corresponding of the change of curvature in the rise of C_p obtained by heating the system at a constant rate of 10 K/min, from the amorphous solid state.
The mechanisms underlying the glass transition have been studied for decades and a vast variety of theories have been proposed. Notwithstanding, the nature of the glass and the glass transition itself remain, as Philip W. Anderson, a Nobel Prize-winning physicist at Princeton, wrote in 1995, "*the deepest and most interesting unsolved problem in solid state theory*" [13]. A general view of some of the different approaches can be found in Refs. [14–17].

1.2 Potential energy landscape

In 1969 Goldstein proposed a useful topographic description of the dynamics of deeply supercooled liquids and glass transition by looking at the evolution of the system in the space of the configurational coordinates [18, 19]. For example, a system with N particles is characterized by $3N$ coordinates. Each different configuration of the system is described by a point in this space and the dynamics can be thought as the motion of this point over the potential energy landscape (PEL),

[1] Close to T_g the system behaves as a viscoelastic liquid where G_∞ is the infinite-frequency shear modulus ($\sim 10^9$ Pa).
[2] 10 poise = 1 Pa· s.

the surface given by the representation of the potential energy $U(r_1, r_2, ..., r_{3N})$ of the system as a function of the $3N$ particles coordinates in a $3N + 1$ dimensional space. The probability distribution for the potential energy of a state point depends on the temperature, through the Boltzmann factor.

Albeit metastable with respect to crystals, at low temperatures glasses are me-

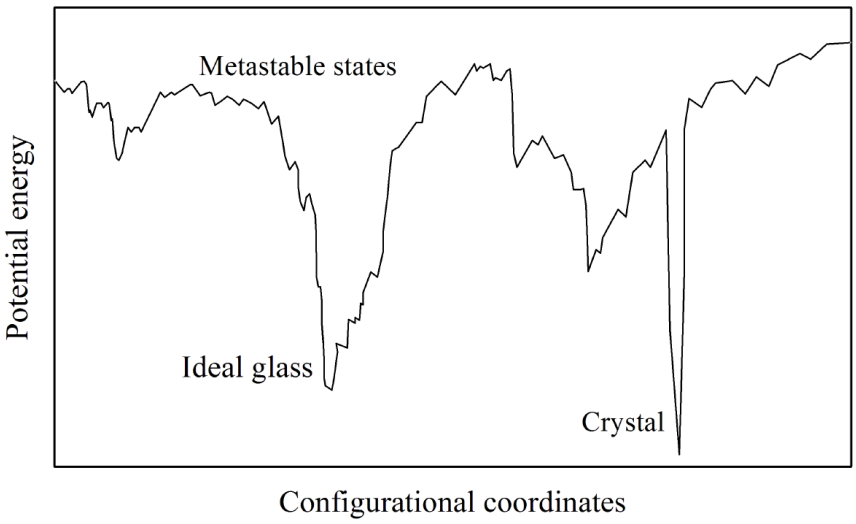

FIGURE 1.3: Potential energy landscape scenario. The crystal state corresponds to the absolute minimum, while the glassy state can occupy different local minima [20].

chanically stable, and by applying a small perturbation the atoms tend to return to their equilibrium positions. These stable configurations of the system correspond to local minima of the potential energy. In general the potential energy surface consists of an absolute minimum, associated to the crystalline state, and a variety of local minima of different depths, always higher than the crystal one, corresponding to particles arrangements that are completely lacking long-range crystalline order (Figure 1.3).

The different minima in the U surface are separated by potential energy barriers. At low temperatures in the supercooled liquid phase, the system can explore the different amorphous minima through activated jumps across the barriers. As Goldstein pointed out, " the transition over a potential barrier in U space is in some sense *local*, in the sense that in the rearrangement process leading from one minimum to a *near-by* one, most atomic coordinates change very little, and only those in a small region of the substance change by appreciable amounts".

As reported in the next sections this scenario is able to give an intuitive description of several phenomenological features of glass forming systems.

1.3 The supercooled liquid phase

For what said above, it is intuitive thinking that the vitrification process should influence the dynamics of the system more that the structure. The average distribution of particles separation is described by the static structure factor S(Q). On crossing the glass transition temperature, the S(Q) of supercooled liquids and that of the corresponding glasses are very similar. From the density point of view, it is possible to see a small difference between the high temperature liquid (above the melting temperature) and the supercooled one. The S(Q), correspondingly, shows a small variation of the first sharp diffraction peak (FSDP) position, which on cooling shifts toward higher wave-vectors due to the decreasing density.
On the other side, the dynamics of glass forming liquids displays an extremely complex behavior that keeps attracting many researchers. In the following, a brief treatment of some of the most intriguing features of the supercooled phase is presented.

1.3.1 Relaxation processes

Beyond the α process, glass formers exhibit other secondary relaxation processes. These subtle dynamical phenomena are commonly referred to as β relaxations and are always at frequencies higher than the structural α relaxation. Various systems present more secondary relaxations which are governed by different molecular mechanisms. Some are trivial rotational motion of a small isolated group of the entire molecule and others are nontrivial as in rigid molecular glass formers or polymers that have no side group [21]. Among the different secondary relaxations, the most famous one is the Johari-Goldstein (JG) β relaxation, due to its intermolecular character and presence in all types of glass formers [22, 23]. The origin of this process is a matter of dispute and many theoretical and experimental works have been performed on this topic. The mechanism of the interplay between the fast β JG and the slow α relaxation process in the liquid-glass transformation is indeed sometimes considered as the key to understand how and why a glass forms from an equilibrium melt. According to Johari, the β JG relaxation is a nonhomogeneous process, associated to the presence of "islands of mobility" in the system, due to local rearrangements of molecules. Figure 1.4 shows the relation between the α and β JG relaxation in the case of sorbitol [24]. While the slow process "diverges" at the glass transition temperature, the fast one persists also in the glassy state below T_g.

The JG process can be described, both in the glassy and in the supercooled liquid state, by an Arrhenius law $\tau_\beta = \tau_\infty exp(E_a/K_BT)$, thus with a Boltzmann factor containing the activation energy of the process E_a and a high-temperature constant τ_∞, related to the vibrational dynamics. While this behavior below T_g is commonly observed, the Arrhenius behavior above T_g is more controversial [24]. The α-process, instead, shows a different behavior as explained in the next section. It is interesting here noting that in the case of sorbitol, reported in Figure 1.4, the Arrhenius temperature dependence of τ_β below T_g changes to a second, steeper

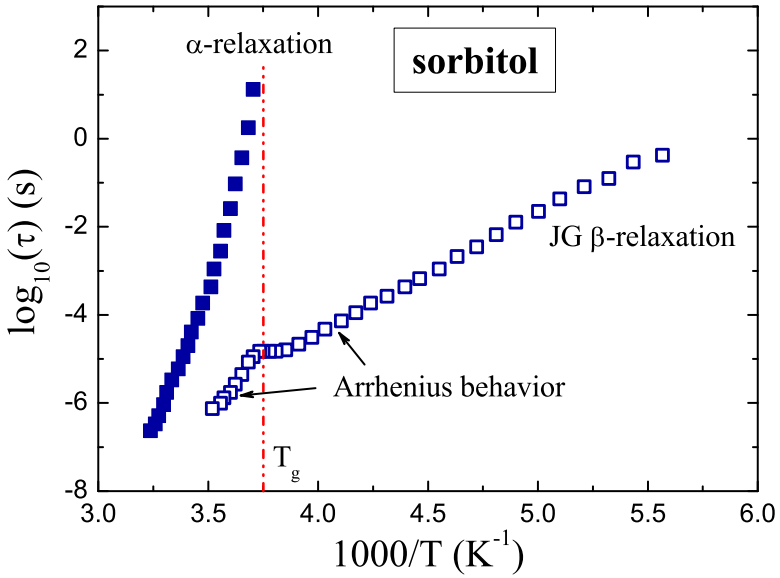

FIGURE 1.4: Relaxation times of sorbitol for the α-process (full squares) and the secondary β JG-process (open squares) as a function of the inverse temperature $1000/T$. The dashed red line indicates the glass transition temperature. Adapted from [24].

(larger value of E_a) Arrhenius trend above T_g [24]. Many other systems exhibit the same behavior and the change in slope at the glass transition temperature has been interpreted as mimicking of the abrupt but steady change of enthalpy, entropy, and volume when crossing T_g [25]. These evidences imply that a strong interaction should exist between structural α and Johari-Goldstein relaxation in a wide temperature range [26].

The relaxation time of a system at a given temperature can be measured by means of different techniques, such as photocorrelation or dielectric spectroscopy. In general the way in which a system relaxes after a perturbation is applied is described by a response function, thus a function that describes the temporal or frequency evolution of the response to the external disturbance. Figure 1.5 shows the dielectric loss spectra of two different glass formers, diethyl phthalate (a) and propylene carbonate (b). In both cases the peak related to the α-process is well defined at low frequencies, while the secondary relaxation is evident only in the case of diethyl phthalate. Nevertheless, propylene carbonate presents as well an extra feature at higher frequency with respect to the α-peak. The appearance of this "excess wing" (EW) has been detected also in other systems and its nature has been highly disputed. Some authors identified the EW as an inherent part of the α-relaxation while recent experimental results suggest that the EW is nothing but the high-frequency side of a JG peak masked by the structural one[3] [8, 26].

[3]This assertion comes from the observation of the evolution of the EW into a β peak on increasing pressure.

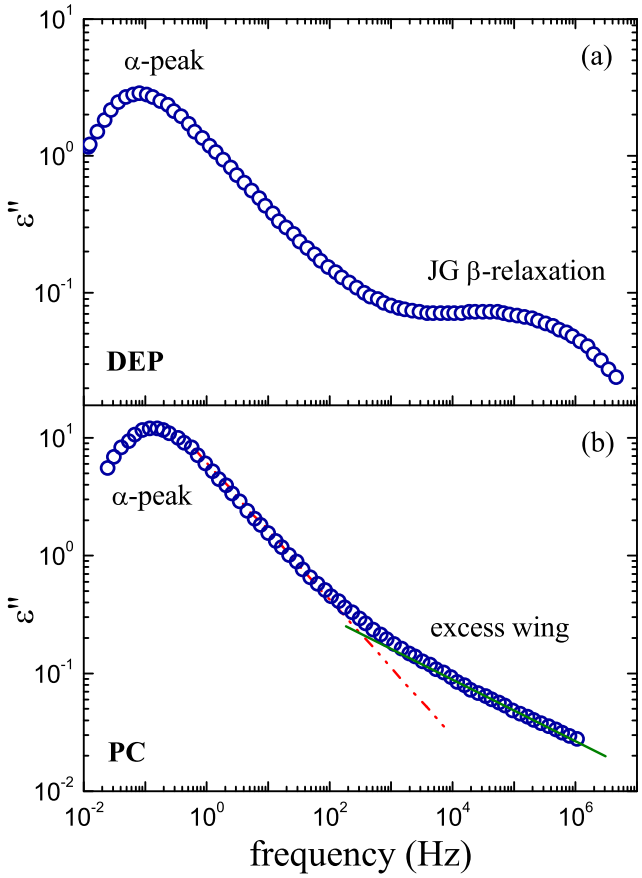

FIGURE 1.5: Dielectric spectra of (a) diethyl phthalate [27], which has a resolved JG-peak, and (b) propylene carbonate [28], which has an unresolved secondary relaxation (excess wing). The green solid line in the lower graph shows the additional power law with a weaker slope than the α-relaxation (red dash-dotted line). Adapted from [8].

Relaxation process in supercooled liquids can be investigated also by measuring at a given temperature the normalized autocorrelation function $\phi_Q(t)$, which monitors the decay of density fluctuations $\delta\rho$ being

$$\phi_Q(t) = \frac{\langle \delta\rho_Q^*(0)\delta\rho_Q(t)\rangle}{\langle \delta\rho_Q^*(0)\delta\rho_Q(0)\rangle} \tag{1.1}$$

In the simplest case the relaxation function is exponential so that there is a unique time τ characterizing the process. This is not the case for viscous liquids close to T_g. In fact these systems exhibit a clear non-exponential, or multi-step decay pattern due to the presence of secondary relaxation processes. In Figure 1.6 a sketch of the temporal behavior of $\phi_Q(t)$ of a supercooled liquid close to the glass transition is reported [29]. At short time the decay is related to the free motion of the atoms and to their collisions. The microscopic regime is then followed by a first step and a long time plateau. The presence of a secondary relaxation process

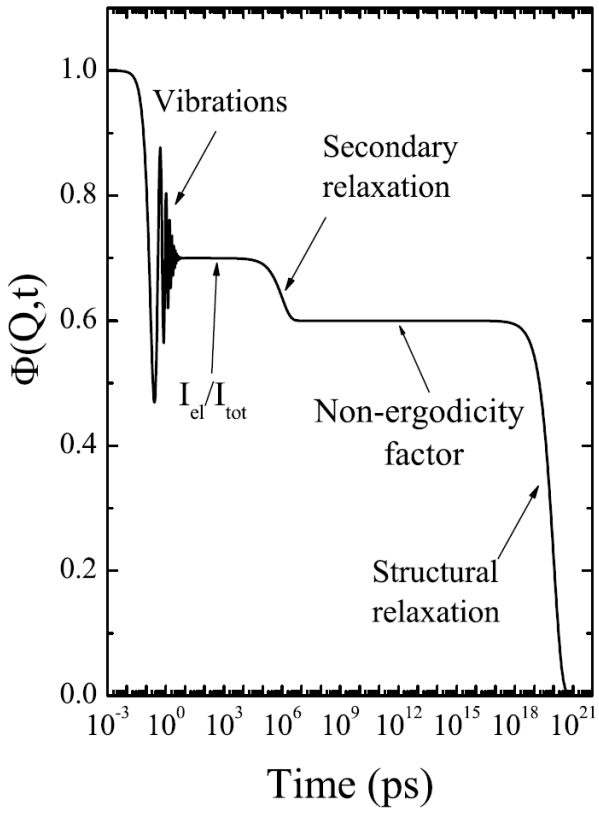

FIGURE 1.6: Sketch of the temporal evolution of the density correlator 1.1. The various temporal regimes are described in the text. Taken from [29].

leads to the appearance of an additional step. This situation will be treated more detail in section 2.4. The α-relaxation occurs on a longer timescale and can be often described by a stretched exponential, or Kohlrausch-Williams-Watts (KWW) function

$$\phi_Q(t) = exp\left[-(t/\tau_K)^{\beta_K}\right] \tag{1.2}$$

In this expression τ_K is the characteristic relaxation time and β_K the stretching parameter, with $0 < \beta_K < 1$, which quantifies the deviation from a simple exponential behavior.

The microscopic dynamics close to the glass transition can be quantitatively described by the "Mode Coupling Theory" (MCT) [17, 30] and, in fact, the approach to the long time plateau of $\phi_Q(T)$ is often called the mode coupling (MC) β process. Albeit the name, this process is completely distinct from the other secondary relaxations described above. In frequency space, the MC β relaxation corresponds to a minimum of the susceptibility instead than a loss peak as for ordinary secondary relaxation [21].

Figure 1.7 shows the self part of $\phi_Q(T)$ obtained from a molecular dynamic simulation of a supercooled binary Lennard-Jones system [31]. On approaching the vitrification, thus on lowering the temperature, the two-step shape associated to the α and MC β process becomes clearly more marked. The rising separation between these two processes has been often related to an increase of the nonexponentiality of the structural relaxation close to T_g (see equation 1.2), which leads

to a decrease of the stretching parameter β_K close to T_g [32, 33].

The two-step behavior of the dynamical correlation function can be described in

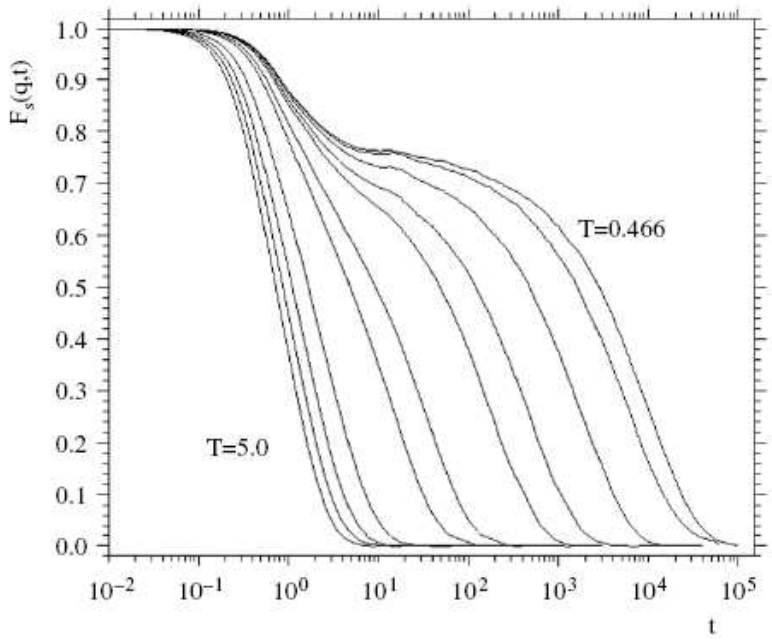

FIGURE 1.7: Temporal evolution of the self part of the density correlator 1.1 in a binary Lennard-Jones system [31]. The MC β relaxation process becomes more visible on approaching the glass transition temperature.

the potential energy landscape framework. Indeed glass formers can be considered as composed by small groups of particles trapped in cages formed by their neighbors, in which the particles are entangled for a time that increases on decreasing the temperature due to the raising viscosity. The MC β relaxation is related to the particle vibrations within their local cages, while the structural relaxation time τ_α associated to the α process corresponds to the time necessary for a particle to escape the cage. This scenario has been supported by several studies on the temporal evolution of the mean square displacement of the particles [31].

In Goldstein's representation, the vibrations of the particles within their cages correspond to vibrations around a local minimum of the potential energy surface, whereas the jumps across different barriers represent the local decaging of some particles. On increasing the number of activated rearrangements, thus of decaging processes, the system decorrelates and the intermediate scattering function overtakes the plateau, giving raise to the α relaxation [19].

The presence of a relaxation process can be observed also by looking at the frequency dependence of the sound velocity and absorption of the acoustic waves. Figure 1.8 shows a sketch of the frequency dependence of these two quantities in the presence of the structural α relaxation process. In particular the sound velocity exhibits a typical step behavior changing from the relaxed value v_0 at zero frequency to the fully unrelaxed value v_∞ at higher frequencies. At the same time the acoustic absorption displays a maximum when the angular frequency $\omega_\alpha = 2\pi\nu_\alpha$ fulfills the condition $\omega\tau_\alpha = 1$. From the Figure it is also evident that on increasing the temperature, the dynamics shifts toward higher frequencies. The

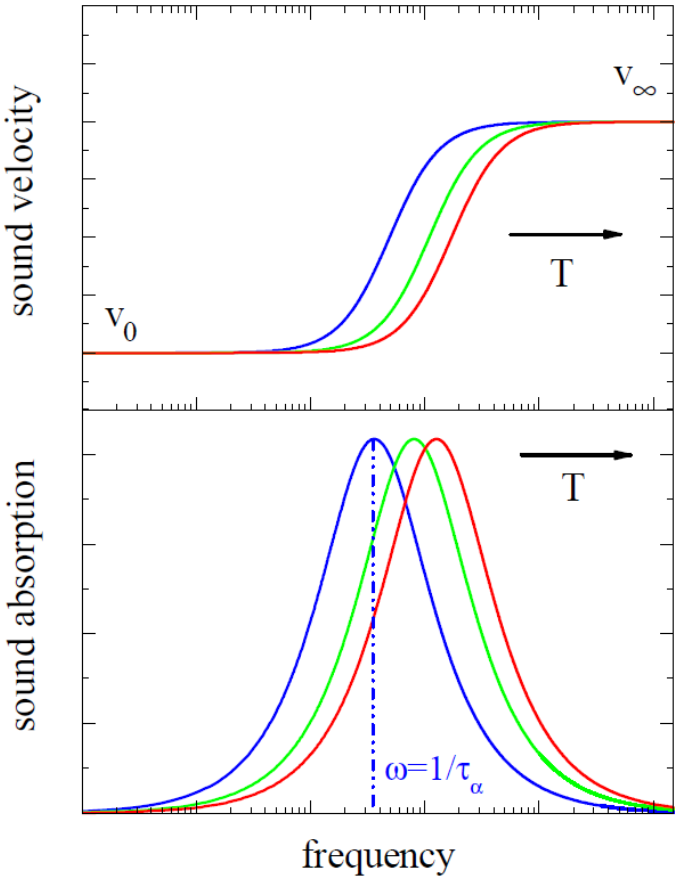

FIGURE 1.8: Sketch of the frequency dependence of the acoustic sound velocity (a) and absorption (b) of glass formers.

simultaneous presence of a secondary β relaxation process leads to the appearance of an intermediate step between v_0 and v_∞ in the behavior of the sound velocity and to a secondary peak in the corresponding acoustic absorption for $\omega_\beta \tau_\beta = 1$ (see Figure 4.22 in section 4.4.1).

1.3.2 Strong and fragile glass forming liquids

One of the most challenging features of the glass transition phenomenology concerns the behavior of the structural relaxation time, or the viscosity, on approaching T_g. As previously reported, on crossing the supercooled liquid phase the vitrification process comes with an enormous slowing down of the structural relaxation. From the viscosity point of view, this behavior corresponds to an increase by several order of magnitude in a narrow temperature range, from values $\sim 10^{-2}$ poise as for a normal liquid, up to values of 10^{13} poise at T_g. Moreover the way in which this raise takes place is strictly related to the nature of the system. Following these observations, C. A. Angell first proposed a classification of supercooled liquids in *strong* and *fragile* systems, depending on the temperature dependence of the viscosity (or τ_α), and consequently on the sensitivity of the liquid structural

rearrangements to temperatures changes.

Figure 1.9 represents the well-known "Angell plot", thus the logarithm of the

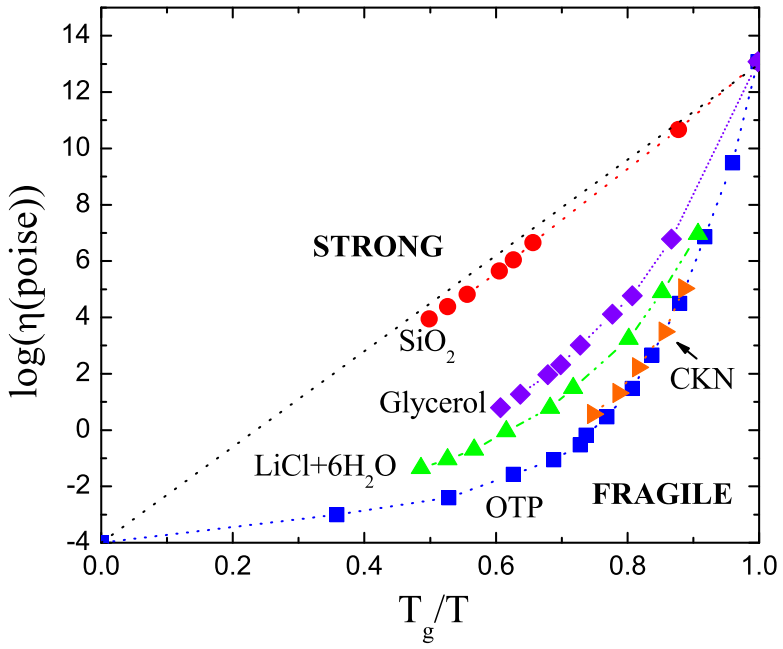

FIGURE 1.9: Angell plot for several glass formers: logarithm of the shear viscosity as a function of the inverse reduced temperature T_g/T, being $\eta(T_g) = 10^{13}$ poise. The black dashed line corresponds to an Arrhenius temperature dependence. The high-temperature limit is fixed at $\eta_\infty = 10^{-4}$ poise. Adapted from [2]

viscosity η as a function of the inverse reduced temperature T_g/T for several glass formers. All those liquids called "strong" show a weak temperature dependence of the viscosity, that can be described by an Arrhenius law

$$\eta = \eta_0^A exp(E_a/K_B T), \tag{1.3}$$

with a high, but nearly constant activation energy E_a and a high-temperature limit η_0^A ($\sim 10^{-4}$ poise) corresponding to a structural relaxation time of $\sim 10^{-14}$ s, typical of purely vibrational degrees of freedom. On the other hand, "fragile" systems are characterized, on approaching T_g, by a much faster temperature dependence of the viscosity which varies in a markedly non-Arrhenius fashion. Looking at their structure, strong materials present covalent or directionally oriented bonds, and can form networking arrangements that strongly decrease the ability of the system to rearrange its structure by varying temperature. SiO_2 and GeO_2 are prototypes of strong systems. Differently, fragile liquids are mainly dominated by simple, non directional Coulomb attractions or by van der Waals interactions forces. Their microscopic structure can be easily changed close to T_g and, with a small thermal excitation, it can be rearranged in a variety of different particle orientations [7].

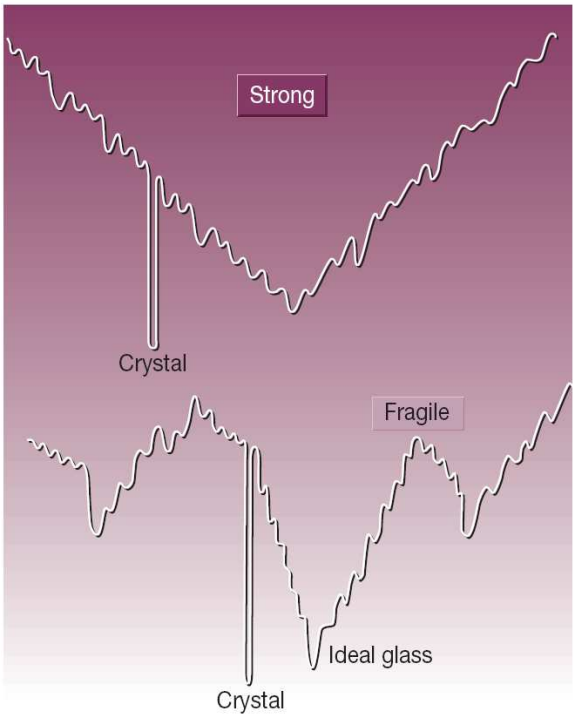

FIGURE 1.10: Schematic representation of the potential energy for strong (top) and fragile (bottom) systems as a function of the configurational coordinates [10].

Ortho-terphenyl (OTP) and polymeric materials are canonical examples of fragile liquids.
From the potential energy landscape point of view, fragile systems are characterized by a high density of local minima separated by relatively low barriers, while strong materials correspond to an energy surface with few minima and high energy walls (Figure 1.10). Hydrogen-bonded materials, such as glycerol, exhibit instead an intermediate behavior. They are believed to be thermodynamically fragile (with a large number of energy minima) and at the same time kinetically strong (high energy barriers for the structural modifications).

Several empirical expressions have been proposed to describe the shape of the viscosity close to the glass transition temperature, but no one is able to well reproduce the data in the whole temperature range [32]. The most used and accepted expression is the Vogel-Tammann-Fulcher (VTF)

$$\eta = \eta_0^{VF} exp\left(\frac{T_A}{T - T_0}\right) \tag{1.4}$$

where T_A and T_0 are just phenomenological parameters. In the limiting case $T_0 = 0$, the VTF law converts into equation 1.3, instead the extrapolation of the viscosity below T_g leads to a divergence at $T = T_0$. In the case of polymeric systems an equivalent relation, known as Williams-Landel-Ferry (WLF), is employed [34]. In general the stronger the non-Arrhenius behavior, the closer is the parameter T_0

to the glass transition value. In many fragile glass formers, the Vogel-Tammann-Fulcher law reproduces reasonably well the data, at least over a limited number of orders of magnitude in viscosity. Other expressions, containing a larger number of parameters, can describe the behavior of fragile systems in a wider temperature range but no one is really able to fit the increase of the viscosity from the melting temperature up to T_g, and many of them do not rest on theoretical bases.
The strong/fragile attitude of supercooled liquids is reflected in the configurational heat capacity. As shown in Figure 1.2, strong materials display a small jump ΔC_p on crossing T_g, while fragile ones present a marked discontinuity. The relationship between viscosity (or τ_α) and heat capacity is not strange. The configurational heat capacity just mirrors the structural changes described by the activation energies related to the shape of the viscosity on approaching T_g. For this reason, the jump in the heat capacity ΔC_p is bigger in systems in which the apparent activation energy increases (more than a factor five) between the melting point and the glass transition [11].
The system-dependent behavior of the viscosity can be described through the fragility parameter m_A. This quantity was introduced and developed by Angell and in its kinetic version describes how fast the viscosity or the structural relaxation time increases with decreasing temperature on approaching the glass transition temperature T_g, being

$$m_A = \left[\frac{d\log(\eta(T))}{d(T_g/T)}\right]_{T=T_g} \tag{1.5}$$

The fragility ranges from $m_A = 20$ for strong systems such as silica, up to values $\simeq 150$ for fragile materials as polymers. The fragility is often, but not always, correlated with an alternative metric,

$$F_{1/2} = 2\left(\frac{T_g}{T^*}\right) - 1, \tag{1.6}$$

where T^* is the temperature where the viscosity is half way, on a log scale, between the value η_∞ and $\eta(T_g)$

$$\frac{[\lg(\eta(T_g)) + \lg(\eta(T_\infty))]}{2} = \lg(\eta(T^*)).$$

The two expressions do not give always the same results being the former sensitive to transitions like liquid-liquid or ring-chain, while the latter, $F_{1/2}$, not [35, 36].
Several fragility expressions have been proposed and they can be classified mainly in two categories related to a kinetic (as above) or thermodynamic approach, and a variety of relationships among these two classes have been controversially suggested [37–39]. Martinez and Angell showed that the kinetic fragility can be correlated to the excess entropy $S_{ex}(T)$, which represents the difference in entropy between the supercooled liquid and the corresponding stable crystalline phase [38]. This quantity, indeed, has a prominent role in the vitrification process.
The influence of entropy was first pointed out by Kauzmann in 1948, by observing that during cooling many liquids loose entropy faster with respect to their crystalline counterparts [40, 41]. The entropy of a glass is strictly related to the

behavior of the heat capacity on crossing T_g from the supercooled liquid phase. Below T_g, the crystalline and glassy state present almost the same heat capacity values, due to vibrational contributions, while the excess above the glass transition is related to the configurational degrees of freedom related to the liquid phase. Since the rate of cooling influences the glass transition temperature, being the slower the rate the lower T_g, there should exist a low limiting value of T_g below which the supercooled liquid phase cannot exist. If it did, the total entropy of the liquid would fall *below* that of the crystal. To avoid this paradox it should exist an ideal glassy state possessing zero residual entropy, characterized by a glass transition temperature T_K where $S_{liq.}(T_K) = S_{cryst.}(T_K)$.
As previously reported, it is possible to define a thermodynamic fragility through the excess entropy. In fact, by looking at the quantity $S_{ex}(T_g)/S_{ex}(T)$ as a function of the inverse rescaled temperature T_g/T, one obtains a plot very similar to the well-known Angell one, where the different systems stand in the same order[4] [38]. From this observation and following equation 1.6, it comes natural to define a thermodynamic fragility as

$$F_{3/4} = 2\left(\frac{T_g}{T^*}\right) - 1 \tag{1.7}$$

where T^* is given by

$$\frac{S_{ex}(T_g)}{S_{ex}(T^*)} = \frac{3}{4}$$

In this case, the value 3/4, and not 1/2, has been chosen because of the difficulties associated on determining the excess entropy at low T_g/T in strong liquids. $F_{3/4}$ has been found strictly related to the corresponding dynamic one $F_{1/2}$ [38]. Owing the limited available data for the excess entropy, this relation cannot be checked in many systems and, consequently, its validity is not supported by the whole scientific community.
Wang and coworkers suggested another relation by defining the thermodynamic fragility through the formula

$$m_T = \frac{\Delta C_p(T_g)}{\Delta S_m} \tag{1.8}$$

where ΔS_m is the entropy of fusion at the melting temperature

$$\Delta S_m = \frac{\Delta H_m}{T_m} = \int_{T_K}^{T_m} \frac{C_p^{liquid}(T) - C_p^{crystal}(T)}{T} dT, \tag{1.9}$$

and $\Delta C_p(T_g) = [C_p^{liquid}(T_g) - C_p^{glass}(T_g)]$ [42, 43]. Moreover the authors found a phenomenological relationship $m_A = 40 m_T$ between these two fragility definitions, which is followed by a great variety of non-polymeric systems[5].
In the last years several works have been done to connect the rapid increase of the α-relaxation time, expressed by the different fragility metrics, to other properties

[4] This statement is not valid in the case of vitreous silica.

[5] In the case of polymeric systems the situation is more complicated being the fragility dependent from other factors as well, such as the molecular weight.

of glass formers in both the liquid and glassy phase. In particular, the discovery of a link between the slowing down of the diffusive motion in the supercooled liquid phase and the vibrational dynamics in the deep glassy phase has intrigued many researchers [3–6, 44–46]. This relation would imply, in principle, the possibility to get kinetic information on τ_α (or on the viscosity η) above T_g by studying the acoustic properties well below T_g, and this would correspond to the existence of a signature of the glassy properties in the liquid phase.
Despite of the great amount of work done in this direction, the origin of these correlations is still not completely understood and their validity is no longer unanimously accepted [47]. This subject will be treated in more detail in the next chapter where the vibrational properties of glasses will be discussed.

1.3.3 Dynamic heterogeneities

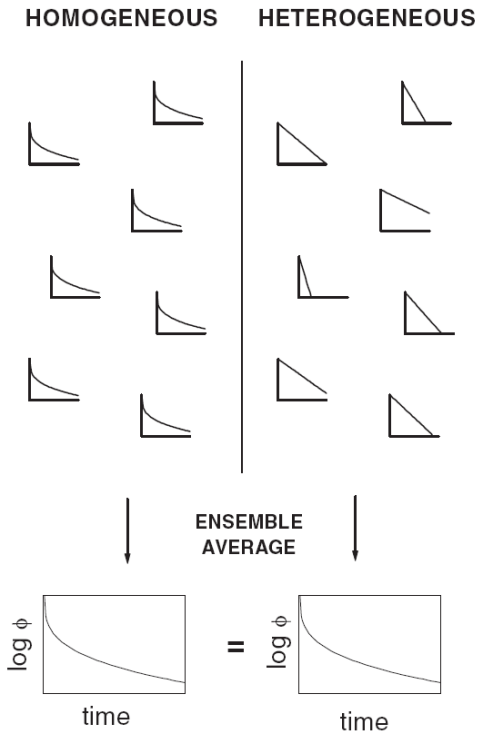

FIGURE 1.11: Schematic representation of the homogeneous and heterogeneous approach on describing the supercooled dynamics [48].

The increase of the nonexponential behavior of the relaxation function described in section 1.3.1 has been often attributed to dynamical heterogeneities that come out with the vitrification process. In general two different approaches could describe the observed deviations from a simple exponential decay: the spatially dynamical *homogeneous* scenario and the *heterogeneous* one [48]. This is schematically described in Figure 1.11. In the first case (left column), the stretched character of the intermediate scattering function $\phi(t)$ (Equation 1.2) is an intrinsic property

of the system in the sense that the relaxation is equally nonexponential in the whole material, and the local dynamics is the same as the ensemble-averaged one. In the dynamical heterogeneous approach (right column), instead, the relaxation of the entire system is nonexponential because different regions have significantly different relaxation times, each one described by a single pure exponential decay, that together with the other processes gives rise to the observed nonexponentiality. This scenario would imply the existence in the system of groups of slow or fast particles displaced in different regions.
Several simulations and experiments have directly established that the dynamical slowing down encountered in glassy materials is accompanied by the existence of a growing correlation length scale over which local dynamics is spatially correlated, thus supporting the heterogeneous scenario [49, 50]. The detection of these spatial correlations of the dynamics requires the study of a "four-point" dynamic susceptibility $\chi_4(t)$, which quantifies the amplitude of spontaneous fluctuations around the average dynamics. This quantity can be measured through the determination of the time-dependent autocorrelation function $F(t) = \langle \delta A(t) \delta A(0) \rangle$ of the spontaneous fluctuations of an observable $A(t)$, such as the density, from its ensemble average $\langle A \rangle$. $F(t)$ is the average of a two-point quantity $C(t,0) = \delta A(t) \delta A(0)$. The presence of dynamic correlation leads to large fluctuations of $C(t)$, whose amplitude gives information on $\chi_4(t)$, being $\chi_4(t) = N \langle \delta C(t,0)^2 \rangle$, where $\delta C(t,0) = C(t,0) - F(t)$, and N the number of particles in the system.
In general $\chi_4(t)$ can be directly accessed in simulations while its experimental determination can be achieved through the evaluation of a three-point dynamic susceptibility, $\chi_x(t) = \partial F(t)/\partial x$, defined as the response of a two point correlator to a perturbing field x. In particular, the temperature three-point dynamic susceptibility, $\chi_T(t)$, allows the experimental determination of the temperature evolution of the number of molecules N_{corr} that are dynamically correlated during the structural relaxation process. A recent study shows that on approaching the glass transition temperature, N_{corr} systematically grows confirming the heterogeneous scenario [50].

1.4 The glassy state

As reported in the previous section, the dynamics of glass forming materials is characterized by many distinguishing behaviors on approaching the glass transition from the liquid phase. Below T_g liquids solidify into a disordered structure, which lacks the long range order typical of crystalline samples. For this reason, it should be natural to think of glasses as of a class of systems showing the same dynamical properties of crystals for wavelengths large enough that the microscopic details are negligible, and with marked system-dependent behaviors on length scales of the order of the interatomic distances. Actually this is not the case. As it will be shown in the following and in the whole thesis, glasses display several universal behaviors on different length scales, which make the study of glasses extremely challenging.

Despite of the presence of structural disorder, the low temperature thermal properties of glasses, such as heat capacity and thermal conductivity, exhibit an unusual universal behavior that strongly differs from that of the crystalline counterparts. The main differences with respect to the corresponding ordered systems appear at low temperatures, thus in a range where the thermally populated acoustic vibrations of the solid have wavelengths much larger that the atomic length scale. Being dependent on these collective excitations, the thermal properties should not be sensible to the internal structure and should present the same behavior for both crystals and glasses. Surprisingly different behaviors were however discovered first by Zeller and Pohl in 1971 [51] and they attracted immediately the interest of the scientific community being related to a very intriguing feature of glasses, the boson peak, as explained in the next chapter.

1.4.1 Classical elasticity and Debye model

The low temperature thermal properties of crystals are well described by the famous Debye's model that is strictly connected with the classical theory of elasticity. In order to understand the glassy phase, a good knowledge of such theories is mandatory. Indeed saying that glasses show different behaviors in the low temperature thermal proprieties with respect to crystals, means that they show a strong departure from Debye's predictions. In the following a brief summary of the Debye model and classical elasticity theory are presented.

Continuum theory of elasticity

The continuum theory of elasticity describes the elastic behavior of a solid on a macroscopic length scale through the behavior of an infinitesimal element of volume interacting with short range forces: it ignores the microscopic atomic structure of the solid, and treats it as a continuum [52]. A general deformation of the system can be described through a continuous displacement field $\mathbf{u}(\mathbf{r})$, specifying the vector displacement of the part of the solid that in equilibrium occupies the position $\mathbf{r}$. The fundamental assumption of the theory is that the contribution to the energy density of the solid at the point $\mathbf{r}$ depends only on the value of $\mathbf{u}(\mathbf{r})$ in the immediate vicinity of $\mathbf{r}$, or, more precisely, only on the first derivatives of $\mathbf{u}(\mathbf{r})$ at the point $\mathbf{r}$.
In general the deformation of a solid can be described through a stress tensor σ_{ij} and a strain tensor ϵ_{kl}. The relation among these two quantities, called Hooke's law, is given by [53]:

$$\sigma_{ij} = \sum_{kl} C_{ijkl}\epsilon_{kl} \tag{1.10}$$

where $i, j, k, l = 1, 2, 3$. In the previous relation, the stress tensor is defined in terms of a force in the i direction acting on a surface element dA_j with the normal

vector in the j direction by

$$dF_i = \sum_j \sigma_{ij} dA_j \tag{1.11}$$

while the strain tensor is defined in terms of the infinitesimal displacement $\mathbf{u}(\mathbf{r})$ at $\mathbf{r}$ by

$$\epsilon_{ij} = \frac{1}{2}\left(\frac{\partial u_j}{\partial u_i} + \frac{\partial u_i}{\partial u_j}\right) \tag{1.12}$$

In the case of isotropic materials, the Hooke tensor C_{ijkl} depends only on two independent elastic constants, the Lamé coefficients λ and μ, through the relation

$$C_{ijkl} = \lambda \delta_{ij}\delta_{kl} + \mu\left(\delta_{ik}\delta_{jl} + \delta_{il}\delta_{jk}\right) \tag{1.13}$$

The Lamé coefficient μ is equivalent to the shear modulus G, while the combination of the two values gives information on the bulk and longitudinal modulus K and M through the relations:

$$K = \lambda + \frac{2}{3}\mu \tag{1.14}$$

$$M = \lambda + 2\mu = K + \frac{4}{3}G \tag{1.15}$$

The propagation of elastic waves in an elastic and isotropic medium in absence of external forces, is given by:

$$\rho \frac{\partial^2 u_i}{\partial t^2} = \sum_{l=1}^{3} A_{il} u_l \tag{1.16}$$

with

$$A_{il} = \lambda \partial_i \partial_l + \mu\left(\partial_l \partial_i + \nabla^2 \delta_{il}\right)$$

By considering plane wave solutions $\mathbf{u}(\mathbf{r}, t) = \mathbf{u} e^{i[\mathbf{kr} - \omega t]}$, the equation of motion 1.16 becomes

$$\omega^2 u_i = \sum_l D_{il} u_l \tag{1.17}$$

where D_{il} is the dynamical matrix

$$D_{il} = \frac{1}{\rho}\left[\left(\lambda + \mu\right) k_i k_l + \mu k^2 \delta_{il}\right] \tag{1.18}$$

This means that the equation of motion is reduced to find the eigenvalues of the dynamical matrix. This can be simplified by choosing the direction of the wave-vector $\mathbf{k}$ on the z axis. In this case D_{il} reduces to

$$D = \frac{1}{\rho}\begin{pmatrix} \mu k^2 & 0 & 0 \\ 0 & \mu k^2 & 0 \\ 0 & 0 & \left(\lambda + 2\mu\right) k^2 \end{pmatrix} \tag{1.19}$$

There are three independent sound waves, two transverse ones ($\mathbf{u} \perp \mathbf{k}$) with sound velocity $c_T = \sqrt{G/\rho} = \sqrt{\mu/\rho}$, and a longitudinal acoustic wave ($\mathbf{u} \| \mathbf{k}$) with sound

speed $c_L = \sqrt{M/\rho} = \sqrt{(\lambda + 2\mu)/\rho}$. The Lamé coefficients assume always positive values and, as a consequence of the previous relations, the longitudinal sound velocity in an elastic isotropic solid is always larger than the transverse one.

Connection with classical harmonic theory

The continuum theory of elasticity can be derived also from the long wavelength limit of the harmonic theory for lattice vibrations [54]. In general, the theory of the dynamical properties of a solid can be easily treated by recurring to the adiabatic and the harmonic approximation. The first approximation is based on the fact that typical electronic velocities are much greater than typical ionic velocities. For this reason the electronic dynamics can be disentangled from the corresponding nuclear one and at any moments the electrons can be assumed to be in their ground state for that particular ionic configurations. The harmonic approximation is instead based on the expectation that the atoms will not deviate substantially from their equilibrium positions with respect to the interatomic distance.
Considering a system composed of N particles, the deviation from the average equilibrium position, $\mathbf{R}$, can be written as $\mathbf{r}(\mathbf{R}) = \mathbf{R} + \mathbf{u}(\mathbf{R})$, where the term $\mathbf{u}(\mathbf{R})$ contains the temporal evolution of the system. The interaction among the particles can be described by a pair potential, Φ, and the sum over the all contributions gives the potential energy of the system $U = \frac{1}{2}\sum_{\mathbf{R},\mathbf{R'}} \Phi(\mathbf{r}(\mathbf{R}) - \mathbf{r}(\mathbf{R'})) = \frac{1}{2}\sum_{\mathbf{R},\mathbf{R'}} \Phi(\mathbf{R} - \mathbf{R'} + \mathbf{u}(\mathbf{R}) - \mathbf{u}(\mathbf{R'}))$.
In the harmonic approximation the deviations $\mathbf{u}(\mathbf{R})$ are small and the potential energy can be expanded in Taylor series about its equilibrium position leading to

$$U = \frac{N}{2}\sum \Phi(\mathbf{R}) + \frac{1}{2}\sum_{\mathbf{R},\mathbf{R'}} (\mathbf{u}(\mathbf{R}) - \mathbf{u}(\mathbf{R'})) \cdot \nabla\Phi(\mathbf{R} - \mathbf{R'}) \qquad (1.20)$$
$$+\frac{1}{4}\sum_{\mathbf{R},\mathbf{R'}} \left[(\mathbf{u}(\mathbf{R}) - \mathbf{u}(\mathbf{R'})) \cdot \nabla\right]^2 \Phi(\mathbf{R} - \mathbf{R'}) + ...$$

The linear term vanishes because there are no forces between the particles at equilibrium. As a consequence, the first non vanishing correction to the equilibrium potential energy $U^{eq} = \frac{N}{2}\sum \Phi(\mathbf{R})$ is given by the harmonic quadratic term, which can be expressed as:

$$U^{harm} = \frac{1}{4}\sum_{\substack{\mathbf{R},\mathbf{R'} \\ \mu,\nu=x,y,z}} \left[(u_\mu(\mathbf{R}) - u_\mu(\mathbf{R'}))\right] \Phi_{\mu\nu}(\mathbf{R} - \mathbf{R'}) \left[(u_\nu(\mathbf{R}) - u_\nu(\mathbf{R'}))\right], \quad (1.21)$$

being

$$\Phi_{\mu\nu}(\mathbf{r}) = \frac{\partial^2\Phi(\mathbf{r})}{\partial r_\mu \partial r_\nu}$$

Since the equilibrium term U^{eq} is just a constant, the dynamics of the system is completely described by the harmonic term, which can be written in a more

general form as

$$U^{harm} = \frac{1}{2} \sum_{\substack{\mathbf{R},\mathbf{R'} \\ \mu,\nu}} u_\mu(\mathbf{R}) M_{\mu\nu}(\mathbf{R} - \mathbf{R'}) u_\nu(\mathbf{R'}) \tag{1.22}$$

by defining the dynamical matrix $M_{\mu\nu}(\mathbf{R} - \mathbf{R'}) = \delta_{\mathbf{R},\mathbf{R'}} \sum_{\mathbf{R''}} \Phi_{\mu\nu}(\mathbf{R} - \mathbf{R''}) - \Phi_{\mu\nu}(\mathbf{R''} - \mathbf{R'})$.
The dynamical matrix fulfills the symmetric property:

$$M_{\mu\nu}(\mathbf{R} - \mathbf{R'}) = M_{\nu\mu}(\mathbf{R'} - \mathbf{R}) \tag{1.23}$$

The 3N equations of motion (one for each of the three components of the displacement of the N particles) are given by:

$$\rho \ddot{u}_\mu(\mathbf{R}) = -\frac{\partial U^{harm}}{\partial u_\mu(\mathbf{R})} = -\sum_{\mathbf{R'}\nu} M_{\mu\nu}(\mathbf{R} - \mathbf{R'}) u_\nu(\mathbf{R'}) \tag{1.24}$$

or, in matrix notation,

$$\rho \ddot{\boldsymbol{u}}(\mathbf{R}) = -\sum_{\mathbf{R'}} \mathbf{M}(\mathbf{R} - \mathbf{R'}) \mathbf{u}(\mathbf{R'}) \tag{1.25}$$

Equation 1.24 is the equivalent of the equation of motion 1.16 found within the elastic theory. By considering plane waves solutions, the problem can be re-conducted to the search of the eigenvalues of the dynamical matrix of the harmonic vibrations.

Debye's model

At the beginning of last century, Einstein proposed a model for describing the vibrations in a solid, by considering the system as a collection of 3N independent oscillators, all with the same frequency, characterized by a set of discrete allowed energies values. Despite of the success in describing the temperature dependence of heat capacity, this model was clearly deficient at very low temperatures.
In 1912, Peter Debye introduced a quantum mechanical model which provided a good approximation to the observed heat capacity for solids in a wide temperature range. Debye's model ignores the details of the atomic structure and treats the solid as a continuous elastic medium [55, 56]. The lattice vibrations are described as collective atomic vibrations or elastic waves, which move through the solid with the speed of sound. They may be polarized either longitudinally or transversally, and travel with velocity c_L or c_T respectively. In general a sound wave is described by its frequency, ω, and its wave-vector k. The latter defines the direction of the propagation of the sound wave and its modulus is $k = 2\pi/\lambda$, where λ is the wavelength of the sound wave. Longitudinal sound waves correspond to waves oscillating along the propagation direction, while transverse waves vibrate perpendicular to that direction. Moreover, an isotropic continuum medium is characterized by only one longitudinal and two transverse branches, the latter being degenerate.

In general the sound velocity has a different values for each polarization. As it would be for a classical elastic continuum, the frequency ω and the wave-vector k are related by the sound velocities values through linear dispersion relations:

$$\omega = c_L k \qquad \omega = c_T k \tag{1.26}$$

Debye imposed that the number of vibrational modes is fixed to the numbers of atoms. This consideration together with the continuum approximation yields to a wave-vector cutoff k_D, being

$$3N = \sum_{\substack{\boldsymbol{k} \\ |\boldsymbol{k}|<k_D}} = \frac{V}{(2\pi)^3}\int_{|\boldsymbol{k}|<k_D} d^3\boldsymbol{k} = \frac{V}{2\pi^2}\int_0^{k_D} dk k^2 = \frac{V}{6\pi^2}k_D^3 \tag{1.27}$$

In general k_D corresponds to the typical inverse inter-particle separation in the material.
Many thermodynamic properties of a solid can be described through the evaluation of the vibrational density of states DOS $g(\omega)$, which is usually expressed as

$$g(\omega) = \frac{1}{3N}\sum_{\lambda}\sum_{\boldsymbol{k}} \delta(\omega - \omega_\lambda(\boldsymbol{k})) \tag{1.28}$$

where λ is the polarization index.
The quantity $g(\omega)d\omega$ represents the number of modes with frequencies in the infinitesimal range between ω and $\omega + d\omega$. By using the linear relations 1.26, and the cutoff wave-vector k_D, one obtains the Debye density of states:

$$g_D(\omega) = \frac{1}{3N}\frac{V\omega^2}{2\pi^2}\left(\frac{1}{c_L^3} + \frac{2}{c_T^3}\right) = \frac{3\omega^2}{\omega_D^3} \tag{1.29}$$

The Debye frequency ω_D introduced in the last equality, is achieved from the relation $\omega_D = v_D k_D$, where v_D is the Debye sound velocity given by

$$v_D = \left[\frac{1}{3}\left(\frac{1}{c_L^3} + \frac{2}{c_T^3}\right)\right]^{-1/3} \tag{1.30}$$

This description of the vibrational density of states allows for a correct evaluation of the heat capacity, being

$$C_{Debye} = 3Nk_B\int_0^{\omega_D} g(\omega)\left(\frac{\hbar\omega}{k_B T}\right)^2 \frac{e^{(\hbar\omega/k_B T)}}{[e^{(\hbar\omega/k_B T)} - 1]^2} d\omega \tag{1.31}$$

At high temperatures the model gives the temperature independent Dulong-Petit value, while in the low temperature limit the heat capacity follows a $\sim T^3$ temperature behavior

$$C_{Debye} = \frac{2\pi^2}{15}\frac{k_B^4}{\hbar^3}\left(\frac{1}{c_L^3} + \frac{2}{c_T^3}\right)T^3 \tag{1.32}$$

This approximation holds rigorously for any insulating crystalline material while, as shown in the next section, it is not able to describe the heat capacity of glasses.

1.4.2 Thermal anomalies in glasses

The low frequency part of the vibrational spectrum of glasses is generally acknowledged to be one of the major unsolved problems in solid state physics [56]. In this context, low frequency means lower than fews THz. According to quantum mechanics, a vibration of that frequency contributes only a little to the heat capacity or the thermal conductivity until the temperature gets to about 10 K. This means that the vibrations with frequencies ≤ 1 THz dominate the low-temperature thermal properties of insulator glasses. These vibrations correspond to wavelengths so long that the system would be expected to appear as a continuum and, as a consequence, the thermal properties should behave in the same way independently of whether the system is a glass or a crystal. In the light of such argument, it was particularly surprising that quantities such as the specific heat and the thermal conductivity exhibited strong departures from the Debye continuum approximation theory.
Moreover, this discovery is even more surprising considering that in glasses there are well-defined sound waves, following the linear dispersion relations 1.26, up to at least fews THz [57].

Heat capacity

Figure 1.12 (a) shows the temperature behavior of the heat capacity C_p for vitreous and crystalline silica, measured by Zeller and Pohl [51]. The two systems display a markedly different behavior in the low temperature range. In particular, the heat capacity of vitreous silica decreases much more slowly with temperature. This behavior has been found in all glasses.
As reported above, in crystalline materials such as α-quartz, C_p is well described by the Debye model and follows a $\sim T^3$ temperature dependence at low temperatures. The heat capacity of glasses, instead, deviates strikingly from Debye predictions and can be described adding a linear term, being:

$$C_p \sim aT + bT^3 \tag{1.33}$$

Below 1 K, the heat capacity is essentially linear in temperature, indicating a more or less constant density of states in addition to the density of states of the sound waves, which increases with the frequency squared. Above 1 K, C_p starts to deviate from this quasilinear temperature behavior and, at about $\sim$ 10 K shows a "bump" with respect to the cubic temperature dependence predicted by Debye (Figure 1.12 (b)).

The very low linear temperature behavior can be described by the two level system model (TLS)[56]. This model assumes the existence of local structural instabilities of the glass, capable of tunneling among different configurations of the system. This means that the anomalous behavior below 1 K is not due to the sound waves themselves, but rather to additional excitations, the tunneling states, which scatter the sound waves.

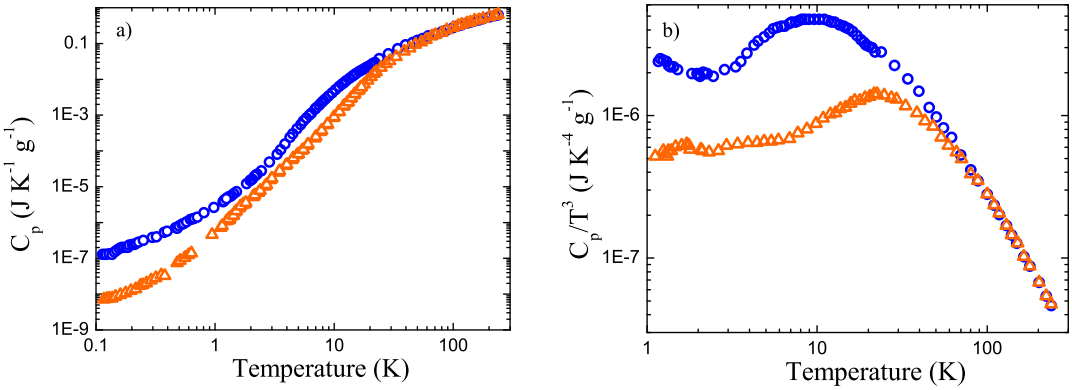

FIGURE 1.12: Temperature dependence of the heat capacity C_p (a) and reduced heat capacity C_p/T^3 (b) for vitreous silica (blue symbols) and α-quartz (orange symbols), reported in log-log scale. Adapted from [51].

While the TLS model is generally accepted by the scientific community, the excess of heat capacity at higher temperatures represents a strongly controversial topic. As shown in Figure 1.12 (b), the "bump" in C_p/T^3 is present in crystalline α-quartz as well. In this case, however, this excess appears at higher temperatures and is usually related to the effect of transverse acoustic vibrational excitations near the boundary of the first Brillouin zone.
The increase in the heat capacity with respect to the Debye prediction at $\sim$ 10 K has been widely investigated but its origin is still poor understood. Moreover this feature comes out in the same range where the thermal conductivity displays a peculiar behavior as well.

Thermal conductivity

In crystals heat is carried by phonons, which represent the quantum description of the ionic displacement field. In particular acoustic phonons correspond to the quantum description of elastic waves. The thermal conductivity of a system can be described by:

$$k = \frac{1}{3}\sum_{\lambda=1}^{3}\int_0^{\omega_m} C_\lambda(\omega)v_\lambda(\omega)l_\lambda(\omega)d\omega \tag{1.34}$$

where the sum is over all phonon branches λ, $v_\lambda(\omega)$ and $l_\lambda(\omega)$ are the sound velocity and the mean free path respectively, $C_\lambda(\omega)$ the contribution to the heat capacity of phonons of the λ^{th} branch, and ω_m is the highest excited mode.
Debye described the thermal conductivity of dielectric solids following the result of the kinetic theory of gases [55]. In this case the previous expression reduces to:

$$k = \frac{1}{3}C_{Debye}v_D l \tag{1.35}$$

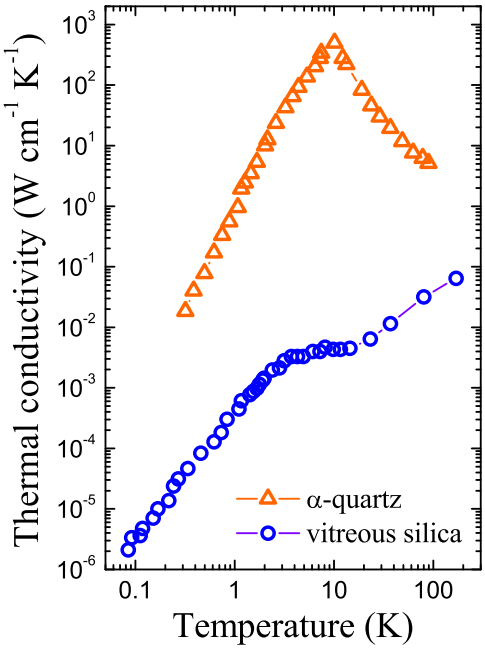

FIGURE 1.13: Temperature dependence of thermal conductivity of amorphous silica (blue symbols) and α-quartz (orange symbols), reported in log-log scale. Adapted from [51].

where C_{Debye} is given by 1.31, v_D is the Debye sound velocity 1.30 and l is an average mean free path.

For crystals, the mean free path is constant at low temperatures and the thermal conductivity is completely governed by the $\sim T^3$ temperature dependence of the heat capacity (orange symbols in Figure 1.13). On increasing the temperature, k reaches a maximum when the scattering length becomes equal to the sample dimensions and then it decreases due to the increasing Umklapp processes.

The thermal conductivity of glasses is completely different (blue symbols Figure 1.13). Firstly it is several orders of magnitude smaller with respect to that of the corresponding crystals. Secondly it displays a peculiar temperature behavior represented mainly by the presence of a *plateau* in correspondence of the maximum of k in crystals (at about $\sim$ 10 K), and by a quadratic temperature dependence of the thermal conductivity below 1 K.

As for the heat capacity, the very low temperature behavior can be justified in terms of the two level system model, while the constant regime at higher temperatures is still matter of debate. Indeed, the plateau in k always appears in the same temperature range where the heat capacity of glasses shows an excess with respect to the Debye expectation (Figure 1.12 (b)). These peculiarities are universal in glasses and they can be related to the presence of vibrational modes in excess with respect to the Debye density of states 1.29. As it will be explained in the next chapter, the nature of this excess of modes represents a challenging topic in solid state physics as it is believed to represent the key to understand the vibrational

spectrum in glasses.

Résumé du chapitre 2

Les comportements anomaux des propriétés thermiques des verres à basse température, comme la capacitè thermique et la conductivitè thermique, rapportés dans le premier chapitre sembleraient être liés à un excès dans la densité d'états vibrationnels, surnommé "Boson Peak" (BP), par rapport à la valeur prédite par le modéle de Debye. L'origine de cette caractéristique spécifique des verres, et son rapport avec la dynamique vibrationnelle est aujourd'hui un intéressant problème de la physique des solides.
En particulier, la nature des excitations avec une énergie comparable à celle du Boson Peak (1-10 meV) est largement débattue. Le probléme principal est que ces modes correspondent á des régions de fréquence qui est dans le THz, où la longueur d'onde est comparable avec la distance moyenne entre deux particules, et donc leur caractère est affecté par le désordre structurel.
Dans la première partie du chapitre on fournira un bref aperçu de quelques modèles qui décrivent cette caractéristique vibrationnelle du verre. Dans le reste du chapitre, on présentera les aspects généraux de la dynamique à haute fréquence (dans la région de fréquence de THz), tandis que dans la dernière partie la corrélation entre le BP et les propriétés élastiques de verres sont discutés.

Chapter 2

Acoustic dynamics in the mesoscopic range

The failure of Debye's model to describe the thermal properties of glasses in the $\sim$ 10 K temperature range is related to an anomalous feature in the low energy part of the vibrational density of states $g(\omega)$. In the previous chapter, it has been shown that both the heat capacity and the thermal conductivity of a material can be estimated from $g(\omega)$ through the relations 1.31 and 1.34. For this reason, it is natural to think of the presence of a signature in the VDOS corresponding to the low temperature anomalies of glasses. In fact this is the case: both the excess of C_P with respect to the $\sim T^3$ Debye-law, and the corresponding plateau in the thermal conductivity are related to the ubiquitous existence at frequencies of ~ 1 THz of an excess of modes in the $g(\omega)$ over the $\sim \omega^2$ Debye-model prediction 1.29.

This enhancement of vibrational states, called "Boson Peak" (BP), is universal in glasses and appears as a characteristic broad asymmetric peak when plotting the reduced density of states $g(\omega)/\omega^2$ as a function of the excitations energy [58]. Figure 2.1 shows the density of states and the boson peak of glassy sorbitol, the main system studied in this work, as a function of energy. Beyond its universal occurrence in glasses, the boson peak always appears in the same energy range of fews millielectronvolts ($\sim 1 - 10$ meV), thus in a range where the wavelength of the atomic vibrations is still larger than the interatomic distances, and thus where the continuum elastic medium approximation, described by Debye's model, should work.

The boson peak can be detected using different techniques; the most used are inelastic neutron and light scattering spectroscopies, but it can be measured as well by means of nuclear inelastic scattering experiments [1, 58, 59].

Albeit the BP was first discovered more than 40 years ago, no agreement exists on its physical origin and it still remains the subject of an increasing number of theoretical and experimental works. Its understanding, indeed, represents an important step for the general comprehension of the vibrational dynamics of glasses in the crucial energy range where it starts to behave distinctly different from Debye's predictions.

Several theoretical models are able to justify a peak in the reduced density of

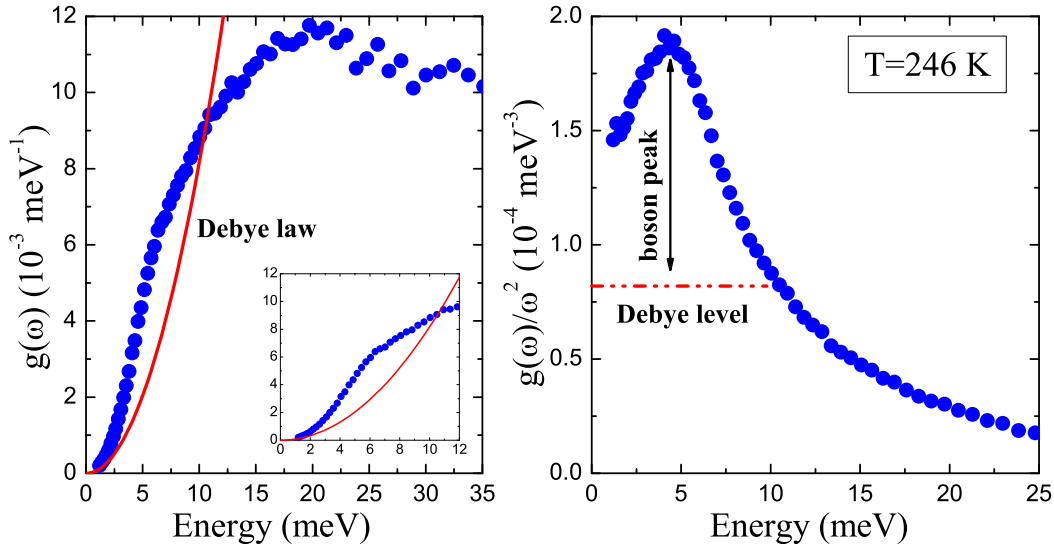

FIGURE 2.1: Left panel: density of states of glassy sorbitol measured with inelastic neutron scattering (see section 5.2) together with the Debye's prediction (red line). Right panel: reduced VDOS of sorbitol. The red dash-dotted line represents the value predicted by Debye's model, while the black arrow indicates the intensity of the boson peak.

states, however an agreed upon solution is still lacking. The main difficulty on approaching this subject resides in the rough knowledge of the nature of the high frequency acoustic modes present in the energy range of the boson peak. In fact, the BP models can be classified mainly in two categories depending on an *acoustic* or *non-acoustic* nature of the modes contributing to the BP. As a consequence, the most intuitive way to discriminate among these different theoretical approaches consists in the study of the relation between the reduced VDOS and the acoustic properties. For such purpose, a deep knowledge of the nature of the high frequency collective excitations in glasses is fundamental.

The BP seems to be correlated to several properties of glass-formers as well. For instance, in the last years it has been proposed a direct link between the excess of vibrational modes and the fragility of the corresponding supercooled liquid. In particular, it seems that the stronger the melt, the higher is the intensity of the peak in the reduced VDOS [60]. Furthermore in some strong systems, such as B_2O_3, the boson peak is still well evident in the molten phase above T_g.

In the next section an overview of the most widely diffused BP models is presented, while in the rest of the chapter the state of the art of the high-frequency dynamics of glasses and its relation with the boson peak will be discussed.

2.1 Boson peak models

There is a general agreement that the boson peak is a manifestation of disorder, but, as reported above, the main question of whether this peak depends on a peculiar behavior of the acoustic excitations present in the corresponding energy range or on the existence of some additional modes, proper to the glassy state, is still unanswered.
Three main different scenarios have been proposed to explore the origin of the boson peak. One assumes the existence of additional quasilocal modes, which coexist and hybridize with the sound waves at the boson peak energy (Soft potential model) [61–63]; another ascribes the non-Debye-like excess of modes to the effect of disorder on the sound wave excitations (strong scattering of sound waves from disorder) [64–68], while the third one attributes the boson peak to inhomogeneities of the elastic response of glasses on the nanometric length scale (vibrational heterogeneities on the nanometric scale) [69–74].
Albeit based on very distinct assumptions, these various models are all qualitatively compatible with the measured vibrational properties of glasses. From the experimental point of view is therefore extremely difficult to make a clear distinction between the different existing theories.

Soft potential model

The Soft Potential Model (SPM) assumes the existence of additional *quasi-local* vibrations (QLV) that interact with the sound waves, giving rise to the boson peak. This model can be considered as an extension at higher temperature of the two level system model (TLS), describing the thermal anomalies of glasses below 1 K (see section 1.4.2). In fact the SPM predicts that in addition to two-level systems there are soft modes in glasses which are responsible for their universal behavior, especially at higher temperatures. These excitations are intimately related as they can be described by an unique anharmonic soft atomic potential [61].
The physical origin of these low frequency local vibrations of small groups of atoms can be traced to local defects of the amorphous structure, or to low-lying optical modes in parental crystals. In the last case, the disorder in amorphous materials would destroy the long range coherence of the optical modes, making them practically indistinguishable from quasilocal modes.
The additional QLV can be described as low frequency harmonic oscillators (HO), which weakly couple to the sound waves of the elastic continuum medium. This coupling in turn leads to a dipole-dipole interaction between different HO, which destabilizes the quasilocalized harmonic modes. The vibrational instability is controlled, under a certain frequency $\omega_c << \omega_{Debye}$, by the anharmonicity and creates a new stable universal spectrum of harmonic vibrations with a boson peak feature and an asymmetric double-well potential, where the latter is typical of the TLS tunneling modes [62]. In the SPM, the boson peak energy depends on the interaction strength among the different HO. The stronger the interaction, the higher is the energy of the boson peak maximum. In this way the model is able to explain

the large variety of BP parameters found in experiments.
The SPM allows the use of a single theory describing the universal anomalous behavior of glasses in the whole low temperature range. Moreover, a recent work pointed out a direct link between boson peak and two-level systems: the raising of a peak in the reduced vibrational density of states seems to inevitably lead to the creation of two-level systems and vice versa [63].

Strong scattering of sound waves from disorder

Models based on purely harmonic modes in glasses, are also able to describe the vibrational and thermal properties of disordered solids.
In the model proposed by Taraskin and coworkers [64] the atoms occupy ideal crystalline positions and the system can be described as composed by coupled harmonic oscillators interacting through random independent elastic force constants K_{ij}, whose strengths are controlled by a certain probability distribution, $P(K_{ij})$. This scenario corresponds to the simplest type of disorder and allows for a well-developed analytical approach.
On increasing the width of the distribution $P(K_{ij})$, the system becomes unstable, thus with negative force constants K_{ij}, and this instability gives rise to the well-know excess of modes in the vibrational density of state. This model shows that it is not necessary to postulate the existence of localized states or strongly anharmonic effects, as in the soft potential model, to obtain an excess contribution in the reduced VDOS. More precisely, the enhancement in the reduced VDOS is here associated with the lowest van Hove singularity in the spectrum of the reference crystalline system, pushed down in frequency by disorder-induced level-repelling and hybridization effects [64].
In the force constants disorder model, moreover, the types of vibrational modes (acoustic/optic, transverse/longitudinal) present in the boson-peak region are also dictated by the types of phonons responsible for the lowest van Hove singularity in the corresponding crystalline counterpart, though they generally seem to be related to transverse branches.
Parisi and coworkers proposed a different microscopic harmonic approach based on topological disorder of the atoms [65, 66]. This model supports the idea that the boson peak marks the transition between acoustic-like excitations and a disorder-dominated regime for the vibrational spectrum.
A more recent model, based on a macroscopic tensorial elastic and lattice-independent approach, has recently been proposed by Schirmacher and coworkers [67]. In this model the system is considered as an elastic continuum in which the transverse elastic constant is assumed to vary randomly in space. On increasing the degree of disorder the boson peak position shifts toward lower frequencies and its intensity increases. The model predicts also a strict correlation between the excess in the vibrational density of states and the sound damping of the acoustic waves present in the corresponding energy range [68]. A more detailed description of this model is reported in section 5.3.2 together with an evaluation of the proposed correlation in the case of glassy sorbitol.

Vibrational heterogeneities on the nanometric scale

Another approach consists on ascribing the BP to the inhomogeneous cohesion of glasses at the nanometric scale [69, 70]. In this case the system is assumed to be inhomogeneous, consisting of an aggregate of "regions" with different elastic constants with respect to the matrix. The materials are, consequently, characterized by more cohesive domains separated by softer interdomain zones on the nanometric spatial range and the boson peak arises from vibrational modes spatially localized in such regions.

The presence of elastic inhomogeneities in the mesoscopic spatial range does not imply automatically the existence of visible static density inhomogeneities as well [70]. A fluctuation of elasticity can in fact correspond to a negligible density fluctuation.

In the model reported in Ref. [70], the excess of modes in the VDOS is viewed as the signature of the hybridization of acoustic modes with modes of localized nature, inherent to the elastic heterogeneities.

A correlation between the size of these elastic heterogeneities and the fragility of the different materials has been proposed as well. The idea is that stronger glasses would display a more inhomogeneous elastic response with respect to fragile systems. This situation would explain why the amplitude of the boson peak is higher in strong materials. In the case of fragile systems, instead, the excess of modes would become broader and less intense due to the disappearance of the elastic heterogeneities.

The heterogeneous elastic response at the nano-scale can possibly be related to the existence of dynamical heterogeneities observed in supercooled liquids above the glass transition (see section 1.3.3). In this sense, it is likely that the glass transition preserves the memory of these dynamical heterogeneities, so that cohesion heterogeneities in glasses originate from the mobility heterogeneities in the supercooled state. This idea would imply that the spatially correlated dynamics of the molecules in the melt is somehow "frozen in" at the glass transition, and leads to the creation of softer and harder zones in the glassy phase.

The existence of such vibrational, elastic heterogeneities has been recently confirmed in several numerical simulations [71–74].

In the case of a monatomic glass, whose atoms interact trough the Lennard-Jones potential, the existence of rigid zones has been found within which strongly correlated atoms show small displacements in harmonic vibrations, and soft zones where correlated atoms show large displacements [71]. Similar results have been found in silica and in some fragile systems as well [72–74]. In these works, the authors studied the response of the system to an elastic affine, thus linear, deformation. The classical elasticity implies that if the system is uniformly strained at large scales, e.g. by compressing or shearing a rectangular simulation box, the strain is uniform at all scales, so that the atomic displacement field should be affine with respect to the macroscopic deformation. In the case of glasses, instead, this assertion fails on the nanometric length scale, where the system behaves in a strong nonaffine way. This means that after applying a uniform macroscopic strain and keeping the shape of the simulation box constant, the system relaxes to the

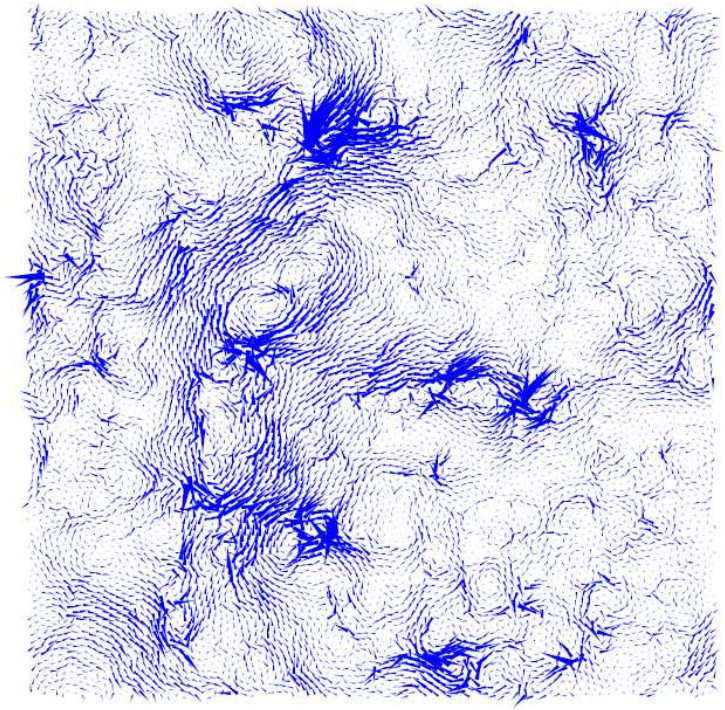

FIGURE 2.2: Snapshot of the nonaffine displacement field in a 3D Lennard-Jones amorphous system undergoing uniaxial macroscopical extension [75].

nearest energy minimum releasing about half of the elastic energy gained from the initial deformation. The difference between the initial, i.e. after the strain is applied, and the final, i.e. after the relaxation, atoms positions defines the nonaffine displacement of the particles reported in Figure 2.2 a). In this scenario, the boson peak appears exactly at the edge of the characteristic length scale of the nonaffine displacement field and can be viewed as a consequence of the inapplicability of the continuum theory on shorter wavelengths [73].

2.2 High frequency vibrational modes

Vibrational excitations are related to microscopic thermal motions; they depend on the interactions or forces between neighboring atoms and determine the thermal properties of the system (see section 1.4). A large number of scientific works have been devoted to understand the differences between vibrational excitations in glasses and crystals. Several questions were raised, like up to what point the structural disorder influences the spatial extent of vibrational modes or whether the concept of a phonon remains appropriate in disordered media.
At low frequencies (up to ~ 300 GHz), thus in the long wavelengths limit, a glass appears as a continuum elastic medium and the disorder does not affect the vibrational dynamics. If anharmonicity can be neglected, the acoustic modes can be described in terms of plane waves, as in the crystalline case, with well defined dispersion curves, which give information on the sound velocity in the material

(eq. 1.26).
At sufficiently high frequencies ($\sim$ THz), thus for wavelengths of the order of fews nanometers, the lack of periodicity does not allow for a plane waves description of the collective excitations and the wavevector Q cannot be considered any longer a well defined quantum number. However, the presence of propagating acoustic phonon-like excitations in glasses down to wavelengths comparable to the interparticle distance has been observed [57]. On decreasing further the wavelength, the structure becomes more and more important and the collective modes convert in a more complex pattern of atomic motions, loosing completely their propagating character.
The vibrational excitations can be studied experimentally by various techniques such as Brillouin light scattering (BLS) at low frequencies, or inelastic scattering of x-rays (IXS) and neutrons (INS) at higher frequencies. These techniques allow for the measurement of the dynamical structure factor $S(Q,\omega)$, which represents the space and time Fourier transform of the density-density correlation function

$$S(Q,\omega) = S(Q)\int_{-\infty}^{+\infty} dt e^{-i\omega t}\Phi_Q(t) \tag{2.1}$$

where $S(Q) = \left\langle \delta\rho_Q^*(0)\delta\rho_Q(0)\right\rangle$ is the static structure factor and $\Phi_Q(t)$ is the density correlator defined in equation 1.1. At high frequencies (thus in the meV energy

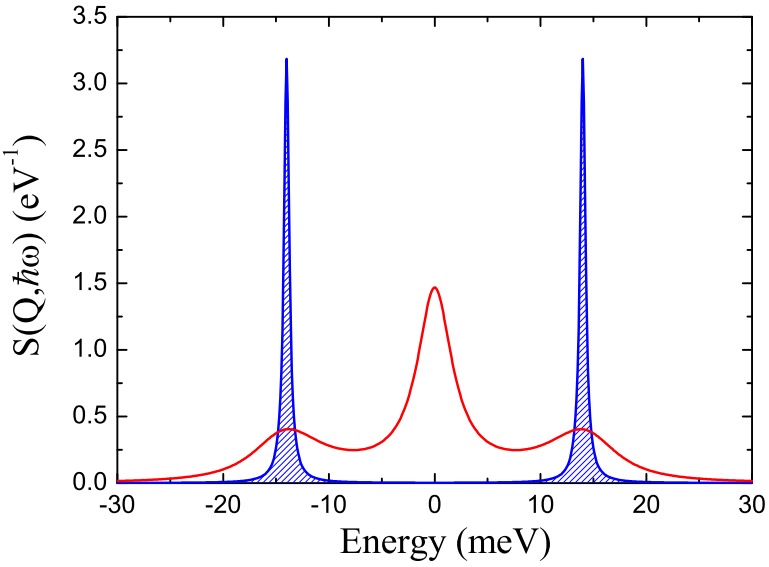

FIGURE 2.3: Sketch of the typical dynamic structure factor $S(Q,\hbar\omega)$ of a glass (full areas) and of a crystal (filled line) measured in the mesoscopic region.

range) the disorder induces essentially a broadening of the spectral features related to the vibrational modes observed in crystals. A typical example is reported in Figure 2.3. The dynamic structure factor of glasses is characterized by an elastic peak and two inelastic features shifted symmetrically with respect to the

elastic line. The central peak arises from density fluctuations related to the α structural relaxation that are frozen in the glassy state. Its width is due to the finite value of the energy resolution of the technique. The two spectral inelastic peaks are the Stokes and anti-Stokes components of the Brillouin doublet (see section 4.1.2). They correspond to the collective excitations and the experimental determination of their position and width yields information on the sound velocity and attenuation in the material [76].

In order to clarify the role of the high frequency excitations in the appearance of the boson peak, a clear knowledge of their nature is mandatory. The point of the controversy is to determine whether the excess of modes has an acoustic nature or is due to different kind of excitations, such as soft modes. Furthermore the existence itself of collective propagating modes at frequencies corresponding to the boson peak has been extremely debated in the last years.

The main difficulty of dealing with these problems comes from the experimental limitations of the available techniques. In many systems, indeed, the modes present in the fews meV energy range of the BP can be investigated only by means of IXS and they correspond to a $(Q, \hbar\omega)$ range at the edge of the capacities of such spectroscopy. Up to now IXS experiments are currently limited to $Q \geq 1$ nm^{-1} with an energy resolution of ~ 1 meV.

Despite of such difficulties, there are some features of the high frequency modes that are commonly accepted. In particular the dispersion curve of glasses, thus the function that describes the dependence of the energy of the excitation on the wave-vector Q, displays a strict resemblance to that of polycrystalline samples [77, 78]. Figure 2.4 A reports the dispersion curve of glycerol glass measured with IXS [57]. The Brillouin position values exhibit an almost linear behavior, up to a value Q_m that corresponds to energy excitations of about ~ 10 meV, and thus well above the energy of the boson peak (4 meV, black arrow in the Figure). Beyond Q_m, the Brillouin peaks in the $S(Q, \hbar\omega)$ become overdamped; their energy is no more well defined and the modes loose their propagating character. In general, the shape of the dispersion curve measured with IXS, allows to define the first pseudo Brillouin zone in glasses, marked as well by the Q value that corresponds to half of the first maximum in the static structure factor.

The shape of the dispersion curve gives information on the apparent sound velocity of the material $v(Q) = \Omega/Q$ [79, 80]. In several experiments the sound speed has been found to be almost constant in the low Q region of fews nm^{-1}, and equal to the elastic macroscopic value, measured with BLS at lower frequencies.

Another debated issue on the high frequency vibrational dynamics regards the limiting value Q_m, beyond which the modes loose their propagating character. There are glasses showing well defined acoustic-like excitations up to energies corresponding to Q values of the order of several inverse nanometers (Figure 2.4 A) [81, 82], while in other systems the modes display already a more non-propagating character at lower Q values [83–85]. In the first case, the acoustic-like behavior persists well above the boson peak energy, while in the second one the modes loose their acoustic nature at energies close to that of the BP maximum. This non-propagating behavior, moreover, can suggest the existence of some hybridization or interaction of the high frequency collective interactions with the modes giving rise to the boson peak.

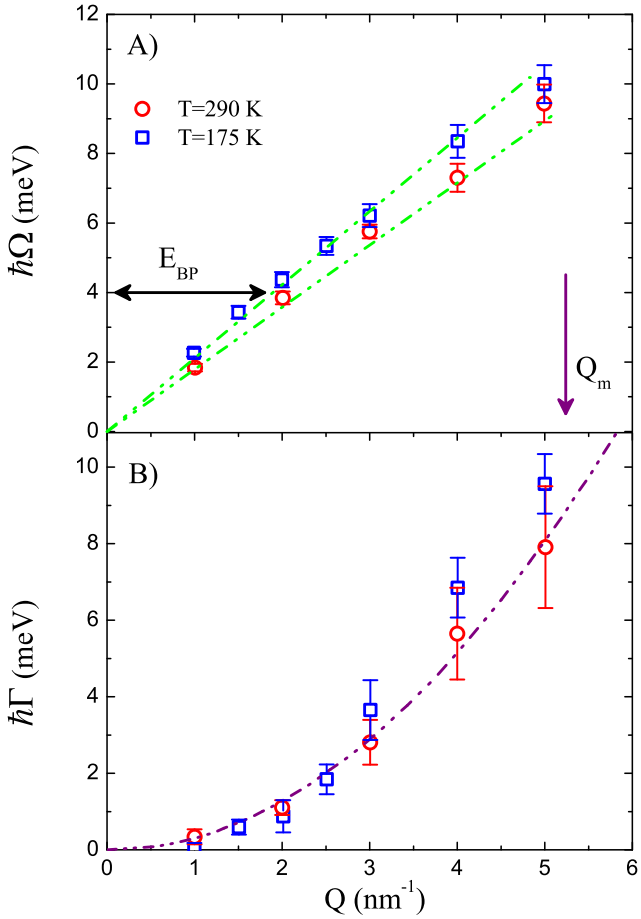

FIGURE 2.4: A) Dispersion curve of a glycerol glass (symbols) measured with IXS for $T = 290$ K and $T = 175$ K. B) Temperature dependence of the Brillouin width as a function of the wave-vector Q. The dashed lines in A and B show the low Q linear and quadratic behavior of the Brillouin position and width respectively. Adapted from [57].

In general the dynamic structure factor is related to the longitudinal current

$$J(Q, \hbar\omega) = \frac{(\hbar\omega)^2}{Q^2} S(Q, \hbar\omega) \tag{2.2}$$

and gives informations on the longitudinal modes in the system [76]. The transverse modes cannot be experimentally measured with IXS or INS because of the lack of a reciprocal lattice: there is no way for the density fluctuations to couple with transverse modes. However, the absence of order leads sometimes to a mixing of modes polarization and it is possible to observe of a second peak in the $S(Q, \hbar\omega)$ due to transverse excitations. These modes have been observed experimentally in the case of vitreous silica and glycerol and as well in molecular dynamics simulations [79, 86]. In these systems, the high-frequency upper limit of this non-dispersive branch has been considered as a possible cause of the

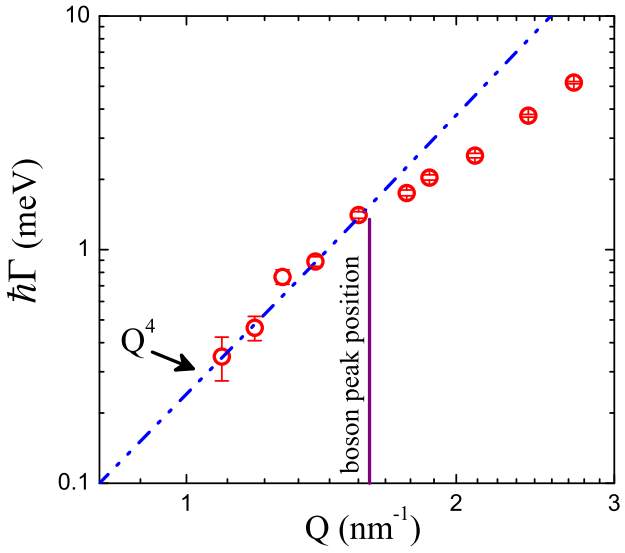

FIGURE 2.5: Q dependence of the acoustic attenuation in a Li_2O-$2B_2O_3$ glass measured at $T = 573$ K with IXS. Adapted from [91].

enhancement in the vibrational density of states at the boson peak.

2.2.1 Acoustic attenuation

At low frequencies, the acoustic sound attenuation is dominated by dynamical, anharmonicity-dependent, processes, like the Akhiezer mechanism [87, 88]. These processes rule the sound damping for wave-vectors up to ~ 0.05 nm^{-1}; they can be studied looking at the Q-dependence of the broadening $\hbar\Gamma$ of the Brillouin peaks, which is in turn proportional to the sound attenuation coefficient α being

$$\alpha = l^{-1} = \Gamma/v \tag{2.3}$$

where l is the mean free path and v is the sound velocity. When it is dominated by anharmonicity, the width of the Brillouin peaks displays a quadratic $\hbar\Gamma = A(T)Q^2$ behavior, where the coefficient $A(t)$ is strongly affected by temperature.
At higher frequencies, the mechanism underlying the sound attenuation is still unclear. In several glasses, the damping follows a $\sim Q^2$ (or $\sim \hbar^2\omega^2$) power law dependence, whose nature has be ascribed to the structural disorder (see Figure 2.4 B) [57, 89, 90].

This non-dynamic, temperature independent behavior cannot be extrapolated from the low frequency one and, as a consequence, requires the existence of an intermediate regime between the low and high frequency sound attenuation. Several models for vibrations in disordered systems suggest the presence of an intermediate Rayleigh-like scattering process from point-like defects in the elastic medium. This mechanism corresponds to a strong increase in the damping, which should

follow a $\sim Q^4$ (or $\sim \hbar^4\omega^4$) power law dependence. Such behavior, moreover, is necessary in order to explain the plateau observed in the low temperature thermal conductivity in glasses and related to the excess of modes in the VDOS with respect to the Debye level (see section 1.4.2) [51, 68, 92, 93].
Unfortunately, the range between the few nanometers scale and hundreds of nanometer scale is not accessible to both experimental and numerical techniques, leading to controversial discussions on where in frequency the Rayleigh scattering should appear.
In a recent inelastic ultraviolet scattering (IUVS) work the dynamic structure factor of vitreous silica was measured in an extended Q-region, up to 0.013 nm^{-1}, thus partially covering a previously unexplored range [94]. These measurements revealed the existence of a Rayleigh-like damping regime for frequencies at about 150 GHz, thus well below the boson peak. This results would exclude the existence of any connection between such strong attenuation and the plateau in the thermal conductivity. However this result is widely debated. A more recent work reports a contrasting result, showing that the sound damping of vitreous silica is compatible with the low frequency anharmonic dependence, up to frequencies of about 300 GHz [95].
Evidences of Rayleigh-like growth of the sound attenuation have also been found also in few other intermediate and strong glasses by means of IXS [85, 91, 96]. In these systems the strong damping takes place in a frequency range just below the boson peak position (see Figure 2.5), suggesting a strict connection between the acoustic damping and the excess in the VDOS.
The experimental difficulties to explore the vibrational excitations with energies just below the boson peak maximum, do not permit an in depth investigation of many systems, and makes the information on sound attenuation at high frequencies extremely scattered. As reported in the following, the intense development of the inelastic x-ray scattering technique during the last years, has allowed the observation of peculiar features of the high frequency modes, which could give important informations on the nature of the boson peak as well [96].

2.2.2 Breakdown of the Debye continuum approximation

The high frequency vibrational dynamics of glycerol glass has been recently measured with unprecedented accuracy by Monaco and Giordano [96]. The analysis of the data has revealed the existence of elastic anomalies in the mesoscopic spatial range of fews nanometers that were not previously observed (Figure 2.4) [57].
In particular, despite the presence of an almost linear dispersion curve at low Q values, such as in Figure 2.4 A, the acoustic-like modes exhibit a clear departure from Debye's prediction. This anomalous behavior is well evident looking at the apparent sound velocity reported in the top panel of Figure 2.6. Debye's theory predicts a linear dispersion of the acoustic waves with a consequent constant sound velocity equal to the macroscopic value measured at lower frequencies. Instead, the sound velocity of glycerol abruptly decreases in a narrow Q range, before showing

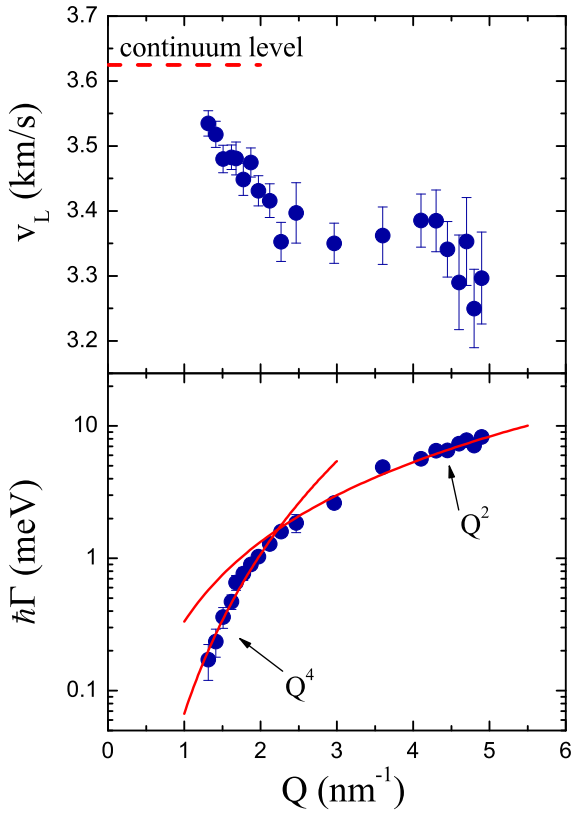

FIGURE 2.6: Q-dependence of the sound velocity (top panel) and attenuation (bottom panel) of a glycerol glass at $T = 150.1$ K. Top panel: the red dashed line represents the macroscopic limit taken from Brillouin light scattering. Bottom panel: the red lines correspond to the best Q^4 and Q^2 functions fitting the low and the high Q portion of the IXS data, respectively. Adapted from [96].

the typical sine-like behavior observed at high Q. This softening of the acoustic-like modes has been revealed thanks to technical improvements of the technique and to the choice of measuring a thinner grid in Q with respect to the previous experiments.

The negative dispersion comes out together with a strong, Rayleigh-like, regime for the sound attenuation (lower panel Figure 2.6), in correspondence to the boson peak energy. This phenomenology has been recently confirmed by experiment and molecular dynamics simulations [97, 98] and, as it will be shown in the following chapters, seems to be universal in glasses.

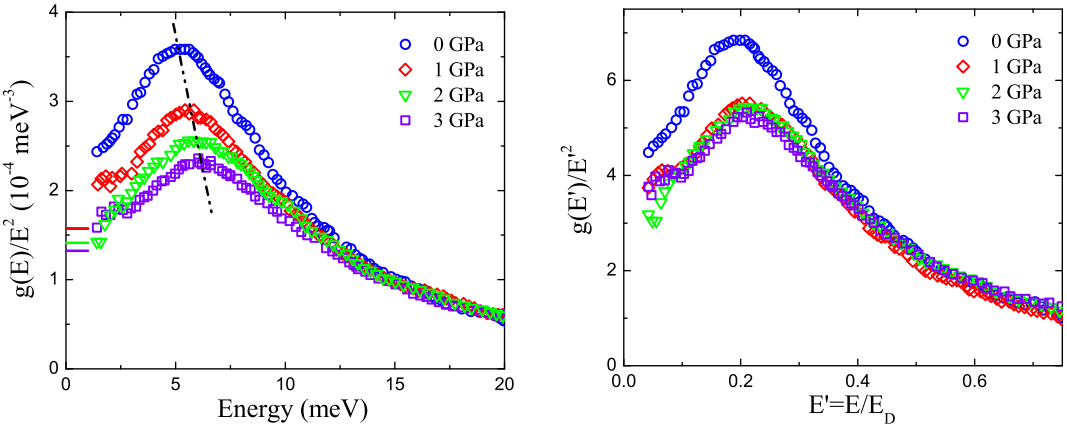

FIGURE 2.7: Left panel: reduced density of states of glassy $Na_2FeSi_3O_8$ for different pressures, together with the indication of the corresponding Debye level (horizontal lines). The black dashed line emphasizes the shift of the BP with densification. Right panel: same data as in the left panel after rescaling in Debye units. Adapted from [99].

2.3 Boson peak and elasticity in glasses

Despite of the active research on the vibrational properties of glasses, the absence of a clear theoretical frame to serve as a reference and the difficulty of disentangling system specific effects from universal behaviors in both experimental and numerical simulation results makes in fact slow the progress in the field.
As previously reported, the study of the nature of the collective excitations in the THz frequency range is fundamental in order to clarify their role in the appearance of the boson peak. Their properties, like absorption and velocity, can be then compared to the predictions of different available models in order to perform a more stringent test. Another approach consists, instead, on comparing the dependence of the boson peak on a control parameter, such as pressure [99–101] or temperature [102, 103], to the corresponding dependence of the sound velocities in order to investigate the connection between boson peak and elastic properties.
In the experimentally measured VDOS, the Debye level is never clearly reached due to the presence of broadening of the elastic line in the INS data, which masks the low energy side of the boson peak [103]. For this reason the comparison to the macroscopic elastic properties, thus with the Debye level (eq. 1.29), needs the combination of independent measurements of vibrational density of states with measurements of sound velocities, the latter ones being usually obtained by means of ultrasonic or Brillouin light scattering techniques in the MHz or GHz frequency range, respectively.
For the time being, the available results are still scarce and do not lead to a clear picture. However there exist some common features. In particular on increasing the pressure, and thus the density of the system, the boson peak shifts towards higher energies and becomes less intense (see Figure 2.7, 2.8 and 2.9). Moreover

the shape of the boson peak remains in general the same: spectra corresponding to different densities collapse in a single master curve if plotted as a function of the rescaled energy E/E_{BP}, where E_{BP} corresponds to the boson peak maximum.

Notwithstanding, different systems behave differently when compared with the

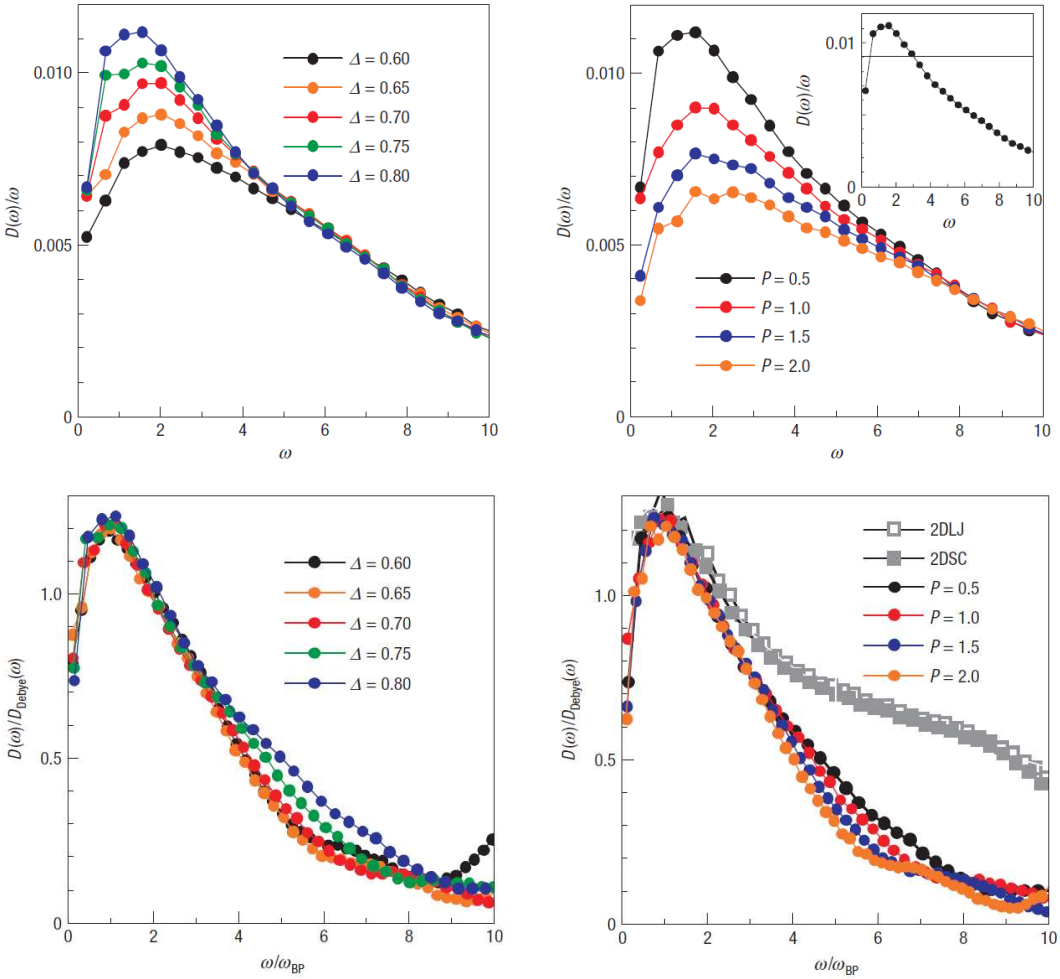

FIGURE 2.8: Upper panels: reduced density of states of glassy 2DSLS for different fragility values (left panel) and for different pressures in the case of a strong system (right panel). The insert in the right panel reports the reduced VDOS for P =0.5 compared to the Debye value (horizontal solid line) calculated from longitudinal and transverse sound velocities. Lower panels: same data as above after rescaling to Debye units [104].

continuum properties. In some cases the boson peak follows the corresponding transformation of the elastic medium. The left panel of Figure 2.7 shows the boson peak of a $Na_2FeSi_3O_8$ glass measured as a function of pressure using nuclear inelastic scattering [99]. In order to check whether a connection between the excess in the vibrational density of states and the macroscopic properties of the system exist, the VDOS of the glass should be compared to the Debye level (eq. 1.29). This comparison is reported in the right panel of Figure 2.7 as a function of the rescaled energy E/E_D, being E_D the Debye energy. In this sodium-silicate glass all the curves collapse in a single master curve, after rescaling in Debye units (right

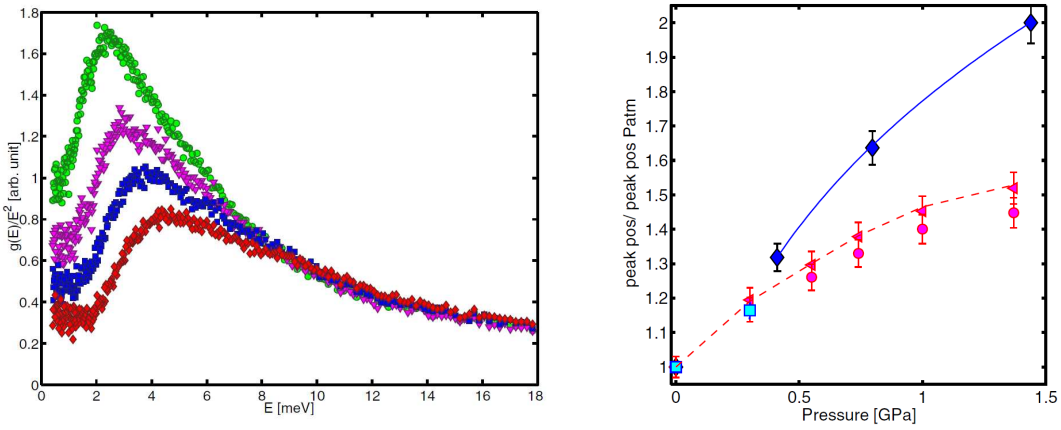

FIGURE 2.9: Left panel: reduced density of states of poly(isobutylene) at different pressures: atmospheric pressure (●), 0.4 (▼), 0.8 (■), and 1.4 GPa (♦). Right panel: relative shift in energy as a function of pressure. Boson peak (♦), BLS longitudinal modes (◄), BLS transverse modes (●), IXS longitudinal modes (■). The solid line represents a $P^{1/3}$ fit of the higher pressure values of the boson peak energy and the dashed line the corresponding changes with P of E_{Debye} [100].

panel). The spectrum measured at ambient pressure does not rescale on the top of the others due to the presence of structural changes on increasing pressure from 0 to 1 GPa. This means that in absence of local structural transformations, the Debye level and the excess of vibrational states above it have the same dependence on density, and the evolution of the VDOS is fully described by the transformation of the elastic medium.

The previous result is confirmed by a recent molecular dynamic study on a 2D spin liquid system (2DSLS) performed by Shintani and Tanaka [104]. They investigated the evolution of the VDOS by varying both the fragility of the system and by changing the pressure in the case of a strong glass (upper panels in Figure 2.8). The fragile character has been changed by varying the degree of frustration Δ of the system. In these systems the fragility plays the same role as the density variations: on increasing the fragile character of the glass-formers, thus on decreasing Δ, the boson peak shifts towards higher energies and its intensity decreases. Moreover in both cases, thus on changing pressure or fragility, the VDOS rescales to a single curve once the Debye contribution is taken into account (lower panels in Figure 2.8). This behavior confirms the direct link between BP variations and elastic deformations of the systems.

As reported at the beginning of the section, there are systems, such as polymeric glasses, which do not follow this Debye-like scaling law [100, 101]. In the case, for instance, of poly(isobutylene) (PIB) the boson peak is affected by pressure more than the continuum medium properties are [100]. The absence of a Debye scaling behavior is well evident looking at right panel of the Figure 2.9. This Figure reports the relative shift in energy as a function of pressure, with respect to ambient pressure, for both the boson peak maximum and the low and high frequency acoustic modes energies. The maximum in the reduced VDOS clearly increases more strongly than the sound velocities. This result implies that it cannot be

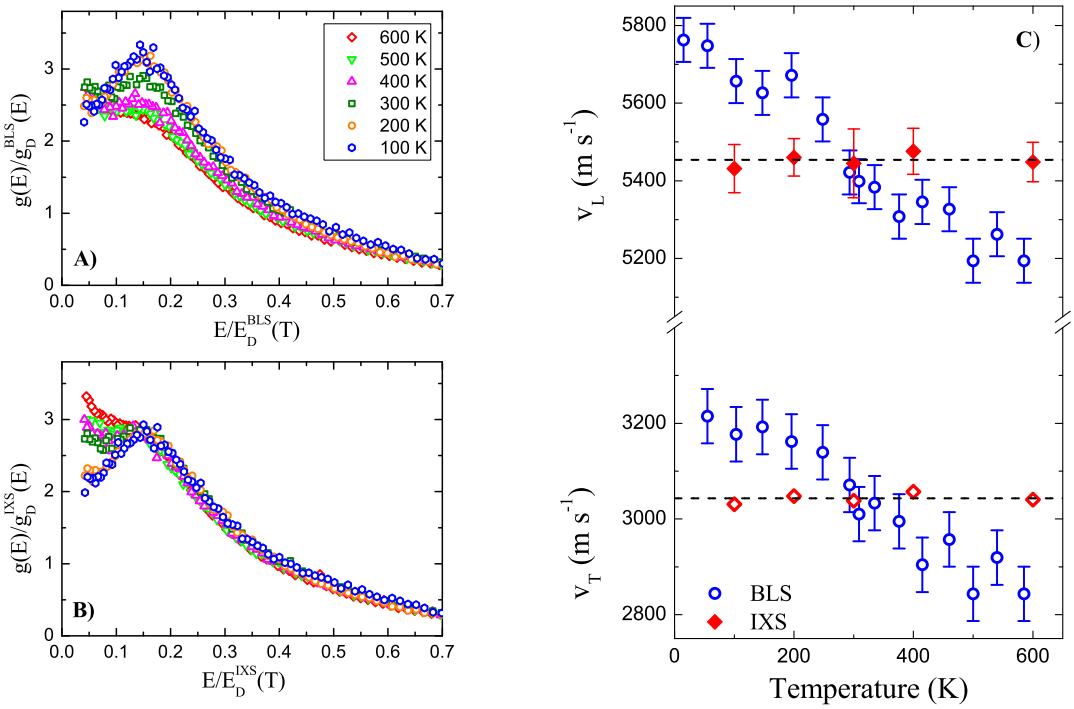

FIGURE 2.10: Elastic properties of $60SiO_2 - 40Na_2O$ glass. Left column: VDOS in Debye units, where the Debye energy is determined starting from the low frequency BLS sound velocity values (A) and starting from the high frequency IXS data (B). Right column: Temperature dependence of the longitudinal, v_L, and transverse, v_T, sound velocity: BLS data (open circles), IXS data (full diamonds). The high-frequency transverse sound velocity (open diamonds) is determined from a Cauchy-like relation for isotropic solids [105, 106]. The dashed lines correspond to the best fitted longitudinal and transverse sound velocities in the high frequency limit [103].

described by a simple elastic continuum deformation. The stronger effect of pressure on the BP maximum comes together with an increase of its intensity relative to the Debye level [100]. Such a behavior suggests that while in the previously described cases the scaling of the VDOS with the elastic transformations hints to an acoustic origin of the boson peak, the results on polymeric glasses, like PIB, arise from extra non-acoustic modes in the vibrational density of states.

A recent study of the temperature dependent of the VDOS of a silicate glass, $60SiO_2 - 40Na_2O$, reports as well deviations from a simple elastic scaling law (Figure 2.10 A) [103]. However, here the non-Debye transformations are ascribed to the presence of anharmonic or relaxational processes in the macroscopic continuum range.

In general, the Debye level is determined from the low frequency sound velocity values measured with Brillouin light scattering. Nevertheless the presence of anharmonicity in the GHz frequency range can affect the sound speed, which becomes frequency dependent and does no more correspond to the fully unrelaxed frequency limit needed to characterize the elastic properties of the medium. If this

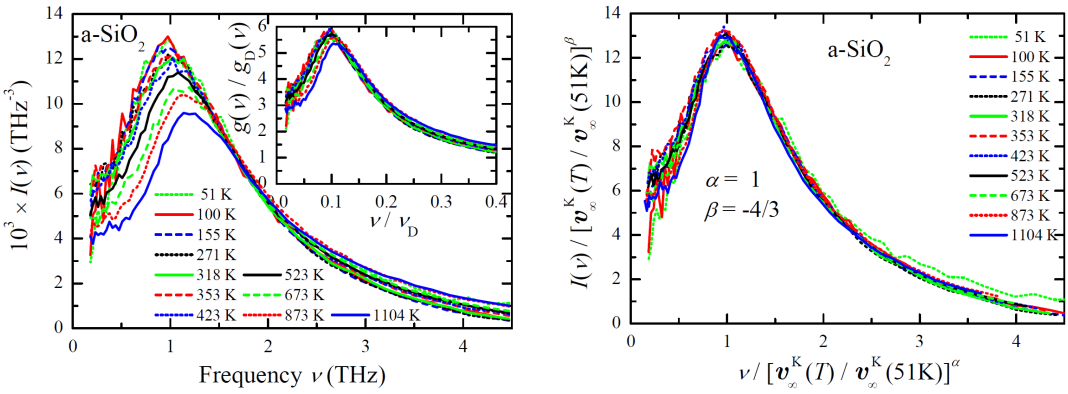

FIGURE 2.11: Elastic properties of vitreous silica. Left panel: Temperature dependence of the VDOS of vitreous silica after subtraction of the Debye level. The inset shows the VDOS in Debye units. Right panel: Same data scaled with exponents $\alpha = 1$ and $\beta = -4/3$ [107]. See text for details.

is the case, sound velocity corresponding to higher frequencies should be used to estimate correctly the elastic level.

Figure 2.10 B clearly shows that the BP scales with the Debye level when the high-frequency, IXS values of the sound velocity are used. These, indeed, are the correct values for the sound velocity to be considered, since the Debye approximation rests on the idea of an elastic continuum.

The presence of anharmonic contributions at low frequency in $60SiO_2 - 40Na_2O$ glass, is confirmed by the strong temperature dependence of the BLS data with respect to the almost temperature independence of the high frequency IXS ones (Figure 2.10 C).

A more recent study on vitreous silica points out the importance of the bulk sound velocity in the scaling of the vibrational density of states [107]. The left panel of Figure 2.11 reports the temperature dependence of the excess $I(\nu) = (g(\nu) - g_D(\nu))/\nu^2$, obtained by subtracting from the VDOS the Debye level. In this case the Debye scaling does not lead to a satisfactory master curve, not so much because of the poor scaling of the intensities, but mainly because the BP positions do not superimpose. The authors relate the observed temperature dependence to a progressive polyamorphic transformation of the system.

The structural evolution of silica with temperature can then be better described by considering the temperature evolution of the BP maximum, $\nu_{BP}(T)$ and its intensity, $I_{BP}(T)$, as a function of the infinite frequency bulk velocity defined by the relation $(v_\infty^K)^2 = (v_\infty^{LA})^2 - \frac{4}{3}(v_\infty^{TA})^2$, being LA and TA related to the longitudinal and transverse acoustic modes respectively. In fact, both $\nu_{BP}(T)$ and $I_{BP}(T)$ can be well described by a simple power law $\sim [v_\infty^K]^{\alpha,\beta}$, where the exponent $\alpha = 1$ reproduces the BP maximum behavior while the exponent $\beta = 4/3$ describes the BP intensity evolution. By rescaling the VDOS with these power law dependence, all the curves collapse into a single master curve (right panel Figure 2.11). In the Figure the data have been reported as a function of the reduced unrelaxed bulk velocity $v_\infty^K(T)/v_\infty^K(51K)$, where $v_\infty^K(51K)$ corresponds to the lowest measured temperature.

In this case, the scaling exponents α and β are found to be in good agreement with

the prediction of the soft potential model, suggesting the existence of quasilocal vibrations in the BP range.

2.4 Fragility of supercooled liquids and elastic properties of glasses

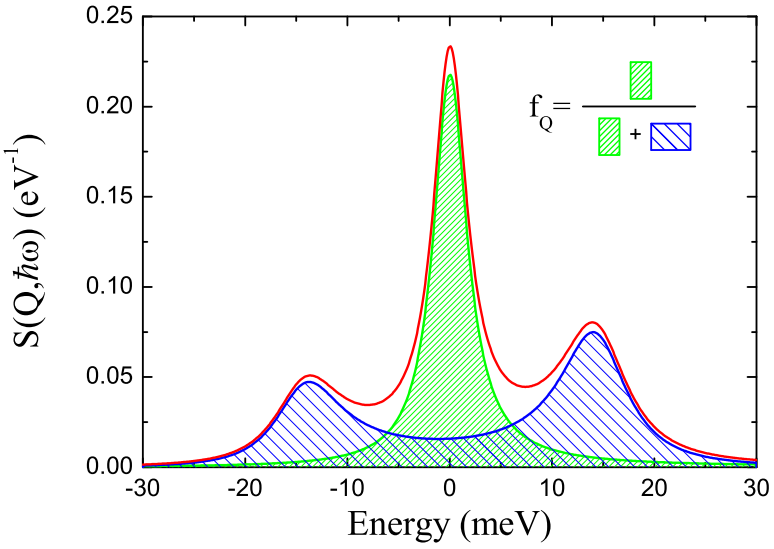

FIGURE 2.12: Example of the $S(Q, \hbar\omega)$ (red line) predicted by the model function used in the data analysis of the IXS spectra (see section 4.2.1). The nonergodicity factor f_Q can be estimated through the ratio of the elastic (green area) to total (green and blue areas) integrated intensity of the $S(Q, \hbar\omega)$.

An interesting open question in the physics of disordered systems is whether there exists a connection between the high-frequency elastic properties of glasses and the viscous properties of the corresponding deeply undercooled melts above the glass transition temperature, T_g. The latter ones are commonly considered to be efficiently grasped by the kinetic fragility of the melt (see section 1.3.2).
For example, as it has been previously reported, the boson peak of strong systems is more intense and located at higher energies with respect to that one of fragile materials [60]. It is obvious to expect that this is not the only observed relation. Some years ago Scopigno et al. proposed a correlation between the kinetic fragility, m_A, and a parameter α that describes the temperature dependence of the long-wavelength limit of the non-ergodicity factor, $f(Q, T)$, in the glassy state [3]. The latter quantity represents the long time limit of the density correlator $\phi_Q(t)$ (see equation 1.1); that is, the density-density correlation function $F(Q, t)$, normalized

to the static structure factor $S(Q)$:

$$f(Q,T) = \lim_{t\to\infty} \phi_Q(t) = \lim_{t\to\infty} \frac{F(Q,t)}{S(Q)} \tag{2.4}$$

$f(Q,T)$ corresponds, thus, to the long time plateau of $\Phi_Q(t)$ in the glassy limit

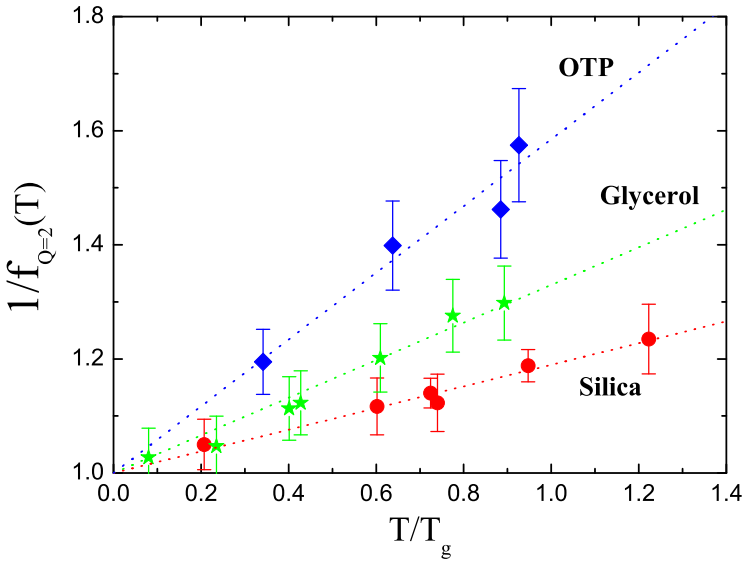

FIGURE 2.13: Values of $f_Q(T)^{-1}$ for $Q = 2$ nm^{-1} as a function of the rescaled temperature T/T_g. The dashed lines represent the best fit line shapes obtained using equation 2.5. Adapted from [3].

(see Figure 1.7). The quantity $1 - f(Q,T)$ represents the amount of decorrelation introduced by the vibrational dynamics, and it depends on both the (T-dependent) amplitude of the vibrations and the degree of disorder of the glassy structure.
The non-ergodicity factor can be experimentally measured using the inelastic to total integrated intensity ratio in the IXS spectra (see Figure 2.12). At low Q, the system is homogeneous for what concerns its density and the $S(Q)$ is flat. In this range and at low temperatures, the temperature dependence of $f(Q,T)$ can be described by a simple linear relation:

$$f(Q \to 0, T) = \frac{1}{1 + \alpha \frac{T}{T_g}} \tag{2.5}$$

Figure 2.13 shows the temperature dependence of the quantity $1/f(Q,T)$ for three different kind of glasses: silica (strong), glycerol (intermediate) and OTP (fragile). This representation strongly remembers the famous Angell plot for supercooled liquids (see Figure 1.9). In this case, the more fragile is the system, the higher is the parameter α in the relation 2.5.
Within the harmonic approximation, the parameter α only depends on the vibrational properties of the system in its inherent structure. Looking at the behavior in

Figure 2.13, Scopigno and coworkers found a direct link between the α parameter, and thus the vibrational properties of glasses and the fragility of the corresponding melts, being:

$$m_A = 135\alpha \tag{2.6}$$

As shown in Figure 2.14 the correlation among α and m_A seems to be fulfilled for

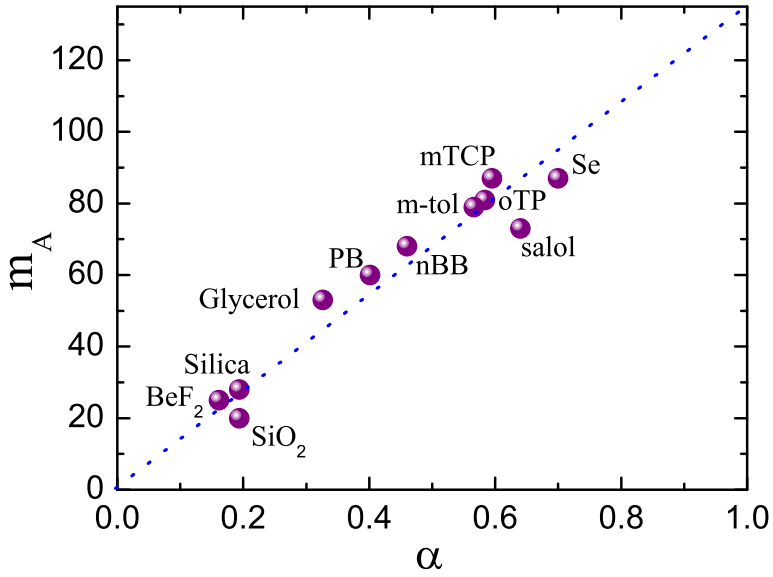

FIGURE 2.14: Relation between the kinetic fragility m_A and the α parameter obtained from equation 2.5 for different systems. The two quantities are proportional through the relation $m_A = 135\alpha$ (dashed line). Adapted from [3].

several systems.

After this work, a few glasses that do not follow the proposed linear relation have been identified [6, 46]; however, the basic idea of a correlation between elastic properties and fragility remains at least qualitatively valid [4–6, 45, 46], even though none of the proposed correlations seems to hold for all glasses at a quantitative level.

Recently Scopigno and coworkers proposed an explanation for the observed failure of relation 2.6 in several systems [29]. The idea is that this relation is valid only for that systems in which the dynamics is mainly governed by the structural relaxation process, which is therefore dominating the nonergodicity factor. If the systems are characterized by the presence of secondary relaxations almost as large as the structural process, the nonergodicity factor does no more correspond to the elastic to total integrated intensity ratio in the IXS spectra and equation 2.5 leads to an incorrect value of the α parameter. This is more clear looking at temporal evolution of the density correlator $\phi_Q(t)$ reported in Figure 1.6. In this case the vibrational contribution accessible to IXS differs from the value of the plateau associated to the nonergodicity factor. Consequently, the corresponding $S(Q, \hbar\omega)$ measured with IXS (see Figure 2.15) contains an additional contribution related

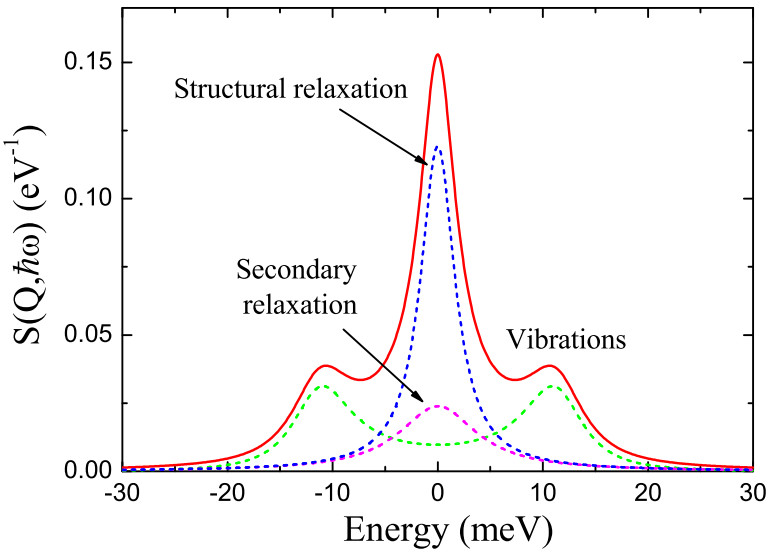

FIGURE 2.15: Sketch of the $S(Q, \hbar\omega)$ (red line) predicted by the model function used in the data analysis of the IXS spectra (see section 4.2.1) in presence of a relevant secondary relaxation process (magenta dashed line). The blue dashed line represents the contribution due to the structural relaxation while the green one corresponds to the Brillouin doublet. Adapted from [29].

to the secondary relaxation (magenta dashed line) that should be properly taken into account in order to estimate the correct value of the nonergodicity factor. Moreover relation 2.6 is not valid mainly in fragile systems, such as polymeric glass formers, thus in systems where the dynamics is usually characterized by the presence of additional fast relaxation processes. The authors suggest a way to quantify the effect of these "extra" processes through the evaluation of their contribution to the excess entropy at the glass transition temperature, leading to a partial reconciliation with the previous results [29].

Résumé du chapitre 3

L' étude des excitations à haute fréquence et de la relation entre élasticité et densité des états vibrationnels dans les verres demande la connaissance des propriétés macroscopiques du système. En général ces propriétés peuvent être étudiées grâce au comportement des ondes acoustiques dans la limite des grandes longueurs d'onde et donc pour des fréquences jusqu'à 300 GHz. La dynamique des verres dans cette gamme de fréquence peut, par exemple, être étudiée au moyen de la spectroscopie Brilluoin de diffusion de la lumière qui permet de mesurer la vitesse du son et l'atténuation des ondes acoustiques longitudinales et transversales.

Dans la première partie de ce chapitre nous reportons un résumé des aspects théoriques et expérimentaux de BLS. Le reste du chapitre présente les mesures BLS de deux verres différents. En premier lieu on discute la dynamique de basse fréquence de sorbitol. Comme on démontrera le sorbitol est caractérisé par des propriétés élastiques similaires à celles des verres intermédiaires alors que son comportement de la diffusion dans la phase liquide est celui des systèmes fragiles.

Dans la dernière partie du chapitre nous présentons la dynamique d'un verre de soufre. Malgré sa simplicité, le soufre existe en plusieurs formes et il devient un verre singulier grâce à un processus de polymérisation qui a lieu dans la phase liquide.

Chapter 3

Brillouin light scattering studies

The investigation of both the high frequency excitations and the relation among elasticity and vibrational density of states in glasses, requires first the knowledge of the macroscopic properties of the system. As previously reported, these properties can be studied through the behavior of the acoustic waves in the long wavelength limit, thus for frequencies up to $\sim$ 300 GHz. The dynamics of glasses in this frequency range can for example be studied by means of Brilluoin light scattering spectroscopy, which allows to measure the sound velocity and attenuation of both longitudinal and transverse acoustic waves.
In the first section of this chapter a brief summary of the theoretical and experimental basis of BLS is reported. In order to get information on the continuum properties of glasses, a quantum mechanical description of the radiation-matter interaction is not necessary. The light scattering process can be considered as a result of local fluctuations of the dielectric constant of the medium, and as a consequence, the theory will be treated in the classical electromagnetism framework.
The rest of the chapter reports BLS measurements of two different glasses. First, the low frequency dynamics of sorbitol is discussed. As it will be shown, this hydrogen-bond molecular system displays elastic properties similar to those of intermediate glasses, while its diffusion behavior in the liquid phase is typical of that of fragile materials.
In the last section the dynamics of a glass of sulfur is reported. Despite of the simplicity of the material, sulfur exhibits several different forms and becomes a peculiar glass, thanks to a polymerization process that takes place in the liquid phase.

3.1 Brillouin Light Scattering

Electromagnetic radiation is one of the most important probes of the structure and dynamics of matter. When light impinges on a solid, the electric field of the light induces an oscillating polarization of the electrons in the molecules. The molecules then act as secondary sources of light. The frequency spectrum of the

scattered radiation is determined by the molecular interactions in the scattering medium and gives information on the vibrational modes of the entire system [108].

In a light scattering experiment a monochromatic beam of light impinges on a

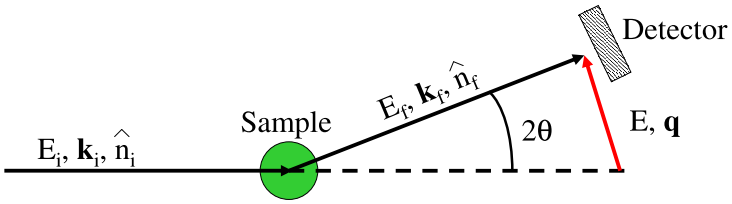

FIGURE 3.1: Scheme of a light scattering experiment. The incident light impinges on the sample and, by means of a filter, only the scattered light of wavevector $\boldsymbol{k}_f$ and polarization $\boldsymbol{n}_f$ arrives at the detector.

sample and is scattered into a detector placed at an angle 2θ with respect to the transmitted beam (Figure 3.1). The incident electromagnetic field exerts a force on the charges in the sample, that accelerate and radiate light. The scattered light field at the detector at a given time is the sum of all the electric fields radiated from all the charges in the medium. The incident electric field can be described in a plane wave form as

$$\boldsymbol{E}_i(r,t) = \boldsymbol{n}_i E_0 e^{i(\boldsymbol{k}_i \cdot \boldsymbol{r} - \omega_i t)} \tag{3.1}$$

where $\boldsymbol{n}_i$ is the polarization of the incident wave, E_0 the field amplitude, ω_i the angular frequency and $\mathbf{k}_i$ the wave vector.

The illuminated medium can be described by a local dielectric constant $\boldsymbol{\epsilon}(\boldsymbol{r},t) = \epsilon_0 \boldsymbol{I} + \delta\boldsymbol{\epsilon}(\boldsymbol{r},t)$, where ϵ_0 is the average dielectric constant, $\delta\boldsymbol{\epsilon}(\boldsymbol{r},t)$ is the dielectric constant fluctuation tensor at position $\boldsymbol{r}$ and time t, and $\boldsymbol{I}$ indicates the unit tensor.

The radiated electric field at a large distance R from the scattering volume, V, is given by [108]

$$\boldsymbol{E}_s(r,t) = \frac{E_0}{4\pi R \epsilon_0} e^{ik_f R} \int_V d^3 r e^{i(\boldsymbol{q}\cdot\boldsymbol{r} - \omega_f t)} \left[\boldsymbol{n}_f \cdot [\boldsymbol{k}_f \times (\boldsymbol{k}_f \times (\delta\boldsymbol{\epsilon}(\boldsymbol{r},t) \cdot \boldsymbol{n}_f))]\right] \tag{3.2}$$

where $\boldsymbol{n}_f$ is the polarization of the field, $\mathbf{k}_f$ the wavenumber vector and ω_f the angular frequency of the scattered radiation. The vector q is defined by the scattering geometry as $\boldsymbol{q} = \boldsymbol{k}_i - \boldsymbol{k}_f$ and its magnitude is given by

$$q = 2k_i sin\left(\frac{2\theta}{2}\right) = \left(\frac{4\pi n}{\lambda}\right) sin\left(\frac{2\theta}{2}\right), \tag{3.3}$$

being λ the wavelength of the incident laser light and n the refractive index of the medium ($n = \sqrt{\epsilon_0}$)[1].

The quantity measured in a light scattering experiment is the spectral density

[1] In the scattering process the wavelength of the incident light is changed very little so that $|\boldsymbol{k}_i| \cong |\boldsymbol{k}_f|$.

of the radiation scattered into the detector, thus the Fourier transform of the autocorrelation function of the electric field

$$I_{if}(\boldsymbol{q},\omega,R) = \frac{1}{2\pi}\int_{-\infty}^{\infty} dt e^{-i\omega t}\left\langle E_s^*(R,0)E_s(R,t)\right\rangle = \left[\frac{k_f^4 E_0^2}{16\pi^2 R^2 \epsilon_0^2}\right]\frac{1}{2\pi}\int_{-\infty}^{\infty} dt\left\langle \delta\epsilon_{if}^*(\boldsymbol{q},0)\delta\epsilon_{if}(\boldsymbol{q},t)\right\rangle e^{-i\omega t} \tag{3.4}$$

In the previous expression $\delta\epsilon_{if}(\boldsymbol{q},t) \equiv \boldsymbol{n}_f \cdot \delta\boldsymbol{\epsilon}(\boldsymbol{q},t)\cdot\boldsymbol{n}_i$, where $\delta\boldsymbol{\epsilon}(\boldsymbol{q},t)$ is the Fourier transform of the dielectric fluctuations and $\omega \equiv \omega_i - \omega_f$.
The scattering process can be viewed in terms of momentum and energy conservation. The interaction with the matter gives to a "photon-in/photon-out" process, where an incident photon of energy $\hbar\omega_i$ and momentum $\hbar\boldsymbol{k}_i$ impinges on the matter and a photon with energy $\hbar\omega_f$ and momentum $\hbar\boldsymbol{k}_f$ is scattered into the detector, thereby creating (or annihilating) an excitation in the medium of energy $\hbar\omega$ and momentum $\hbar\boldsymbol{q}$.
Generally, the incident light weakly interacts with matter so that the system can be assumed to respond linearly to it. As a consequence, the response to an external disturbance is equal to the one to the spontaneous microscopic thermal fluctuations that always occur in a system at finite temperature.
The local dielectric fluctuations can be expressed in terms of density, ρ, and temperature, T, variations as

$$\delta\epsilon(\boldsymbol{r},t) = \left(\frac{\partial\epsilon}{\partial\rho}\right)_T \delta\rho(\boldsymbol{r},t) + \left(\frac{\partial\epsilon}{\partial T}\right)_\rho \delta T(\boldsymbol{r},t) \tag{3.5}$$

In practice, the thermal variations of the dielectric constant are much smaller than the ones due to density fluctuations and can be neglected. Consequently, the response of the system to an external perturbation is completely governed by local density fluctuations and gives, then, information on the acoustic vibrational properties of the medium.
The expression 3.4 can be also formulated in molecular terms through the polarizability tensor $\boldsymbol{\alpha}$. In fact, from macroscopic electrodynamics this quantity can be related to the dielectric tensor by

$$\boldsymbol{\epsilon} = 1 + 4\pi\boldsymbol{\alpha} \tag{3.6}$$

In this way the spectral density of the scattered field is proportional to

$$I_{if}^{\alpha}(\boldsymbol{q},\omega) = \frac{1}{2\pi}\int_{-\infty}^{\infty} dt e^{-i\omega t}\left\langle \delta\alpha_{if}^*(\boldsymbol{q},0)\delta\alpha_{if}(\boldsymbol{q},t)\right\rangle \tag{3.7}$$

where

$$\delta\alpha_{if}(\boldsymbol{q},t) = \sum_{j=1}^{N}{}' \alpha_{if}^j(t) exp(i\boldsymbol{q}\cdot\boldsymbol{r}_j(t)) \tag{3.8}$$

is the Fourier component of the polarizability density[2]. In the above expression $\alpha_{ij}^{j}(t)$ represents the projection of the molecular polarizability tensor $\boldsymbol{\alpha}^{j}$ of molecule j onto the initial and final polarization directions of the light wave $\boldsymbol{n}_i$ and $\boldsymbol{n}_f$.
The polarizability (or dielectric) fluctuations depend on the polarization direction of the incoming and final wave vectors. By considering the scattering geometry

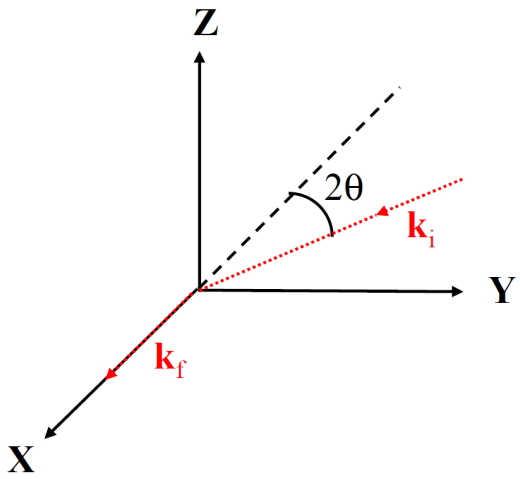

FIGURE 3.2: Scheme of the Brillouin light scattering geometry. The XY plane is the scattering plane. $\boldsymbol{k}_i$ and $\boldsymbol{k}_f$ are the incoming and the final wave vectors, respectively, and 2θ is the scattering angle.

reported in Figure 3.2 it is possible to define two main configurations: the vertical-vertical polarized configuration (VV), defined by $\boldsymbol{n}_i = \boldsymbol{n}_f = \hat{\boldsymbol{z}}$, and the vertical-horizontal fully depolarized configuration (VH), where $\boldsymbol{n}_i = \hat{\boldsymbol{z}}$ and $\boldsymbol{n}_f = \hat{\boldsymbol{y}}$. In these cases the polarizability fluctuations are given by

$$\delta\alpha_{VV}(\boldsymbol{q},t) = \delta\alpha_{zz}(\boldsymbol{q},t) \tag{3.9}$$

and

$$\delta\alpha_{VH}(\boldsymbol{q},t) = \delta\alpha_{zy}(\boldsymbol{q},t) \tag{3.10}$$

It is clear, then, that the scattered intensity will give different information depending on the scattering angle and the polarization directions. In good approximation, the polarizability tensor can be divided in an isotropic and an anisotropic part. The isotropic part is independent of the molecular orientation and gives rise to an isotropic scattering contribution $I_{iso}(\boldsymbol{q},t)$, which in turn is proportional to the dynamic structure factor of the system and gives, thus, information on the longitudinal waves. Moreover this term does not appear in the fully depolarized configuration (VH).
Differently, the fluctuations of the anisotropic part of the polarizability depend both on the translational and rotational motion of the molecules. In the case of glasses and supercooled liquids by considering the correlation between the rotational motions of different molecules, the intensity of the depolarized spectrum

[2]The prime on the sum indicates that the sum is only over molecules in the scattering volume.

contains two contributions and can be written as [109]

$$I_{VH}(\boldsymbol{q},\omega) = \frac{I_0}{\omega} Im\left[R(\omega) + R_1(\boldsymbol{q},\omega) cos^2\left(\frac{2\theta}{2}\right)\right] \tag{3.11}$$

The first term does not depend on the momentum transfer and corresponds to the spectrum detected in the backscattering geometry. It describes the orientational fluctuations dynamics of the molecules. The second term is instead $\boldsymbol{q}$-dependent and reflects the transverse dynamics in the system. It is in fact usually expressed through the frequency dependent shear viscosity, the rotation-translation coupling function and the rotational friction force [109]. In the high frequency limit, thus in the case of glasses, equation 3.11 becomes

$$I_{VH}(q,\omega) = I_0 \frac{\gamma q^2 v_T^2}{(\omega^2 - q^2 v_T^2)^2 + (\omega\gamma)^2} cos^2\left(\frac{2\theta}{2}\right) \tag{3.12}$$

where I_0 is a constant, γ is the linewidth of transverse Brillouin peaks, and v_T is the transverse sound velocity.
The second term in the previous expression is forbidden by a selection rule in the polarized spectrum and its intensity depends on the scattering angle, being zero in the backscattering configuration ($2\theta = 180°$) [110]. In conclusion it is then possible to measure the longitudinal modes by working in backscattering configuration, and the transverse ones by using a depolarized 90° scattering geometry.

3.1.1 Experimental setup

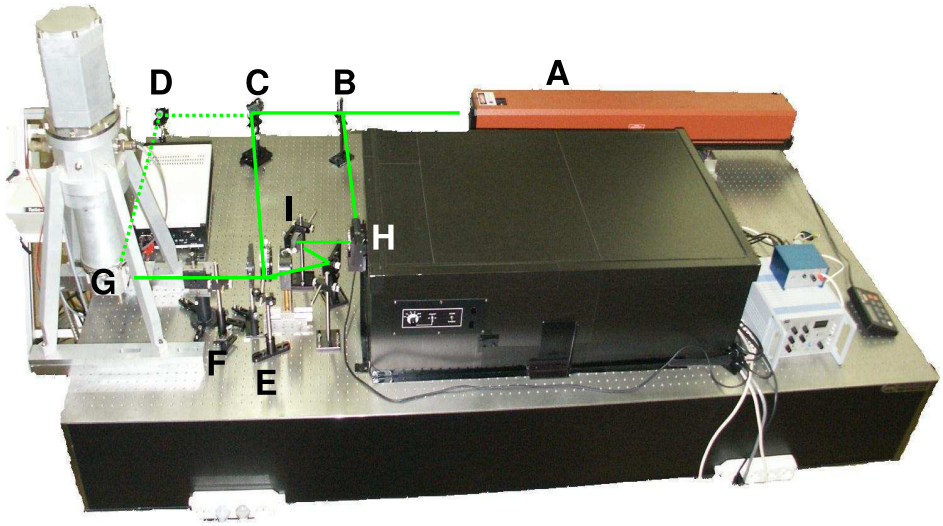

FIGURE 3.3: Experimental set up for Brillouin light scattering measurements. The green line represents the laser path for both the backscattering geometry (full line) and the 90° degree configuration (dotted line).

Brillouin Light Scattering measurements have been performed in collaboration with the group of Prof. D. Fioretto in his laboratory at the Department of Physics of Perugia. The experimental set-up used for the measurements is reported in Figure 3.3. It consists of a laser (A), a Fabry-Perot interferometer (H) and of optical elements (B-F) used to focus the light on the sample (G) and to collect the scattered radiation.
The incident beam comes from a diode pumped solid state laser, which produces a coherent radiation with a wavelength of 532 nm, vertically polarized with respect to the scattering plane. The light scattered from the sample is analyzed by means of a Sandercock type $(3+3)$-pass tandem Fabry-Perot interferometer. This device consists of two Fabry-Perot interferometers. The scattered radiation goes three times through each interferometer and then is collected by a photomultiplier and visualized as a function of the frequency via an acquisition system. Each interferometer works as a resonant cavity. It consists of a couple of mirrors, which works as a filter by transmitting only light with frequencies $\omega_{nc} = n\omega_c$ that are multiples of a characteristic frequency $\omega_c = \frac{n\pi c}{L}$. In this expression c is the speed of the light and L represents the distance between the mirrors. The two interferometers are rotated of a fixed angle of $\sim 20°$ one with respect to the other, and the distance between the mirrors of each couple is slightly different. This condition is necessary to produce the tandem effect: the coupling of the two filters allows only a single mode to be transmitted without loosing intensity. The second cavity is, in fact, tuned in order to accept only one mode from the first one and suppresses the remaining ones.
The two couples of mirrors are installed on the same support and the distance between the mirrors is changed by means of a piezo-electric crystal. In this way, a variation of the distance L in the first filter implies the same variation on the second one, without affecting the tandem operation.
The distance between two consecutive modes defines the Free Spectral Range (FSR) $\delta\nu = c/2L$ of the instrument. By changing L from $\sim$ 0.1 mm to $\sim$ 25 mm it is possible to span a frequency range from 1 GHz to hundreds GHz around the incident frequency. The frequency scan is performed by changing the distance between the mirrors, and can cover a range of one or more FSR.
The performance of the $(3+3)$-pass tandem Fabry-Perot interferometer is largely described by two parameters: the "finesse" and the "contrast". The first one is defined as the ratio between the FSR and the linewidth of a single mode, thus the instrumental resolution of the interferometer. The frequency resolution depends on the quality of the mirrors, the level of vibrations in the system and it increases on increasing the distance between the mirrors. The contrast, instead, is related to the intensity of the radiation transmitted, I_T, through the interferometer and is higher than 10^9. In general I_T can be written as

$$I_T = \frac{I_0}{1 + \left(\frac{4F^2}{\pi}\right) sin^2\left(\frac{2\pi L}{\lambda}\right)} \tag{3.13}$$

where I_0 is the maximum transmission of the two Fabry-Perot interferometers and F is the finesse. The contrast represents the ratio between the maximum (for all the even multiples of $L = \lambda/4$) and the minimum (for all the odd multiples of

$L = \lambda/4$) of the intensity of the transmitted radiation.
The external optical elements allow measuring BLS spectra for different scattering geometries. In Figure 3.3 a scheme is reported of the path of the light in the case of the backscattering geometry (full green line), and in the case of a $2\theta = 90°$ configuration (dotted green line). In general, the light produced by the laser impinges on a beamsplitter (B), which sends a part of the beam directly into the interferometer (H). This secondary light acts as a reference beam in order to check the parallelism between the mirrors of the two Fabry-Perot. The rest of the incident light goes instead to another mirror (C), which is used to select the $2\theta = 180°$ or $2\theta = 90°$ geometry.
In the backscattering configuration, the light is reflected then by a cylindrical mirror (E) and impinges on the sample (G) after being focused by a lens in front of it (F). The backscattered radiation is then collected by the same lens (F) and guided then into the interferometer through another couple of mirrors (I). The radiation coming into the interferometer is controlled by a pinhole placed at its entrance (H).
In the case of the $2\theta = 90°$ geometry, the incident light selected from the beamsplitter is reflected by a mirror (D) into another focusing lens, placed just before the sample (hidden by the sample in the Figure). The radiation scattered in the perpendicular direction (thus at 90°) with respect to the incident beam, follows then the same path as in the backscattering configuration.

3.2 Sorbitol

Among the different kind of glasses, the added complexity of associated liquids makes them especially interesting. In general, associated liquids are characterized by hydrogen bonding, which is an especially strong kind of attraction between a hydrogen atom with an electronegative atom, like nitrogen, oxygen or fluorine. The hydrogen bond is stronger than a van der Waals interaction, but weaker than a covalent bond. Polyhydric alcohols, such as glycerol, are typical examples of hydrogen bonding glass formers. In the "Angell plot" classification, they usually occupy an intermediate position, with a more or less Arrhenius-like behavior of the structural relaxation (see section 1.3.2).
In associated liquids, the number of hydrogen bonds can vary with temperature and pressure. Temperature is usually the control variable. In fact, the structural relaxation in associated liquids is less sensitive to pressure (the value of T_g is not too sensitive to pressure variations), while the structural relaxation time in the supercooled regime is strongly affected by temperature [8].
Sorbitol ($C_6H_8(OH)_6$, Figure 3.4) is a peculiar hydrogen bonded glass former. It is very fragile (i.e., the relaxation time exhibits a super-Arrhenius temperature dependence) and yet is chemically very similar to glycerol, which is among the strongest molecular liquids (i.e., exhibits a more nearly Arrhenius temperature dependence).
Consistent with its large fragility value (m$\sim$ 107 [42]), the structural relaxation

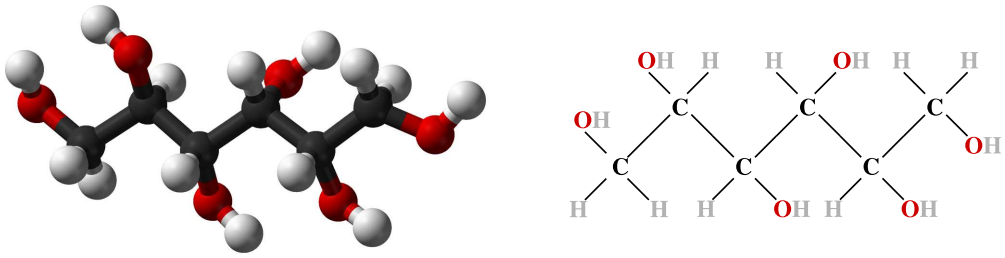

FIGURE 3.4: Scheme of the structure of sorbitol.

peak in the dielectric loss spectra is quite broad as observed in numerous studies using dielectric spectroscopy [111]. In particular, sorbitol is considered a perfect system to investigate the relation between the α and the JG β relaxation processes, being the JG β process well evident both below and above the glass transition temperature (see section 1.3.1 and Figure 1.4).
Sorbitol vitrifies close to ambient temperature ($T_g = 267$ K [112]) and has a stable supercooled liquid phase. The glassy state can be easily obtained by quick quenching the liquid phase from above the melting temperature $T_m = 368$ K.
Inelastic neutron scattering measurements on polyhydric alcohols have suggested the existence of a systematic relation among the boson peak energy, the boson peak intensity and the hydrogen-bond density, where the latter is defined as the ratio of the number of hydroxyl groups to that of carbon atoms (N_{OH}/N_C)[113]. Beyond this correlation the authors of Ref. [113] found also that in systems characterized by the same N_{OH}/N_C ratio, the boson peak position decreases and its intensity increases upon decreasing the hydrogen-bonds (N_{OH}) (see first three systems in Table 3.1). Albeit sorbitol was not included in this work, the previous result suggests the presence in this system of a higher boson peak energy with respect to the one of the other glasses studied in Ref. [113].
Preliminary measurements on glassy sorbitol have confirmed the general trend observed in Ref. [113]: the boson peak in sorbitol is located at about 4.5 meV [114], thus at energies higher with respect to those of other stronger polyhydric alcohols, such as glycerol ($E_{BP} \sim 4$ meV [115]) having the same N_{OH}/N_C ratio. Table 3.1 reports the values of T_g, the kinetic fragility and the energy of the boson peak maximum for several polyhydric alcohols, including sorbitol. It is interesting to note that all the quantities increase on increasing the hydrogen-bond number.

The high BP value makes of sorbitol an ideal candidate for the investigation of the relation between boson peak and elasticity, giving the possibility to access experimentally the energy region both below and above the boson peak maximum. In fact usually fragile systems display a lower E_{BP} value ($\sim 1 - 2$ meV) than strong materials. As a consequence, the acoustic excitations in the corresponding energy range are outside the experimental window accessible with IXS and cannot be studied. For this reason it is extremely difficult to investigate the high frequency dynamics of fragile glasses in the crucial energy range close to the boson peak maximum.
It is interesting to observe that the very fragile character of sorbitol is typically only found in polymeric systems. This class of materials usually does not follow

system	formula	T_g [K]	m_A	E_{BP} [meV]
Ethylene glycol	$C_2H_4(OH)_2$	151	50	3.3
Glycerol	$C_3H_5(OH)_3$	184	53	4.0
Threitol	$C_4H_6(OH)_4$	229	79	4.4
Sorbitol	$C_6H_8(OH)_6$	266	107	4.5

TABLE 3.1: Glass transition temperature, kinetic fragility and boson peak maximum energy of different polyhydric alcohols. All the quantities increase on increasing the number of hydrogen bonds. The values of T_g and m_A are taken from Ref. [42] for ethylene glycol, glycerol and sorbitol, and from Ref. [116] for thereitol. The value of E_{BP} are all taken from Ref. [113] for all the systems with the exception of sorbitol [114].

the correlations between fragility and elastic properties of glasses presented in section 2.4. For this reason sorbitol is as well an excellent molecular candidate to test the validity of these correlations.

Sorbitol has been widely studied in the last years. The possibility to get in-

T [K]	ρ [g/cm^3]	χ_T [10^4 MPa^{-1}]	C_P [J/gK]
267	1.466	1.57 ± 0.05	2.40
256	1.467	0.77 ± 0.14	1.41
246	1.469	0.77 ± 0.14	1.34
220	1.472	0.76 ± 0.14	1.20
150	1.480	0.73 ± 0.13	0.80
80	1.488	0.71 ± 0.13	0.41

TABLE 3.2: Density, isothermal compressibility and constant pressure heat capacity of sorbitol at different temperatures. The data are taken from Ref. [117] except the C_P data that are taken from Ref. [118].

formation on both thermodynamic [117] and calorimetric [118] data, allows us to estimate several relations between macroscopic and microscopic properties of glasses. Table 3.2 reports the density ρ, the isothermal compressibility χ_T, and the constant pressure heat capacity C_P at some representative temperatures. The errorbar for ρ and C_P is not indicated being less than 0.05% and 0.7%, respectively.

3.3 Low frequency dynamics in sorbitol

3.3.1 Experimental details

Sorbitol of $\sim$ 99% purity was purchased from Sigma-Aldrich Chemicals and kept for two days under vacuum at about 383 K to obtain a homogeneous and well transparent liquid, free from gas content. Two samples were prepared. The first one was obtained from a liquid sorbitol 80 μm thick film placed into a container with an optically polished silicon plate at the bottom and closed with a quartz window on top. The sample glass was prepared by quenching the liquid film in mixed ice and salt (T$\sim$ 255 K). The sample preparation was carried out in a nitrogen atmosphere to avoid contamination with water. The second glass sample was prepared as the first one but using this time as holder a silicate glass tube with an inner diameter of 2 mm and an outer diameter of 6 mm.
Brillouin spectra were collected in the temperature range 20–294 K, and a Cryomech ST405 cryostat was used to regulate the temperature. The measurements were taken both on cooling and on heating the sample, without any polarization analysis (VU configuration) for several scattering configurations, while for the 90° one both a vertical (VV) and a horizontal (HV) polarization analysis has been performed.
A first set of measurements was performed using the sorbitol film as sample and

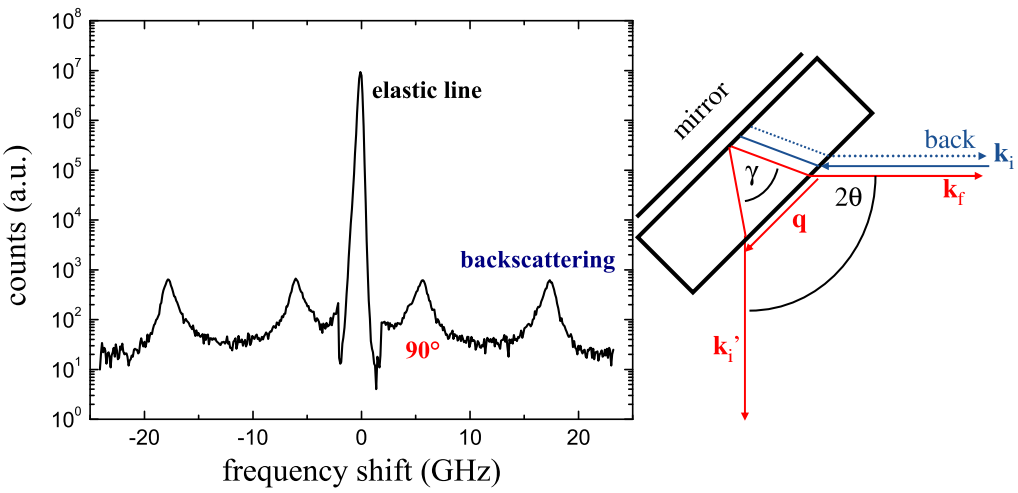

FIGURE 3.5: BLS spectrum of glassy sorbitol at T=281 K. The elastic line, that can be considered to a good approximation as the instrumental function, is here presented on a y-scale different from that corresponding to the inelastic signal. Two Brillouin doublets are present, corresponding to the two different scattering angles 2θ probed at the same time as schematically shown on the right. The incident and scattered beams are represented by the arrows $\vec{k_i}$ and $\vec{k_f}$ for 2θ=180°, and by $\vec{k_i'}$ and $\vec{k_f}$ for 2θ=90°.

using a distance of $L = 5$ mm between the mirrors in the interferometer in order to

obtain a good luminosity while keeping the instrumental resolution to a still reasonably good level (≈380 MHz FWHM). The choice of the experimental setup was determined by the interest to measure the momentum transferred in the scattering process (Eq. 3.3). In fact, to the best of our knowledge no published data of the refractive index of glassy sorbitol were available. As shown schematically on the right panel of Figure 3.5, putting the sample at 45° with respect to the incident beam and measuring the backscattered radiation it is possible to simultaneously probe two scattering geometries [119]: (i) the backscattering geometry (blue vectors in the Figure), with transferred momentum $q_{back} =\mid \vec{k_f} - \vec{k_i} \mid = 4\pi n/\lambda$, and (ii) the 90° scattering angle geometry (red vectors), allowed by the fact that the beam reflected by the mirror behind the sample acts as a secondary incident beam with wavenumber $\vec{k_i'}$. In this second case, the momentum transfered is given by $q_\gamma = (4\pi n/\lambda) sin(\gamma/2)$. However, by using the Snell law,

$$sin(\gamma/2) = \frac{1}{n} sin(2\theta/2) = \frac{1}{n}\frac{\sqrt{2}}{2} \tag{3.14}$$

the exchanged momentum becomes $q_{90°} =\mid \vec{k_f} - \vec{k_i'} \mid = 4\pi/(\lambda\sqrt{2})$, and thus it is the same as in a scattering process at an angle 2θ in air.
An example of a spectrum obtained with this configuration is shown in Figure 3.5. If we assume that no dispersion in the sound velocity takes place between the two probed q values, the ratio of the frequency positions ν of the two Stokes or anti-Stokes peaks directly gives the refractive index:

$$n = \frac{\nu_{back}}{\nu_{2\theta=90°}}\frac{\sqrt{2}}{2}. \tag{3.15}$$

This scattering configuration was used in the temperature range 150-294 K to obtain the refractive index of glassy sorbitol. At temperatures lower than about 150 K, the sample cracked, thus leading to a large increase in stray light that made the measurements of the refractive index impossible. A second set of measurements was then performed in the 20-294 K temperature range using only the standard backscattering configuration on both the prepared samples, in order to accurately measure the position and the width of the Brillouin peaks. In this case a distance of $L = 17$ mm between the mirrors in the interferometer was employed to obtain an instrumental resolution of ≈140 MHz. For each temperature various measurements were taken on both heating and cooling the sample to check the reproducibility of the data. No differences were found neither among the different sets of data nor between the two samples.
A third set of measurements was performed using the second sample in a 90° scattering geometry (see Figure 3.3). This set-up was necessary in order to measure the transverse sound waves. Due to the low intensity of these modes, a distance $L = 4$ mm between the mirrors in the interferometers was employed. It implies a large instrumental resolution, which allows only for a reliable measurement of the peaks position and not of the linewidth.
The transverse modes were measured only at five temperatures in the $235 - 281$ K range. At lower temperatures the intensity of the inelastic peaks was too low,

while close to room temperature the modes quickly disappeared under the tails of the structural relaxation process.

3.3.2 BLS results

Longitudinal acoustic modes

From the first set of measurements we obtained for the refractive index n the value 1.52±0.01, basically constant in the 150-294 K temperature range. In order to evaluate the temperature dependence of n down to the lowest temperatures investigated in the second set of measurements, we made use of the Clausius-Mossotti relation [54]

$$\frac{n^2(T)-1}{n^2(T)+2} = \frac{4\pi N_A \alpha}{3v(T)} \tag{3.16}$$

where $v(T)$ the specific volume of the system, N_A is the Avogadro's number and α is the optical polarizability. The temperature dependence of the specific volume has been derived from available pressure-volume-temperature (PVT) data reported in Ref. [117] (see table 3.2). The optical polarizability has been instead calculated by inverting relation 3.16 and using the experimental data for n obtained from relation 3.15 at different temperatures and reported in the left panel of Figure 3.6. The resulting values of α are reported in the right panel of the same Figure. We find an average effective optical polarizability $\alpha = 29.7 \pm 0.2$ Å^3.

Figure 3.7 shows some examples of BLS spectra of sorbitol collected in the

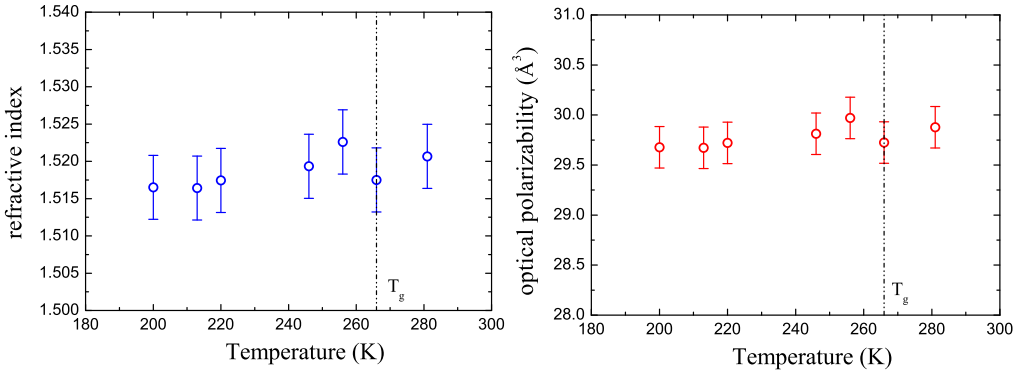

FIGURE 3.6: Right panel: experimental refractive index n of sorbitol obtained from relation 3.15. Right panel: optical polarizability of sorbitol obtained from the inversion of relation 3.16 using the data reported in the left panel.

backscattering geometry (second set of measurements) for different temperatures above and below the glass transition temperature. For all spectra the Brillouin doublet corresponding to the longitudinal acoustic modes is shown. Two features are immediately evident: the rapid decrease of the width of the Brillouin peaks

and the clear shift of their position toward higher frequencies on decreasing the temperature.

To determine the frequency position Ω and the full width at half maximum Γ

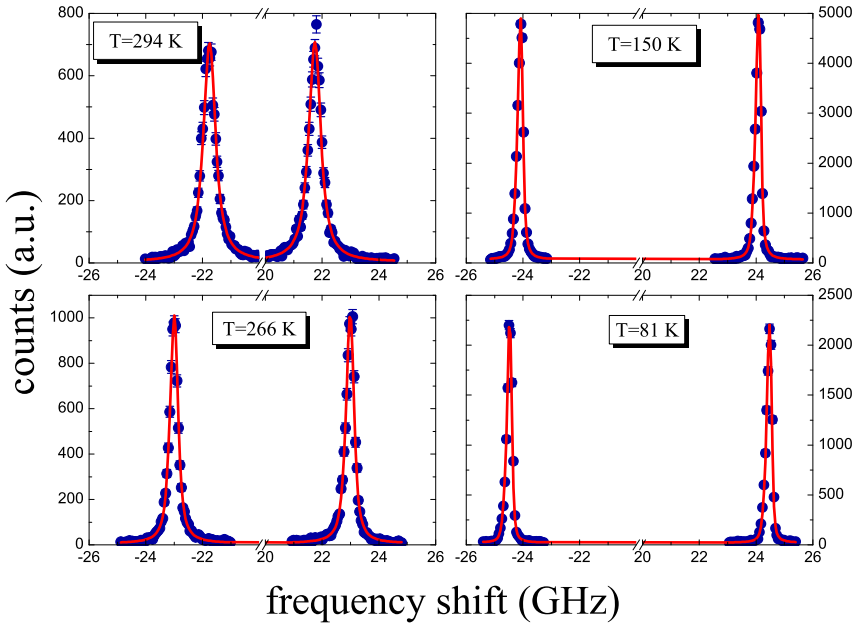

FIGURE 3.7: Brillouin light scattering spectra of sorbitol at the indicated temperatures collected in the backscattering configuration. The red lines corresponds to the best fitting lineshape obtained from the model of equation 3.17 convoluted to the instrumental resolution.

of the longitudinal acoustic modes, the spectra were fitted in a narrow frequency range around the Brillouin peak using a damped harmonic oscillator model function

$$I(Q,\omega) = I_0 \frac{\Gamma\Omega^2}{(\omega^2 - \Omega^2)^2 + (\Gamma\omega)^2} \tag{3.17}$$

convoluted to the instrumental resolution (red line in Figure 3.7). The values of Ω and Γ obtained by this fitting procedure are reported in Figure 3.8. There is a clear change of slope in the temperature dependence of the Brillouin peak position that comes together with a rapid increase of the linewidth when crossing T_g. Such features are typically found in glass-formers; in particular, the second one is due to the structural relaxation entering, above T_g, the frequency window explored by BLS. From the linear behavior of Ω close to T_g (both in the glass and in the undercooled liquid) it is possible to estimate the Grüneisen parameter for the longitudinal acoustic modes. The Grüneisen parameter of a material reflects the role played by the anharmonicity of the interatomic potential on the acoustic

frequencies and is generally defined in terms of thermodynamic parameters as

$$\gamma_{th} = \frac{\alpha_P V}{\chi_T C_V} = \frac{\alpha_P V}{\chi_S C_P} \tag{3.18}$$

where V is the volume, $\alpha_P = (\partial ln(v(T))/\partial T)_P$ the isobaric thermal expansion coefficient, χ_T and χ_S the isothermal and isentropic compressibilities, and C_V and C_P the isochoric and isobaric heat capacities [120]. In the quasi-harmonic approximation the anharmonicity is considered as a weak effect that induces a temperature dependence of the vibrational frequencies following the dependence of density on temperature. In this case, the Grüneisen parameter can be also expressed as the weighted average of generalized parameters γ_i

$$\gamma_{th} = \sum_i \gamma_i c_i / \sum_i c_i \tag{3.19}$$

where

$$\gamma_i = -(\partial \ln(\Omega_i)/\partial \ln(V)) = -(1/\alpha_P)(\partial \ln(\Omega_i)/\partial T)|_V \tag{3.20}$$

describes the volume dependence of the vibrational frequency for a mode i, while c_i represents the heat capacity associated with that mode. Each mode is characterized by a different value of γ_i that can be either positive or negative. As a consequence, $|\gamma_{th}|$ is usually smaller than the absolute value for a single vibrational mode.

In the case of sorbitol we estimated the mode Grüneisen parameter of the longitudinal acoustic modes in the GHz frequency range, using the isobaric thermal expansion coefficient that we derived from the available PVT data [117]. γ_{LA} comes out to be equal to 3.6±1.1 in the glass and to 4.7±0.3 in the liquid phase. It is interesting to observe that these two values are basically compatible within errorbars, thus indicating that in good approximation the change of slope observed in the temperature dependence of the Brillouin frequency in Fig. 3.8 directly reflects the corresponding change in the slope of the temperature dependence of the density.

The Grüneisen parameter plays a role in the description of the sound attenuation of the longitudinal modes. In fact, for large wavelengths the observed damping can be expressed through the Akhiezer model of anharmonicity. In this model the sound waves cause a disturbance of the thermally excited modes present in the system and the equilibrium is re-established by energy dissipation leading to the absorption of sound at finite temperatures [87, 121, 122]. After the perturbation of the thermal vibrations by the acoustic waves, the system returns to the equilibrium situation in an average relaxation time τ_{th}. In the glassy phase, τ_{th} turns out to be almost temperature independent close to the glass transition temperature, while its value changes at low temperatures due to the corresponding variation of the Grüneisen parameter [120].

In the simple Akhiezer model of anharmonicity the Grüneisen parameter enters in the description of the linewidth of the longitudinal acoustic waves through the relation [87, 121]:

$$\Gamma = \gamma_{LA}^2 \frac{c_V T v_{LA}}{2 v_D^3} \Omega^2 \tau_{th} \tag{3.21}$$

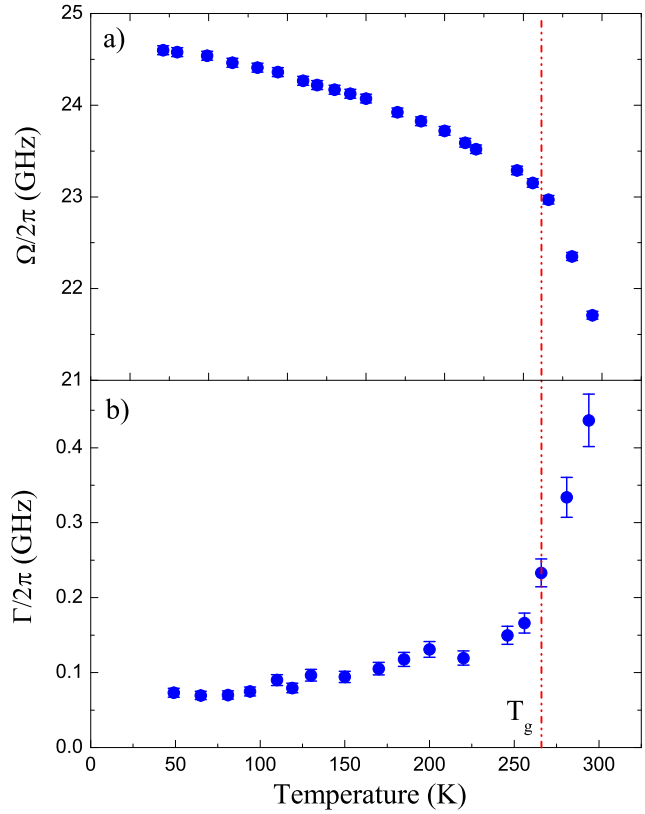

FIGURE 3.8: Temperature dependence of the frequency shift $\Omega/2\pi$ (top panel) and of the linewidth $\Gamma/2\pi$ (bottom panel) of the longitudinal acoustic modes. The dashed line indicates $T_g = 266$ K.

where c_V is the constant volume specific heat, v_{LA} the longitudinal sound velocity and v_D the Debye velocity. The thermodynamic quantities present in this equation have been taken from Refs. [117, 118], while the Debye sound velocity has been calculated using the transverse sound velocity data as explained later in the text. Eq. 3.21 can be used to calculate the relaxation time τ_{th} which turns out to be almost temperature independent close to T_g with an average value of $\tau_{th} = 0.09$ ps. This value is similar to that estimated in other systems such as OTP and SiO_2 [87, 123].

The frequency position and the linewidth of the Brillouin peaks can be used to obtain the real part (M') and imaginary part (M'') of the longitudinal elastic modulus M, through the relations $M'(\Omega) = \Omega^2\rho/q^2$ and $M''(\Omega) = \Gamma\Omega\rho/q^2$, where ρ is the density. Alternatively, the same information can be reported in terms of the sound velocity $v_{LA} = \sqrt{M'/\rho} = \Omega/q$ and of the mean free path $l = v_{LA}/\Gamma$ of the longitudinal acoustic excitations, as shown in figure 3.9 (a) and (b), respectively. In the glassy phase the longitudinal sound velocity reaches values higher than ~ 4000 m/s that are quite exceptional for a fragile system such as sorbitol.

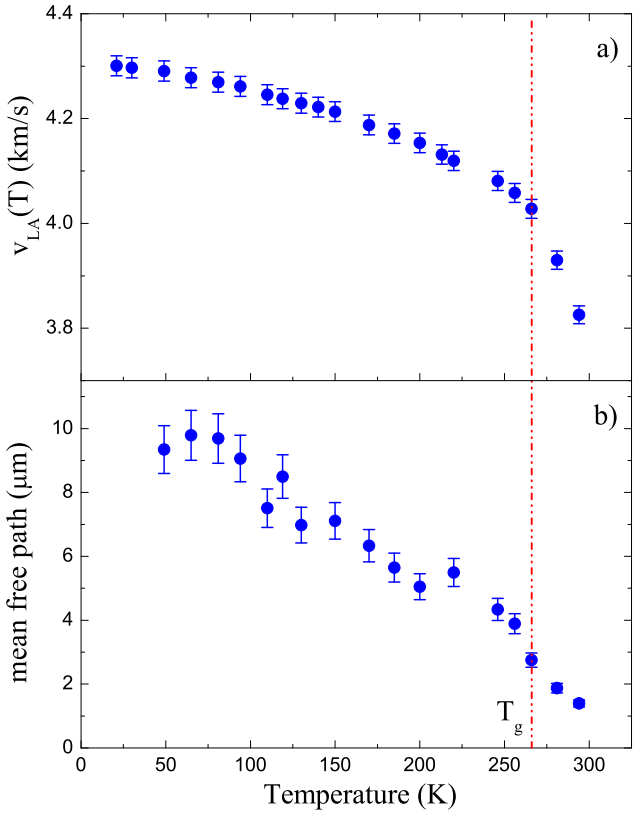

FIGURE 3.9: Temperature dependence of the sound velocity v_{LA} (a) and of the mean free path l (b) of the longitudinal acoustic modes in sorbitol. The dashed line indicates $T_g = 266$ K

Transverse acoustic modes

As previously reported, the transverse sound modes were measured on the second sample by using a 90° scattering configuration. The shape of the glass tube used as sample holder can produce an error on the nominal scattering angle. For this reason the data have been corrected by multiplying the transverse frequencies for a factor C obtained from the comparison of the longitudinal modes measured in this configuration to those collected in backscattering. The frequency of the longitudinal modes measured at 90° should then correspond to

$$\nu_{LA,90°expected} = \nu_{LA,back} sin(45°) = \nu_{LA,back} \frac{\sqrt{2}}{2} \tag{3.22}$$

The ratio between the measured and the expected frequency of the longitudinal modes gives the correction factor C

$$C = \frac{\nu_{LA,90°expected}}{\nu_{LA,90°measured}} \tag{3.23}$$

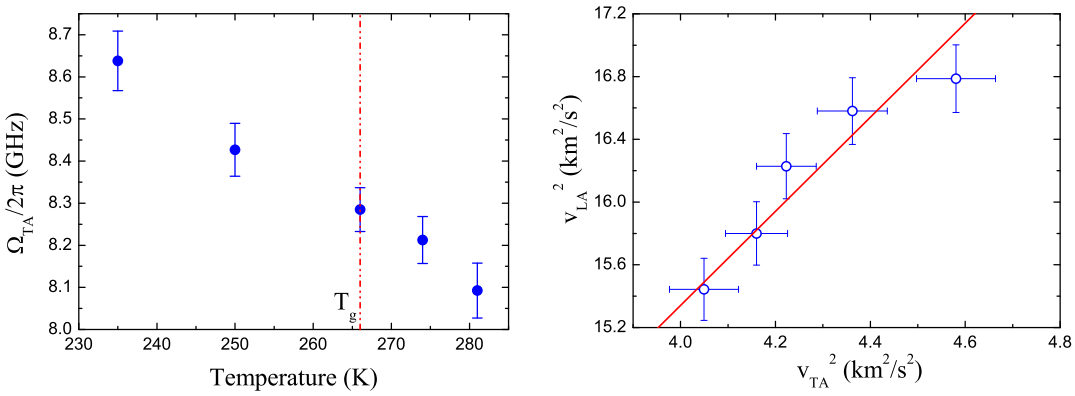

FIGURE 3.10: Left panel: Temperature dependence of the frequency shift $\Omega_{TA}/2\pi$ of the transverse sound waves. The dashed line represents T_g. Right panel: Cauchy-like relation between longitudinal and transverse acoustic modes. The dashed line corresponds to the best fit lineshape described by equation 3.24.

We found an error of $\sim 0.6\%$ on the expected frequencies corresponding to a less than 1° error on the scattering angle.
The left panel of Figure 3.10 reports the temperature dependence of the frequency of the transverse acoustic waves. Using the refractive index we can calculate the corresponding sound velocity $v_{TA} = \sqrt{G'/\rho}$, where G' is the shear modulus being $v_{TA} = 2\pi\Omega_{TA}/q_{90^\circ}$ and $q_{90^\circ} = (4\pi n/\lambda)\sqrt{2}/2$.
The values of the transverse sound velocity at temperatures outside the probed range can be obtained through a Cauchy-like relation for isotropic solids [105, 106]

$$v_{LA}^2 = A + 3v_{TA}^2 \tag{3.24}$$

where A is a material dependent but temperature independent parameter.
This relation works very well in many glasses and polymers. It implies that the longitudinal and transverse sound velocities are directly related at any temperature and allows us to estimate the Debye sound velocities at low temperatures even if only longitudinal sound velocities are known, as it is often the case.
In the right panel of Figure 3.10 the square of the sound velocities is reported together with the best fit lineshape obtained from equation 3.24. In the case of sorbitol we found $A = 3.34 \pm 0.09$ km^2/s^2.
From the longitudinal modes we can alternatively estimate the transverse sound velocity using thermodynamic data. In general in a glass G' is given by $G' = \frac{3}{4}[M' - B']$ where B' is the real part of the bulk modulus. The bulk modulus, in turn, can be calculated from the available PVT and calorimetric literature data [117, 118], being $B' = 1/\chi_{S\infty}$, where $\chi_{S\infty}$ is the high-frequency adiabatic compressibility

$$\chi_{S\infty} = \chi_{T\infty} - \frac{T\alpha_P^2}{\rho c_P} = \frac{\chi_{T\infty}}{\gamma} \tag{3.25}$$

In this expression $\gamma = c_P/c_V$ is the constant pressure to constant volume specific heat ratio and $\chi_{T\infty}$ is the high frequency isothermal compressibility. From

these relations we calculate a transverse sound velocity of 2300 ± 400 m/s at T_g. Such a value is higher but compatible than the corresponding measured ones, $v_T^{BLS} = 2055 \pm 15$ m/s. This difference is likely due to the approximations adopted to calculate $\chi_{T\infty}$ from the Tait equation describing the PVT data in the glassy state [117], which in fact lead to an uncertainty on $\chi_{T\infty}$ of $\sim 18\%$ (see table 3.2).

3.3.3 On the connection between microscopic and macroscopic properties

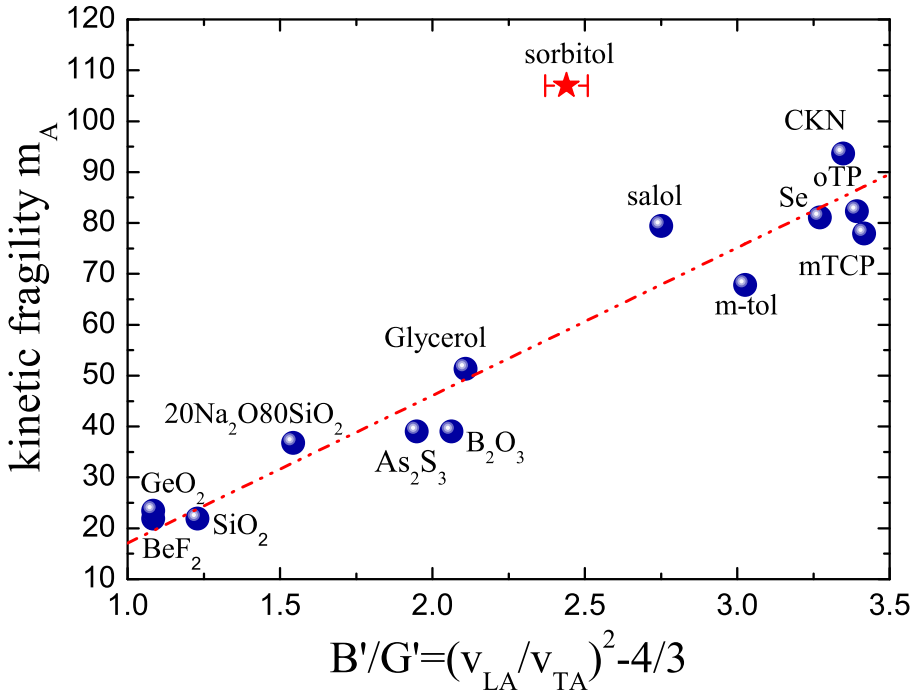

FIGURE 3.11: Correlation of kinetic fragility, m_A, with the ratio of the bulk and shear modulus B'/G'. The straight line shows the relation described by Eq. 3.26. Adapted from [5].

The knowledge of the elastic moduli of glassy sorbitol can be used to test some of the proposed correlations between elastic properties of glasses and fragility (see sections 2.4). For example, Novikov and coworkers found that the weaker a glass resists to shear stress in comparison to bulk one (higher B'/G' ratio), the more fragile is the behavior of the corresponding melt [5, 6]. This correlation is quantified by the relation

$$m_A = 29(B'/G' - 0.41), \tag{3.26}$$

where $B'/G' = (v_{LA}/v_{TA})^2 - 4/3$. This correlation is reported in Figure 3.11. In the case of glassy sorbitol $B'/G' = 2.44 \pm 0.07$, which would lead to $m_A = 59 \pm 2$ according to the previous relation. This value has been obtained from the BLS data and is in clear disagreement with the one obtained using dielectric measurements in the supercooled liquid ($m_A \sim 107$) [42]. The existence of systems showing strong deviations from the previously recalled simple linear relation was underlined already in Refs. [5, 6], such for instance polystyrene. Novikov and coworkers suggested that the systems showing such deviations might be those who do not follow the relation between the kinetic and the thermodynamic fragility (see section 1.3.2). In fact, in the case of polystyrene the correlation between elastic moduli and fragility seems to be recovered once the thermodynamic fragility is considered [5, 6]. However, this explanation does not seem to hold for the case of glassy sorbitol where the two fragilities were found to be very similar [42]. In other words, sorbitol really seems to be a peculiar system: from the elasticity point of view it shows a behavior similar to that of intermediate glasses, with high elastic moduli values, while it presents at the same time features of fragile systems, i.e. a strong departure of the structural relaxation time from the Arrhenius behavior above T_g.

Following Buchenau and Wischnewski [4] we can introduce a vibrational com-

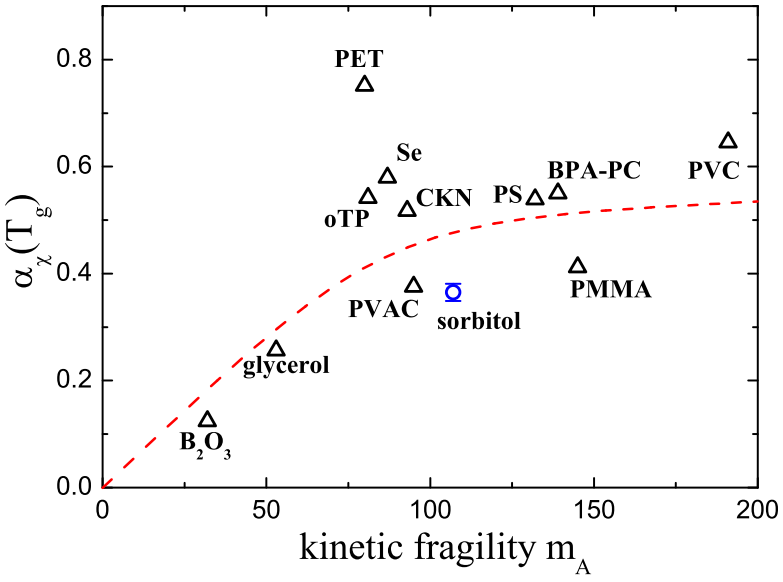

FIGURE 3.12: Correlation between the ratio α_χ of vibrational to relaxational compressibility at T_g and the kinetic fragility m_A. The empty symbols are taken from Ref. [4], while the full circle corresponds to sorbitol. The dashed line is a guide for the eye.

pressibility $\chi_v = 1/M'$ and we can estimate the ratio α_χ between the vibrational

and relaxational compressibility:

$$\alpha_\chi(T_g) = \frac{\chi_v(T_g)}{\chi_T(T_g) - \chi_v(T_g)} \tag{3.27}$$

where χ_T is the isothermal compressibility measured in the liquid phase close to T_g (see table 3.2). As far as the harmonic approximation holds to calculate the nonergodicity factor up to T_g, this ratio coincides with the α parameter introduced by Scopigno *et al.* [3] and which was proposed to be simply proportional to the kinetic fragility through the relation $m_A = 135\alpha$ (see section 2.4). In the present case, using the PVT data for $\chi(T_g)$ [117] , we find $\alpha_\chi = 0.365 \pm 0.016$, which – given the known fragility of sorbitol – is a value too low to fulfill the linear relation proposed by Scopigno *et al.*, being the estimated fragility equal to 49 ± 2. In any event, it is of some interest to add the α_χ vs. m_A value of sorbitol to the compilation reported in Ref. [4], as shown in Fig. 3.12. The point corresponding to sorbitol agrees with the general trend shown by Buchenau and Wischnewski, suggesting that while a general correlation between α and m_A seems to hold, the data of α_χ flatten out to become basically fragility independent for systems with high fragility [46].

3.4 Sulfur

Sulfur has unique physical properties which have puzzled scientists and engineers for more than 100 years and which have no parallel in any other substance [124, 125]. Despite of the apparent simplicity of the system, it shows an extremely complex behavior in both liquid and solid phases and is the element displaying the largest number of allotropes.

At ambient conditions sulfur is a pale yellow solid. It melts at about 392 K to form a molecular low-viscosity liquid composed of eight-membered rings (S_8). Upon increasing the temperature, the shear viscosity η of the system decreases like in simple liquids and it reaches a minimum value of ~ 0.07 poise at 430 K (see Figure 3.13). On crossing the temperature T_λ=432 K, η abruptly increases by more than four orders of magnitude in the small temperature range of 428 - 463 K. The viscosity reaches a maximum of 932 poise at 460 K and then it decreases again and reaches a simple liquid-like value of ~ 0.01 poise at the boiling temperature $T_b = 718$ K [126]. This phenomenology represents the signature of the so-called λ-transition, a thermo-reversible process which is fascinating researchers since several decades. Many other physical properties display an anomalous behavior on crossing the transition temperature, such as the specific heat, the refractive index and the density [127–131]. The name λ transition comes from the shape of the specific heat which remembers the greek letter. Figure 3.14 shows a photo of liquid sulfur below and and above the λ transition. The color of the liquid changes reversibly from honey-yellow in the low viscosity phase below 432 K to dark red-brown in the extremely viscous phase.

All these temperature-related changes of the physical properties are completely

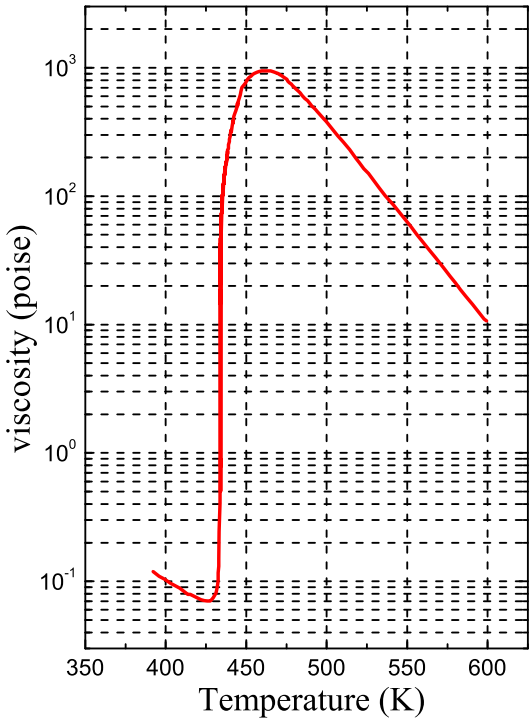

FIGURE 3.13: Viscosity of liquid sulfur as a function of temperature. On crossing the λ transition, the viscosity increases by several orders of magnitude in a narrow temperature range. Adapted from [126].

reversible if the melt is cooled down slowly and are due to internal structural changes. The transition is in fact due to a reversible polymerization process in which a fraction of S_8 rings coverts in long polymeric chains. Above T_λ, the system is composed of monomers and polymers in equilibrium polymerization, i.e. in a process of polymerization without termination in which the liquid is composed of a mixture of cycloocta rings and long chains in equilibrium [132]. The chains formation is responsible of the huge increase in the viscosity at T_λ (Figure 3.13). On increasing further the temperature, the kinetic energy of the polymeric chains increases as well. Consequently the chains break leading again to a low, normal liquid-like, value of the viscosity.

Several theories have been developed to explain the mechanism underlying this peculiar transition, but no one is still able to well reproduce the experimental data [133, 134].

The polymer content present in the liquid phase above the λ transition can be isolated and measured by quenching the high temperature melt at very low temperatures, and by dissolving the resultant material in carbon disulfide at 20° C [135]. Figure 3.15 reports the temperature dependence of the polymer weight fraction $\phi(T)$: for $T < T_\lambda$ the liquid is composed only by monomers, while on increasing the temperature, the polymer weight fraction increases steadily and then

FIGURE 3.14: Liquid sulfur below (left one) and above (right one) the λ transition.

it reaches a constant value at about 300 K. Several techniques are able to give information on $\phi(T)$. Albeit they agree close to the polymerization transition, distinct results have been found at higher temperatures [136, 137].

Recently, the polymeric phase has been investigated by means of inelastic x-ray

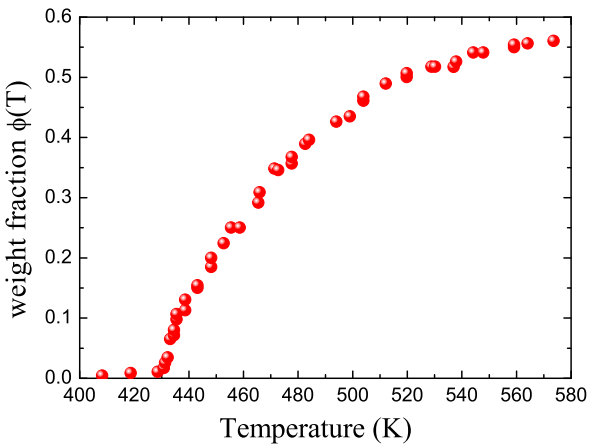

FIGURE 3.15: Temperature dependence of the polymer concentration $\Phi(T)$ in liquid sulfur. Adapted from [135].

scattering (IXS) and Brillouin light scattering (BLS) techniques and by infrared photon correlation spectroscopy (PCS) [138–140]. A strong relaxation is clearly present in the longitudinal modulus between the GHz frequency range and the THz range, at temperatures both below and above the λ transition threshold (see Figure 6.12). It corresponds to the main structural relaxation, which moreover, results to be slightly affected by the polymerization transition [139]. The huge

increase in the viscosity at T_λ appears instead to be related to the presence of a secondary slow relaxation process in the millisecond time scale (thus in the kHz frequency region).
The existence of a very low-frequency relaxation, suggested first from BLS and IXS results [138, 139], was demonstrated by means of PCS spectroscopy [140]. This process is typical of concentrated solutions of linear uncross-linked polymers and can be related to the entanglement of the chains in the melt. As for concentrated polymer solutions, if liquid sulfur is rapidly quenched from above T_λ, it is possible to freeze the equilibrium situation present at higher temperatures into a glassy phase. When crossing the glass transition temperature T_g=243 K (−30° C) [141] on increasing the temperature, the shear modulus shows a peculiar behavior typical of a polymer (Figure 3.16). There is a glassy region characterized by elas-

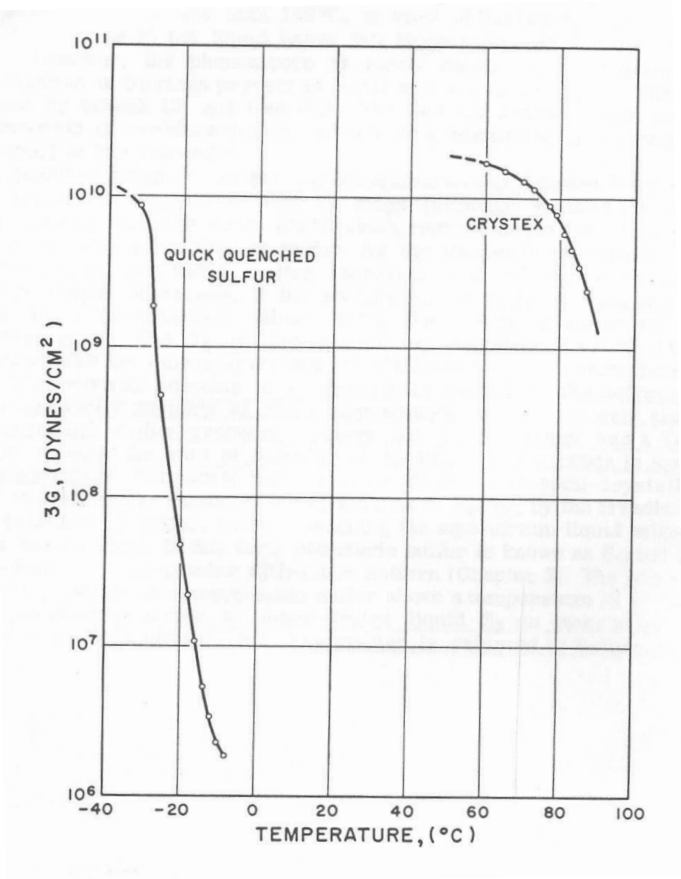

FIGURE 3.16: Temperature dependence of the shear modulus $3G$ of elastic sulfur and pure polymeric sulfur (crystex) [142].

tic moduli with typical solid-like values of about 10^9 Pa followed, just above T_g, by a transition region and a rubbery plateau [142]. The presence of this plateau together with that of the relaxation in the millisecond time scale have lead to a re-evaluation of the dynamics of liquid sulfur in the framework of a viscoelastic model [138, 140]: the increase of the shear viscosity at the λ transition is simply marking the onset of this rubber-like dynamics, and is quantitatively given by the product of the rubber shear modulus and of the characteristic time of the slow

relaxation, i.e. by the usual Maxwell relation. Thus, the presence of two relaxation process can be described by the relation $\eta = (G_\infty - G_c)\tau_\alpha + G_c\tau_c$ where G_c and τ_c are the shear modulus and the relaxation time of the slow process. As for any other viscoelastic system, this scenario implies that the transport properties of the high temperature liquid can be predicted from the knowledge of the elastic properties in the low temperature phase.
In order to shed light on the complex behavior around the λ transition, several experiments have been performed on elastic sulfur, thus on the amorphous solid above T_g. For example, it is known that the monomers present above the λ transition act as a plasticiser lowering the glass transition temperature from 368 K, the value characteristic of pure polymeric liquid sulfur (crystex in Figure 3.16), down to 243 K. The glassy phase, instead, has been poorly investigated. Only few neutron diffraction and Raman scattering studies have been carried out on this disordered state [136, 143–145]. For example, by comparing the static structure factor of the high temperature polymeric liquid and the low temperature glass, the similarity of these two phases comes out very clearly [143, 144].
The study of the vibrational dynamics of glassy sulfur in different frequency ranges will allow us to get further insight into the connection between the glass and the high-temperature liquid above T_λ. Moreover, due to its peculiar semi-polymeric nature, sulfur is as well an interesting candidate for the investigation of the proposed universal properties of glasses.

3.4.1 The fragility of polymeric sulfur

To the best of our knowledge no information on the kinetic fragility of polymeric sulfur is available in the literature. As reported in section 1.3.2 the fragility describes the behavior of the α structural relaxation process in the supercooled liquid phase on approaching T_g. In the case of polymeric sulfur the fragility cannot be directly estimated from the behavior of the viscosity (or the structural relaxation time) due to the presence of a secondary relaxation mechanism with comparable relaxation times [146]. This secondary relaxation mechanism, called χ process, has been studied in Ref. [146] and corresponds to bond S-S interchange in small segments of the polymeric chains. As a consequence the viscosity of the system contains an additional contribution with respect to that related to the simple molecular flow, and can be written as [146]

$$\frac{1}{\eta} = \frac{1}{\eta_\alpha} + \frac{1}{\eta_\chi}, \tag{3.28}$$

where $\frac{1}{\eta_\alpha}$ and $\frac{1}{\eta_\chi}$ are the viscosities due to the α process and to the additional χ relaxation mechanism, respectively. Figure 3.18 reports the measured viscosity together with the value estimated in Ref. [146] for $\frac{1}{\eta_\alpha}$ and $\frac{1}{\eta_\chi}$ as a function of $T - T_g$.

It is important to note that the secondary χ process becomes more and more important on approaching T_g, and becomes dominant close to T_g. We used these information to estimate the kinetic fragility m_A of polymeric sulfur. It is clear,

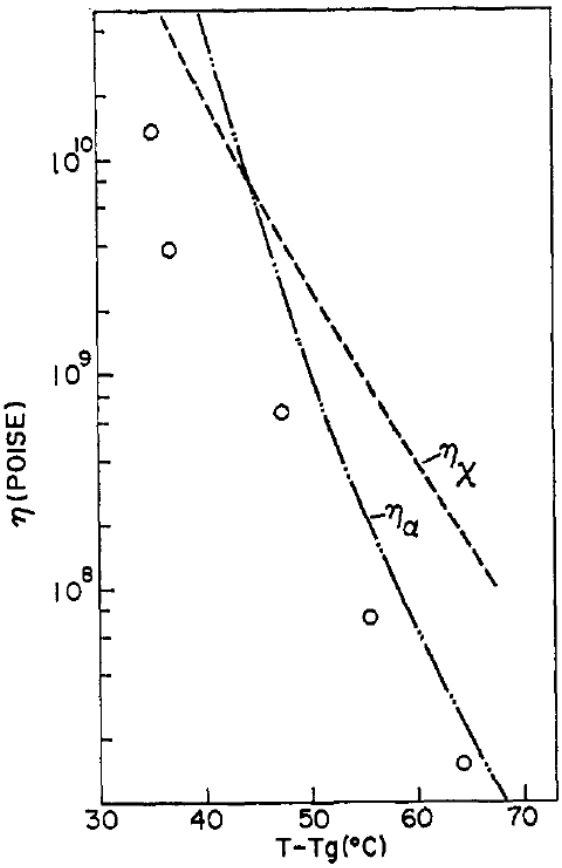

FIGURE 3.17: The total viscosity (dots) and the calculated viscosities due to the α (dashed-dotted-dotted line) and χ (dashed line) relaxation mechanisms for polymeric sulfur [146].

indeed, that it cannot be directly calculated from the experimental data reported in Figure 3.17, which in fact lead to a very low value of $m_A = 28 \pm 2$ very unusual for a polymeric system. A correct value of m_A should be related in fact only to the α relaxation mechanism. Figure 3.18 reports the logarithm of η_α as a function of the rescaled temperature T_g/T. As reported in section 1.3.2, in the case of polymeric systems, such as sulfur, the viscosity is well described by the Williams-Landel-Ferry (WLF) equation [34]

$$log(\eta_\alpha) = A + C_1 \frac{T - T_g}{C_2 + T - T_g}, \tag{3.29}$$

where A, C_1 and C_2 are fitting parameters. In general $A = 13$ is related to the value of the viscosity at T_g, being $A = log(\eta_\alpha(T_g))$. The best fit line shape of η_α using equation 3.29 and $T_g = 243$ K is reported in Figure 3.18. The obtained parameters are reported in table 3.3. The value of A is in clear disagreement with the WLF equation model, being almost three times larger than the expected value of 13.

We can also estimate the kinetic fragility of sulfur. Following the definition 1.5,

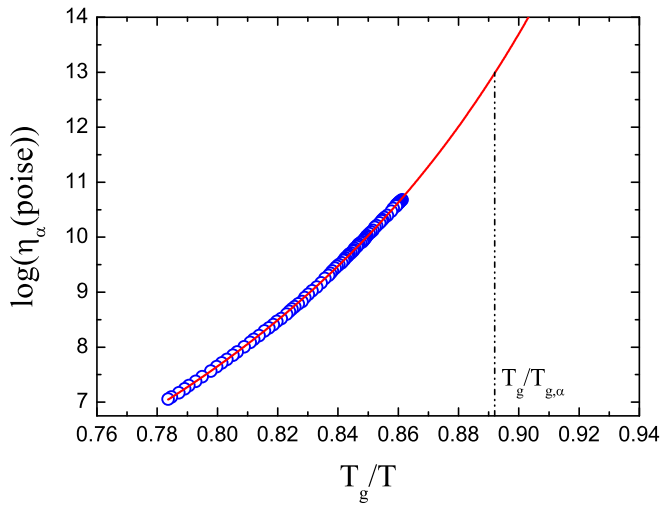

FIGURE 3.18: Estimated η_α component of the viscosity taken from Ref. [146] as a function of the rescaled temperature T_g/T. The red line is the best fit line shape of the WLF equation 3.29 used to determined the ideal glass transition temperature related to the α process as explained in the text.

A	C_1	C_2
34 ± 1	-35 ± 1	19 ± 1

TABLE 3.3: Parameters of the best fit line shape of η_α with equation 3.29, reported in Figure 3.18.

m_A can be written as

$$m_A = \left(\frac{\frac{-C_1 C_2}{T_g}}{(\frac{C_2 x}{T_g} + 1 - x)^2} \right)_{x=1} \tag{3.30}$$

with $x = T_g/T$. Using the values reported in table 3.3 we find $m_A = 453$, a value clearly very high. This apparent incongruity can be explained looking at the definition of the glass transition temperature. As usually, the value of T_g (246 K in Ref. [146]) is taken from calorimetric measurements of polymeric sulfur. Due to the presence of the strong secondary relaxation mechanism close to T_g, this value does not correspond to the condition $\eta_\alpha(T_g) = 10^{13}$ poise. The fragility should instead be estimated with respect to the ideal glass transition temperature $T_{g,\alpha}$ related to the structural relaxation process from the condition $log(\eta_\alpha(T_{g,\alpha})) = 13$ (dashed-dotted-dotted line in Figure 3.18). Using $T_{g,\alpha} = 276$ K (and thus $x = 0.892$) relation 3.30 gives $m_A = 86 \pm 7$. This estimation, typical of fragile systems, can be considered as a reference value for the fragility of polymeric sulfur.
Using the correct limit $log(\eta_\alpha(T_{g,\alpha})) = 13$ and the estimated value for $T_{g,\alpha}$ the parameters of the WLF equation 3.29 become $C_1 = -13.5 \pm 0.5$ and $C_2 = 48.1 \pm$

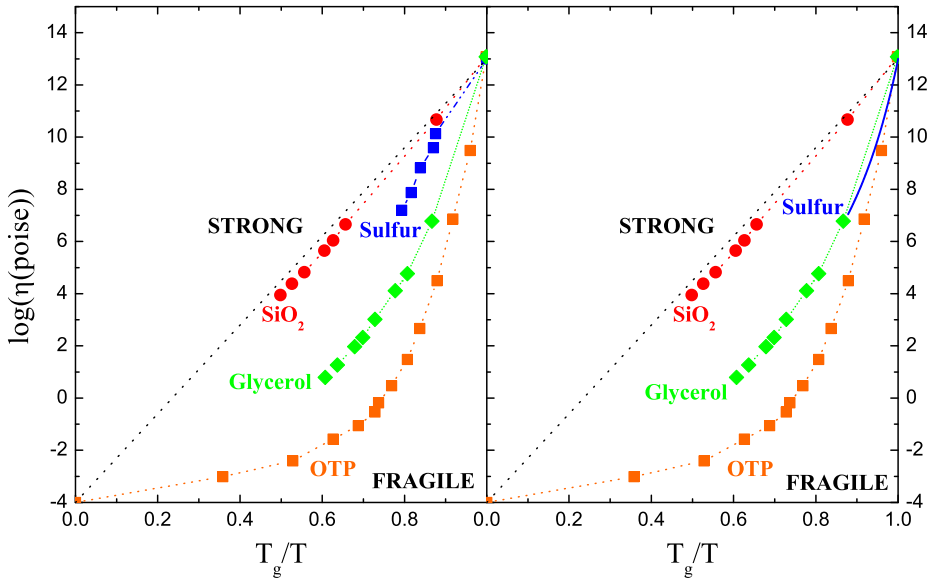

FIGURE 3.19: Left panel: Angell plot for several glass formers. The data of sulfur correspond to the total measured viscosity η (blue dots) and are reported as a function of the rescaled temperature T_g/T, by using the calorimetric glass transition temperature. Right panel: same data as for the left panel except for sulfur. In this case only the α component of the viscosity is reported (blue line) as a function of the rescaled temperature T_g/T, by using the ideal glass transition temperature $T_g = T_{g,\alpha}$ as explained in the text. All the values for sulfur are taken from Ref. [146].

0.2. These values are in agreement with those of other glass-forming systems and represent thus a confirmation of the validity of the whole procedure [34].
The above observations are summarized in Figure 3.19, which adds sulfur to the Angell plot. In particular, the left panel shows the measured total viscosity η of sulfur as a function of the rescaled temperature T_g/T, using the calorimetric T_g, while in the right panel only the η_α contribution is reported by rescaling the temperature with $T_{g,\alpha}$. Including the secondary χ relaxation process, the η data are clearly shifted toward too high temperatures, leading thus to an "illusory" strong character of polymeric sulfur (left panel).

3.5 Low frequency dynamics in sulfur

3.5.1 Experimental details

The glass of sulfur has been obtained starting from a highly purified powder in order to avoid the presence of organic contaminations that could alter the structure. The sulfur purification process is relatively complex and has been carried out through multiple distillations in vacuum as described in Ref. [147]. The final product, characterized by a 99.999% purity, was put in a rectangular container 12x8 mm^2 in size and 200 μm in thickness, sandwiched between a quartz window and an optically polished silicon plate (acting as a mirror). The sample and the container were first heated up to 473 K and then quick quenched in liquid air. A translucent glass was obtained.
As in the case of sorbitol, the choice of the sample holder was dictated by the necessity to measure also the refractive index. In order to reduce the local heating of the sample, a neutral filter was used to keep the laser power on the sample below 13 mW. This value of incident power was checked to produce power-independent light scattering spectra of still good enough quality.
Brillouin spectra were collected in the temperature range $80-236$ K, and a cryo-

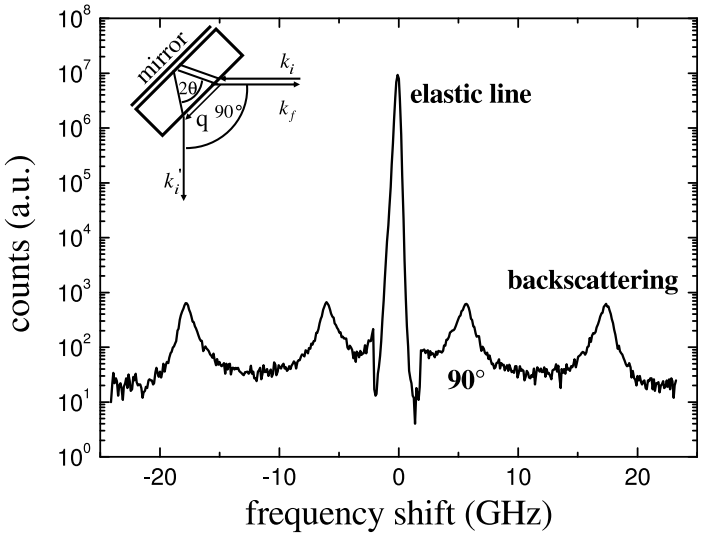

FIGURE 3.20: Brillouin light scattering spectrum of glassy sulfur at T=220 K, measured using a distance $L = 6$ mm between the mirrors in the interferometer. Two Brillouin doublets are present, corresponding to the two different scattering angles 2θ probed at the same time as schematically shown in the inset. The incident and scattered beams are represented by the arrows $\vec{k_i}$ and $\vec{k_f}$ for 2θ=180°, and by $\vec{k_i'}$ and $\vec{k_f}$ for $2\theta_{ext}$=90°.

stat was used to regulate the temperature. The data were taken using mainly a distance L=12.59 mm between the mirrors in the interferometer, which allowed us to obtain a sufficient good counting rate while keeping the instrumental resolution at a reasonably good level (160 MHz). The measurements were performed without

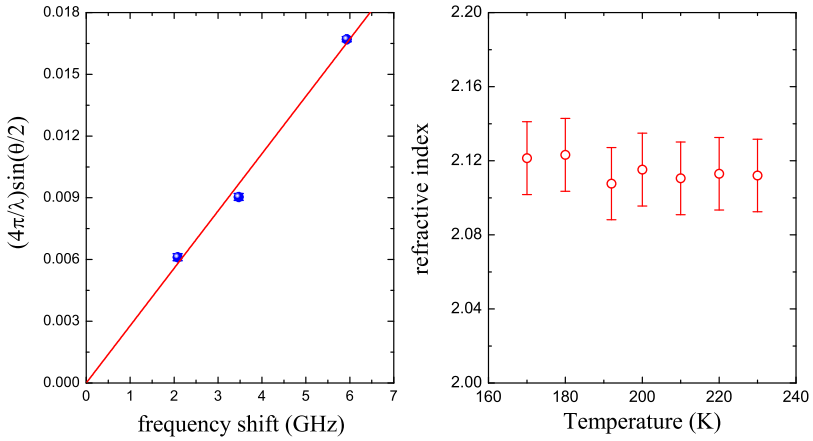

FIGURE 3.21: Left panel: dependence of the momentum transfer q on the frequency position of the Brillouin peaks corresponding to $2\theta_{ext} = 90°$, 45° and 30° scattering angles, together with the linear best fit (red line). The slope of the line corresponds to the inverse of the longitudinal sound velocity. Right panel: refractive index of sulfur obtained from relation 3.15.

any polarization analysis of the scattered light (VU configuration), and on both heating and cooling the sample. No differences were found among the different sets of data. In order to measure both the refractive index n of the sample and the longitudinal acoustic modes at the same time, the sample was aligned at 45° ($2\theta_{ext}$=90°) with respect to the incident laser beam in the whole temperature range, while for $T = 200$ K, the geometries corresponding to $2\theta_{ext}$=30° and 45° have been used too. Figure 3.20 shows an example of a spectrum measured with the sample aligned at 45° with respect to the incident laser beam. This scattering configuration was used in the temperature range 150 - 236 K to obtain the refractive index of glassy sorbitol. At temperatures lower than about 150 K, the sample cracked, thus leading to a large increase in the stray light that made the measurements of the refractive index impossible. As for the sorbitol, the ratio of the positions $\Omega/2\pi$ of the Brillouin peaks corresponding to the two scattering angles gives information on the refractive index via the relation $n = (\Omega_{180°}/\Omega_{2\theta_{ext}})sin(\theta_{ext})$. Using the data collected in the backscattering and in the 90° scattering geometries, and thus relation 3.15, we found a basically temperature-independent refractive index value of $n = 2.11 \pm 0.02$ (see the right panel of Figure 3.21). The lack of information on the temperature dependence of the density of glassy sulfur does not allow the determination of the temperature dependence of the refractive index through the Clausius-Mossotti relation 3.16. For this reason n has been taken constant in the whole investigated temperature range.

As previously reported, the used relation is correct under the assumption that the sound velocity of the longitudinal modes is frequency independent in the corresponding frequency range. Such assumption has been directly checked at T=200 K measuring Brillouin spectra corresponding to the sample aligned at 45, 22.5 and

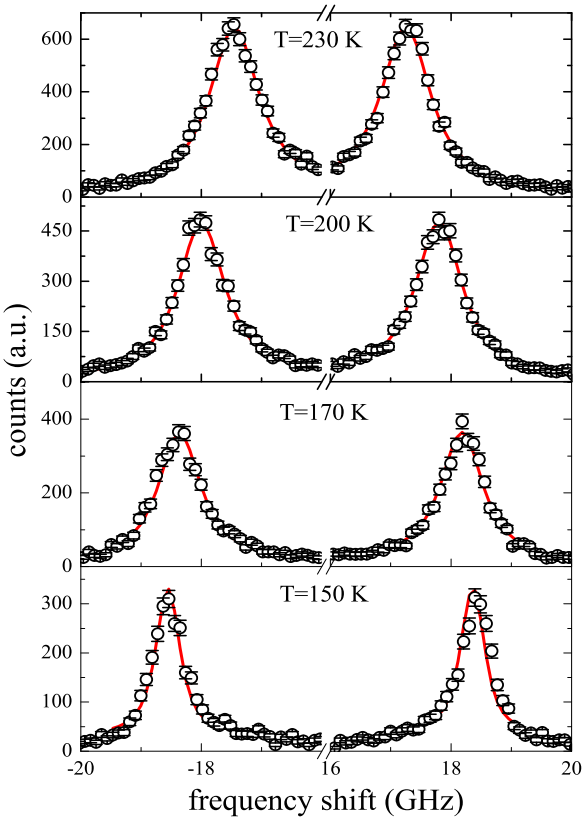

FIGURE 3.22: Brillouin light scattering spectra of sulfur at the indicated temperatures collected in backscattering configuration. The red lines correspond to the best fitting lineshape obtained from the model of equation 3.17 convoluted with the instrumental resolution.

15°. Figure 3.21 reports the the exchanged momentum q as a function of the position of the corresponding Brillouin peaks. Indeed, as explained in section 3.3.1, those Brillouin peaks can be viewed as due to a scattering process with an exchanged wave-vector given by $q = (4\pi/\lambda)\sin(\theta_{ext})$ and thus independent of the refractive index n. Therefore, the slope Ω/q of the data in Figure 3.21 corresponds directly to the inverse of the sound velocity, v_{LA}, of the longitudinal acoustic modes. The linear behavior observed in Figure 3.21 confirms then the frequency independence, within the experimental uncertainty, of the sound velocity in the frequency range covered here, and thus the validity of the expression used above to derive n. From the knowledge of the sound velocity and the frequency position of the Brillouin peaks corresponding to the backscattering configuration, we can obtain another estimation for the refractive index at 200 K from the relation $n = \lambda\nu_{180°}/2v_{LA}$. We find $n = 2.11 \pm 0.04$, in nice agreement with the previously determined value. It is interesting to observe that this value is quite close to the one measured in the liquid phase above T_λ, reflecting the polymeric character of the system ($n_{liquid} \sim 1.93$)[148].

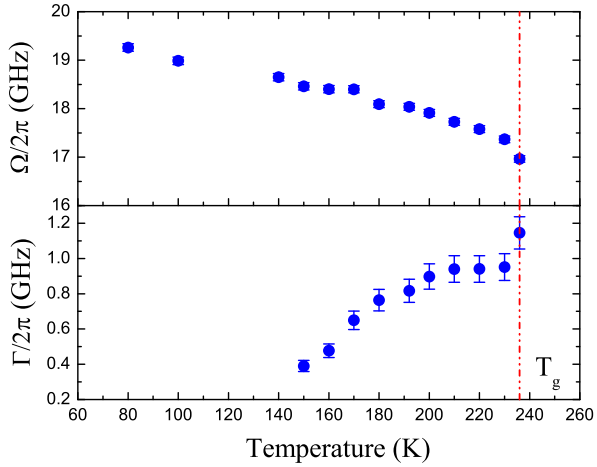

FIGURE 3.23: Temperature dependence of the frequency shift $\Omega/(2\pi)$ (top panel) and of the linewidth $\Gamma/(2\pi)$ (bottom panel) of the longitudinal acoustic modes probed in the backscattering configuration. The dashed line indicates T_g=236 K.

3.5.2 BLS results

Figure 3.22 shows a subset of BLS spectra collected for different temperatures in the backscattering geometry. In all the spectra the Brillouin doublet is well visible at frequencies around 17 GHz, and is due to the longitudinal acoustic modes propagating in the glass.
To determine the frequency position Ω and the full width at half maximum Γ of the longitudinal acoustic modes, the spectra have been fitted in a narrow frequency range around the Brillouin peaks using the damped harmonic oscillator model function described in equation 3.17. This function has been convoluted to the instrumental resolution before being fitted to the experimental data. The values of Ω and Γ are reported in Figure 3.23. Due to the presence of cracks in the sample for temperatures lower than about 150 K, the linewidth of the longitudinal modes could be reliably obtained only at higher temperatures. The Brillouin linewidth shows a rapid increase and the Brillouin peak position a slight decrease on approaching T_g from the glassy phase, as expected in glasses. In particular, the Brillouin broadening shows a sudden increase at the highest measured temperature that we attribute to the structural relaxation entering the frequency window explored by BLS. This abrupt increase of the peak broadening at $T \sim 236$ K suggests the possibility that the glass transition temperature is lower than its nominal value of 243 K [141]. As previously recalled, T_g is strictly related to the fraction of monomers presents in the liquid phase above the λ transition, which increases on increasing the temperature (see Figure 3.15). In fact, the value of $T_g = 243$ K has been found after quenching the polymeric liquid from $T = 523$ K, where the fraction of monomers is almost ~ 50 % [135]. The glass reported here has been prepared heating the liquid up to 473 K, where a higher concentrations of

monomers should be present (~ 65 %), and this is compatible with the glass transition temperature being shifted to lower values.

The frequency position and the linewidth of the Brillouin peaks can be used to

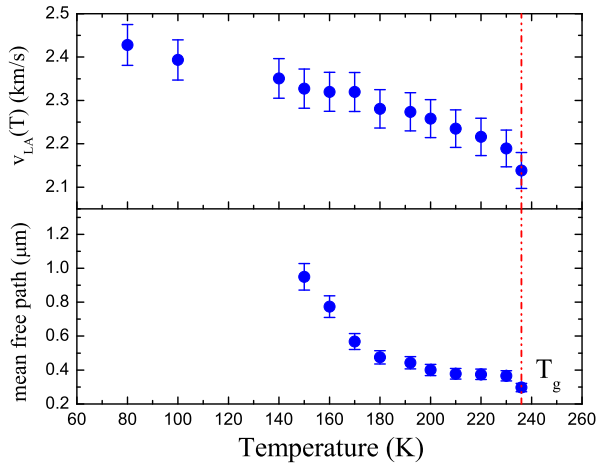

FIGURE 3.24: Temperature dependence of the sound velocity v_{LA} (top panel) and of the mean free path l (bottom panel) of the longitudinal acoustic modes. The dashed line indicates $T_g = 236$ K.

obtain information on the sound velocity $v_{LA} = \sqrt{M'/\rho} = \Omega/q$ and on the mean free path $l = v_l/\Gamma$ of the longitudinal acoustic excitations, as shown in Figure 3.24. We can observe that the mean free path is of the order of 400 nm at T_g, about one order of magnitude less than what typically observed in organic glass-formers, e.g. in sorbitol (see Figure 3.9). This suggests that the sulfur glass is characterized by strong anharmonic or relaxation effects that strongly damp the propagating acoustic waves.

From the behavior of the shear modulus (Figure 3.16) and of the density of glassy sulfur reported in Ref. [141] we can estimate the value of the transverse sound velocity at the glass transition temperature $v_{TA} = \sqrt{G'/\rho}$. At T_g, using $G' = 1$ GPa and $\rho = 1.92$ g/cm^3, we find $v_{TA} = 721$ m/s. Such a low value is similar to that of very fragile systems, such as glassy selenium and polycarbonate (BPA-PC) [4]. By using the relation 3.26 between the shear and the bulk modulus we find $m_S = 210 \pm 8$, a very high value indeed with respect to that estimated from viscosity measurements (see section 3.4.1). However as shown in the case of sorbitol, the validity of the relation proposed by Sokolov and coworkers is not always correct, especially in polymeric systems [6].

Résumé du chapitre 4

Dans le deuxième chapitre nous avons discuté l'importance de la diffusion inélastique des rayons X pour l'étude des excitations à haute fréquence dans la région mésoscopique de quelques nanomètres. Dans la première partie du présent chapitre nous présentons un bref résumé de la théorie générale de IXS et de l'équipement expérimental utilisé pour nos mesures. Dans la deuxième partie du chapitre nous discuterons la dynamique à haute fréquence d'un verre de sorbitol. Ce système est, en effet, un candidat idéal pour l'étude des propriétés vibrationnelles des verres dans la région de quelques nanomètres. Le caractère fragile du sorbitol et la valeur élevée de la position du maximum du BP nous a permis d'effectuer une étude précise de la dynamique à haute fréquence aussi bien pour des énergies inférieures que supérieures de celle du maximum du BP. Dans le chapitre nous présentons une analyse détaillée de la nature des excitations à haute fréquence mesurée à différentes températures. Comme nous montrerons, les excitations acoustiques longitudinales démontrent des anomalies élastiques qui ne peuvent pas être attribuées à des fluctuations de densité statique. En outre ces anomalies ont lieu dans la même gamme d'énergie du BP, ce qui suggère l'existence d'une forte corrélation entre BP et élasticité. Dans la dernière section de ce chapitre nous présentons une analyse détaillée de la dépendance en température des anomalies élastiques à haute fréquence.

Chapter 4

High frequency dynamics of sorbitol

In the second chapter we have discussed the importance of Inelastic X-ray Scattering for the investigation of the high frequency collective excitations in the mesoscopic spatial range of fews nanometers. In the first part of this Chapter, a brief summary on the general theory of IXS and of the experimental set-up used for our measurements is presented. The second part of the Chapter will deal with the high frequency dynamics of a glass of sorbitol. As reported in section 3.2 this system is an ideal candidate for the investigation of the vibrational properties of glasses in the crucial spatial range of fews nanometers. The fragile character of sorbitol together with a high boson peak energy maximum allow for an accurate study of the high frequency dynamics both below and above the excess in the reduced vibrational density of states. Section 4.3 reports a detailed analysis of the character of the high frequency excitations measured at the lowest investigate temperature. As it will be shown there, the longitudinal acoustic-like excitations display some elastic anomalies that cannot be attributed to static density fluctuations. Moreover these anomalies take place in the same energy range of the boson peak, suggesting the existence of a strong correlation between them. The high frequency dynamics has been studied also as a function of temperature, ranging from the deep glassy phase up to the glass transition temperature. A detailed analysis of the temperature dependence of the high frequency elastic anomalies is reported in last section of this Chapter, while a deeper investigation of their relation with the excess of modes in the vibrational density of state will be the argument of the next one.

4.1 Inelastic X-ray Scattering

The first part of this section reports the theory of Inelastic X-ray Scattering. In particular a description of the IXS cross section and the determination of the dynamic structure factor of the system under investigation is discussed. In the second part, instead, the basic working principles of an IXS spectrometer are illustrated, with reference to beamline ID16 at the European Synchrotron Radiation Facility (ESRF).

4.1.1 IXS cross section

The IXS spectrum provides a direct determination of the coherent dynamic structure factor, $S(Q,\omega)$, whenever the listed hypotheses hold [149, 150]:

- The scattering process is dominated by the Thomson term and both the resonant and the spin-dependent contributions to the electron-photon interaction can be neglected.
- The center of mass of the electron cloud follows without delay the nuclear motion, i.e. the adiabatic approximation is valid.
- There are no electronic excitations in the considered energy transfer range.

The kinematics of the scattering experiment is the same as for the BLS measurements and is reported in Figure 4.1 for clarity. Here, and in the following, the suffixes i and f refer to the incident and scattered photon, respectively. As for BLS the incoming photon is characterized by an energy, $\hbar\omega_i$, wave-vector, $\vec{k}_i$, and polarization, $\widehat{\varepsilon}_i$. It is scattered by the sample and collected at an angle 2θ within a solid angle $d\Omega$. The scattered photon energy, wave-vector and polarization is denoted by: $\hbar\omega_f$, $\vec{k}_f$ and $\widehat{\varepsilon}_f$, respectively. According to energy and momentum conservation laws the momentum and energy transfer to the sample are:

$$\hbar\omega \equiv \hbar(\omega_f - \omega_i) \qquad \text{and} \qquad \hbar\boldsymbol{Q} \equiv \hbar\left(\boldsymbol{k}_f - \boldsymbol{k}_i\right) \tag{4.1}$$

In the limit $\omega \ll \omega_i$, which is the case of IXS, the modulus of $\boldsymbol{k}_i$ and $\boldsymbol{k}_f$ are basically the same, and the modulus of the exchanged momentum is entirely determined by the scattering angle 2θ:

$$|\boldsymbol{Q}| = 2|\boldsymbol{k}_i| sin(2\theta/2) \tag{4.2}$$

The double differential cross section, $\partial^2\sigma/\partial\Omega\partial\omega_f$, representing the fraction of photons having frequency $\omega_f \pm d\omega_f$, scattered into a solid angle $d\Omega$ around the direction

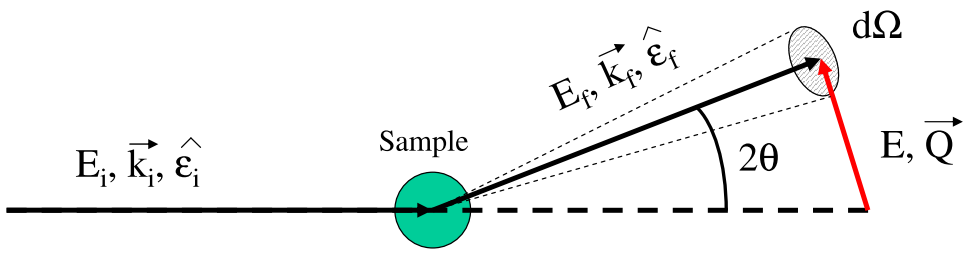

FIGURE 4.1: Kinematics of a scattering experiment.

defined by $\vec{k}_f$, can be calculated within the frame of linear response theory assuming a weak coupling between the probe and the system. In this approximation the double differential cross section can be regarded as an intrinsic property of the unperturbed sample, being independent of the incident photon flux. Neglecting the interaction of the photon electromagnetic field with the nuclei, the probe-system interaction, in the weak relativistic limit, is described by the photon-electron interaction Hamiltonian, H_{int}. It consists of four different terms [151]:

$$H_{int} = H_1 + H_2 + H_3 + H_4$$

where

$$H_1 = \frac{e^2}{2m_e c^2} \sum_j (\mathbf{A}(\mathbf{r}_j, t) \cdot \mathbf{A}^*(\mathbf{r}_j, t)) \tag{4.3}$$

$$H_2 = +\frac{e}{2m_e c} \sum_j (\mathbf{A}(\mathbf{r}_j, t) \cdot \mathbf{p}_j) \tag{4.4}$$

$$H_3 = -\frac{e}{m_e c} \sum_j \mathbf{s}_j \cdot (\nabla \times \mathbf{A}(\mathbf{r}_j, t)) \tag{4.5}$$

$$H_4 = -\frac{e^2}{2m_e^2 c^4} \sum_j \mathbf{s}_j \cdot (\dot{\mathbf{A}}(\mathbf{r}_j, t) \times \mathbf{A}(\mathbf{r}_j, t)) \tag{4.6}$$

The sum extends over all the electrons in the system. Here m_e and e are the electron mass and charge respectively, while c is the speed of light. Finally $\boldsymbol{A}(\boldsymbol{r}_j, t)$ is the electromagnetic field vector potential at $\boldsymbol{r_j}$, coordinate of the $j-th$ electron which has momentum $\boldsymbol{p_j}$ and spin $\boldsymbol{s}_j$. In the quantum electrodynamics representation with the gauge $\nabla \cdot \boldsymbol{A}(\boldsymbol{r}_j, t) = 0$, the vector potential of the photon electromagnetic field can be written in terms of plane waves as:

$$\boldsymbol{A}(\boldsymbol{r}_j, t) = (\frac{4\pi c^2}{V})^{1/2} \sum_\lambda [a_\lambda \hat{\epsilon}_\lambda e^{i(\boldsymbol{Q}_\lambda \cdot \boldsymbol{r}_j)} + a_\lambda^* \hat{\epsilon}_\lambda e^{-i(\boldsymbol{Q}_\lambda \cdot \boldsymbol{r}_j)}], \tag{4.7}$$

where a_λ and a_λ^* are the $\lambda - th$ component of the photon annihilation and creation operator, and $\hat{\epsilon}_\lambda$ is the polarization of the electromagnetic field.

In a first order perturbation treatment, the first two terms 4.3 and 4.4 of the interaction Hamiltonian describe respectively the scattering of the photon electric field from the electron charge (Thomson scattering) and the processes in which photon quanta are fully absorbed or emitted by the electron system (photoelectric absorption). The other two terms are considerably smaller and describe the magnetic coupling between the electron system and the electromagnetic field. In fact, for photon energies of the order of 20 keV (i.e. $\ll mc^2$, m being the rest mass of the electron) the magnetic terms are by a factor 10^{-2} smaller than the first two terms, and can therefore be neglected in the following. Furthermore, the paramagnetic contribution 4.4 can be neglected if we consider photons with energies away from any absorption resonance. This condition is always satisfied in an IXS experiment and therefore the interaction Hamiltonian reduces to the Thomson contribution:

$$H_{int} = \frac{e^2}{2mc^2} \sum_j \boldsymbol{A}(\boldsymbol{r}_j, t) \cdot \boldsymbol{A}^*(\boldsymbol{r}_j, t) \tag{4.8}$$

The double-differential cross-section can be determined in the framework of first order perturbation theory, making use of the Fermi golden rule [152]. Considering the initial and final photon states, $|I\rangle$ and $|F\rangle$ as plane waves the double-differential cross-section can be written as:

$$\frac{\partial^2\sigma}{\partial\Omega\partial\omega_f} = r_0^2 \left(\frac{k_f}{k_i}\right) (\widehat{\varepsilon}_f \cdot \widehat{\varepsilon}_i)^2 \sum_{I,F} P_I \left| \left\langle F \left| \sum_j e^{i\boldsymbol{Q}\cdot\boldsymbol{r}_j} \right| I \right\rangle \right|^2 \delta(\hbar(\omega - \omega_F + \omega_I)) \tag{4.9}$$

where $r_0 = e^2/mc^2$ is the classical electron radius and P_I is the statistical weight, i.e. the equilibrium population, of the initial states.
Within the validity of the adiabatic approximation, the atomic quantum state, $|S\rangle$, can be factorized into its electronic, $|S_e\rangle$, and nuclear, $|S_n\rangle$, part. This approximation is particularly good for exchanged energies that are small with respect to the electronic excitations energies. In this case the contribution to the total scattering coming from the valence electrons close to the Fermi level is small compared to the contribution coming from the core electrons. Consequently, the difference between the initial and final state is substantially due to excitations of the ion system. The double differential cross section, under these hypotheses, can be written as:

$$\frac{\partial^2\sigma}{\partial\Omega\partial\omega_f} = r_0^2 \left(\frac{k_f}{k_i}\right) (\hat{\epsilon}_f \cdot \hat{\epsilon}_i)^2 \sum_{I_n,F_n} P_{I_n} \left| \left\langle F_n \left| \sum_j f_j(Q)\, e^{i\boldsymbol{Q}\cdot\boldsymbol{R}_j} \right| I_n \right\rangle \right|^2 \delta(\hbar(\omega - \omega_F + \omega_I)) \tag{4.10}$$

where $f_j(Q)$ is the atomic form factor of the j^{th} atom with position vector $\boldsymbol{R_j}$, while the suffix n refers to the nuclear states. Now the sum extends over all the atoms of the system. Assuming that all the scattering units in the system are equal, this expression can be further simplified by the factorization of the form

factor. In the limit $Q \to 0$, $f(Q)$ is equal to the number of electrons in the atom. For increasing values of Q the form factor decays almost exponentially, with a decay constant determined by the radial distribution of the electrons in the atomic shells of the considered atom. Using the Van Hove pair correlation function, the $S(Q,\omega)$ can be formally introduced as [153]:

$$S(\boldsymbol{Q},\omega) = \frac{1}{2\pi\hbar N}\int_{-\infty}^{+\infty} e^{i\omega t}\langle\sum_{jk} e^{i\boldsymbol{Q}\cdot\boldsymbol{R}_j(t)}e^{-i\boldsymbol{Q}\cdot\boldsymbol{R}_k(0)}\rangle dt \tag{4.11}$$

where N is the number of particles in the system. Combining equations 4.11 and 4.10 one obtains:

$$\frac{\partial^2\sigma}{\partial\Omega\partial\omega_f} = r_0^2(\frac{k_f}{k_i})(\hat{\epsilon}_f\cdot\hat{\epsilon}_i)^2|f(Q)|^2 S(\boldsymbol{Q},\omega) \tag{4.12}$$

This derivation is strictly valid for monatomic systems. In the case of non-crystalline samples with different atoms the procedure to determine the scattering cross section is more complicated but it can be easily generalized to molecular systems with several atomic species by replacing the atomic form factor with the molecular one. In this case the cross section splits into two components: a coherent and an incoherent term. The latter is associated with fluctuations of the form factor while the former is proportional, through the mean value of the form factor, to $S(\boldsymbol{Q},\omega)$ [150]:

$$\frac{\partial^2\sigma}{\partial\Omega\partial\omega_f} = r_0^2(\frac{k_f}{k_i})(\hat{\epsilon}_f\cdot\hat{\epsilon}_i)^2[\langle f(Q)\rangle^2 S(\boldsymbol{Q},\omega) + \langle\delta f(Q)^2\rangle S_s(\boldsymbol{Q},\omega)] \tag{4.13}$$

Here $\langle f(Q)\rangle^2$ is the average value of the form factor over the whole system while $\langle\delta f(Q)^2\rangle$ is the average of its fluctuation squared. The incoherent part of the cross section is given by $S_s(Q,\omega)$ which describes the single particle dynamics rather than the collective behavior.
Besides the cross-section, the realization of an IXS experiment requires also the knowledge of the scattered signal. In order to derive the effective intensity of the collected radiation, absorption processes have to be considered as well. In fact, the number of photons (N) that, per unit time, are scattered into the solid angle ($d\Omega$) and in the frequency interval ($d\omega$) is given by [150]:

$$N = N_0\frac{\partial^2\sigma}{\partial\Omega\partial\omega}d\Omega d\omega\rho L e^{-\mu L} \tag{4.14}$$

where N_0 is the number of incident photons per second, ρ is the density of the scattering sample, L is its length along the scattering path and μ is the total absorption coefficient. The maximum IXS signal is achieved for $L = 1/\mu$, and consequently $N \propto 1/\mu$. Considering X-ray energies of $\approx 20\ keV$ and $Z > 3$, μ is almost completely determined by the photoelectric absorption process. In this

process $\mu \propto Z^4$, with important modifications at energies close to the electron absorption edges. Consequently, the scattering volume of high Z materials is very much reduced, while, on the other hand, the scattering cross section increases as Z^2. Figure 4.2 reports the effective scattering intensity for an IXS experiment, as a function of Z, in the case of a sample with optimum thickness and incident photon energy of 17.8 keV.

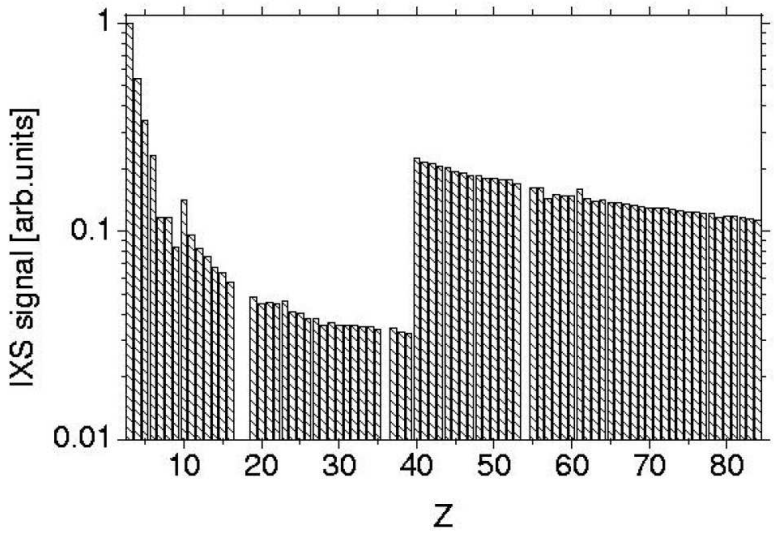

FIGURE 4.2: Relative IXS signal, for an optimal sample thickness ($L = 1/\mu$), as a function of the atomic number Z at the photon energy of 17.8 keV, in the small Q-limit (i.e. $f(Q) = Z$). The large discontinuity between $Z = 39$ and $Z = 40$ is due to the K absorption edge of Zirconium.

4.1.2 Dynamic structure factor and phonons

In this paragraph it is shown how the dynamic structure factor is directly linked to the quanta of the vibrational field: the phonons [150]. The simplest case is represented by an ideal Bravais lattice with only one atom per unit cell. Being $\vec{u}_j(t)$ the atomic displacement of atom j with respect to its lattice equilibrium position, $\vec{R}_j$, its instantaneous position, $\vec{R}_j(t)$, can be expressed as follows:

$$\boldsymbol{R}_j(t) = \boldsymbol{R}_j + \boldsymbol{u}_j(t) \tag{4.15}$$

The dynamic structure factor (see equation 4.11) reads:

$$S(Q,\omega) = \frac{1}{2\pi\hbar N} \sum_{j,k} e^{i\boldsymbol{Q}\cdot(\boldsymbol{R}_j - \boldsymbol{R}_k)} \int_{-\infty}^{+\infty} e^{i\omega t} \langle e^{-i\boldsymbol{Q}\cdot\boldsymbol{u}_k(0)} e^{i\boldsymbol{Q}\cdot\boldsymbol{u}_j(t)} \rangle dt \tag{4.16}$$

In the framework of second quantization the atomic displacement is given by [154]:

$$\boldsymbol{u}_j(t) = \sqrt{\frac{\hbar}{2MN}} \sum_{s,\boldsymbol{q}} \frac{\hat{\epsilon}_{s,\boldsymbol{q}}}{\sqrt{\omega_s(\boldsymbol{q})}} [a e^{i(\boldsymbol{q}\cdot\boldsymbol{R}_j - \omega_s(\boldsymbol{q})t)} + a^+ e^{-i(\boldsymbol{q}\cdot\boldsymbol{R}_j - \omega_s(\boldsymbol{q})t)}] \tag{4.17}$$

here the suffix s indicates the Cartesian indexes and a and a^+ are the annihilation and creation phonon operators. $\boldsymbol{q}$ and $\omega_s(\boldsymbol{q})$ represent the phonon momentum and frequency, while $\hat{\epsilon}_{s,\boldsymbol{q}}$ is the phonon polarization. Exploiting the commutation rules of a and a^+, and some general relations, equation 4.16 becomes:

$$S(\boldsymbol{Q},\omega) = \frac{1}{2\pi\hbar N} \sum_j e^{i\boldsymbol{Q}\cdot\boldsymbol{R}_j - 2W(Q)} \int_{-\infty}^{+\infty} e^{-i\omega t} e^{\langle(\boldsymbol{Q}\cdot\boldsymbol{u}_0(0))(\boldsymbol{Q}\cdot\boldsymbol{u}_j(t))\rangle} dt \tag{4.18}$$

Where the quantity $e^{-2W(Q)} = e^{-\langle(Q\cdot u_i(0))^2\rangle}$ is usually called the Debye-Waller factor. Since we are dealing with small displacements, the argument of the integral can be expanded as:

$$e^{\langle(\boldsymbol{Q}\cdot\boldsymbol{u}_0(0))(\boldsymbol{Q}\cdot\boldsymbol{u}_j(t))\rangle} = 1 + \langle(\boldsymbol{Q}\cdot\boldsymbol{u}_0(0))(\boldsymbol{Q}\cdot\boldsymbol{u}_j(t))\rangle + ... \tag{4.19}$$

The first term leads to elastic Bragg scattering, while the second one represents the inelastic scattering with the creation or annihilation of one phonon. Higher order terms can be omitted since only small momentum transfers, compared to the inverse of the typical atomic displacements, are considered. Within this approximation the inelastic part of the dynamic structure factor can be expressed as:

$$S(Q,\omega) = \frac{1}{4\pi MN} e^{-2W(Q)} \sum_j e^{i\boldsymbol{Q}\cdot\boldsymbol{R}_j} \frac{(\boldsymbol{Q}\cdot\hat{\epsilon}_{s,\boldsymbol{q}})^2}{\omega_{js}} [\delta(\omega-\omega_{js})\langle n(\omega)+1\rangle + \delta(\omega+\omega_{js})\langle n(\omega)\rangle] \tag{4.20}$$

where ϵ and ω_s represent respectively the phonon polarization and frequency, and $\langle n(\omega)\rangle$ is the Bose occupation number.
Thus according to the previous equation, in a crystal where the $S(Q,\omega)$ is dominated by the Brillouin contribution, we have two inelastic lines located at $\pm\omega_{js}$. These lines have an intensity that reflects the probability of creating and annihilating phonons. The ratio between the intensity of $S(Q,\omega)$ at energies $\pm\omega_{js}$ is equal to :

$$\frac{S(Q,\omega_s)}{S(Q,\omega_{-s})} = \frac{\langle n(\omega)+1\rangle}{\langle n(\omega)\rangle} = e^{\frac{\hbar\omega_s}{k_B T}} \tag{4.21}$$

Nevertheless the spectral line shape predicted by this harmonic theory presents some relevant differences as compared to the experimental one. In a real crystal the anharmonicity and the interactions of phonons with the imperfections of the material lead to a finite lifetime of the phonon excitations. The vibrational excitations are no longer two delta function ($\delta(\omega-\omega_s)$) but they show a finite width Γ.
In a glass the simple form that $S(Q,\omega)$ assumes in crystals is strongly modified

and there are no models able to describe the dynamic structure factor from first principles (see Figure 2.3). In contrast to the crystalline state a disordered system is characterized by the absence of translational invariance, thus a density fluctuation with wavevector Q is not an "eigenstate" of the system. The dynamics of a glass is influenced by the presence of new degrees of freedom with respect to a crystal: hopping, tunneling and relaxation processes.
According to the complexity of the processes that control the dynamics in a glass, the $S(Q,\omega)$ is not simply structured as in a crystal. However the dynamic structure factor of a glass can be characterized using quantities that have a well defined meaning in the corresponding crystalline state as the energy excitation $\hbar\Omega$, the linewidth $\hbar\Gamma$ and the nonergodicity factor f_Q. The behavior of these parameters in the mesoscopic region has been discussed in Chapter 2.

4.1.3 X-rays *versus* Neutrons

Traditionally the study of the atomic motion in condensed matter in this high frequency region has been the domain of inelastic neutron scattering (INS). Neutrons are particularly suited to these studies mainly for two reasons:

- neutrons with wavelengths comparable to the interparticle spacing have kinetic energy of $\cong$ 100 meV , and therefore, with moderate relative energy resolution, it is possible to study efficiently the collective atomic excitations.
- neutrons scatter from the nuclei with an interaction strength sufficiently small to allow a large penetration in most materials.

The INS technique has been successfully applied to the study of the density fluctuations spectrum of crystalline solids and low density gases. In disordered systems, like liquids, glasses and dense gases, very few neutrons studies have been performed so far. In fact, due to the kinematics of the scattering process, the neutron technique cannot be efficiently applied to study sound modes in materials with a large speed of sound, typically above 1500 m/s. These kinematic limitations do not apply to x-rays which are, therefore, particularly well suited to study the small momentum and large energy transfer regions.
Neutrons directly couple to the nuclei through the Fermi pseudo-potential. Moreover, they have a spin of 1/2, and therefore the magnetic interaction with matter is non negligible. The double differential cross section for neutrons reads [154]:

$$\frac{\partial^2\sigma}{\partial\Omega\partial\omega_f} = (\frac{k_f}{k_i})[|\langle b\rangle|^2 S(\boldsymbol{Q},\omega) + (|\langle b\rangle|^2 - \langle|b|^2\rangle)S_s(\boldsymbol{Q},\omega)] \tag{4.22}$$

where b is the neutron scattering length. Comparing this equation with that for IXS (equation 4.13), it can be noticed that they are identical, once $f(Q)$ is replaced by b. The difference between these two quantities arises from the fact that $f(Q)$ is an electronic property, while b is a purely nuclear property. X-rays are

scattered by different materials according to the number of electrons (Z) of the atomic species ($f(Q) \propto Z$). On the other hand, b depends on Z, A (the atomic number) and $\bar{J}$, the total (electronic + nuclear) magnetic moment. The resulting scattering strength can therefore be very different for different isotopes of the same material, but also for the same isotope with a different orientation of its total magnetic moment. This "sensitivity" can produce very strong deviations of the actual scattering length with respect to its average value, thus leading to a significant contribution of the incoherent term ($\propto |\langle b \rangle|^2 - \langle |b|^2 \rangle$) in the neutron cross section.
On the other hand, neutrons present an enormous advantage. Neutrons with a De Broglie wavelength of about one Å have energies of $\sim 10 \div 100\ meV$, the same order of magnitude of typical inelastic excitations. A moderate instrumental resolution in energy ($\Delta E/E$) and momentum ($\Delta Q/Q$) of $\sim 10^{-2}$ is therefore sufficient to probe the $S(Q,\omega)$ in the $Å^{-1}$ and meV range. In contrast to this, X-rays with wavelengths of a few Å have energies of some keV. A much higher instrumental energy resolution ($\Delta E/E \sim 10^{-7}$) is then needed in order to resolve the same excitations.
Another important difference between IXS and INS concerns the accessible dynamic range. The dynamic range corresponds to the (Q,E) values for which the scattering process is allowed. For neutrons it can be derived by using the general conservation laws (see equation 4.1) and the quantum mechanical relation between energy and momentum:

$$E = \frac{\hbar^2 |\boldsymbol{k}|^2}{2M_n} \tag{4.23}$$

where M_n is neutron mass. The equation that defines the dynamic range for neutrons is then:

$$\frac{|\boldsymbol{Q}|^2}{|\boldsymbol{k_i}|^2} = 2 - \frac{2M_n E}{\hbar^2 |\boldsymbol{k_i}|^2} + 2cos(2\theta)\sqrt{1 - \frac{2M_n E}{\hbar^2 |\boldsymbol{k_i}|^2}} \tag{4.24}$$

This equation can be considered as the equivalent of equation 4.2 for X-rays. It is evident that the momentum transfer, $\boldsymbol{Q}$, is not only determined by the scattering angle, but also by the energy transfer. Plotting equation 4.24 in the (Q,E)-plane, a set of curves, corresponding to different 2θ values, can be derived. The points lying on these curves are the only ones that can satisfy the energy and momentum conservation laws. In the left panel of Figure 4.3 the typical dynamical range for thermal ($300\ K$) neutrons (i.e. $k_i = 35\ nm^{-1}$ and $E_i = 25.8\ meV$) is reported. In the right panel of the same figure the corresponding curves for the X-rays employed in the present study (i.e. $k_i = 120\ nm^{-1}$ and $E_i = 23.724\ keV$) are reported. In both panels typical values for sound-like excitations are reported as straight lines. Inspecting Figure 4.3 it is clear that X-rays can measure high energy excitations even at low-Q (notice the factor 20 between the two energy scales). The limitations imposed by the dynamic range are of primary importance in the study of amorphous systems, like glasses or fluids, where the lack of translational periodicity does not allow for the definition of Brillouin zones. As a consequence the experiment has to be performed at small momentum transfer, at Q-values below

the first diffraction peak. In these cases, the energy of neutrons has to be increased in order to enlarge the dynamical range, at the expense of the energy resolution. Some differences between IXS and INS are listed in table 4.1.

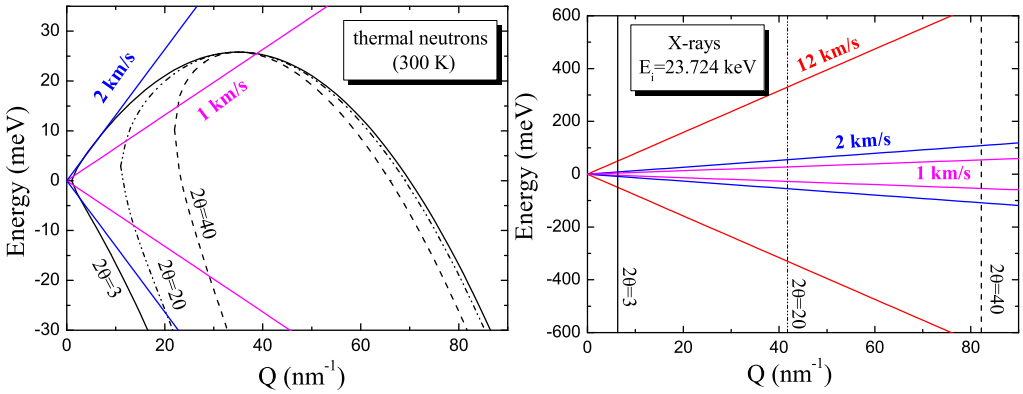

FIGURE 4.3: Dynamical range for neutrons (left panel) and x-rays (right panel). Typical values for sound-like excitations, propagating with the velocity indicated in the respective panels, are plotted as straight lines.

In conclusion the main advantages in using IXS rather than INS to study disor-

IXS	INS
no correlation between momentum and energy transfer	strong correlation between momentum and energy transfer
$\Delta E/E \sim 10^{-7} \div 10^{-8}$	$\Delta E/E \sim 10^{-1} \div 10^{-2}$
$\partial^2\sigma/\partial\Omega\partial E_f \sim r_0^2 Z^2$ (for small Q)	$\partial^2\sigma/\partial\Omega\partial E_f \sim b^2$
strong photoelectric absorption $\Rightarrow$ no multiple scattering	weak absorption $\Rightarrow$ multiple scattering
negligible incoherent scattering	incoherent scattering
insensitive to magnetic excitations	sensitive to magnetic excitations
small beam size: 100 μm or smaller	large beam size: $\sim cm$
small beam divergence: $\sim \mu rad$	large beam divergence: $\sim rad$
low energy resolution ($1 \div 8\ meV$)	high energy resolution ($0.5 \div 5\ meV$)
Q resolution $\sim 0.30\ nm^{-1}$	Q resolution $\sim 1\ nm^{-1}$
"infinite" dynamical range	limited dynamical range

TABLE 4.1: Main characteristic of IXS and INS.

dered systems are the following:

- In some cases, using INS, it is impossible to separate the coherent and incoherent contribution.

- X-rays are not limited by kinematic constraints (dynamical range). They can probe high values of energy transfer even at small momentum transfer.
- IXS can allow for higher Q-resolution than INS.

In the last decade, these advantages of IXS were indeed successfully exploited in the study of the collective dynamics in those cases where INS is difficult to apply (kinematic limitations, large incoherent scattering, multiple scattering, very high momentum resolution, or small samples).

4.1.4 An IXS spectrometer: beamline ID16 at the ESRF

In this section the IXS beamline ID16 at the European Synchrotron Radiation Facility (ESRF) in Grenoble [155] will be briefly described. The experimental strategy used for IXS measurements with meV energy resolution (thus suitable to study the high frequency collective excitations) resembles that of a triple axis neutron spectrometer (see Figure 4.4). The first axis is the backscattering monochromator crystal which selects the energy $\hbar\omega_i$ of the incident photons. The second axis is located at the sample position, and determines the momentum transfer by selecting the scattering angle. Finally the third axis corresponds to the analyser crystal, which selects the scattered photon energy, $\hbar\omega_f$ and focuses the scattered radiation on the detector. The ID16 beamline is equipped with a 9 analysers crystals which allow for the collection of 9 different IXS spectra, corresponding to 9 different transfer momenta, at the same time.

The optical layout of the triple axis inelastic x-ray spectrometer is reported in

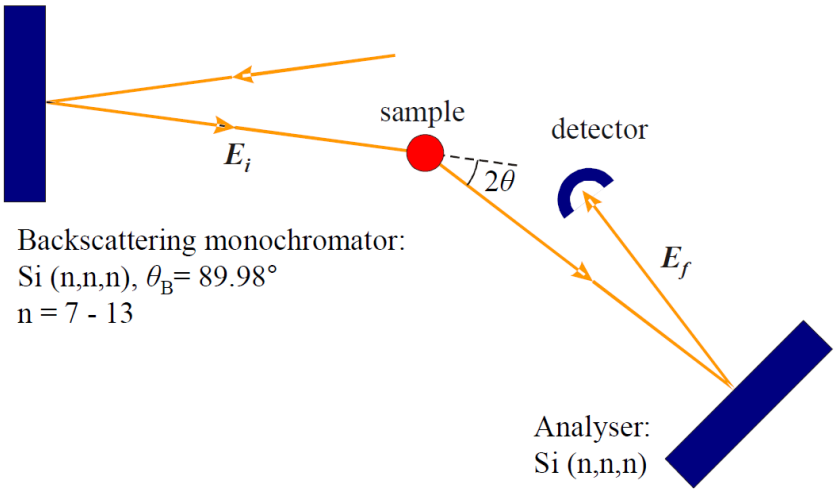

FIGURE 4.4: Principle of a triple axis inelastic x-ray spectrometer.

Figure 4.5. The X-ray source consists of three undulators with a magnetic period in the 26 mm- 35 mm range and a total length of 4.8 m, placed in a straight section

of the electron storage ring. The utilized X-ray radiation energies correspond to the undulator emission at the 3^{rd} or 5^{th} harmonics. The X-ray beam from the undulator odd-harmonics has approximately a 40×20 μrad^2 (horizontal $\times$ vertical) angular divergence (FWHM), a spectral bandwidth $\Delta E/E \sim 10^{-2}$, and an integrated power within this divergence in the order of 200 W.
The X-ray beam from the undulators is pre-monochromatized to a bandwidth $\Delta E/E \approx 1 \cdot 10^{-4}$ using a silicon $(1,1,1)$ double crystal monochromator kept in vacuum and cooled by liquid nitrogen. The main role of the pre-monochromator is to reduce the heat load impinging on the main monochromator. This is mandatory in order to keep the thermal deformation of the silicon crystal below the limits for which the energy resolution starts to deteriorate.
The X-ray photons from the pre-monochromator impinge onto the high energy resolution backscattering monochromator, consisting of an asymmetrically cut silicon crystal oriented along the [111] direction, operating at a Bragg angle of 89.98^o. This extreme backscattering geometry insures the minimization of geometrical contributions to the total energy resolution. The spectral angular acceptance, the so-called Darwin width, is larger than the X-ray beam divergence, and, therefore, all the photons within the desired energy bandwidth are transmitted. High order Bragg reflections and perfect crystals are required in order to obtain the necessary energy resolution of $\Delta E/E \sim 10^{-7} \div 10^{-8}$. For this reason, silicon is used at (n,n,n) reflections, with $n = 7, 8, 9, 11, 12, 13$ [156].

The monochromatic beam is focused in the horizontal and vertical plane by a

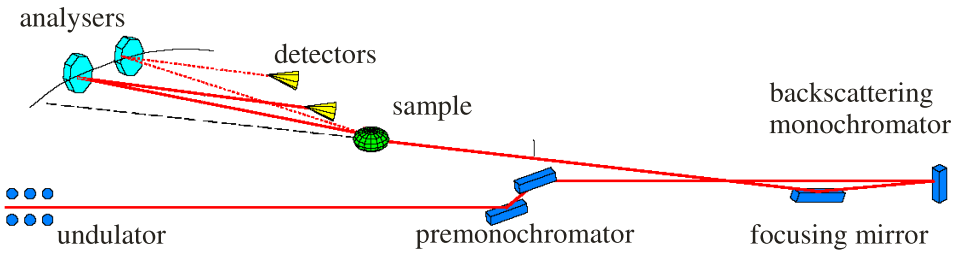

FIGURE 4.5: Optical layout of the beamline ID16 at the ESRF.

platinum coated mirror, located at 26 m from the sample and composed of two regions: a central one with a cylindrical shape in the sagittal direction, and a lateral one which is flat in the sagittal direction. The first region provides a focus at the sample position of 250×100 μm^2 (H×V) FWHM. The lateral part provides a focal size of 60×20 μm^2 (H×V) FWHM, where the horizontal focusing is achieved using a multilayer mirror.

The photons scattered by the sample are then energy-analyzed by the nine spherical analysers which are mounted in a horizontal spectrometer and which operate similarly to the high resolution monochromator (i.e in a near backscattering configuration and at the same reflection order as the backscattering monochromator). Although the problems connected to the energy resolution are conceptually the same for the monochromator and for the analysers, the required angular acceptance is very different. The monochromator can be realized using a flat perfect

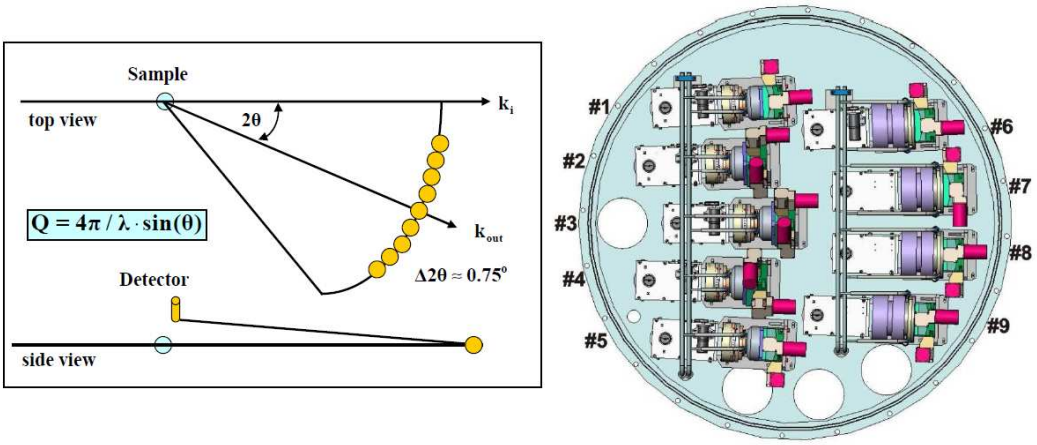

FIGURE 4.6: Left panel: scheme of the position of the nine analysers (yellow disks) employed at the beamline ID16 at ESRF. Right panel: inside of the analyser chamber. The analysers are placed in two rows, with a fixed angular offset of $\sim 0.75°$.

crystal. For the analyser crystals the optimal angular acceptance is dictated by the desired momentum resolution. Considering values of ΔQ in the range of $0.1 \div 0.5$ nm^{-1}, the corresponding angular acceptance of the analysers crystals must be $\sim$ 10 mrad or higher, a value too much larger than the Darwin width. In addition the analysers system has to preserve the single crystal perfection necessary to obtain the desired energy resolution. This constrain automatically excludes the possibility to consider elastically bent crystals. The solution adopted at beamline ID16 consists of laying a large number of undistorted perfect flat crystals on a spherical surface, with the aim to use a 1:1 pseudo-Rowland circle geometry with aberrations kept such that the desired energy resolution is not degraded. These analysers consist of $\sim$12000 silicon perfect single crystals of surface size 0.6×0.6 mm^2 and a thickness of 3 mm, glued on a spherical substrate of a radius equal to the length of the spectrometer arm [157, 158]. The nine independent analysers system is shown in Figure 4.6. The analysers are displaced on two rows with a fixed angular offset among themselves of $\sim 0.75^o$, mounted on a 6.5 m long arm that can rotate around the vertical axis passing through the scattering sample in the 0^o to 13^o angular range. This configuration allows for recording 9 IXS spectra at the same time, with a nearly constant Q-offset.

The spectrometer furthermore features of an entrance pinhole, motorized slits in front of the analyser crystals to set the desired momentum resolution, and a multi-element detector. The detectors are Peltier cooled silicon diodes of 1.5 mm thickness with an active area of 3×8 mm^2, inclined at 20^o in order to enhance the X-ray absorption. They have a very low dark count signal ($\sim$ 1 count in 15 minutes).

Differently from traditional triple axis spectrometers, as a consequence of the extreme backscattering geometry, the energy difference between analysers and monochromator cannot be varied modifying the Bragg angle of one of the two

crystals. The energy scans are therefore performed by changing the relative temperature, ΔT, of the monochromator. This induces a relative variation of the lattice parameters, $\Delta d/d = \alpha(T)\Delta T$, and therefore a relative variation of the diffracted energy, $\Delta E/E = -\Delta d/d$, is induced as well. Considering for the thermal expansion coefficient, α, a value of $\sim 2.58 \cdot 10^{-6} K^{-1}$ at room temperature, the required energy resolution of $10^{-7} \sim 10^{-8}$ implies an accuracy in the temperature control of the monochromator crystal in the mK-range. This task is achieved with a carefully designed temperature bath, and an active feedback system [156], which assures a temperature control with a precision of 0.2 mK in the temperature region around 295 K. In order to convert the temperature scale into the energy scale, the most recent results for $\alpha(T)$ have been considered [159]:

$$\alpha(T) = \alpha_0 + \beta \Delta T \tag{4.25}$$

where $\alpha_0 = 2.581 \pm 0.002 \cdot 10^{-6}\ K^{-1}$, $\beta = 0.016 \pm 0.004 \cdot 10^{-6}\ K^{-2}$, $\Delta T = T - T_0(22.5)\ ^oC$. From equation 4.25 one can precisely calculate the variation of lattice constants at the temperature T:

$$\Delta d/d_0 = \int_{T_0}^{T} \alpha_0 + \beta(T' - T_0)dT' = (\alpha_0 - \beta T_0)\Delta T + \frac{1}{2}\beta(T^2 - T_0^2). \tag{4.26}$$

Finally, the variation of the diffracted energy, $\Delta E/E = -\Delta d/d$, is easily calculated.

Figure 4.7 shows the instrumental response function of one of the nine analy-

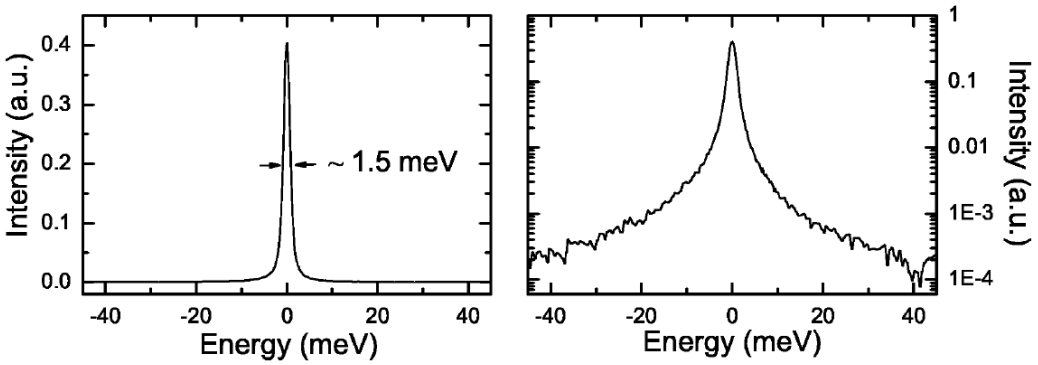

FIGURE 4.7: Measured instrumental resolution function, corresponding to the $Si(11, 11, 11)$ configuration of the spectrometer, plotted both in linear (left panel) and logarithmic (right panel) scale.

sers, corresponding to an energy resolution of 1.5 meV, when operating at the $Si(11, 11, 11)$ reflection . It has been recorded by measuring the scattering from a disordered sample (Plexiglass) at a temperature of 10 K and at a Q-transfer corresponding to the first maximum of its static structure factor (10 nm^{-1}). In this way the elastic contribution to the scattering is maximized. Table 4.2 summarizes the main characteristics of the 6.5 m long horizontal spectrometer.

n	Energy $[keV]$	ΔE $[meV]$	Q_{max} [Å^{-1}]	ΔQ $[nm^{-1}]$	Flux [photons/s/200mA]
7	13.839	7.6 ± 0.2	2.0	0.95	$1.0 \cdot 10^{11}$
8	15.816	5.5 ± 0.2	2.3	0.55	$7.6 \cdot 10^{10}$
9	17.793	3.0 ± 0.2	2.6	1.25	$2.4 \cdot 10^{10}$
11	21.747	1.5 ± 0.1	3.2	1.50	$4.6 \cdot 10^{9}$
12	23.724	1.3 ± 0.1	3.5	1.65	$3.4 \cdot 10^{9}$
13	25.701	1.0 ± 0.1	3.8	1.75	$1.0 \cdot 10^{9}$

TABLE 4.2: Main characteristics of the ID16 6.5 m long horizontal spectrometer, for different $Si(n,n,n)$ reflections. Energy indicates the incident photon energy, ΔE is the total energy resolution, Q_{max} indicates the maximum momentum transfers and ΔQ indicates the Q-spacing between adjacent analyzers. The photon flux values are measured at the sample position.

4.2 IXS measurements

Inelastic X-ray scattering (IXS) measurements were carried out at the beamline ID16 at the European Synchrotron Radiation Facility in Grenoble [155]. In order to get the highest exploitable energy resolution, an incident beam with an energy of 23.724 keV and the silicon (12,12,12) reflection order for the main backscattering monochromator have been employed. The overall energy resolution of the spectrometer was 1.3 - 1.5 meV full-width-half-maximum, depending on the analyser crystal, and has been determined from the elastic scattering measurements from a Plexiglass sample at low temperature, as explained in the previous section. The energy scans have been performed by varying the temperature of the monochromator and keeping the temperature of the analysers fixed. Dynamic structure factor spectra, $S(Q,\omega)$, have been collected in the exchanged momentum, Q, range between 1.3 and 12 nm^{-1} and have been normalized to the intensity of the incident beam. Several experiments have been performed in order to collect information on the acoustic-like dynamics of sorbitol in a wide temperature range from the deep glassy phase up to the glass transition temperature. The Q resolution was defined by slits in front of the analysers and was kept at about $\sim$ 0.34 nm^{-1}. For each momentum transfer several scans have been added to enhance the measurements accuracy. Each scan has been performed in the -30/+30 meV energy range around the elastic line by using a step of 0.2 meV in the central part of the spectrum (-20/+20 meV) and a step of 0.4 meV in the tails. Each step has been counted at least for 60 s. The total acquisition time for each spectrum has been chosen between 4 and 8 hours depending on the investigated temperature.

The glass of sorbitol has been obtained by rapidly quenching in liquid nitrogen a sample of liquid sorbitol kept for some hours under vacuum at about 383 K in order to obtain an homogeneous and well transparent liquid, free of any gas content. A Pyrex glass tube, 4 mm of inner diameter and 19 mm of length, closed with

FIGURE 4.8: Sample holder (left) and cryostat (right) used for the IXS measurements on glassy sorbitol.

two diamond single crystal disks of 0.5 mm of thickness has been used as sample holder (left panel Figure 4.8). The cell length was chosen in order to match the photoelectric absorption length of sorbitol at the chosen incident energy (see equation 4.14). The temperature of the sample was controlled using a Cryomech ST15 cryostat (right panel Figure 4.8). The absence of crystallization has been checked during all the experiments by measuring the static structure factor of the system (see Figure 4.9).

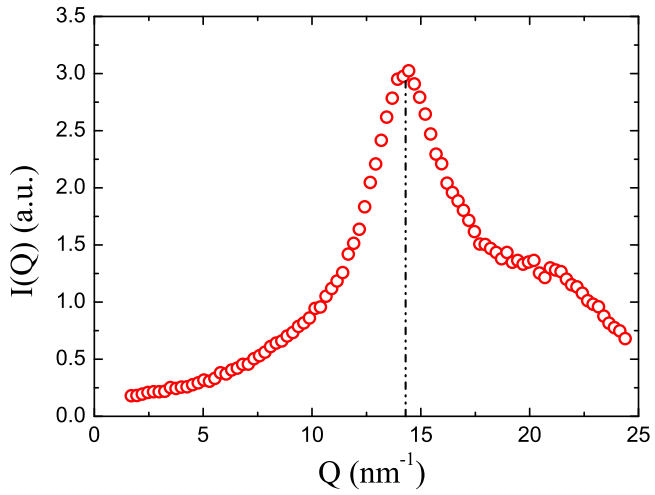

FIGURE 4.9: Scattered intensity of sorbitol measured at T=80 K. The dashed line represents the position of the first sharp diffraction peak.

4.2.1 Data analysis

Figure 4.10 shows a selection of dynamic structure factor spectra collected at the lowest investigated temperature (T= 80 K) for several different exchanged momentum (Q) values. The spectra are composed by a central peak at zero energy transfer and two inelastic features corresponding to the Stokes and anti-Stokes components of the Brillouin doublet and thus related to the acoustic-like modes. On increasing the momentum transfer Q in the scattering process, the doublet clearly shifts toward higher energies and becomes broader. The temperature dependence of the spectra is shown in Figure 4.11 for T=80, 150 and 246 K and for two different exchanged wave vectors. On decreasing the temperature the intensity of the inelastic doublet decreases while the excitation energy and broadening do not display any visible change. In both Figures the intensity of the spectra is reported on an absolute scale following the procedure described below. The good signal-to-noise ratio can be appreciated by the smoothness of the points on the tail of the spectrum.
In general, the IXS spectra can be formally expressed as [96]

$$I(Q,\hbar\omega) = A(Q)\hbar\omega\frac{n(\hbar\omega)+1}{k_BT}S_L(Q,\hbar\omega) \tag{4.27}$$

where $S_L(Q,\hbar\omega)$ is the dynamic structure factor corresponding to the longitudinal modes, $n(\hbar\omega)$ is the Bose factor and $A(Q)$ is a normalization factor mainly reflecting the Q dependence of the atomic form factor. The $S_L(Q,\hbar\omega)$ can be modeled as the sum of a delta function to describe the elastic line and a damped harmonic oscillator model (DHO) for the inelastic component:

$$S(Q,\hbar\omega) = S(Q)\left[f_Q\delta(\hbar\omega) + (1-f_Q)\frac{1}{\pi\hbar}\frac{\Omega(Q)^2\Gamma(Q)}{[\omega^2-\Omega(Q)^2]^2+\omega^2\Gamma(Q)^2}\right] \tag{4.28}$$

In this expression the parameter f_Q is the non ergodicity factor (see section 2.4) and corresponds to the inelastic to the total integrated intensity ratio.
The IXS measured intensity has been fitted through the convolution of the model function described by equation 4.28 with the instrumental response function times an intensity parameter. A baseline has also been added to account for background noise. In Figure 4.10 and 4.11 the experimental data are reported together with the best fitting line shape, the DHO contribution corresponding to the inelastic features and the instrumental resolution.

4.2.2 Spectra normalization

The reliability of the measurements is strictly related to the possibility of reporting the spectra on an absolute scale. In neutron scattering experiments the measured spectra can be properly normalized using a reference scatterer. The use of X-rays does not allow us to simply use such procedure, since geometrical effects can critically affect the relative intensity. Such a problem can be avoided using

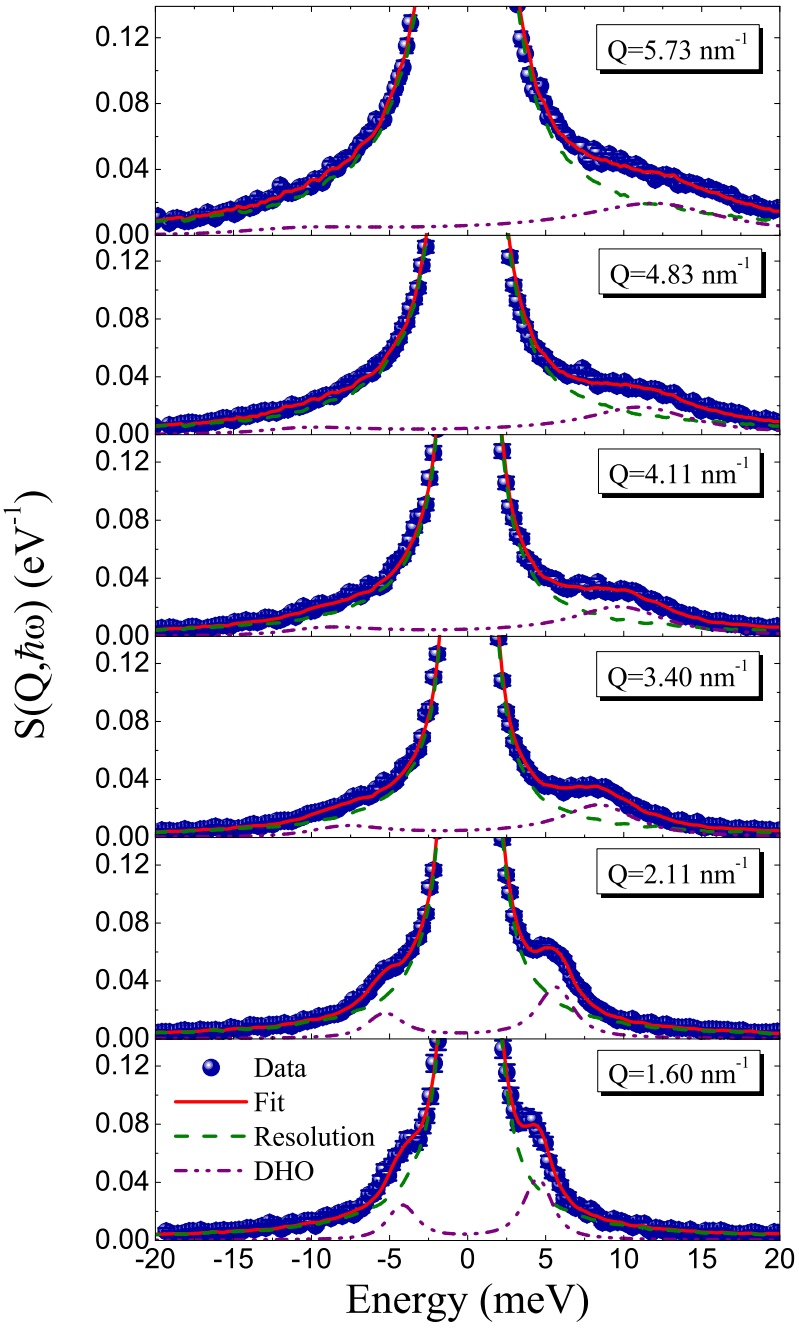

FIGURE 4.10: Selected IXS spectra of glassy sorbitol at T=80 K for different exchanged wave-vectors Q together with the best fitting line shape (red line). The elastic (dashed green line) and the inelastic (dashed-dotted-dotted purple line) components of the DHO model are reported after convolution with the instrumental resolution. The intensity is reported in absolute scale as explained in the text.

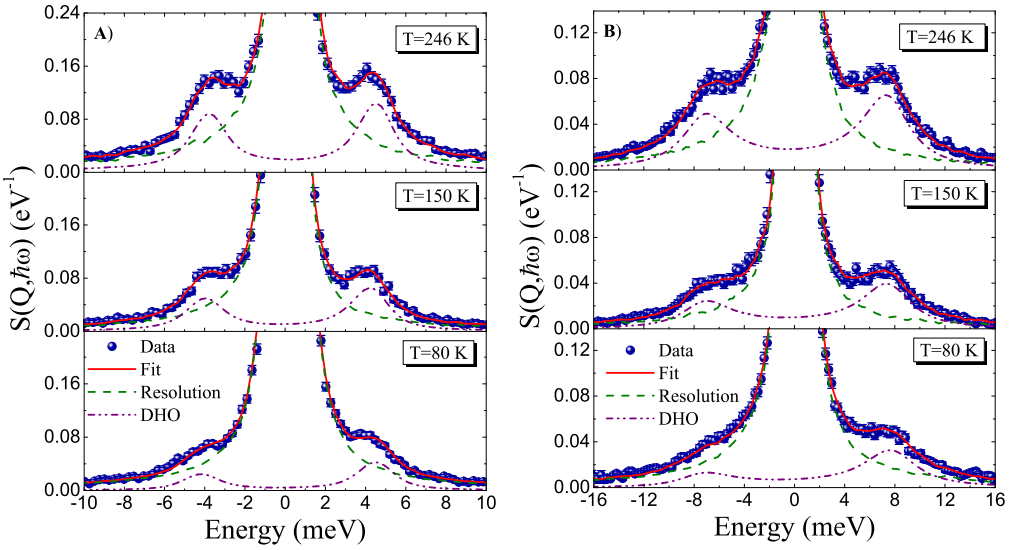

FIGURE 4.11: Selected IXS spectra of glassy sorbitol at T=80, 150 and 246 K for Q=1.60 nm^{-1} (A) and Q=3.06 nm^{-1} (B) together with the best fitting line shape (red line). The elastic (dashed green line) and the inelastic (dashed-dotted-dotted purple line) components of the DHO model are reported after convolution with the instrumental resolution. The intensity is reported in absolute scale as explained in the text.

the frequency moments of the dynamic structure factor as a tool to normalize the measured intensity [76]. For such purpose, the second moment is the most appropriate. In its classic description, it is given by the relation

$$M^{(2)}(Q) = \int_{-\infty}^{+\infty} d\omega \omega^2 S(Q,\omega) = \frac{Q^2 k_B T}{M} \tag{4.29}$$

where k_B is the Boltzmann constant, T the temperature, ω the angular frequency, and M the molecular mass of the system. The experimental dynamic structure factor has then been normalized using the factor $A(Q)$ where

$$A(Q) = \frac{1}{M^{(2)}(Q)} \int_{-\infty}^{+\infty} d\omega \omega^2 S_{exp}(Q,\omega) \tag{4.30}$$

being $S_{exp}(Q,\omega)$ given by equation (4.28) using the parameters obtained in the fit routine.
This procedure allows for the determination of S(Q) integrating the quantity $(1/A(Q))S_{exp}(Q,\omega)$.
It is important here to stress that the S(Q) can be, of course, obtained only in the investigated Q range and that the whole procedure is an approximation being all the integrals performed in the limited experimental energy range.

A check of this normalization procedure and, more in particular, of the use of the DHO model (see equation 4.28) in the analysis of the spectra, is confirmed by the

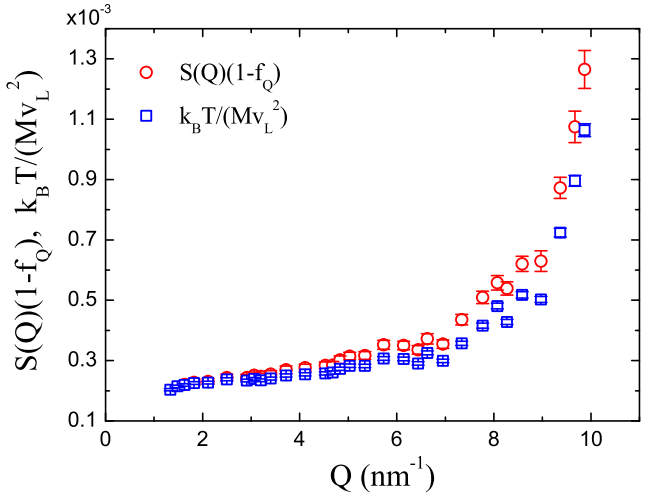

FIGURE 4.12: The two sides of equation 4.31. The equality between the two quantities represents a check of the consistency for the data analysis of the IXS spectra.

following equality

$$S(Q)(1-f_Q) = \frac{k_B T}{M}\frac{1}{v_\infty^2} \tag{4.31}$$

between the inelastic intensity $S(Q)(1-f_q)$ and the quantity $\frac{k_B T}{M}\frac{1}{v_\infty^2}$. In fact this relation is just a consequence of the application of the second moment rule to the DHO function. The two sides of the equation have been calculated and are reported in Figure 4.12. The relation 4.31 is well fulfilled in the whole investigate range range confirming the validity of our data analysis procedure.

4.2.3 Static structure factor and compressibility

Once the static structure factor has been computed, we can study its value in the $Q \to 0$ limit. In the case of equilibrium systems, such as liquids and gases, the macroscopic limit of the static structure factor gives information on the isothermal compressibility χ_T, being

$$S(Q \to 0) = \frac{\rho k_B T \chi_T}{M} \tag{4.32}$$

where ρ is the density.
In a glass, thus in a non equilibrium system, this relation must be modified taking into account the relaxational processes that are frozen in at the glass transition temperature T_g [160–162]. By considering these non-propagating density fluctuations that are kinetically arrested at T_g the low Q limit of the $S(Q)$ (4.32) becomes

$$S(Q \to 0) = \frac{\rho k_B}{M}\left\{T_g\left[\chi_T^0(T_g) - M_\infty^{-1}(T_g)\right] + T M_\infty^{-1}(T)\right\} \tag{4.33}$$

where $M_\infty(T)$ is the real part of the high-frequency longitudinal modulus, related to the sound velocity of the acoustic-like modes through the relation $M_\infty(T) = \rho(T)v_\infty^2(T)$, and $\chi_T^0(T_g)$ is the isothermal compressibility in the liquid phase at the glass transition temperature (see table 3.2). The previous equation assumes, thus, that the fluctuations not frozen in below the glass transition arise from long-wavelength propagating vibrational modes due to high-frequency longitudinal excitations. In particular, the two relations 4.32 and 4.33 differ mainly in the case of fragile systems, such as sorbitol, and less in strong materials. In fragile systems, in fact, the compressibility is characterized by a bigger jump at the glass transition than in strong materials and only by properly considering this jump it is possible to estimate the correct long wavelength limit of the density fluctuations amplitude. From the low Q limit of $A(Q)$ we find $S(Q \to 0) = (2.8 \pm 0.1) \times 10^{-3}$ for T=80 K. Such value is compatible with the one estimated from relation (4.33), $S(Q \to$

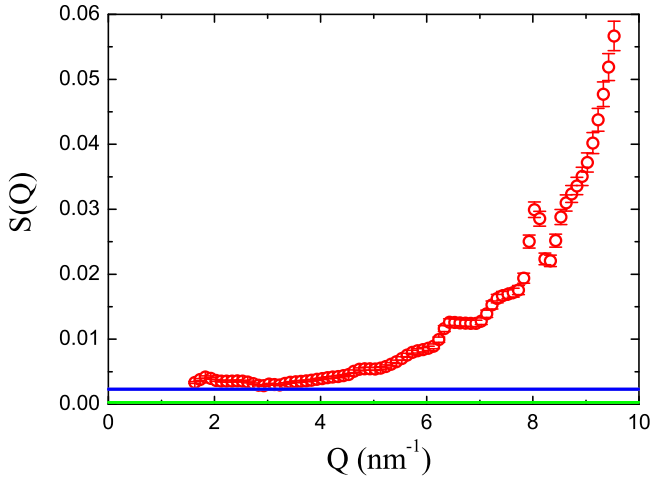

FIGURE 4.13: Static structure factor of sorbitol obtained from the zero-th moment of the normalized IXS spectra at T=80 K. The blue line represents the long wavelength limit estimated from relation 4.33, while the green solid line represents the macroscopic prediction 4.32.

$0) = (2.3 \pm 0.1) \times 10^{-3}$, obtained from thermodynamic measurements [117] and low-frequency Brillouin light scattering data (see section 3.3). Figure 4.13 shows the value of the $S(Q)$ obtained at T=80 K together with the limits corresponding to equations 4.33 and 4.32. The simple hydrodynamic expression 4.32 gives a too low value with respect to the data leaving a difference that can be completely accounted for by taking into account the presence of density fluctuations frozen in at T_g.

The value of the low Q limit of the $S(Q)$ has been checked also at the other investigated temperatures, thus for T=150, 220, 246, 256 and 267 K as well. The obtained limits are reported in table 4.3 together with the ones estimated from relations 4.32 and 4.33. In the case of the macroscopic limit 4.32, the values have been obtained using the low frequency BLS data for all the temperatures, except

for T_g where v_0 has been obtained using also PVT measurements. There is a good agreement between the experimental data for $S(Q)$ and the limit 4.33 for all temperatures. The validity of this relation represents a strong confirmation of the whole normalization process and, thus, of the reliability of the measured spectra.

T [K]	$S(Q \to 0)_{exp.}$ $[10^{-3}]$	$S(Q \to 0)_{therm.}$ $[10^{-3}]$	$S(Q \to 0)_{macr.}$ $[10^{-3}]$
80	2.8 ± 0.1	2.3 ± 0.1	0.29 ± 0.02
150	2.4 ± 0.1	2.5 ± 0.1	0.55 ± 0.03
220	3.0 ± 0.1	2.7 ± 0.1	0.84 ± 0.05
246	3.1 ± 0.1	2.7 ± 0.1	0.95 ± 0.06
256	3.4 ± 0.1	2.8 ± 0.1	1.00 ± 0.06
267	3.8 ± 0.2	2.8 ± 0.1	2.8 ± 0.1

TABLE 4.3: Long wavelength limit of the amplitude of the density fluctuations at different temperatures as obtained by the zero-th moment of the normalized IXS spectra, $S(Q \to 0)_{exp.}$, together with the values obtained from equation 4.33 using thermodynamic and low frequency data, $S(Q \to 0)_{therm.}$, and from the macroscopic equation 4.32, $S(Q \to 0)_{macr.}$. The latter has been calculated using the isothermal compressibility estimated from the BLS data with the exception of the value at T_g which comes from PVT measurements.

4.3 Acoustic properties of sorbitol at T=80 K

Figure 4.14 reports the acoustic dispersion curve of sorbitol for T=80 K as a function of the momentum Q transferred in the scattering process. The corresponding estimated static structure factor is reported as well. As generally observed, the dispersion curve of glasses shows a striking resemblance with that of polycrystalline samples [77]. The Brillouin energies show indeed a seemingly linear dependence at low Q, which seems to correspond to the elastic macroscopic limit measured at low frequency with Brillouin light scattering (dashed red line in Figure 4.14). The analogy with respect to polycrystalline samples allows for the identification of a pseudo-Brillouin zone with a border at ~ 7 nm^{-1}, a value that corresponds to half of the first diffraction peak position (see Figure 4.9). The green line in Figure 4.14 represents the energy of the maximum of the boson peak of sorbitol measured with inelastic neutron scattering (see next Chapter). It is clear, here, that the high frequency modes maintain their propagating character well beyond the energy maximum in the reduced VDOS, confirming the same behavior observed in other glasses [57].

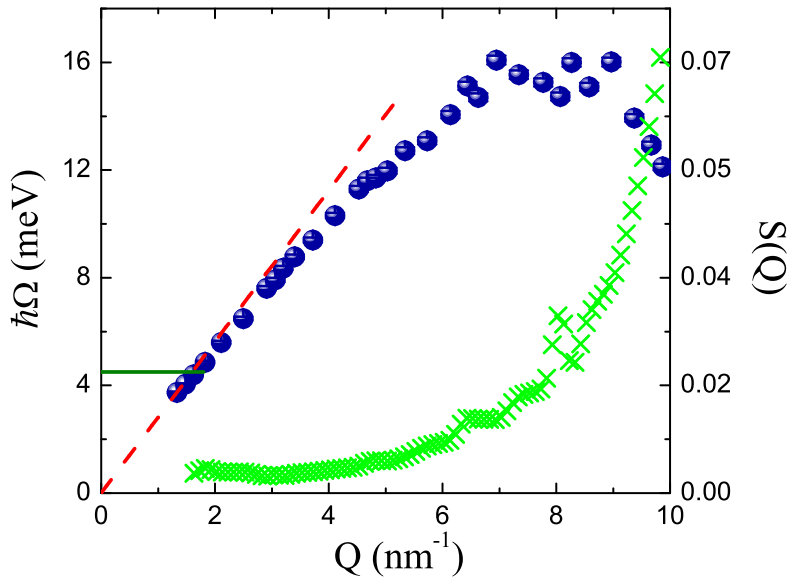

FIGURE 4.14: Dispersion relation of the longitudinal acoustic-like excitations of sorbitol measured at T= 80 K. The data (blue dots, left y axis) are reported as a function of the momentum transfer Q together with the static structure factor $S(Q)$ (green crosses, right y axis). The dark green line indicates the energy of the boson peak maximum while the red dashed line corresponds to the macroscopic elastic limit measured with Brillouin light scattering.

4.3.1 Breakdown of the Debye continuum approximation

The shape of the dispersion curve yields information on the apparent phase velocity $v_L(Q) = \Omega(Q)/Q$ that is reported as a function of Q in Figure 4.15 in the whole investigated range (left panel) and in the low Q region (right panel). The data do not show the smooth, sine-like decrease proposed from early experimental results (see section 2.2). Rather, they present an abrupt decrease from the macroscopic value (horizontal line, from BLS data) to a lower plateau at $\sim$2 nm^{-1}, while only for higher Q values they show the expected sine-like decrease on approaching the border of the pseudo-Brillouin zone ($\sim$ 7 nm^{-1}). The presence of the low-Q negative dispersion cannot be associated with static density fluctuations. Indeed, as shown in the same Figure, in the low Q region the static structure factor is almost flat and the medium can still be considered as a continuum from the density point of view. This means that the softening of the sound speed is related to the existence of extra degrees of freedom with respect to the elastic macroscopic level. Using Figure 4.14 to convert energies into Q values, it is easy to realize that this flattening of the sound velocity appears exactly in the energy range of the boson peak, which corresponds to $Q \sim 1.7$ nm^{-1} and that, of course, a flattening of the sound velocity implies an excess of acoustic modes in the VDOS over the Debye,

continuum medium prediction[1]. This mode softening, which is a quite marked effect of the order of 8% confirms the results recently found in glassy glycerol [96]: the Debye continuum approximation in glasses holds up to ∼1 nm^{-1} and above that it undergoes an abrupt breakdown, whilst it still works reasonably well in that same Q range for the corresponding crystals.
Differently from the case of glycerol (see the top panel of Figure 2.6), in sorbitol the IXS apparent sound velocity reaches the macroscopic limit already at the lowest probed Q-values, thus indicating the absence of relevant anharmonic, relaxational and/or other Q-dependent effect in the frequency interval comprised between the THz range probed by IXS and the 10 GHz range probed by BLS.

The presence of a negative dispersion of the sound velocity in the mesoscopic

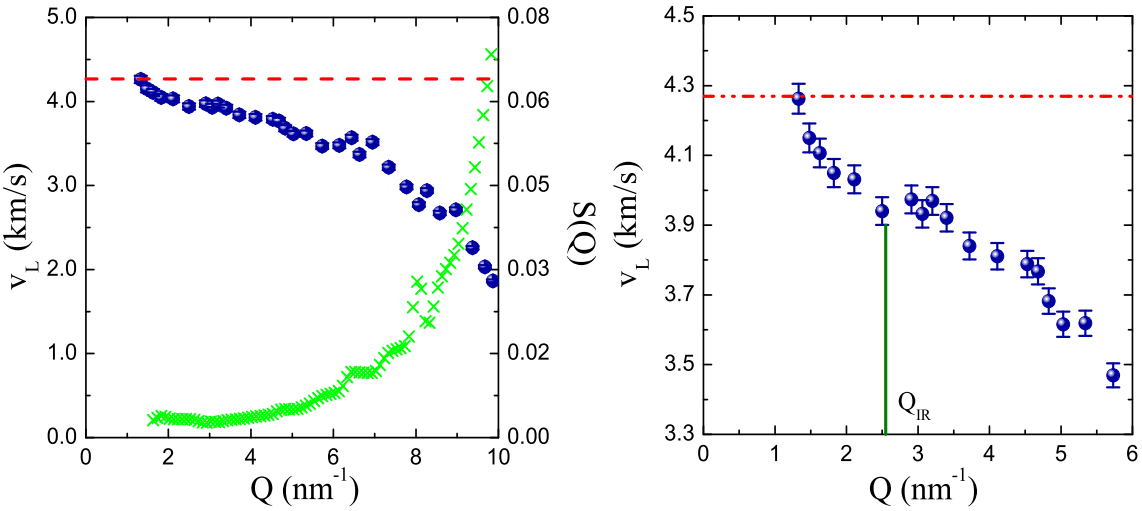

FIGURE 4.15: Left panel: sound velocity of sorbitol measured a T=80 K (blue dots) as a function of the momentum transfer Q (blue dots) together with the static structure factor $S(Q)$ (green crosses). The red dashed line corresponds the macroscopic elastic limit measured with Brillouin light scattering. Right panel: same data in a smaller Q range. The vertical green line represents the Q corresponding to the Ioffe-Regel limit, as discussed in section 4.3.3.

spatial range has been recently found in a molecular dynamics study of a Lennard-Jones monatomic glass model as well [98] and can be related to the inhomogeneities of the elastic response at the nano-scale [74].

4.3.2 Acoustic attenuation

The width of the Brillouin peaks gives information on the sound attenuation of the acoustic-like excitations in the THz frequency range. In fact the absorption

[1]The vibrational density of states can be described in terms of the sound velocity being $g(\omega) \propto dQ/d\Omega$ [55].

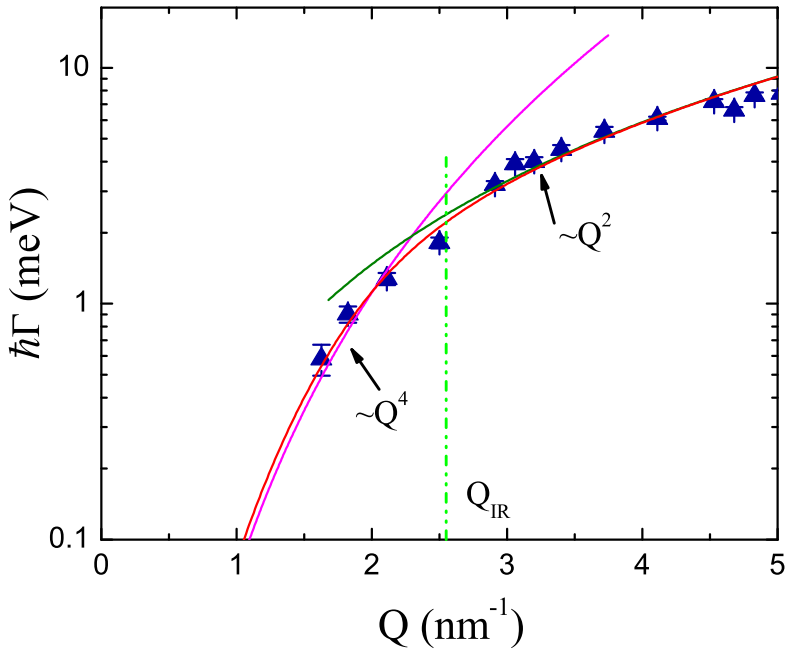

FIGURE 4.16: FWHM of the Brillouin peak as a function of the exchanged wavevector. The red line is best fit line shape obtained from the phenomenological function 4.34 describing the crossover from a $\sim Q^4$ power law dependence at low Q (pink line) to a quadratic behavior at higher Q (green line). The vertical light green line represents the Q corresponding to the Ioffe-Regel limit, as discussed in the next section.

coefficient α_{abs}, given by the inverse of the mean free path l, can be expressed as $\alpha_{abs} = l^{-1} = (v_L\tau)^{-1} = \Gamma/v_L$, being τ the finite life time of the excitations.
In Figure 4.16 the Q-dependence of $\hbar\Gamma$ is reported in log-linear scale for T=80 K. This parameter clearly displays a strong Q-dependence, changing continuously (red line) from $\sim Q^4$ at low-Q (pink line) to $\sim Q^2$ at high-Q (green line), thus supporting the universality of the low-Q $\sim Q^4$ dependence previously observed in other few glasses [85, 91, 96].
The red line in the Figure is obtained by using the phenomenological function

$$\hbar\Gamma(Q) = A\frac{Q^2}{\left[1+\left(\frac{Q_c}{Q}\right)^{(4-2)\delta}\right]^{\frac{1}{\delta}}} \tag{4.34}$$

describing the crossover from a $\sim Q^4$ power law dependence at low Q to a quadratic behavior at higher Q. The obtained parameters are reported in table 4.4 As reported in section 2.2, this Rayleigh regime ($Q \sim Q^4$) in the mode damping is predicted by substantially different theoretical models for the vibrations in disordered solids [68, 92, 93]. In fact, the existence of a plateau in the low temperature thermal conductivity of glasses requires the mean free path of the propagating

A	Q_c	δ
0.37±0.01	2.13 ± 0.30	3.44 ± 1.23

TABLE 4.4: Values of the parameters entering equation 4.34 in the description of the behavior of the sound attenuation reported in Figure 4.16.

acoustic excitations to decrease at least with the fourth power of energy [51]. The existence of a strong scattering process in the nanometer spatial range has already been observed only in fews other intermediate and strong glasses [85, 96]. Sorbitol represents the first fragile system showing such behavior. It is in fact generally very difficult to measure the high frequency modes in fragile systems for energies close or below the boson peak one.
It is worth emphasizing that this peculiar $\sim Q^4$ dependence of the broadening $\hbar\Gamma$ appears in the same Q range where the negative dispersion of the high-frequency sound velocity is detected, clearly indicating that these two features must be strictly related. As it will be shown in the next Chapter, these elastic anomalies not only appear in the same energy range of the boson peak, but, as in the case of glycerol [96], they can be used to evaluate quantitatively the shape of the boson peak.

4.3.3 The Ioffe-Regel criterion

The analysis of the high frequency dynamics allows us to calculate the Ioffe Regel (IR) limit for the acoustic-like excitations of sorbitol. This limit is usually defined as the energy where the mean free path becomes comparable to half of the wavelength of the propagating plane-wave excitations, and corresponds to the condition

$$\pi\Gamma_{IR}/\Omega_{IR} = 1 \tag{4.35}$$

for longitudinal and transverse modes. The IR criterion represents an upper limit for a well-defined plane-wave approach to describe the acoustic-like excitations [163].
In several systems the IR limit for the longitudinal acoustic-like modes takes place at energies close to that of the boson peak maximum, suggesting the existence of a strict correlation [91]. Nevertheless this result is highly controversial [164].
In the case of sorbitol, the Ioffe-Regel condition for the longitudinal branch is fulfilled at about $\Omega_{IR} \sim 6.7$ meV, thus at energies higher than that of the boson peak (see Figure 4.17). Such result is in agreement with recent molecular dynamics studies in which the equality $\hbar\Omega_{IR} = \hbar\Omega_{BP}$ seems to hold only for the transverse excitations, while the longitudinal modes reach that limit at higher energies [98, 104]. Notwithstanding in some glasses the correlation between boson peak and Ioffe Regel energy applies for both the longitudinal and transverse branches [165].

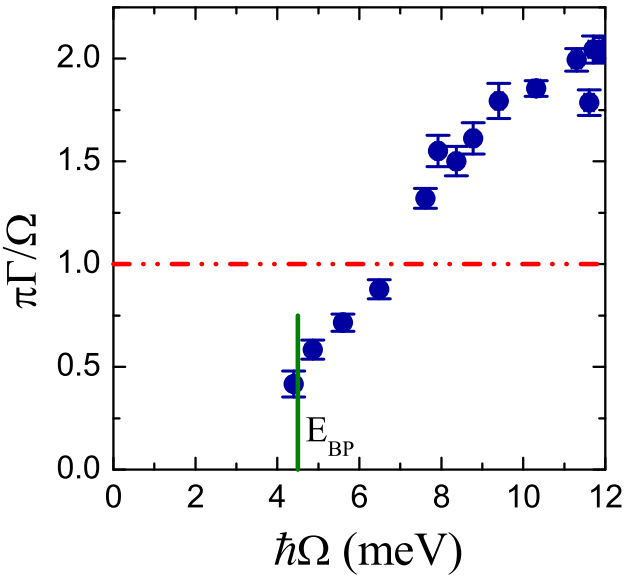

FIGURE 4.17: Ioffe Regel limit for the longitudinal acoustic-like waves at T=80 K. The IR energy is given by the intersection between the data and the red dashed line defined by equation 4.35. The solid green line marks the energy of the boson peak maximum.

Using the dispersion curve (see Figure 4.14) to convert energies into Q values, it is possible to define a IR wave-vector Q_{IR}, which in the case of sorbitol corresponds to $Q_{IR} \sim 2.55$ nm^{-1}. This value corresponds to the upper end of the elastic anomalies detected at low Q for the longitudinal modes (see Figures 4.15 and 4.16), thus in a spatial range where the continuum approximation is no longer valid.

4.3.4 Nonergodicity factor

Figure 4.18 shows the Q dependence of the nonergodicity factor of sorbitol measured at T=80 K. At this low temperature the f_Q has been correctly measured only for Q values above $Q = 2.91$ nm^{-1}. Generally f_Q follows in phase the oscillations of the static structure factor and reaches an almost constant value in the low Q region where $S(Q)$ is flat.
For a system at thermodynamic equilibrium, the low Q limit of the nonergodicity factor is given by the relation

$$f_Q(Q \to 0) = 1 - \frac{v_0^2}{v_\infty^2} \tag{4.36}$$

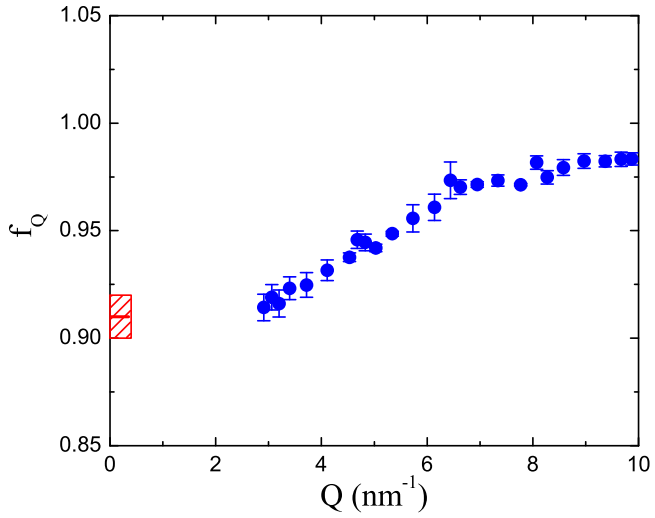

FIGURE 4.18: Nonergodicity factor of sorbitol measured at T=80 K. The red rectangle represents the continuum limit calculated from relations 4.37 and 4.38.

where v_0 and v_∞ are the relaxed and unrelaxed sound velocity, respectively (see Figure 1.8). In the case of glasses, relation 4.36 should be modified by taking into account the jump of the isothermal compressibility at T_g. A correct macroscopic limit estimation should indeed consider the relaxational processes that are frozen in at the glass transition temperature as well as in the case of the static structure factor. By using the correct low Q limit for the $S(Q)$ given by equation 4.33, and using equation 4.31 we obtain

$$f_Q(Q \to 0) = \frac{1}{1 + \alpha_\chi(T)\frac{T}{T_g}} \tag{4.37}$$

where the parameter $\alpha_\chi(T)$ is given by

$$\alpha_\chi(T) = \frac{M_\infty^{-1}(T)}{\chi_T^0(T_g) - M_\infty^{-1}(T_g)} \tag{4.38}$$

where $\chi_T^0(T_g)$ is the isothermal compressibility in the liquid phase at T_g and M_∞ the real part of the high frequency longitudinal modulus. Expression 4.37 is formally identical to the relation 2.5 proposed by Scopigno and coworkers [3]. The main difference between these two relations resides in the definition of the parameter α (or α_χ) in the denominator. In the case of Ref. [3] this relation was deduced from an harmonic description of the atomic vibrations and the parameter α contains all the microscopic details of the system. In the present case, instead, the parameter α_χ is described only through macroscopic quantities and turns out to be nothing else that the extension for $T < T_g$ of the relation between the vibrational and relaxational compressibility 3.27 proposed by Buchenau and Wischnewski [4] and discussed in section 3.3.3.

The obtained continuum limit of the nonergodicity parameter 4.37 is also reported in Figure 4.18. There is a clear good agreement with the experimental data at low Q. The hydrodynamic value described by relation 4.36 corresponds to $f_Q(Q \to 0) = 0.31 \pm 0.03$, a value so low that cannot be reported in the same Figure. As for the static structure factor, the long wavelength limit of the nonergodicity factor is clearly reached only by considering that part of the density fluctuations are frozen in at the glass transition.

4.4 Temperature dependence of the high-frequency dynamics

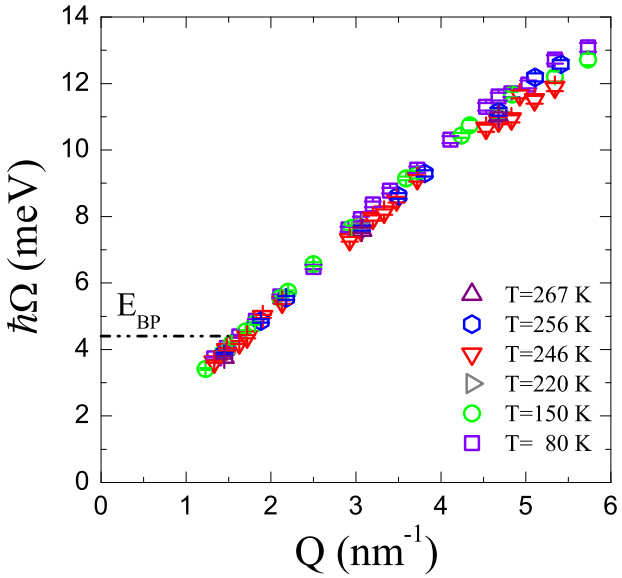

FIGURE 4.19: Dispersion curves of sorbitol at different investigated temperatures. The black line marks the energy of the boson peak maximum, which is constant in the investigated temperature range.

The acoustic properties of sorbitol have been investigated in a wide temperature range, from 80 K up to the glass transition temperature. As shown in Figure 4.11 a simple glance at the experimental data do not allow for a determination of any remarkable temperature dependence of the inelastic features. The energy excitations seems to be not very much affected by temperature variations. This is also evident by looking at Figure 4.19 where the dispersion curve is reported as a function of the momentum transfer Q for all the investigated temperatures. All the results found at the lowest temperature- such as the existence of a pseudo Brillouin zone with border at ~ 7 nm^{-1} and the existence of propagating modes

well above the boson peak energy- are valid up to the glass transition temperature.
The same observation can be drawn for the sound attenuation as well. Figure

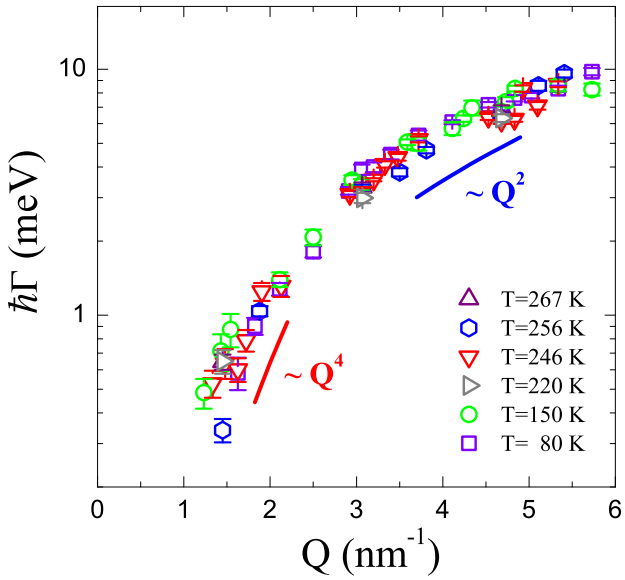

FIGURE 4.20: Q-dependence of $\hbar\Gamma$ in log-linear scale for the different considered temperatures. The two lines emphasize the change in the Q-dependence of $\hbar\Gamma$ from a power law compatible with Q^4 at low Q to one compatible with Q^2 at high Q.

4.20 shows the Q-dependence of $\hbar\Gamma$ in log-linear scale for the different considered temperatures. Both the Rayleigh $\sim Q^4$ dependence at low Q and the quadratic Q-dependence at higher Q are present in whole investigated temperature range. These data represent the first measurements of the temperature dependence of the low Q strong damping regime found in some glasses [85, 91, 96]. The determination of the line width at so low exchanged wave vectors requires indeed high accuracy in the IXS experiments. In particular, it was here possible to obtain reliable measurements of $\hbar\Gamma$ down to $\sim$1.3 nm^{-1}, where $\hbar\Gamma$ is only about one fourth of the FWHM of the instrumental function.
It is interesting here to note the temperature independence of $\hbar\Gamma$ in the whole Q-range. This result extends similar observations previously limited to the high-Q Q^2-range [89], and confirms the non-dynamic origin of sound wave attenuation in the whole explored Q-range.
Looking more carefully at the data, the dispersion curve comes out to be not really temperature independent. The temperature effects can be emphasized looking at the apparent sound velocity, which is reported in Figure 4.21 a). The sound speed is marked by a clear temperature dependence in the whole Q range.
It is interesting to observe that the temperature dependence of the IXS apparent sound velocity curve follows that of the macroscopic one measured with BLS in the whole explored Q-range, and in particular in the region where the plateau at

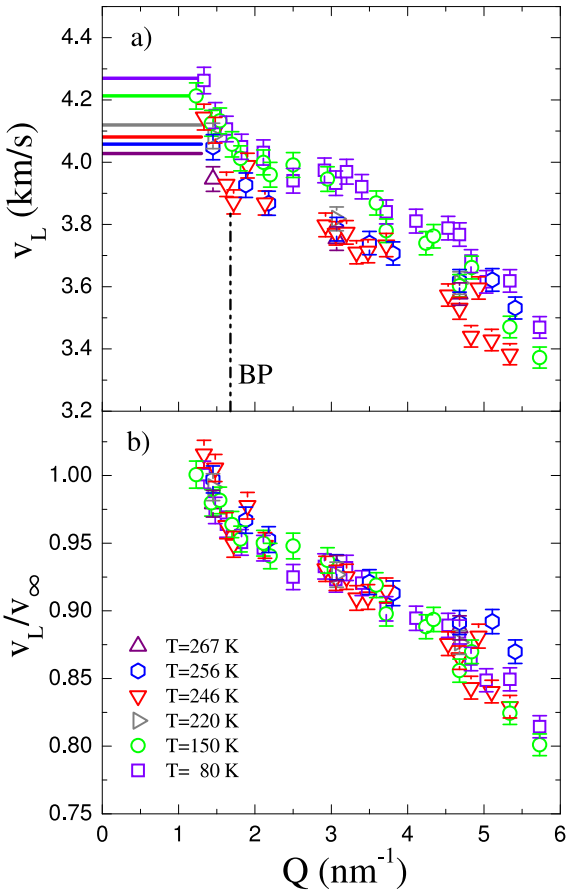

FIGURE 4.21: Inelastic x-ray scattering results for the apparent sound velocity $v_L = \Omega/Q$ of the longitudinal acoustic excitations of glassy sorbitol at the indicated temperatures. The macroscopic limits for the sound velocity obtained from BLS measurements (see section 3.3) are reported as well (horizontal lines). The vertical dot-dashed line marks the Q-value corresponding to the boson peak position via the dispersion relation of Figure 4.19. (b): same data as in (a) but rescaled for the macroscopic sound velocity.

$\sim$2 nm^{-1} in the apparent sound velocity is observed: the shape of the dispersion curves in this interesting range turns then out to be temperature independent. This observation is verified in Figure 4.21 b), where the IXS sound velocity data at the different temperatures are reported after rescaling for their macroscopic limit. A single curve is obtained. This result implies that the dispersion curves in the explored Q range can be completely described by the modifications of the elastic medium.

4.4.1 The quasi harmonic nature of the high frequency excitations

The temperature dependence of the high-frequency acoustic dispersion curves of glassy sorbitol can be described to a good approximation within a quasi-harmonic approach.
In order to understand the role played by the temperature on the high frequency sound velocity in glassy sorbitol, the data must be considered together with the corresponding attenuation data, $\hbar\Gamma$. As reported in section 3.3 these two quantities are in fact not independent: they are related to the real (M') and the imaginary (M'') part of the longitudinal elastic modulus $M(\omega) = M'(\omega) + iM''(\omega)$, being $M' = v_L^2\rho$ and $M'' = \Gamma v_L \rho/Q$, where ρ is the mass density.

The scaling of the high frequency sound velocity data with the elastic continuum and the non-dynamic origin for the sound attenuation require the absence of anharmonic effects in the frequency range explored by IXS. In section 3.3 we have seen that the low frequency sound attenuation measured with BLS displays a strong temperature dependence (see bottom panel of Figure 3.8). This behavior represents a typical signature of the presence of anharmonic contribution in the GHz frequency range explored by BLS [88]. The temperature dependence of the IXS data imply instead that this contribution must be completely negligible in the high frequency range here investigated.

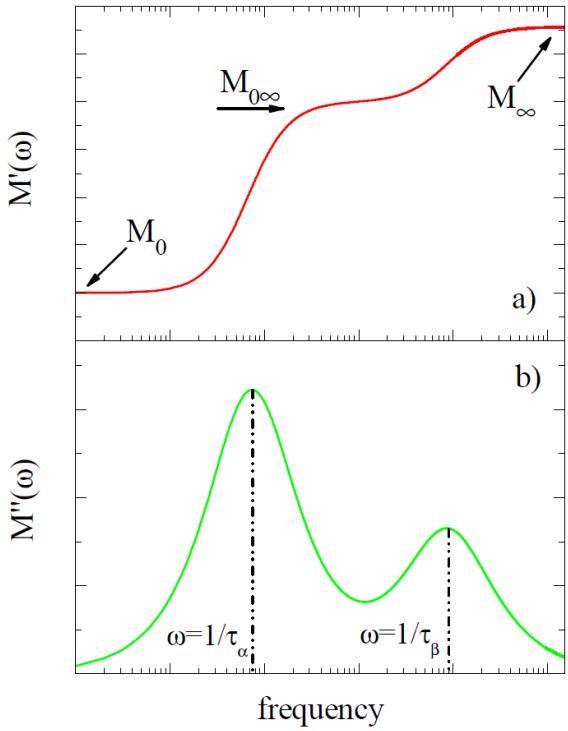

FIGURE 4.22: Scheme of the frequency dependence of the real and imaginary part of the longitudinal modulus in presence of an additional anharmonic or relaxational contribution. The details are explained in the text.

In general the role of anharmonicity can be quantitatively evaluated from the analysis of the low frequency longitudinal modulus. The frequency behavior of the sound velocity and absorption - proportional, respectively, to M' and M'' - has been already reported in Figure 1.8 in presence of the structural relaxation alone. The effect due to the presence of an additional secondary relaxational or anharmonic contribution is schematically reported in Figure 4.22 for the real and imaginary part of the longitudinal modulus. The anharmonicity leads to the appearance of a second step in M' (or in the sound velocity) with a corresponding second peak in M'' (or in the absorption) when the angular frequency fulfills the condition $\omega_\beta = 1/\tau_\beta$.
The temperature dependence of M' and M'' obtained from BLS (see section 3.3) and thermodynamic [117] measurements of glassy sorbitol are reported in Figure 4.23. The observed temperature dependence of the longitudinal modulus can be

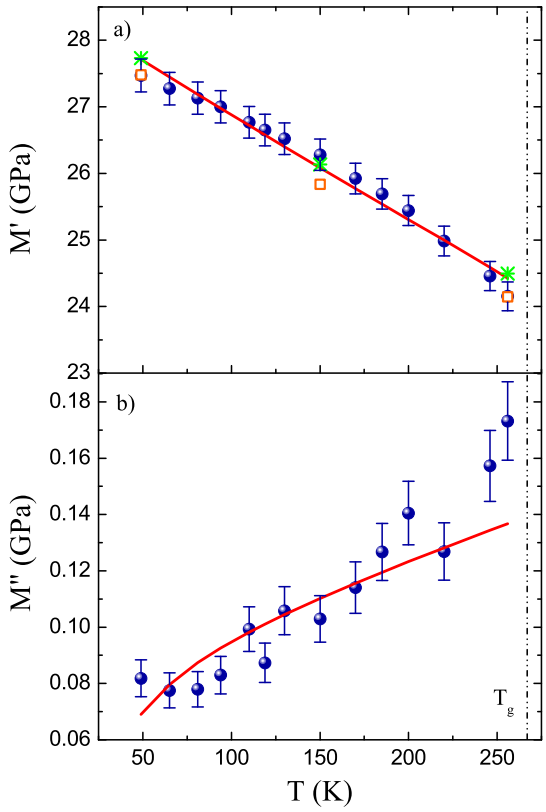

FIGURE 4.23: Temperature dependence of the real and imaginary part of the longitudinal modulus of glassy sorbitol derived from BLS (see section 3.3) and thermodynamic [117] measurements. The red full lines are the best fitting curves using the model of equation 4.39. In the top panel the fully relaxed (orange empty squares) and unrelaxed (green stars) values of M' are reported for some representative temperatures, in order to emphasize the small effect on M' of the purely anharmonic term of the model.

described taking into account two important contributions: i) quasi-harmonic effects that induce a temperature dependence of the sound velocity following the dependence of density on temperature [166, 167]; ii) purely anharmonic effects that, as said above, play an important role on the acoustic absorption (and then on M'') in the GHz frequency range probed with BLS [88]. In addition to that, the IXS data add further constraints: iii) M' must be basically frequency-independent in the frequency range between the frequencies probed in the BLS experiment (∼20 GHz) and those probed in the IXS one at the lowest considered Q value (∼1 THz); iv) the Γ probed in the IXS experiment is clearly of non-dynamic origin, which implies that anharmonic contributions must be negligible at the corresponding frequencies. Following Ref. [168], it is then possible to set up a simple model to describe the BLS data. Indeed the longitudinal modulus can be expressed as

$$M(\omega) = M_\infty - \frac{\Delta_M^2}{1 + i\omega\tau}, \tag{4.39}$$

where $M_\infty = \rho v_\infty^2$ is the fully unrelaxed longitudinal modulus that one can measure at frequencies high enough for the anharmonic contributions to be completely negligible, and v_∞ is the corresponding sound velocity; $\Delta_M^2 = M_\infty - M_{0\infty}$ represents the strength of the anharmonic process, where $M_{0\infty}$ is the fully relaxed longitudinal modulus that one would measure if there were no anharmonicity, and τ is an average relaxation time [168]. In this simple model M' is then given by the quasi-harmonic term M_∞ corrected for the anharmonic contribution, while M'' is completely determined by the anharmonic term, being

$$M' = M_\infty - \frac{\Delta_M^2}{1 + \omega^2\tau^2} \qquad \text{and} \qquad M'' = \frac{\Delta_M^2\omega\tau}{1 + \omega^2\tau^2} \tag{4.40}$$

In order to use equation 4.40 to describe the BLS data in Figure 4.23, with the additional constraints posed by the IXS data, it is necessary to fix the temperature dependence of the various parameters that intervene in it.
In a quasi-harmonic picture the purely elastic velocity, v_∞ can be taken to be linearly dependent on density [166, 167], and therefore linearly dependent on temperature, that is $M_\infty(T) = M_\infty^0(1+aT)^2$ with M_∞^0 and a temperature independent parameters. Moreover, for consistency reasons, the strength Δ^2 can be defined as $\Delta^2 = \Delta_0^2(1 + bT)^2$, with again Δ_0^2 and b temperature independent parameters. Finally, the relaxation time τ can be for simplicity reasons assumed to have an exponential behavior $\tau = \tau_0 e^{\frac{E_n}{T}}$, with τ_0 and E_n again assumed to be temperature independent.
The model of equation 4.40 can then be adjusted to the data of Figure 4.23 (with the additional constraints posed by the IXS ones) using the six parameters above as free parameters. The best fitting curve obtained from this analysis is reported as well in Figure 4.23, and well reproduces the experimental data [2]. From the model of Equation 4.40 we obtain the parameters reported in table 4.5. In particular we find a value E_n ∼30 K and a characteristic time τ ∼15 ps at 150 K, which

[2]The increase in M'' observed in the BLS data at high temperatures is due to the structural relaxation entering the frequency window probed by BLS and cannot be accounted for by our simple model (see section 3.3).

M^0_∞ [GPa]	a [10^{-4}K^{-1}]	Δ^2_0 [GPa]	b [10^{-4}K^{-1}]	τ_0 [ps]	E_n [K]
28.5	2.48	0.23	9.0	12.5	27.3

TABLE 4.5: Values of the parameters of the equation model 4.40 used to describe the temperature behavior of M' and M'' of sorbitol.

are quite common figures for glasses [88]. The values of $M_{0\infty}(T)$ and $M_\infty(T)$ are also reported in Figure 4.23 at some representative temperatures, in order to give a visual idea of the obtained M^0_∞, Δ^2_0, a and b parameters. It is clear that the BLS results for M' (and thus for the sound velocity) basically correspond to the purely elastic limit, with anharmonicity affecting them only very slightly due to its small strength. This clarifies why the sound velocity obtained in the BLS experiment and in the IXS one at the smallest probed Q values are basically coincident, and implies that the observed temperature dependence of the sound velocity both in the BLS and in the IXS range is practically governed by the quasi-harmonic term alone. This explains as well the origin of the scaling observed in Figure 4.21 b). The anharmonic term conversely completely describes M'' in the BLS frequency range while, given the values obtained for Δ^2 and τ, it turns out to be completely negligible in the IXS range.

4.4.2 Fragility and nonergodicity factor

Figure 4.24 shows the Q dependence of the nonergodicity factor for the investigated temperatures. In the Figure the macroscopic limits calculated from relations 4.37 and 4.38 are reported as well (see also values in table 4.6). It is interesting here to note that even if the macroscopic level is not yet completely reached at the lowest investigated Q values, there is a good agreement among the data and the continuum values at all the selected temperatures. This agreement represents a further confirmation of the validity of equations 4.37 and 4.38 for the estimation of the long wavelength limit of the f_Q from low frequency and thermodynamic measurements.
Equation 4.37 can be used as well to determine the Q dependence of the α_{IXS} parameter, which is reported in Figure 4.25 for all the investigated temperatures.
Albeit the continuum macroscopic limit described by equation 4.38 and reported in table 4.6 exhibits a clear temperature dependence, the high frequency data can be considered almost temperature independent within experimental errors, being the latter of the same order of the observed temperature dependence ($\sim$ 10% - 15%). This result confirms the validity of the equality

$$\alpha \equiv \alpha_\chi(T_g) \tag{4.41}$$

suggested by Buchenau and Wischnewski [4], where α is the parameter proposed by Scopigno and coworkers obtained from the temperature dependence of f_Q as

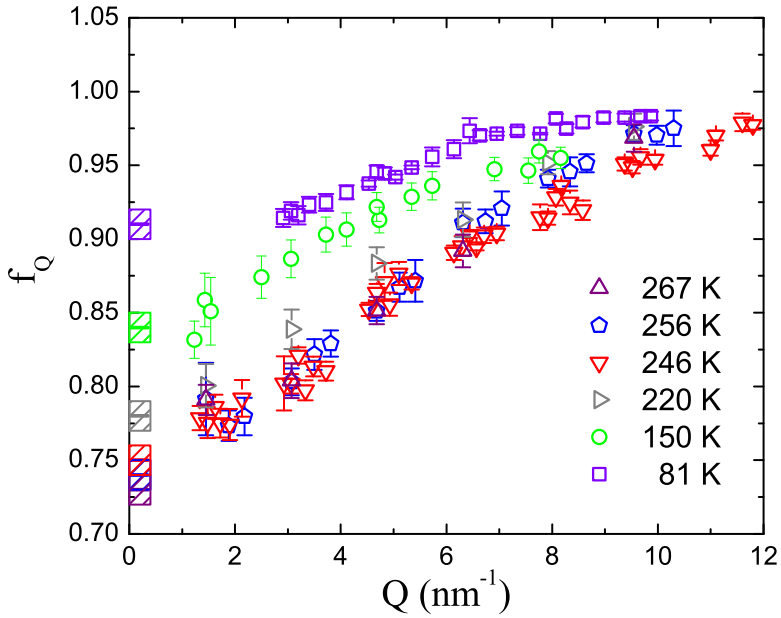

FIGURE 4.24: Nonergodicity factor of sorbitol at the indicated temperatures. The squares at low-Q represent the long wavelength limits estimated from relations 4.37 and 4.38.

expressed by the relation 4.37 (see section 2.4 and 3.3.3). Moreover the strong Q-dependence of the α parameter, which rapidly decreases on increasing the exchanged wave vectors, shows that the macroscopic limit is reached only at the lowest investigated Q value. In many glasses the α parameter has been obtained by the temperature dependence of f_Q for $Q \sim 2$ nm^{-1}. From Figure 4.25 it is clear that the choice of Q is extremely delicate and can be in fact the cause of some discrepancies in the proposed correlation between the α parameter and the kinetic fragility.

Figure 4.26 reports the inverse of the nonergodicity factor for $Q = 1.45$ nm^{-1}

T [K]	$f_{Q,macr.}$	α_χ
80	0.91 ± 0.01	0.32 ± 0.01
150	0.84 ± 0.01	0.33 ± 0.01
220	0.78 ± 0.01	0.35 ± 0.01
246	0.75 ± 0.01	0.35 ± 0.02
256	0.74 ± 0.01	0.36 ± 0.02
267	0.73 ± 0.01	0.37 ± 0.02

TABLE 4.6: Long wavelength limit of the nonergodicity factor and the α_χ parameter obtained from equations 4.37 and 4.38.

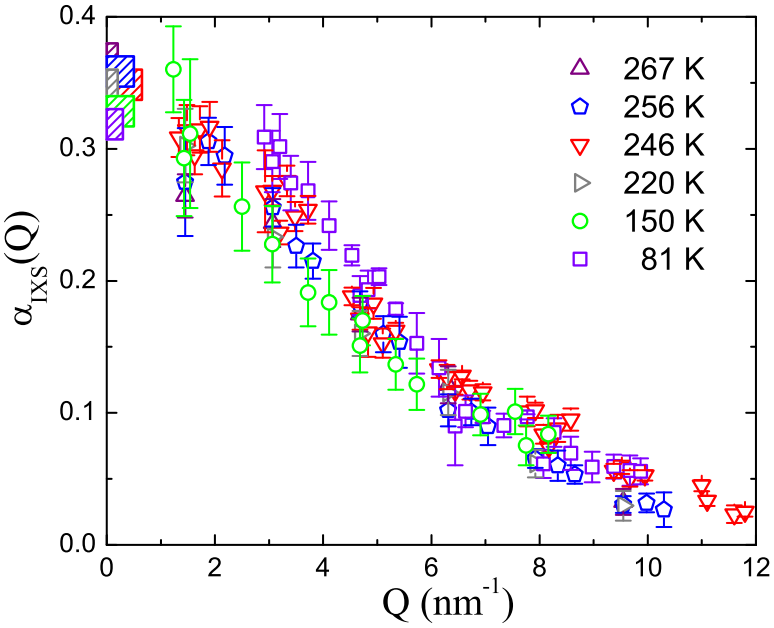

FIGURE 4.25: Temperature dependence of the α_{IXS} parameter obtained by equation 4.37. The lines represent the long wavelength limit α_χ estimated from relation 4.38.

(blue squares) and $Q = 3.06$ nm^{-1} (red circles) as a function of the rescaled temperature T/T_g. As previously reported in section 2.4, this graph corresponds to the analogue of the Angell plot in the glassy state. The two lines represent the best fitting line shapes obtained from relation 4.37 from which we obtain $\alpha = 0.31 \pm 0.01$ and $\alpha = 0.24 \pm 0.01$ for $Q = 1.45$ nm^{-1} and $Q = 3.06$ nm^{-1}, respectively. We remind that the linear relation 4.37 is valid only in the low temperature limit. For this reason the values corresponding at $T = 256$ K and $T = 267$ K have not been considered. The two values of α differ of about $\sim 30\%$. It is then clear that a correct estimation of the α parameter from the $1/f_Q$ *vs* T/T_g behavior is strictly related to the choice of the Q value and requires a good knowledge of the macroscopic continuum limit as well. In the case of sorbitol, albeit the macroscopic limit is not fully reached at the lowest probed Q-value at all the temperatures, the choice of $Q = 1.45$ nm^{-1} can be clearly considered valid for the estimation of the α parameter (see Figure 4.25).

The above results can be viewed also in term of kinetic fragility. Following the correlation $m_A = 135\alpha$ proposed by Scopigno and coworkers [3], we find $m = 42 \pm 1$ from the lowest Q data reported in Figure 4.26. This value is in agreement with the macroscopic one $m_\chi \sim 43 \pm 1$ obtained from the value of $\alpha_\chi(T = 80K)$ reported in table 4.6. These values are not far from the one obtained from the ratio between the bulk and the shear modulus discussed in section 3.3.3 ($m \sim 59$). However all of these correlations are in complete disagreement with the kinetic

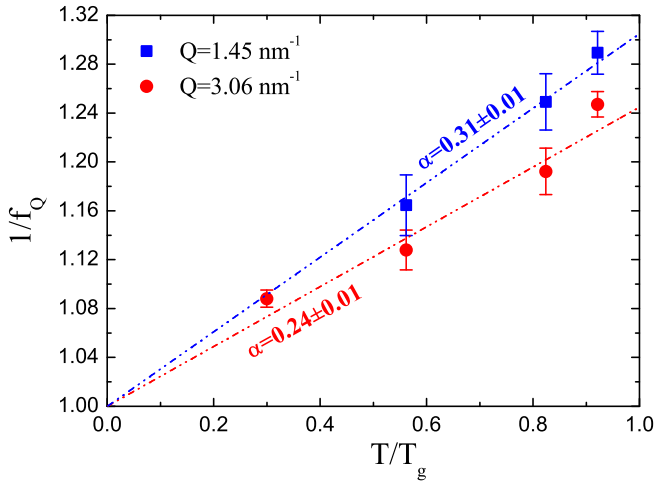

FIGURE 4.26: Inverse of the nonergodicity parameter measured at $Q = 1.45$ nm^{-1} (blue squares) and at $Q = 3.06$ nm^{-1} (red circles) as a function of the rescaled temperature T/T_g. The two dashed lines correspond to the best fit line shapes obtained from equation 4.37.

fragility measured in the supercooled liquid phase ($m_A \sim 107$). As suggested by Buchenau and Wischnewski [4] a possible explanation could be related to the existence of a basically fragility independent α parameter in very fragile systems, such as sorbitol (see section 3.3.3).
Recently the discrepancy between the estimated fragility in the glassy state and the kinetic one has been attributed to the presence of relevant secondary relaxation process, which affect the measurement of the nonergodicity factor (see section 2.4). As shown in the right panel of Figure 2.15, the presence of an anharmonic or secondary contribution adds an extra part to the area of the elastic line in the $S(Q,\omega)$, leading to an incorrect measurement of the f_Q.
In the case of sorbitol, we can easily obtain an estimation of the contribution to f_Q coming from the anharmonicity described in section 4.4.1. It has been shown that at the glass transition temperature the non ergodicity factor is described by equation 4.36, which can be rewritten as $f_Q(T_g) = \Delta^2(T_g)/M_\infty(T_g)$, where $\Delta^2(T_g) = M_\infty(T_g) - M_0(T_g)$ (see Figure 4.22). In presence of anharmonicity the measured nonergodicity factor can be written as

$$f_Q(T_g) = f_{Q,str}(T_g) + f_{Q,ana}(T_g) \tag{4.42}$$

where

$$f_{Q,str}(T_g) = \frac{\Delta^2_{str}(T_g)}{M_\infty(T_g)} \tag{4.43}$$

and

$$f_{Q,ana}(T_g) = \frac{\Delta^2_{ana}(T_g)}{M_\infty(T_g)} \tag{4.44}$$

are the contributions due to the α structural relaxation process and to the anharmonicity, respectively. Using the fitting parameters reported in table 4.5 we find $f_{Q,ana}(T_g) = (1.45 \pm 0.02)10^{-2}$. This value is ~ 50 times smaller than the macroscopic measured one reported in table 4.6. By using the correct value $f_{Q,str}(T_g)$ of the nonergodicity factor to calculate the α parameter (see equation 4.37), we find $\alpha_{str} = 0.40 \pm 0.02$, a value almost $\sim 8\%$ higher with respect to the measured one. The new value is anyway not high enough for a correct estimation of the kinetic fragility through the relation $m_A = 135\alpha$, being $m_{str} = 54 \pm 3$. This value is close to that estimated from the bulk to shear modulus ratio (see section 3.3.3) and seems to confirm the idea of the independence of the fragility from the α parameter for glass formers with high m_A values [4].

Résumé du chapitre 5

Dans ce chapitre nous présentons la relation entre l'élasticité et la densité des états vibrationnels du sorbitol. Les résultats obtenus sur la dynamique acoustique du sorbitol seront ici analysés en relation avec l'étude de la dépendance en température de la densité des états vibrationnels. Celle-ci a été mesurée en utilisant la diffusion inélastique des neutrons.
Dans la première partie du chapitre nous présentons une brève description de la section efficace de INS et les principes de base de la technique de temps de vol utilisée pour nos mesures. Dans la deuxième partie du chapitre nous mettons en relation les résultats de neutrons avec la dynamique vibrationnelle du sorbitol. Comme nous démontrerons le BP est clairement lié aux anomalies observées dans la courbe de dispersion acoustique dans la région mésoscopique des vecteurs d'onde de quelques nm^{-1}. La relation est en plus renforcée par la possibilité de reproduire quantitativement la forme de BP en utilisant la dépendance en Q de la vitesse du son et de l'atténuation à haute fréquence. Ce résultat confirme le rôle central des excitations acoustiques dans le BP et il est en accord avec une théorie récente des excitations vibrationnelles dans les systèmes à désordres élastiques.

Chapter 5

Vibrational density of states and elasticity in sorbitol

In this Chapter the relation between elasticity and vibrational density of states in sorbitol is discussed. The state of the art in this topic has already been presented in section 2.3. As shown there, despite of the effort done in the last years, a general agreement in the scientific community is still missing. In some glasses the changes of the boson peak, when pressure or temperature is applied [99], can be completely described by the corresponding transformation of the continuum medium while in other systems this relation is questioned [100], possibly due to the presence of anharmonic or relaxation contributions in the fews meV energy range [103].
The results obtained on the acoustic dynamics of sorbitol will be here combined with a temperature dependence study of the vibrational density of states. The latter has been measured using Inelastic Neutron Scattering spectroscopy. Such technique is in fact a valuable tool for the investigation of atomic motions in solids and liquids [169].
The first part of the Chapter reports a brief description of the INS cross section and of the basic working principles of the Time-of-Flight (TOF) technique used for the measurements.
In the second part of the Chapter, a comparison between the neutron results and the vibrational dynamics of sorbitol is reported. As it will be shown there, the excess in the VDOS at ∼4.5 meV over the Debye, elastic continuum prediction, is found to be clearly related to the anomalies observed in the acoustic dispersion curve in the mesoscopic wavenumber range of fews nanometers (see section 4.3). The relation is then strengthen by the possibility of quantitatively reproducing the shape of the boson peak on the basis of the Q-dependence of the high frequency sound velocity and sound attenuation. This result confirms the central role of the acoustic excitations in the boson peak and is in agreement with a recent theory of the vibrational excitations in disordered elastic media [67].

5.1 Inelastic Neutron Scattering

Neutrons are a powerful tool for the investigation of the vibrational properties of disordered systems. Some of the main peculiarities of neutrons spectroscopies have already been discussed in section 4.1.3. As reported there, thermal or cold neutrons are characterized by a wavelength λ of $1 - 10$ Å ($0.1 - 1$ nm), thus of the same order of magnitude as interatomic distances, and their kinetic energy is similar to that of several excitations in condensed matter. For these reasons they are suitable for the study of both dynamical and structural properties of many materials. In general, they can be produced in a thermal or cold moderator, either at a high-flux reactor or at a spallation source.
The first part of this section reports a brief summary of Inelastic Neutron Scattering theory. In particular a description of the INS cross section and the connection to the vibrational density of states of glasses is discussed. In the second part the basic working principles of a ToF technique will be illustrated.

5.1.1 INS cross section

The main features of the neutron scattering geometry are the same as for photons and are illustrated in Figure 4.1. In section 4.1.3 it has been shown that the accessible $(\boldsymbol{Q}, \omega)$ space for neutrons, described by the kinematic relation 4.24, is restricted with respect to that of X-rays due to the presence of the neutron mass. This limitation can be overcome in spectroscopy studies of crystalline samples, where the translation invariance allows for the study of the acoustic excitations in high-order Brillouin zones. Of course, this is not the case for topologically disordered systems, where the absence of periodicity imposes that the acoustic excitations must be measured at small momentum transfers.
In analogy to equation 4.9 for X-rays, the double-differential cross-section can be determined in the framework of first order perturbation theory, on the basis of the Fermi golden rule [152]. Considering the initial and final neutrons states, $|I\rangle$ and $|F\rangle$, as plane waves, the double-differential cross-section can be written as [169]:

$$\frac{\partial^2\sigma}{\partial\Omega\partial\omega_f} = \left(\frac{m}{2\pi\hbar^2}\right)\left(\frac{k_f}{k_i}\right)\overline{\sum_{I,F} P_I \left|\left\langle F\left|\hat{V}\right|I\right\rangle\right|^2 \delta(\hbar(\omega - \omega_F + \omega_I))} \tag{5.1}$$

where $\hat{V}$ is the interaction potential operator between the neutron and the target sample. In the previous expression P_I represents the probability of finding the system in the initial state I while the horizontal bar stands for any average not included in P_I, as for example the nuclear spin orientation or the distribution of isotopes.
In the following treatment the magnetic interaction between the neutrons and the nuclei will be completely neglected. Moreover, by considering only the nuclear interaction, which is strong and short ranged ($d \sim 10^{-13}$ cm) [152] and by assuming that the scattering is isotropic, the nuclear potential can be described through the

Fermi pseudo-potential:

$$\hat{V}(\boldsymbol{r}) = \frac{2\pi\hbar^2}{m} b\delta(\boldsymbol{r} - \boldsymbol{R}) \tag{5.2}$$

where $\boldsymbol{R}$ denotes the position of the nucleus.
In reality, this expression is a mathematical description which does not correspond, not even approximately, to the actual nuclear potential, but ensures that the scattering is isotropic and thus described by a single parameter b, which represent the scattering length of the atoms.
For a system of atoms the Fermi pseudo-potential can be written as

$$\frac{m}{2\pi\hbar^2}\hat{V}(\boldsymbol{r}) = \sum_l b_l \delta(\boldsymbol{r} - \boldsymbol{R}_l) = \sum_l \hat{V}_l(\boldsymbol{r} - \boldsymbol{R}_l) \tag{5.3}$$

where $\boldsymbol{R}_l$ is the position vector of the lth scattering nucleus. Inserting Equation 5.3 into Equation 5.1, the double-differential cross-section becomes:

$$\frac{\partial^2\sigma}{\partial\Omega\partial\omega_f} = \frac{k_f}{k_i}\overline{\sum_{I,F} P_I |\langle F| \sum_l \hat{V}_l(\boldsymbol{Q}) e^{i\boldsymbol{Q}\cdot\boldsymbol{R}_l} |I\rangle|^2 \delta(\hbar(\omega - \omega_F + \omega_I))} \tag{5.4}$$

where

$$\hat{V}_l(\boldsymbol{Q}) = \int d\boldsymbol{r} \hat{V}_l(\boldsymbol{r}) e^{i\boldsymbol{Q}\cdot\boldsymbol{r}}. \tag{5.5}$$

Writing the δ function in its integral form and using the Heisenberg operator property $\hat{O}(t) = e^{it\hat{H}/\hbar}\hat{O}e^{-it\hat{H}/\hbar}$, equation 5.4 can be written as

$$\frac{\partial^2\sigma}{\partial\Omega\partial\omega_f} = \frac{k_f}{k_i}\frac{1}{2\pi\hbar}\int_{-\infty}^{\infty} dt e^{-it\omega}\overline{\sum_{ll'}\langle e^{-i\boldsymbol{Q}\cdot\boldsymbol{R}_l}\hat{V}_l^+(\boldsymbol{Q})\hat{V}_{l'}(\boldsymbol{Q},t)e^{i\boldsymbol{Q}\cdot\boldsymbol{R}_{l'}(t)}\rangle} \tag{5.6}$$

where the suffix + indicates the complex conjugate and the angular brackets denote the thermal average of the enclosed quantity being:

$$\langle ....\rangle = \sum\nolimits_I P_I |\langle I|(...)|I\rangle|. \tag{5.7}$$

Supposing that there is no coupling between the target sample states and the interaction potential, the average over nuclear spin orientations and distributions, denoted by the horizontal bar can be considered independent from the thermal average and one obtains:

$$\begin{aligned}\frac{\partial^2\sigma}{\partial\Omega\partial\omega_f} &= \frac{k_f}{k_i}\frac{1}{2\pi\hbar}\int_{-\infty}^{\infty} dt e^{-it\omega}\sum_{ll'}\overline{\hat{V}_l^+(\boldsymbol{Q})\hat{V}_{l'}(\boldsymbol{Q})}\langle e^{-i\boldsymbol{Q}\cdot\boldsymbol{R}_l}e^{i\boldsymbol{Q}\cdot\boldsymbol{R}_{l'}(t)}\rangle \\ &= \frac{k_f}{k_i}\frac{1}{2\pi\hbar}\int_{-\infty}^{\infty} dt e^{-it\omega}\sum_{ll'}\overline{b_l^+ b_{l'}}\langle e^{-i\boldsymbol{Q}\cdot\boldsymbol{R}_l}e^{i\boldsymbol{Q}\cdot\boldsymbol{R}_{l'}(t)}\rangle\end{aligned} \tag{5.8}$$

where

$$\overline{b_l^+ b_{l'}} = |\bar{b}|^2 + \delta_{ll'}[\overline{|b|^2} - |\bar{b}|^2]$$

For a defined element, the average of the scattering length $\bar{b}_l$ over all isotopes and spin is called coherent scattering length, while the mean-square deviation of b_l

from its average values is known as the incoherent scattering length, thus

$$|\bar{b}|^2 = b_{coh}^2 \tag{5.9}$$

and

$$\overline{|b|^2} - |\bar{b}|^2 = b_{incoh}^2 \tag{5.10}$$

with $b_{scatt}^2 = b_{coh}^2 + b_{incoh}^2$. Therefore, it is possible to separate the coherent and the incoherent contribution to the scattering cross section, being

$$\sum_{l,l'} \overline{b_l^+ b_{l'}} \langle e^{-i\boldsymbol{Q}\cdot\boldsymbol{R}_l} e^{i\boldsymbol{Q}\cdot\boldsymbol{R}_{l'}(t)} \rangle = \sum_{l,l} b_{coh}^2 \langle e^{-i\boldsymbol{Q}\cdot\boldsymbol{R}_l} e^{i\boldsymbol{Q}\cdot\boldsymbol{R}_{l'}(t)} \rangle + \sum_{l} b_{incoh}^2 \langle e^{-i\boldsymbol{Q}\cdot\boldsymbol{R}_l} e^{i\boldsymbol{Q}\cdot\boldsymbol{R}_l(t)} \rangle$$

In this way equation 5.8 becomes

$$\frac{\partial^2\sigma}{\partial\Omega\partial\omega_f} = \underbrace{\frac{k_f}{k_i}[b_{coh}^2 S(\boldsymbol{Q},\omega)]}_{(\frac{\partial^2\sigma}{\partial\Omega\partial\omega_f})_{coh}} + \underbrace{\frac{k_f}{k_i}[b_{incoh}^2 S_s(\boldsymbol{Q},\omega)]}_{(\frac{\partial^2\sigma}{\partial\Omega\partial\omega_f})_{incoh}}. \tag{5.11}$$

The same expression can be written also in terms of the coherent $\sigma_{coh} = 4\pi b_{coh}^2$ and the incoherent $\sigma_{incoh} = 4\pi b_{incoh}^2$ scattering cross section, and yields to

$$\left(\frac{\partial^2\sigma}{\partial\Omega\partial\omega_f}\right)_{coh} = \frac{k_f}{k_i}\frac{\sigma_{coh}}{4\pi} S_{coh}(\boldsymbol{Q},\omega) \tag{5.12}$$

and

$$\left(\frac{\partial^2\sigma}{\partial\Omega\partial\omega_f}\right)_{incoh} = \frac{k_f}{k_i}\frac{\sigma_{incoh}}{4\pi} S_{incoh}(\boldsymbol{Q},\omega) \tag{5.13}$$

In the case of coherent nuclear scattering, the interaction potential couples the neutron to the density of the target system. The coherent scattering cross section gives, indeed, information on the collective motions of the atoms, thus on the wavevector and frequency of the vibrational modes, and permits to map the dispersion relations in the $(\boldsymbol{Q},\omega)$ space. The quantity $S_{coh}(\boldsymbol{Q},\omega)$ corresponds in fact to the dynamic structure factor measured with X-rays. On the other hand, the incoherent dynamic structure factor represents the time and space Fourier transform of the self pair correlation function and, consequently, describes the single particle dynamics. As shown in the next paragraph, the incoherent term yields information on the density of vibrational states of the system.

5.1.2 Scattering from nuclei undergoing harmonic vibrations

Substituting the instantaneous position vector of the l-*th* atom $\boldsymbol{R}_l(t) = \boldsymbol{R}_l^0 + \boldsymbol{u}_l(t)$ in the equation 5.8 of the double-differential neutron cross section, one obtains

[169, 170]:

$$\begin{aligned}\frac{\partial^2\sigma}{\partial\Omega\partial\omega_f} &= \frac{k_f}{k_i}\frac{1}{2\pi\hbar}\int_{-\infty}^{\infty} dt e^{-it\omega}\sum_{ll'}\overline{b_l^+ b_{l'}}\langle e^{-i\boldsymbol{Q}\cdot\boldsymbol{R}_l}e^{i\boldsymbol{Q}\cdot\boldsymbol{R}_{l'}(t)}\rangle \\ &= \frac{k_f}{k_i}\frac{1}{2\pi\hbar}\sum_{ll'}\overline{b_l^+ b_{l'}}e^{-i\boldsymbol{Q}\cdot[\boldsymbol{R}_l^0-\boldsymbol{R}_{l'}^0]}\int_{-\infty}^{\infty} dt e^{-i\omega t}\langle e^{-i\boldsymbol{Q}\cdot\boldsymbol{u}_l}e^{i\boldsymbol{Q}\cdot\boldsymbol{u}_{l'}(t)}\rangle. \quad (5.14)\end{aligned}$$

In the harmonic approximation, using the Bloch identity for the argument of the integral, the average can be moved to the exponent, being

$$\langle e^{-i\boldsymbol{Q}\cdot\boldsymbol{u}_l(0)}e^{i\boldsymbol{Q}\cdot\boldsymbol{u}_{l'}(t)}\rangle = e^{-W_l}e^{-W_{l'}}e^{\langle\boldsymbol{Q}\cdot\boldsymbol{u}_l\ \boldsymbol{Q}\cdot\boldsymbol{u}_{l'}(t)\rangle} = e^{-2W}e^{\langle\boldsymbol{Q}\cdot\boldsymbol{u}_l\ \boldsymbol{Q}\cdot\boldsymbol{u}_{l'}(t)\rangle} \quad (5.15)$$

where the exponent W is the Debye-Waller factor. It is equal to $\frac{1}{2}\langle(\boldsymbol{Q}\cdot\boldsymbol{u}_l)^2\rangle$, provided that one has a Gaussian distribution of atomic displacements. In a cubic symmetry, the average is $\frac{1}{6}Q^2\langle u^2\rangle$ and this result is a fair approximation also for isotropic systems.

As previously reported, the mean square displacement can be used as an indicator of a non harmonic behavior of the material or of the existence of relaxational phenomena. Moreover, it is directly connected with the density of states $g(\omega)$ (see Equation 1.28) being

$$\langle u^2\rangle = \frac{\hbar}{2m}\int_0^{\infty}\frac{g(\omega)}{\omega}[2n(\omega)+1]d\omega. \quad (5.16)$$

where m is the molecular mass and $n(\omega)$ the Bose factor.

Using this formalism the coherent and the incoherent contributions to the differential neutron scattering cross section become:

$$\begin{aligned}\left(\frac{\partial^2\sigma}{\partial\Omega\partial\omega_f}\right)_{coh} &= \frac{k_f}{k_i}\frac{1}{2\pi\hbar}e^{-2W}\sum_{ll'}|\overline{b}|^2 e^{-i\boldsymbol{Q}\cdot[\boldsymbol{R}_l^0-\boldsymbol{R}_{l'}^0]}\int_{-\infty}^{\infty} dt e^{-i\omega t}e^{\langle\boldsymbol{Q}\cdot\boldsymbol{u}_l\ \boldsymbol{Q}\cdot\boldsymbol{u}_{l'}(t)\rangle} \\ \left(\frac{\partial^2\sigma}{\partial\Omega\partial\omega_f}\right)_{incoh} &= \frac{k_f}{k_i}\frac{1}{2\pi\hbar}e^{-2W}\sum_{l}[\overline{|b|^2}-|\overline{b}|^2]\int_{-\infty}^{\infty} dt e^{-i\omega t}e^{\langle\boldsymbol{Q}\cdot\boldsymbol{u}_l\ \boldsymbol{Q}\cdot\boldsymbol{u}_l(t)\rangle} \quad (5.17)\end{aligned}$$

Following the general considerations reported in section 4.1.2, thus through the expansion of relation 5.15 (see equation 4.19) and through the expression of the displacement in the framework of the second quantization (see equation 4.17), the incoherent scattering cross section of one-phonons events becomes [169]:

$$\left(\frac{\partial^2\sigma}{\partial\Omega\partial\omega_f}\right)_{incoh,1ph} = \frac{N\sigma_{inc}}{8\pi M}\frac{k_f}{k_i}Q^2e^{-2W(\boldsymbol{Q})}\frac{g(\omega)}{\omega}[n(\omega)+1]. \quad (5.18)$$

This expression means that it is possible to obtain information on the VDOS of a system by measuring the incoherent contribution to the scattering cross section.

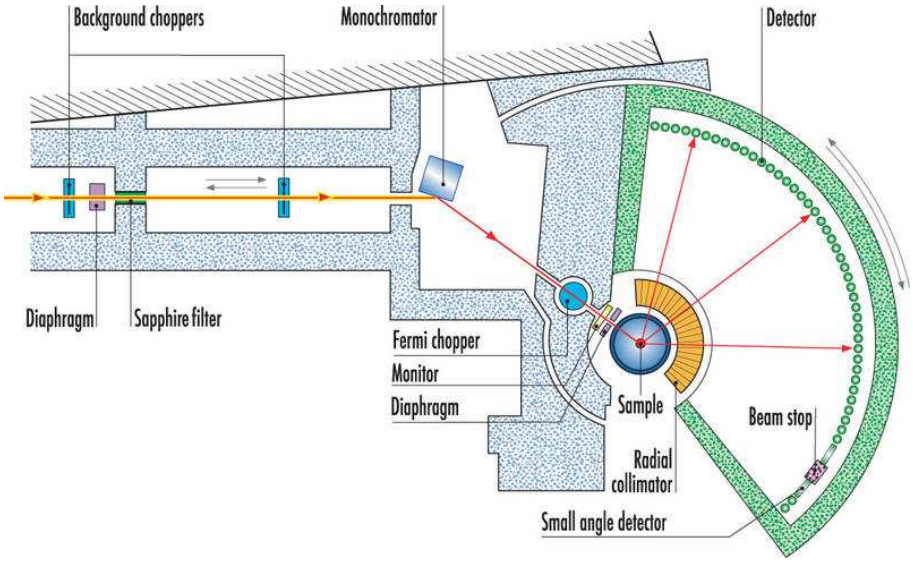

FIGURE 5.1: Scheme of the ToF spectrometer IN4 at the ILL [171].

5.1.3 A ToF spectrometer: IN4 at the ILL

In this section the basic principles of a Time-of-Flight experiment are described, with reference to the neutron thermal spectrometer IN4 at the Institut Laue-Langevin in Grenoble [171].

ToF is a perfect technique for density of states measurements. In fact it allows to explore large sections of the $(\boldsymbol{Q}, \omega)$ space using many detectors, which collect simultaneously neutrons over a wide range of values of the scattered energy.

In general a TOF spectrometer analyses the change of velocity of neutrons after interaction with the sample by measuring their time of arrival at the detectors. The typical structure of a ToF instrument is reported in Figure 5.1.

A series of bursts of monochromatized neutrons is sent to the sample and the energy of the scattered neutrons is then analysed by measuring their time of arrival at the detectors which cover a wide angular range.

In the IN4 ToF spectrometer the incident beam of neutrons (with energies in the 10-100 meV range) passes through two background choppers which act as a low-pass filter, eliminating from the beam most of the fast neutrons and gamma rays that would give background noise in the spectra. The monochromatization of the incoming beam is realized by an assembly of 55 crystal pieces, which also concentrates the divergent incident beam onto a small area at the sample position. The curvature of the monochromator can vary in order to control the time and space focusing conditions at the sample position.

The monochromatized beam is then pulsed by a Fermi chopper, which transmits short neutron pulses (10 ... 50 μs) to the sample. The time-of-flight of neutrons between the chopper and the sample (1 ... 5 ms) can be measured by using precise electronic circuitry. The size of the beam impinging on the sample is of about 2×4 cm^2.

The energy exchange with the sample leads to out coming neutrons with different

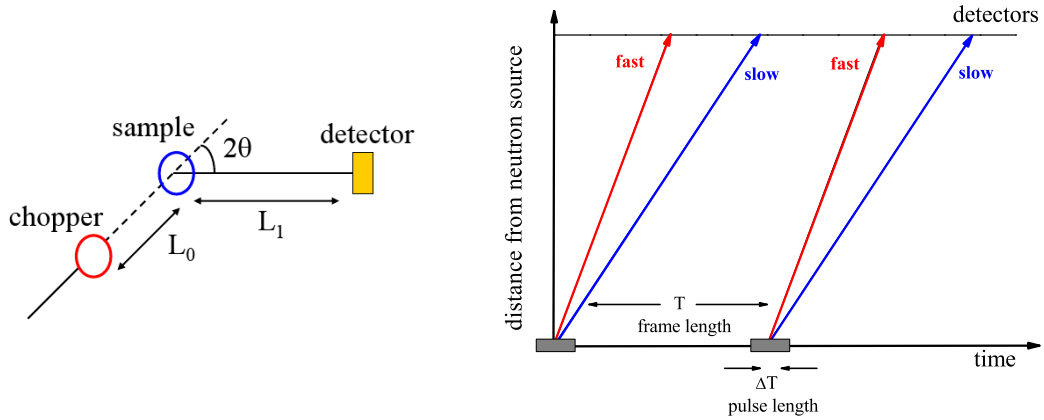

FIGURE 5.2: Scheme of the neutron flight-path in a ToF experiment.

velocities. The flight-path of the scattered neutrons takes place in vacuum to avoid parasitic scattering and a radial collimator around the sample position is used to cut the scattering from the sample environment.
An array of detectors is arranged at a known fixed distance from the sample and covers scattering angles from 13° up to 120°. The scattered neutrons arrive at the detector at a time fixed by their energy. Neutrons that have gained energy from the sample will arrive faster with respect to neutrons which have lost energy (see right panel of Figure 5.2). A scheme of the flight-path of the neutrons is reported in the right panel of Figure 5.2. By considering that a neutron takes a time t_0 to travel from the chopper to the sample at a distance L_0 away, the incident velocity is simply given by

$$v_i = \frac{L_0}{t_0} \tag{5.19}$$

If at the time t the neutron is scattered to a detector, placed at distance L_1 from the sample, then the final neutron speed is

$$v_f = \frac{L_1}{t - t_0} \tag{5.20}$$

where all the quantities are known. The neutron energy and momentum transfer are respectively,

$$E = \frac{m}{2}(v_i^2 - v_f^2) \tag{5.21}$$

and

$$\boldsymbol{Q} = \frac{m}{\hbar}(\boldsymbol{v_i} - \boldsymbol{v_f}) \tag{5.22}$$

This means that from the measured arrival time and the know flight path, the value of the energy exchange can be easily derived and, together with the detector angle, the wave-vector can be readily calculated.

5.2 INS measurements

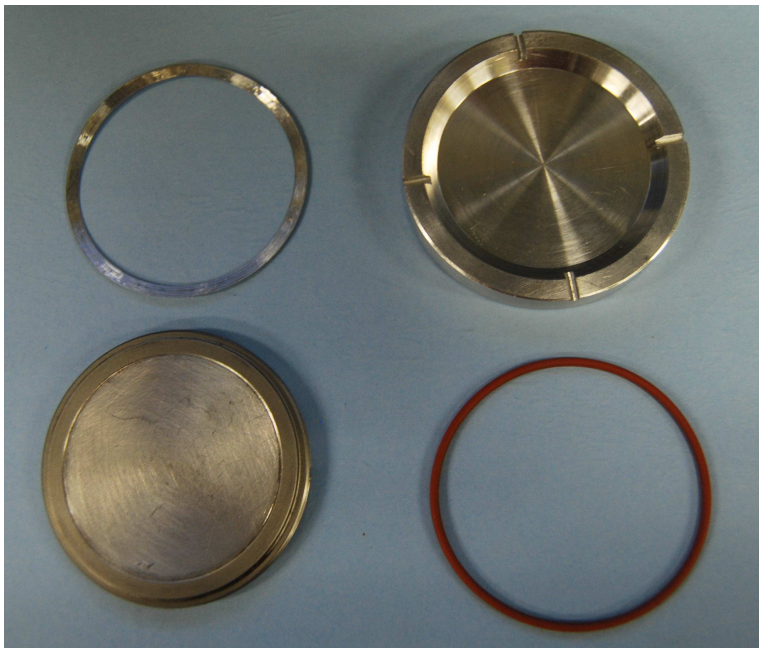

FIGURE 5.3: Photo of the sample holder used for ToF measurements. From top left: Al ring used during the sample preparation, two parts of the Al sample-holder and o-ring used to seal the cell for the measurements.

The neutron spectra were obtained at the thermal time-of-flight spectrometer IN4 at the High Flux Reactor of the Institut Laue-Langevin at Grenoble. The spectra of glassy sorbitol have been collected for T=150, 220 and 246 K. For each measured temperature, the spectra have been collected for several hours in order to increase the statistics. The chosen neutron wavelength of 2.7 Å provides an energy resolution of 0.6 meV FWHM on the elastic line and allows to study the momentum transfer range from 0.5 to 4 $Å^{-1}$.
A disk-shaped sample 200 μm thick and with a diameter of 5 cm was used in order to obtain a transmission of 90% at the used wavelength and to match the neutron beam dimension. Figure 5.3 reports a photo of the sample holder used for the measurements. The cell consists of two Al disks, one of them with an inner hole of the same dimension of the sample. Melt sorbitol was poured into this inner space and the cell was then closed with a thin aluminium disk placed on the external part of the Al disk (left up in Figure 5.3). The presence of this thin spacer is necessary during the sample preparation; it avoids the contact between liquid sorbitol and the internal side of the cell without altering the desired sample thickness. It has allowed us to open the cell and check the quality of the obtained glass. The glass has been obtained by rapidly quenching the cell into liquid nitrogen, paying attention to keep it always in horizontal position. The measurements were done in trasmission geometry, with the sample disk inclined at 45° with respect to the incoming beam in order to maximize the illuminated surface of the sample.
In order to perform a correct data treatment, the empty cell contribution and the

scattering from a vanadium sample, filling the same Al container, were performed as well.

5.2.1 ToF data reduction

Equations 5.12 and 5.13 describe the neutron scattering cross section. An INS experiment allows us to achieve different information depending on the weight of the coherent and incoherent contributions for each element of the material under investigation.
Table 5.1 reports the values for the coherent, incoherent and absorption cross sections of the elements present during the measurements. The huge contribution of hydrogen in the incoherent scattering cross section is well evident. Being hydrogen

Elements	σ_{coh} [barn]	σ_{incoh} [barn]	σ_{abs} [barn]
H	1.7568	80.26	0.3326
C	5.551	0.001	0.0035
O	4.232	0	0
V	0.0184	5.08	5.08
Al	1.495	0.0082	0.231

TABLE 5.1: Neutron scattering cross sections of the elements used during the experiments. The indexes *coh*, *incoh* and *abs* correspond to the coherent, incoherent and the absorption scattering cross sections respectively. Data from [172].

the most abundant element in sorbitol ($C_6H_{14}O_6$), it clearly follows that the double differential cross section of sorbitol is to a very good approximation incoherent and almost totally due to the hydrogen contribution. The coherent contribution to the scattering cross section is in fact just 7% of $\sigma_{tot} = \sigma_{coh} + \sigma_{incoh}$ and can be neglected. This means that the intensity of the spectra will allow us to gain information on the vibrational density of states through equation 5.18.
In reality, the raw data measured in a ToF experiment do not correspond immediately to the $S(\boldsymbol{Q}, \omega)$. They have to be corrected for several factors as the detectors efficiencies, the intensity of the incident flux and the absorption of the sample-holder. Moreover, in order to relate the VDOS of sorbitol to the elastic properties of the system, it is mandatory to obtain the data on an absolute scale.
In general, an inelastic neutron scattering experiment on a ToF spectrometer gives experimental access to the numbers of neutrons, Δn, detected within a time channel of width Δt, by a detector covering a solid angle $\Delta\Omega$. The data capture takes place during an acquisition time T in which the sample is illuminated by an incoming flux Φ_0 of neutrons per second.
In a multi-detector spectrometer, each detector is fixed at an angle $2\theta_k$, between the incoming and the scattered beams. Δt_j is the time width of channel j centered at time t_j (corresponding to energy ω_j). The incoming neutron flux $\Phi(E, t_j)$

$[n^{\circ}_{neut}/cm^2s]$ is measured by a monitor, which is a detector with a very low efficiency. The number of counts at the monitor is given by:

$$N_{m,j} = \eta_m A_m \Phi(E, t_j) T \tag{5.23}$$

where η_m is the monitor efficiency for energy E, A_m is the monitor area and T is the measuring time. During the same experimental time T, the number of scattered neutrons counted by the detector k in the time channel t_j is:

$$N^{s+c}_{k,j} = \eta_k A^s_i T \Phi(E, t_j) I^E_{s+c}(2\theta_k, t_j) \Delta\Omega_k \Delta t_j \tag{5.24}$$

where the suffix $s + c$ refers to the sample and the container, A^s_i is the sample illuminated area and $I^E_{s+c}(\theta_k, \omega_j)$ is the scattered intensity due to the sample and the container. The acquisition time T and the incident flux can be removed from the data by normalizing for the monitor counts, $N_{m,j}$ obtaining:

$$\tilde{N}^{s+c}_{k,j} = \frac{N^{s+c}_{k,j}}{N_{m,j}} = \frac{\eta_k}{\eta_m} \frac{A^s_i}{A_m} I^E_{s+c}(2\theta_k, t_j) \Delta\Omega_k \Delta t_j \tag{5.25}$$

where all the quantities relative to the monitor are known. The same treatment has to be performed for the empty container measurements.
The detector parameters, present in Equation 5.25, can be removed by normalizing $\tilde{N}^{s+c}_{k,j}$ to the data of a predominantly incoherent scatterer with identical scattering geometry as the sample. For this purpose, vanadium is a good candidate, being completely incoherent (see values in table 5.1). The scattering from a vanadium sample is given by:

$$\hat{N}^V_{k,tot} = \sum_j \hat{N}^V_{k,j} = \frac{\eta_k}{\eta_m} \frac{\Delta\Omega_k}{A_m} t A^V_i I^V_{tot} \tag{5.26}$$

where

$$I^V_{tot} = N_V \frac{\sigma^V_i}{4\pi} e^{-2W(Q)}. \tag{5.27}$$

This allows to derive the detector parameters:

$$\frac{\eta_k}{\eta_m} \frac{\Delta\Omega_k}{A_m} = \frac{1}{A^V_i} \frac{\hat{N}^V_{k,tot}}{I^V_{tot}}. \tag{5.28}$$

At this point the contributions to the counted neutrons due to the cell must be removed. In general, the neutrons counted by the detector during an experiment have various origins: they can come from single events in the sample or in the cell before or after the sample and from multiple scattering events in the sample or in the cell or a combination of both. Moreover, there are also environmental neutrons, which are not coming from scattering events but from background noise present even in absence of the sample.
The subtraction of the empty cell has to be performed taking into account the fact that the transmitted beam is attenuated by the sample. The obtained intensity is

consequently given by:

$$I_s = I_{s+c} - T_s I_c \tag{5.29}$$

where T_s is the sample transmission and the index s and c referrer to the sample and empty cell respectively. In the simplest form, T_s can be defined for a rectangular infinite slab as $T_s = e^{-\mu_T L}$ where $\mu_T = N \cdot \sigma_T$ is the absorption coefficient and $\sigma_T = \sigma_{abs} + \sigma_{scatt} = \sigma_{abs} + \sigma_{coh} + \sigma_{incoh}$ is the total cross section. The choice of an Al container allows us to neglect the possible multiple scattering contribution of the cell, being Al almost transparent to neutrons (see values in table 5.1).
A flat additional background, due to the environmental neutrons and to electrical noise has to be removed as well. Several additional standard corrections must then be done in order to take into account the correct detector efficiency and the frame overlap. The latter correction removes the contribution associated to slow neutrons coming from the precedent neutron bunch. In all the previous steps the data are refined as a function of the neutrons time-of-flights. The time to energy conversion can be easily performed through equation 5.21.
All of the above corrections can be done with the program INX at the Institut Laue-Langevin in Grenoble. The multiple scattering corrections can be performed assuming an angle independent multiple scattering contribution. Following the procedure described in Ref. [173], it is possible to deal with the multiple scattering problem in a simple way. A useful approximation consists to assume a Q-independent multiple scattering, which is a good approximation when wide-angle scattering dominates the signal. In practice, it is necessary first to calculate an average spectrum over all detectors (weighted with the sinus of the scattering angle), then fold this average spectrum with itself. The elastic line in one of the spectra has to be converted into a δ-function, in order to avoid a broadening of the elastic line in the folding process. The so-obtained folded spectrum is then subtracted with an appropriate multiple-scattering factor (MSF) from every detector in such a way that the intensity extrapolated to Q equal to zero goes to zero. In fact at low momentum transfer Q, the incoherent inelastic scattering is proportional to Q^2. Then for practical purposes, one can have a good estimate of the inelastic multiple scattering by extrapolating the final intensity to Q equal zero using a Q^2 law. As MSF should be close to $1 - T_s$, this procedure represents also a check of the validity of the subtraction operation.
The multiple scattering contribution has been removed for every set of data, yielding small values of MSF, which agree with the values expected from the transmission. The results have been finally re-binned in Q on a regular grid covering the entire measured (Q,E) region.

The intensity obtained from the whole ToF data reduction corresponds exactly to the one-phonon incoherent cross section 5.18, except for the factor k_f/k_i already removed during the corrections. The resulting data are reported in Figure 5.4 together with those for the vanadium sample. The excess of modes in the vibrational density of state is well evident at about 4.5 meV for all temperatures. To extract information on the vibrational density of states on an absolute scale, the data have been corrected for both the Bose factor and the elastic contribution (and thus the Debye-Waller factor), and then converted into energy (E=$\hbar\omega$). The

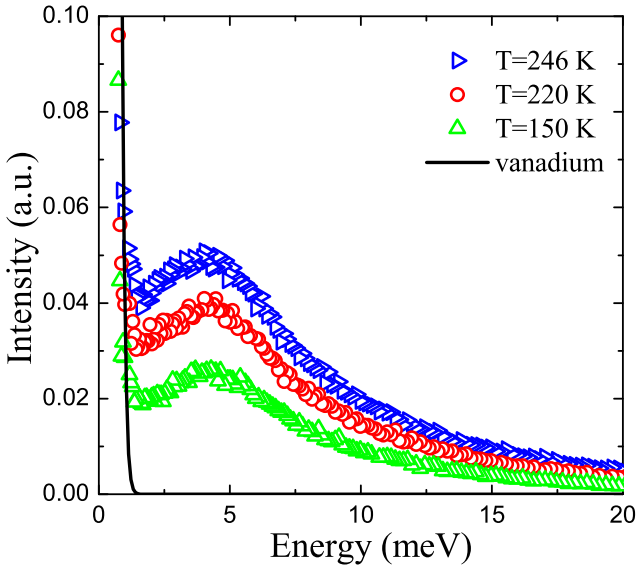

FIGURE 5.4: INS spectra of sorbitol at different temperatures together with the experimental resolution given by the spectrum of a vanadium sample (black line).

measured intensity becomes:

$$Int = \frac{\hbar^2 Q^2}{2M} \frac{g(E)}{E}. \tag{5.30}$$

The boson peak of sorbitol can then be easily obtained by dividing the intensity for the energy itself and the factor $\frac{\hbar^2 Q^2}{2M}$, being M the average molecular mass $M = \frac{1}{N}\sum_i m_i$ [174]. In the limit of low frequencies, thus in the range of interest here, it is possible to neglect all the intra molecular modes of the system, which indeed are located at much higher frequencies. In this way the system dynamics can be related to the dynamics of a unique average molecule, where the double-differential cross section is dominated by the hydrogen atoms.

5.3 Boson peak and elastic properties

The temperature dependence of the reduced vibrational density of states is reported in the upper panel of Figure 5.5 together with the expected low-energy Debye limits

$$g_D(E)/E^2 = 3/E_D^3, \tag{5.31}$$

where

$$E_D^3 = \frac{18\pi^2\rho}{M}\left(\frac{1}{v_{LA}^3} + \frac{2}{v_{TA}^3}\right)^{-1}. \tag{5.32}$$

In the previous expression the transverse and longitudinal sound velocity values

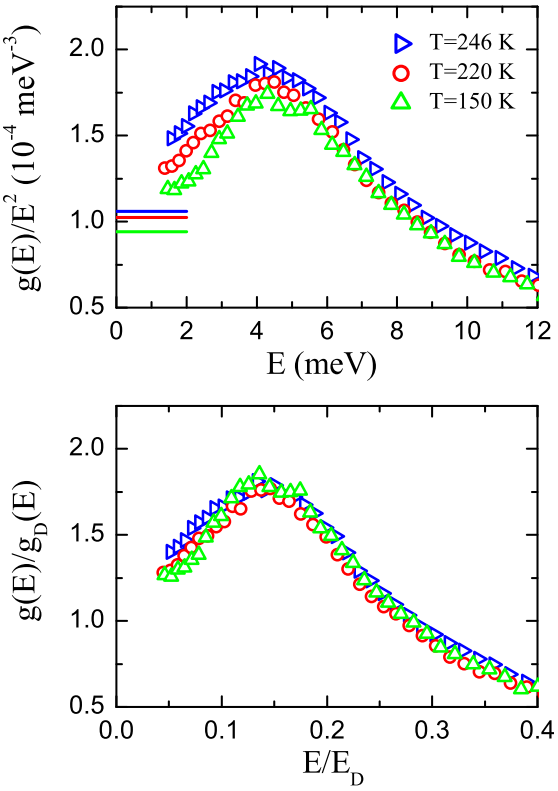

FIGURE 5.5: Upper panel: reduced VDOS of glassy sorbitol for different temperatures, together with the indication of the corresponding Debye level (horizontal lines). Lower panel: same data as above after rescaling in Debye units.

T $[K]$	v_{LA} $[m/s]$	v_{TA} $[m/s]$	v_D $[m/s]$	E_D $[meV]$
246	4081 ± 24	2107 ± 17	2359 ± 26	30.5 ± 0.3
220	4120 ± 25	2131 ± 17	2386 ± 26	30.8 ± 0.3
150	4213 ± 25	2192 ± 18	2453 ± 26	31.7 ± 0.3

TABLE 5.2: Values of the longitudinal, transverse and Debye sound velocity of sorbitol, together with the Debye energy E_D values estimated using relation 5.32.

are taken from the low frequency BLS measurements. In addition, the Cauchy-like relation 3.24 has been used to extrapolate the data for the transverse velocity outside the range where they have been measured. Table 5.2 reports all the values used to estimate the Debye level.

On decreasing the temperature in the glassy state, the intensity of the boson peak slightly decreases as well. The position of the maximum does not display any strong change in the explored temperature range. As reported in section 2.3 this behavior is generally observed in glasses. To check whether there exists or not a relation between the VDOS and the elastic properties of sorbitol, the data have been replotted in Debye units, thus dividing them for the continuum limit 5.31. The corresponding data are reported in the lower panel of Figure 5.5. The result is clear: by re-plotting the reduced VDOS in Debye units, all the curves rescale on a single one in the peak region. This means that the observed temperature dependence can be accounted for by the transformation of the elastic medium, similar to what has been previously observed in some experiments and numerical simulations [99, 104] (see section 2.3).
Though small differences remain in the low energy range of the spectra, the overall validity of the scaling procedure suggests a strong relation between boson peak and elastic properties. This phenomenology is very similar to the one observed for the high frequency sound velocity measured with IXS and reported in Figure 4.21: the temperature dependence of the elastic properties dictates that of both the boson peak and of the acoustic excitations in the corresponding energy range, thus making even stronger the connection between acoustic excitations in the mesoscopic range and the boson peak in glasses.
In section 4.4 it has been shown as the temperature dependence of the high-frequency acoustic dispersion curves of glassy sorbitol can be described to a good approximation within a quasi-harmonic approach, whilst the corresponding acoustic damping ($\hbar\Gamma$) is definitively non-dynamic in origin. This observation then leads to a natural frame for justifying and understanding the observed scaling of the boson peak with the parameters of the elastic medium. Glasses with anharmonic and/or relaxational contributions larger than in sorbitol and for which the quasi-harmonic approximation does not hold might however show a more complex phenomenology.

5.3.1 A model for the boson peak

In the previous chapter it has been shown that both the acoustic dispersion and damping of the high frequency modes display peculiar anomalies which appear in the same energy range of the boson peak and which seem to be universal features of the glasses dynamics [96]. In the case of glycerol the simultaneous presence of a negative dispersion of the sound velocity and a Rayleigh scattering regime for the acoustic attenuation allows for a quantitative description of the shape of the boson peak.
In fact, the vibrational density of states can be estimated from the acoustic dispersion curve. In a simple crystal-like approach, thus neglecting the finite damping of the modes, the reduced VDOS can be expressed as:

$$\frac{g(E)}{E^2} = \frac{1}{Q_D^3}\left[\left(\frac{Q^2}{E^2}\frac{\partial Q}{\partial E}\right)_L + 2\left(\frac{Q^2}{E^2}\frac{\partial Q}{\partial E}\right)_T\right] \tag{5.33}$$

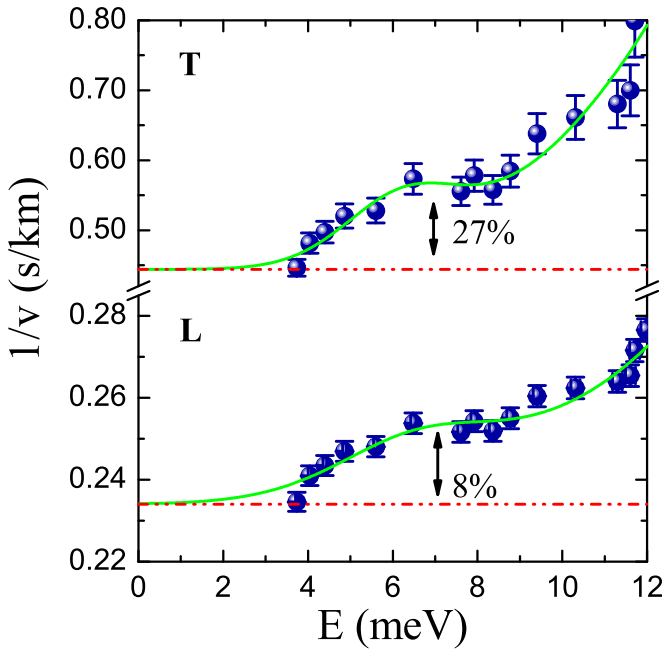

FIGURE 5.6: Inverse of the longitudinal (lower data) and transverse (upper data) sound velocities of sorbitol at T=80 K. The dashed-dotted line corresponds to the macroscopic sound speed measured with BLS, while the green line is the best fit line shape according to equation 5.34. The transverse values have been obtained assuming a constant bulk modulus as explained in the text.

where the index L and T correspond to the longitudinal and transverse branch respectively and Q_D is the Debye wave-vector. Assuming valid a plane-wave description of the modes, the previous relation means that the boson peak can be described in principle starting from the derivative of the inverse of the acoustic sound velocity (thus $\frac{\partial Q/E}{\partial E}$). In order to perform such operation the inverse of the sound velocity has been fitted using the empirical function

$$\frac{Q}{E} = \frac{A}{w\sqrt{\pi/2}} \exp\left[\frac{-2(E-E^*)^2}{w^2}\right] + \frac{q}{\pi E} \arcsin\left(\frac{\pi E}{q v_{(T,L)_{BLS}}}\right) \tag{5.34}$$

where $v_{(T,L)_{BLS}}$ is the continuum limit value, while A, w, E^* and q are simply fitting parameters.
The transverse branch has been estimated from the longitudinal one assuming that the two curves exhibit the same anomalies at the same energy. In particular, a constant bulk velocity has been assumed in the explored energy range, being

$$v_T(E) = \sqrt{\frac{3}{4}(v_L^2(E) - v_B^2(E=0))} \tag{5.35}$$

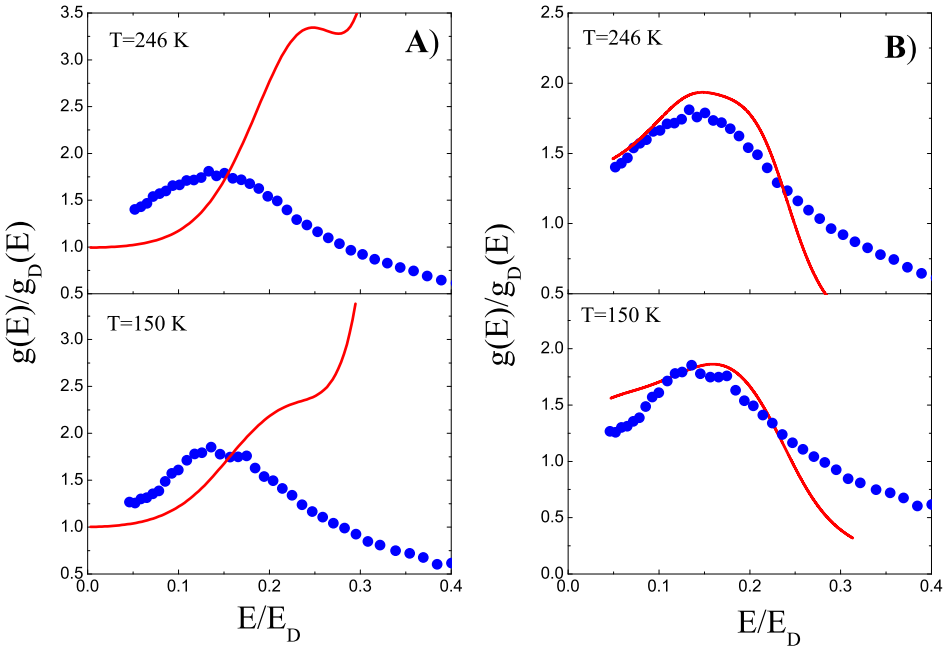

FIGURE 5.7: A): reduced VDOS in Debye units (blue circles) together with the prediction of the crystal-like model equation 5.33 (red lines) using the IXS data at T=246 K and at T=150 K. B): same data as A) (blue circles) together with the prediction of the model equation 5.36 (red lines), which takes into account the broadening of the high frequency excitations as well.

where v_B is the bulk velocity. This assumption has been verified in the case of a Lennard Jones glass [98]. The bulk velocity can be obtained inverting relation 5.35 and using the longitudinal sound speed measured with BLS and the transverse one calculated through the Cauchy-like relation 3.24.

Figure 5.6 shows the inverse of the sound velocity as a function of the excitations energy for the transverse and longitudinal acoustic-like branches for T=80 K. The data are reported together with the best fitting lineshape obtained from equation 5.34 (green line) and the macroscopic limit (red dashed-dotted line). The two velocities display the same behavior. However in the case of the transverse branch, the mode softening is more than three times larger than in the longitudinal one. This result is not surprising, if one considers that the boson peak has predominantly transverse character [73, 104].

The validity of the proposed model was checked by using the IXS data measured at T=246 K and T=150 K. In Figure 5.7 A) the INS reduced density of states is reported as a function of the rescaled energy E/E_D together with the prediction of the model equation 5.33. It is important here noting that this simple crystal-like approach is able to predict the existence of a peak in the VDOS. This means that the excess of modes in the VDOS over the Debye continuum limit approximation originates from deformations of the dispersion curve at the nanometer length scale. However, the model fails on predicting the position of the boson peak maximum,

which is clearly overestimated.
Following always Ref. [96], the model can be improved considering also the broadening of the acoustic-like excitations, which has a finite value in glasses. In this case, the reduced VDOS can be described through the relation [67]

$$\frac{g(\omega)}{\omega^2} = \frac{1}{Q_D^3}\int_0^{Q_D} dQ \frac{M}{k_B T}\left[S_L^I(Q,\omega) + 2S_T^I(Q,\omega)\right] \tag{5.36}$$

where $S_{L,T}^I(Q,\omega)$ are the inelastic part of the dynamic structure factor for the longitudinal and transverse branch respectively, and M is the molecular mass. The DHO model entering in relation 4.28 has been employed to estimate the dynamic structure factors. $S_L^I(Q,\omega)$ has been calculated directly through the fitting parameters obtained from the analysis of the IXS spectra. For the transverse excitations, instead, the excitations energy has been taken from relation 5.35, while the width has been estimated assuming that [165]:

$$\Gamma_L(E) = \Gamma_T(E). \tag{5.37}$$

The result of the equation model 5.36 are reported in Figure 5.7 B) for T=246 K and T=150 K, respectively. We find the same result as for the glycerol glass: the broadening of the Brillouin peaks shifts the results of the crystal-like model to lower energies and allows for a quantitative description of the boson peak. Differently from the case of glycerol, also the intensity of the boson peak is strongly affected by the damping of the high frequency modes present in the corresponding energy range.

5.3.2 Comparison with a model based on random local elastic moduli

The observed behavior of the high frequency sound velocity and attenuation of sorbitol can be compared to the predictions of a model for the vibrational excitations in a disordered elastic medium proposed by Schirmacher and coworkers [68]. As described in section 2.1, this model is based on the assumption that the disorder induces random spatial fluctuations, $\Delta G(\boldsymbol{r})$, of the shear modulus $G(\boldsymbol{r}) = G_0\left[1 + \Delta G(\boldsymbol{r})\right]$ that are Gaussian distributed around an average value with a variance proportional to the degree of disorder γ_G. The model is developed in a mean-field approach using the self-consistent Born approximation for the self-energy $\Sigma(\omega) = \Sigma'(\omega) + i\Sigma''(\omega)$ [67, 68]. The VDOS can then be written as

$$g(\omega) \propto \sum_{|k|<k_D} Im\left\{G_L(k,\omega) + 2G_T(k,\omega)\right\} \tag{5.38}$$

where $G_L(k,\omega)$ and $G_T(k,\omega)$ are the Green's functions related to the longitudinal and transverse susceptibilities through the relations

$$\chi_L(k,\omega) = k^2 G_L(k,\omega) = k^2\left\{-\omega^2 + k^2\left[c_{L,0}^2 - 2\Sigma(\omega)\right]\right\}^{-1} \tag{5.39}$$

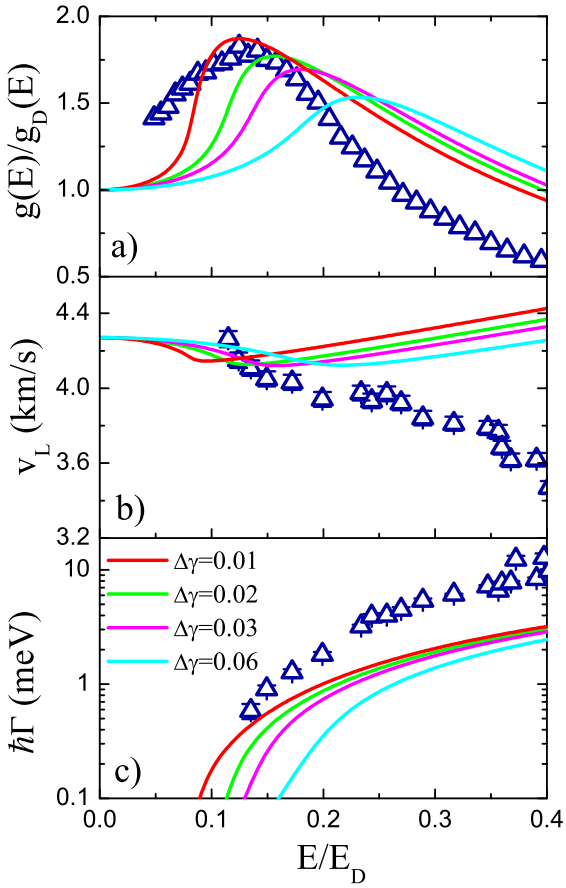

FIGURE 5.8: Comparison among the boson peak in Debye units (a), the high-frequency sound velocity (b) and attenuation (c) at T=80 K, and the predictions of the model proposed by Schirmacher and coworkers [68] for different values of the parameter $\Delta\gamma$. All the quantities are reported as a function of the rescaled energy E/E_D.

and

$$\chi_T(k,\omega) = k^2 G_T(k,\omega) = k^2 \left\{-\omega^2 + k^2 \left[c_{T,0}^2 - \Sigma(\omega)\right]\right\}^{-1}. \tag{5.40}$$

In the previous expression $c_{L,0}$ and $c_{T,0}$ are the sound velocities of the systems without disorder.
The real part of the self energy is related to the sound velocity through the relations

$$c_L^2(\omega) = c_{L,0}^2 - 2\Sigma'(\omega) \tag{5.41}$$

and

$$c_T^2(\omega) = c_{T,0}^2 - \Sigma'(\omega) \tag{5.42}$$

while the imaginary part gives information on the sound damping, being

$$\Gamma(\omega) \approx 2k^2 \frac{\Sigma''(\omega)}{\omega} \tag{5.43}$$

Figure 5.8 shows the boson peak, the sound velocity and the sound attenuation of sorbitol together with the behavior predicted by the model equations 5.38, 5.41 and 5.43 respectively, for different values of the parameter $\Delta\gamma = \gamma_G - \gamma_G^C$. This parameter rules the results of the model and represents the distance between the degree of disorder and the critical value γ_G^C where the system becomes unstable.
For $\Delta\gamma = 0.01$ the model is clearly able to quantitatively account for the excess in the vibrational density of state (Figure 5.8 a)). Both the boson peak maximum and its intensity are in fact well reproduced. Different is the situation for the sound velocity and damping: although the model predicts the existence of both a softening of the acoustic-like modes and a Rayleigh attenuation regime, these features are located at too low energies with respect to the experimental data. On increasing the parameter $\Delta\gamma$ the elastic anomalies shift toward higher energies and a value of $\Delta\gamma = 0.06$ leads to a better agreement with the data, even if the width is definitely underestimated. In any case, the model fails to reproduce all the data sets simultaneously.
The discrepancy between the model and the data concerning the elastic anomalies is probably due to the fact that in the model the Rayleigh regime for the attenuation always takes place below the onset of the excess in the VDOS while the experiments show that this regime dominates the $\hbar\Gamma$ dependence in the boson peak energy range up to energies close to the Ioffe-Regel one and thus, higher than that of the boson peak (see Figures 4.16 and 4.17).
The theory of Schirmacher and coworkers also predicts the existence of a quantitative relation between the excess over the Debye density of states and the width of the Brillouin line, given by:

$$E_D \Delta g(E) = E_D \left[g(E) - g_D(E) \right] = f(c_L, c_T) \frac{\Gamma(E)}{E_D} \tag{5.44}$$

where $f(c_L, c_T) = \frac{2}{\pi}(c_D/c_L)^2 \left[1 + (c_L/c_T)^4\right]$ and c_L, c_T and c_D are the longitudinal, transverse and Debye sound velocity respectively. In Figure 5.9 the two sides of equation 5.44 are reported. The dashed-dotted-dotted (purple) and the solid (green) lines are just two guides for eyes representing a $\sim E^2$ and a $\sim E^4$ behavior respectively.
In Ref. [68] the authors found that the sound attenuation $\hbar\Gamma(E)$ displays a quadratic dependence on the excitations energy in the whole range covered by the boson peak. In the case of sorbitol this is not the case, being the $\sim E^2$ behavior located at higher energies (see Figure 5.9). Moreover, differently from what found in Ref. [68], relation 5.44 is not fulfilled for sorbitol.
Albeit the model is partially able to reproduce the shape of boson peak, the above considerations show the limits of this theoretical approach. The elastic anomalies found in the high frequency dispersion curve of sorbitol clearly indicate a strong connection between the acoustic properties and the BP and they represent the starting point for new improvements of the model. In fact the previous comparison does not allow us to discriminate between the different models for the BP, being not able to give us information on the nature itself of the BP. In particular, the elastic anomalies found here could either be due to effects of disorder on the

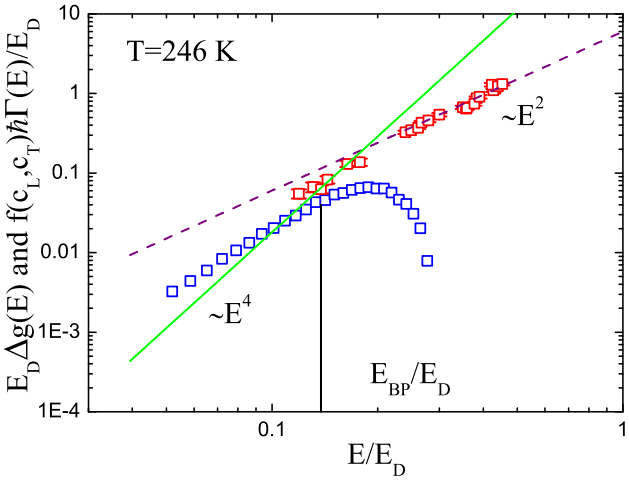

FIGURE 5.9: Excess DOS measured with neutron spectroscopy (blue squares) together with the quantity $f(c_L, c_T)\Gamma(E)/E_D$ obtained from IXS and BLS data (red circles). The two lines are just guides for the eye representing a $\sim E^2$ (purple dashed line) and $\sim E^4$ (green line) behavior, respectively.

elastic constants or either they could be the consequence of the presence of additional modes in the same energy range. This last idea is at the basis of the soft potential model (SPM) described in section 2.1. In the case of sorbitol we could not check the validity of this model due to the lack of information on the thermal conductivity of the system. Anyway, the SPM seems also to well reproduce the experimental data in some systems [100, 175]. It is then clear that a good knowledge of the acoustic modes is fundamental to test the different theoretical approaches and that further experimental investigation in this direction is of course extremely important.

Résumé du chapitre 6

Dans ce chapitre nous présentons la dynamique vibrationnelle à haute fréquence d'un verre polymère de soufre. Les mesures IXS ont été réalisées au cours de mon mémoire de maîtrise en 2006. Ces résultats expérimentaux sont brièvement résumées au début du présent chapitre. Pour comprendre le comportement des excitations collectives dans le gamme des énergies de meV, les données sont ici mises en relation avec les résultats à basse fréquence rapportés dans le troisième chapitre et avec les informations sur la VDOS et sur la fragilité du matériel.

Comme nous démontrerons la dynamique à haute fréquence du soufre ne présente aucun signe des anomalies élastiques trouvées dans le cas du sorbitol ou du glycérol. La courbe de dispersion du soufre semble suivre le comportement typique sinusoïdal qui a été observé dans plusieurs autres systèmes alors que l'atténuation démontre une dépendance quadratique de l'énergie des excitations. Nous constatons un comportement singulier de la vitesse du son à haute fréquence par rapport à la limite macroscopique explorée avec BLS qui peut être expliqué à travers une contribution anharmonique présente dans la région à basse fréquence.

A première vue, la dynamique du soufre pourrait être considérée en désaccord complet avec les résultats discutés dans les chapitres précédents. En réalité, ce n'est pas le cas. L'existence d'anomalies élastiques à haute fréquence est strictement liée au BP qui, dans le cas du soufre, est situé à environ 1.2 meV. Cette valeur est trop faible par rapport à la valeur minimum d'énergie accessible avec IXS. En d'autres termes, il n'est pas possible actuellement d'accéder à des excitations collectives du soufre dans la région des énergies du BP. Ce résultat permet une réconciliation avec le scenario décrit

précédemment qui semble être universel dans les verres, comme expliqué dans le chapitre suivant.

Chapter 6

High frequency dynamics of sulfur

In this Chapter the high frequency vibrational dynamics of polymeric glassy sulfur is presented. The IXS measurements have been performed during my master thesis in 2006. Those experimental results are briefly summarized at the beginning of this Chapter. In order to understand the behavior of the collective excitations in the meV energy range, the data are here discussed in relation to the low frequency results reported in section 3.5 and some information on the VDOS and on the fragility of the material. In fact, as already stressed, a detailed analysis on the vibrational properties of glasses requires a combined experimental study with neutron, X-ray and light scattering probes.
As it will be shown, the high frequency dynamics of sulfur does not display any signature of the elastic anomalies found in the case of sorbitol or glycerol [96]. The dispersion curve of sulfur seems to follow the typical sine-like behavior observed in several other systems [57] while the modes attenuation exhibits an almost quadratic dependence on the excitation energy. Some peculiarities are found in the high frequency sound velocity values with respect to the macroscopic limit explored with BLS that can be explained in terms of an anharmonic contribution present in the low frequency range.
At first sight, the dynamics of sulfur could be considered in complete disagreement with the whole scenario discussed in the previous chapters. Actually this is not the case. The existence of elastic anomalies at high frequency is strictly related to the boson peak, which, in the case of sulfur, is located at about ~ 1.2 meV. This value is too low with respect to the minimum accessible energy value that can be probed with IXS. In other words, it is not currently possible to access to the collective excitations of sulfur in the energy range of the boson peak. This result allows for a reconciliation with the previously described scenario, which seems to be universal in glasses, as explained in the next Chapter.

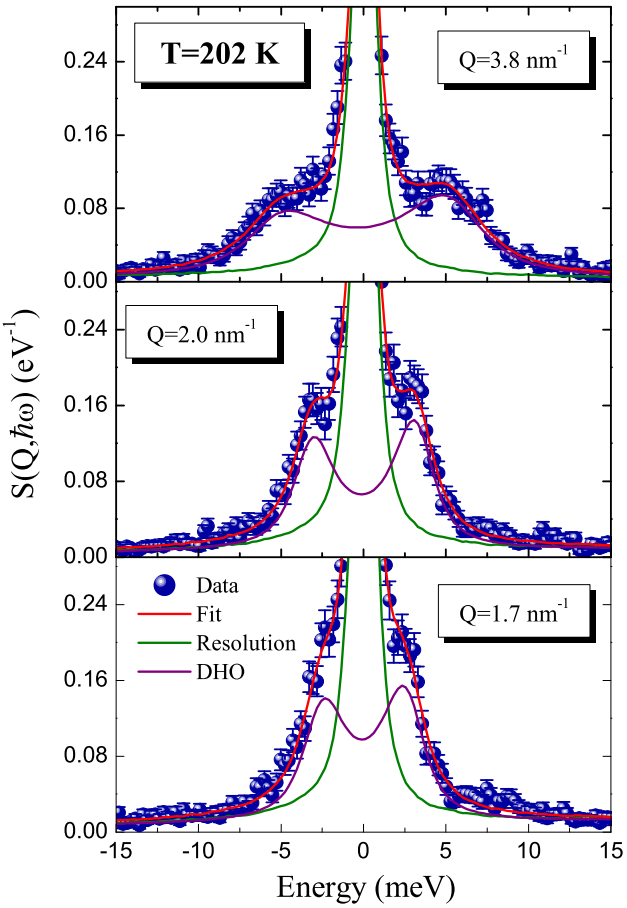

FIGURE 6.1: Selected IXS spectra of glassy sulfur at T=202 K for different exchanged wave-vectors Q together with the best fitting line shape (red line). The elastic (green line) and the inelastic (purple line) components of the DHO model are reported after convolution to the instrumental resolution. The intensity is reported on an absolute scale as explained in the text.

6.1 IXS measurements

Inelastic X-ray scattering measurements were carried out at the beamline ID16 of the European Synchrotron Radiation Facility in Grenoble [155]. As for sorbitol, an incident beam with an energy of 23.724 keV and the silicon (12,12,12) reflection order for the main backscattering monochromator was employed. The energy resolution was of $\sim$ 1.3 meV FWHM. During the experiment the beamline set up was configured in order to measure five different Q values simultaneously.
The high frequency dynamics has been investigated for T=101, 148 and 202 K. At each of the first two temperatures, the dynamic structure factor, $S(Q, \hbar\omega)$, has been measured only at five different wave-vectors, corresponding to the five different analysers, placed at a fixed distance of $\sim$ 3.3 nm^{-1} one from the other.

At T=202 K, the IXS spectra have been collected in the exchanged momentum, Q, range between 1.5 and 17 nm^{-1}, thus up to values close to the one of the first maximum in the static structure factor ($\sim$ 18 nm^{-1}). Depending on the investigated temperature, each point of the spectra was counted between 180 and 360 s in order to reach a good signal to noise ratio.

The glass of sulfur has been obtained by rapidly quenching in liquid nitrogen poly-

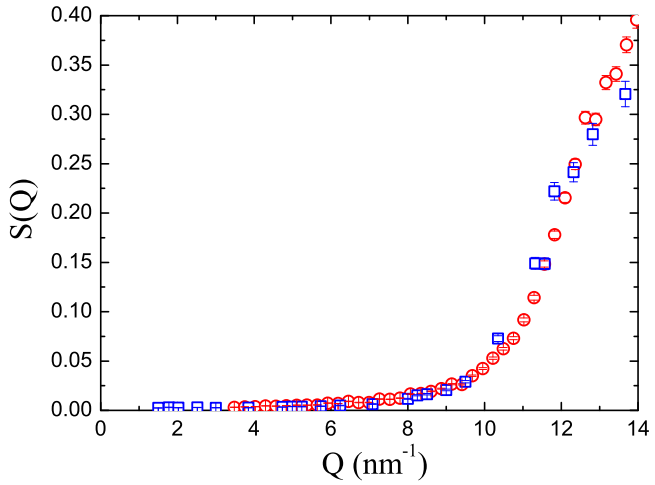

FIGURE 6.2: Comparison between the measured $S(Q)$ corrected for the atomic form factor (red circles) and the one estimated using the zero-th moment rule of the $S(Q, \hbar\omega)$ (blue squares).

meric liquid sulfur heated up to 473 K. A disk-shape sample 1.3 mm thick and with a diameter of 5 mm was used in order to maximize the IXS signal. Due to the low thermal conductivity of sulfur, a second identical sample has been prepared with a thermocouple placed inside it in order to allow for a correct measurements of the sample temperature. In order to avoid any crystallization process, the two samples have been rapidly inserted in a AL125 cryostat kept at 80 K and mounted on the same Cu sample holder.

Figure 6.1 reports a selection of the dynamic structure factor of glassy sulfur measured at $T = 202$ K for different exchanged wave-vectors Q. The Brillouin doublet is well defined close to the elastic line. The data are reported together with the best fit line shape obtained from the the convolution of equation 4.28 with the instrumental resolution. The normalization of the IXS data was performed following the procedure described in section 4.2.2 exploiting the second moment rule. The static structure factor has been calculated as well and is reported in Figure 6.2 together with the one directly measured during the experiment and corrected for the atomic form factor. The latter has been properly shifted in intensity in order to match the estimated one. The good agreement at low Q is a confirmation of the whole normalization procedure.

6.2 Acoustic properties of sulfur

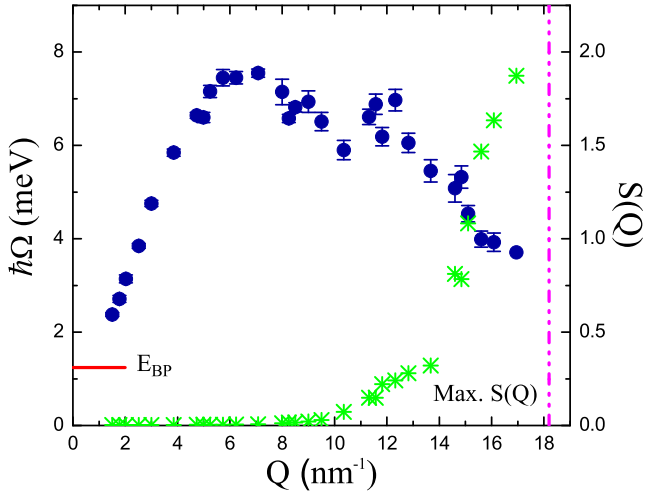

FIGURE 6.3: Dispersion relation of the longitudinal acoustic-like excitations of sulfur measured at T= 202 K. The data (blue dots) are reported as a function of the momentum transfer Q together with the static structure factor $S(Q)$ (green crosses) obtained from the integration of the spectra. The red line indicates the energy of the boson peak maximum while the purple dashed line corresponds to the first sharp diffraction peak of the $S(Q)$.

Figure 6.3 reports the dispersion curve of sulfur for T=202 K as a function of the exchanged momentum Q. The corresponding estimated static structure factor is reported as well (green dots). The dispersion curve displays a linear Q dependence for wave vectors values up to $\sim$ 5.7 nm^{-1}. At higher Q, the curve bends and reaches a minimum in correspondence of the maximum of the static structure factor (dashed line in Figure 6.3). The red line in the Figure represents the energy of the maximum of the boson peak obtained from the Raman measurements [176] reported in Figure 6.4. In general the Raman light scattering intensity can be written as

$$I(\omega) = g(\omega)C(\omega)\frac{[n(\omega)+1]}{\omega} \tag{6.1}$$

where $C(\omega)$ is the photon-vibration coupling coefficient, $[n(\omega)+1]$ is the Bose occupation factor and $g(\omega)$ is the vibrational density of states. In Figure 6.4 the reduced Raman intensity $I_R = C(\omega)g(\omega)/\omega^2$ is reported. A maximum corresponding to the boson peak is well evident at about $\sim$ 15 cm^{-1} (corresponding to 1.9 meV). This value does not coincide with the boson peak position, being I_R related to the boson peak of a glass through the factor $C(\omega)$. Experimentally it has been found that $E_{BP,raman} = 1.5 \cdot E_{BP,neutrons}$ [176]. Through this relation we obtain $E_{BP} = 1.2$ meV for glassy sulfur. This value is typical of fragile systems, such as polymeric glasses, and is out of the energy window accessible to IXS. In fact, as it is shown in Figure 6.3 the boson peak is located at a so low value that it is not

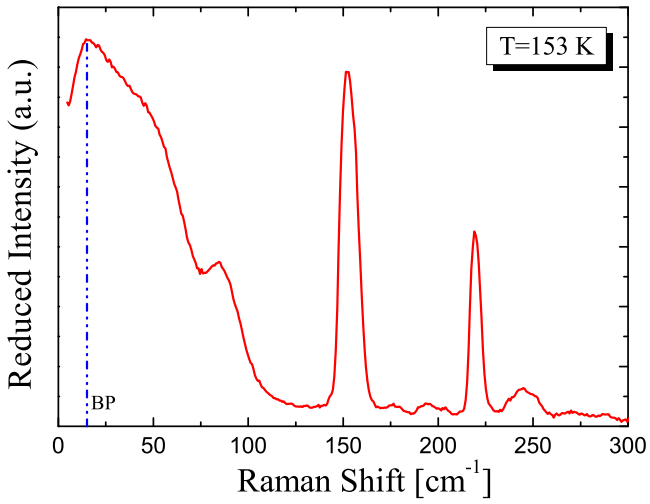

FIGURE 6.4: Reduced Raman intensity $I_R = C(\omega)g(\omega)/\omega^2$ of glassy sulfur at T=153 K [176].

possible, from the experimental point of view, to measure the acoustic-like modes present in the same energy range. This means that an IXS experiment on glassy sulfur allows only the study of the high frequency dynamics well above the excess in the reduced VDOS.

The upper panel of Figure 6.5 shows the apparent sound velocity of sulfur at the investigated temperatures. The macroscopic limits measured with BLS (see section 3.5) are reported as well (horizontal lines). A different scenario is here observed: there is no evidence of the negative dispersion found in glycerol [96] and sorbitol (see Figure 4.15). The sound velocity of sulfur is almost constant up to $Q \sim 4$ nm^{-1} and then smoothly decreases on increasing the momentum transfer in the scattering process. As shown in the previous Chapter, the softening of the modes observed in sorbitol is strictly related to the boson peak, and thus we should expect it in an energy range lower than the one here investigated.

In reality a sort of anomaly in the case of sulfur is also here observed. The high frequency sound velocity is in fact $\sim 4\%$ higher than the corresponding macroscopic limit (see inset in the upper panel of Figure 6.5). As explained in the next paragraph, this difference is due to the presence of an anharmonic contribution at low frequency which affects the values measured with BLS.

The lower panel of Figure 6.5 reports the width of the inelastic features as a function of the exchanged wave vector for different temperatures. As expected from the previous discussions, the damping is temperature independent and follows the typical $\sim Q^2$ behavior usually observed at energies higher than the boson peak one in other glasses [57, 89]. On approaching the FSDP of the $S(Q)$ (see Figure 6.3), the excitations become more and more ill-defined and $\hbar\Gamma$ deviates also from the observed quadratic dependence.

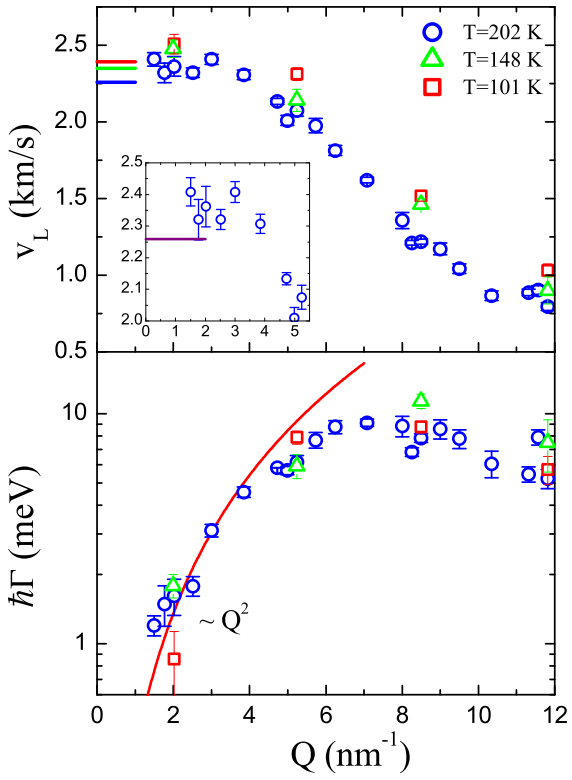

FIGURE 6.5: Inelastic x-ray scattering results for the Q-dependence of the sound velocity (upper panel) and broadening $\hbar\Gamma$ (lower panel) of the longitudinal acoustic-like excitations of glassy sulfur at the indicated temperatures. In the upper panel the horizontal lines mark the macroscopic limits measured with BLS, while the inset shows an enlargement of the low Q behavior of the data taken at T=202 K. In the lower panel the red line represents the quadratic best fit lineshape of the low Q behavior of the data taken at T=202 K.

6.2.1 The quasi harmonic nature of the high frequency excitations

At low frequencies, the vibrational dynamics of glasses is affected by anharmonicity. In section 4.4.1 we have seen that the BLS results can be described in terms of the simultaneous presence of a purely anharmonic and a quasiharmonic contribution. In the case of sorbitol, the anharmonicity is weak and influences the BLS sound velocity only very slightly. In that case, in fact, the low frequency sound velocity basically corresponds to the purely elastic limit measured at the lowest investigated Q value with IXS. The presence of a more "important" anharmonic term, would instead lead to a strong dispersion of the sound speed with frequency (or wavenumber). This scenario explains the observed difference in glassy sulfur

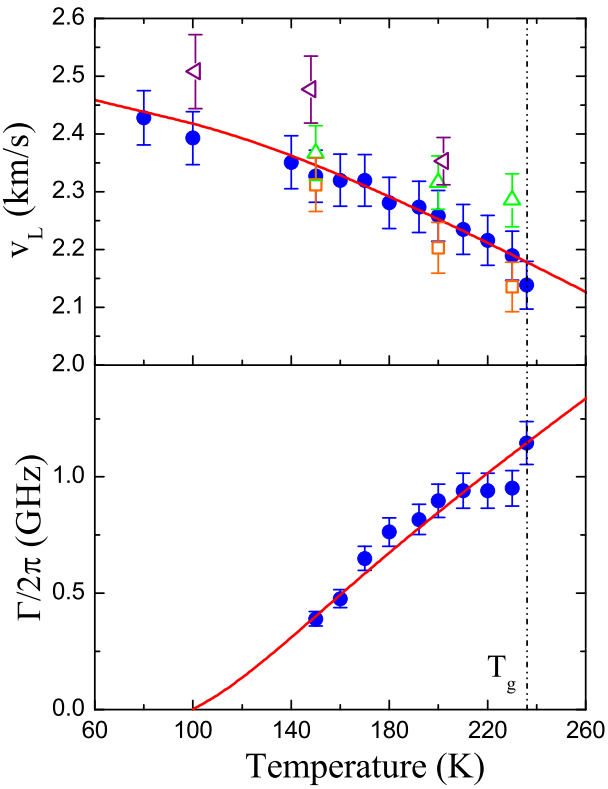

FIGURE 6.6: Temperature dependence of the sound velocity and FWHM of glassy sulfur measured with BLS (see section 3.5). The red full lines are the best fitting curves using the model of equation 6.2. In the top panel the fully relaxed $v_{0\infty}$(orange empty squares) and unrelaxed v_∞ (empty green triangles) sound velocity values are reported for some representative temperatures, in order to emphasize the effect of anharmonicity. The high frequency IXS data of v_L (purple triangles) are plotted as well.

between the high frequency v_L measured with IXS and the low frequency one obtained from BLS measurements (see inset in the top panel of Figure 6.5).
In order to investigate the role played by anharmonicity in glassy sulfur, the low frequency data have been analyzed with the model equation 4.39 proposed in section 4.4.1. Due to the lack of information on the temperature dependence of the density of glassy sulfur, the quasi-harmonic hypothesis used in the case of sorbitol cannot be exploited or tested, and the model has a purely empirical justification. The model reads:

$$v_L^2 = v_\infty^2 - \frac{\Delta^2}{1+\omega^2\tau^2} \qquad \text{and} \qquad \Gamma = \frac{\Delta^2}{v_\infty^2}\frac{\omega^2\tau}{1+\omega^2\tau^2} \tag{6.2}$$

In these expressions, the quasiharmonic term is contained in the description of the fully unrelaxed sound velocity $v_\infty^2 = (v_\infty^0)^2(1+aT)^2$, while the anharmonic process

is described by an average relaxation time $\tau = \tau_0 e^{\frac{E_n}{T}}$, and a strength given by $\Delta^2 = B(T - T_0)$ with $T_0 = 100$ K. The choice of this expression for Δ^2 is due to the limited information on the Brillouin linewidth of the longitudinal modes. In fact, as shown in Figure 6.6 Γ has been measured only at temperatures higher than 150 K. The lack of data for Γ at lower temperatures does not allow us to formulate a more accurate model for the anharmonic contribution. In this situation, a simple approximation to describe Δ^2 is of course given by a linear temperature dependence with the condition $\Delta^2(T_0) = 0$ for $T_0 = 100$ K in order to match the measured data.
The best fitting curves obtained from this analysis are reported in Figure 6.6 together with the experimental data, while the fit parameters are reported in table 6.1. The fit has been performed only in the temperature range where both Γ and v_L have been measured. The simple model described by equation 6.2 is clearly able to well reproduce the experimental data, even if a more elaborate description would be necessary in order to account for the detailed shape of Γ.
Moreover, differently from the case of sorbitol, the model suggests that the sound velocity shows a relevant dispersion up to the THz frequency range probed by IXS, while the anharmonic contribution to the Brillouin width remains negligible in the high frequency range.
The strength of the anharmonic process yields information on the relaxed sound

v_∞^0 $[km/s]$	a $[10^{-4}K^{-1}]$	B $[m^2/s^2K]$	τ_0 $[ps]$	E_n $[K]$
2.51	4.05	5.1	2.50	220

TABLE 6.1: Values of the parameters of the equation model 6.2 used to describe the temperature behavior of $v_\infty(T)$ and $\hbar\Gamma(T)$ of sulfur.

velocity $v_{0\infty}$ - related to $M_{0,\infty}$ reported in Figure 4.22 - being $\Delta^2 = v_\infty^2 - v_{0\infty}^2$. The resulting values are also reported in Figure 6.6 at some selected temperatures together with the v_∞ values estimated from the fit. The low frequency dynamics of sulfur is clearly characterized by a stronger anharmonic contribution than that affecting the dynamics of sorbitol. In particular, for $T = 200$ K we find $(\Delta^2/v_\infty^2)_{sorb} = (1.26 \pm 0.02)10^{-2}$ for sorbitol and $(\Delta^2/v_\infty^2)_{sulf} = (9.52 \pm 0.13)10^{-2}$ for sulfur, thus a value almost eight times higher than in sorbitol.
On increasing the temperature, the strength of the anharmonic contribution increases and the measured sound velocities do not correspond any longer to the pure elastic limit measured at low Q with IXS (purple triangles in Figure 6.6). As consequence, the macroscopic continuum limit of sulfur can be experimentally reached only at low temperatures or through the investigation of the dynamics at higher frequencies. The residual differences between the v_∞ value at $T = 150$ K and the corresponding IXS one is likely due to the low accuracy in the high frequency estimation of v_L, which has been measured for only one Q value (see Figure 6.5). The same argument can be applied probably also to the lower IXS temperature, even if we do not have the estimated value for v_∞.

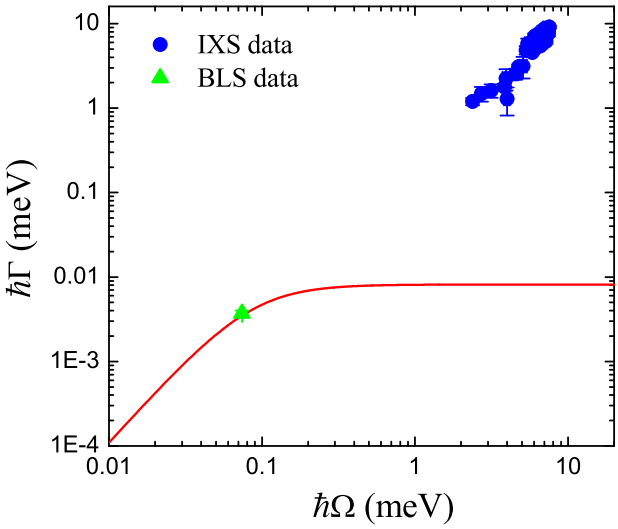

FIGURE 6.7: Brillouin width $\hbar\Gamma$ as a function of the excitation energy measured with IXS (blue circles) and BLS (green triangle). The red line represents the anharmonic contribution to the damping, calculated from equation 6.2.

This situation is similar to that observed in the case of a silicate glass [103] and reported in Figure 2.10 B. In that system, in fact, the presence of anharmonic or relaxational processes at low frequency lead to relevant dispersion of the sound velocity in the GHz range probed by IXS, so that the pure elastic limit can only be reached at high frequency.
From the model 6.2 we find a value $E_n \sim 220$ K and a characteristic time $\tau \sim 7$ ps at T=200 K. These values, together with the corresponding Δ^2 one, can be used to estimate the anharmonic contribution to the damping of the collective excitations at high frequencies. Figure 6.7 reports the Brillouin width $\hbar\Gamma$ measured at T=202 K with IXS together with the anharmonic contribution calculated from equation 6.2 and the corresponding value measured with BLS. In the frequency range explored by IXS, the anharmonic contribution to the damping is expected to be almost three orders of magnitude smaller than the measured excitation broadening and can be completely neglected. This result confirms the non dynamic nature of the sound attenuation at high frequency.

6.2.2 Nonergodicity factor

In section 4.2.2 it has been shown as the second moment sum rule for the dynamic structure factor allows for the determination of the $S(Q)$ of the investigated system. We have seen that the validity of the whole normalization procedure can be

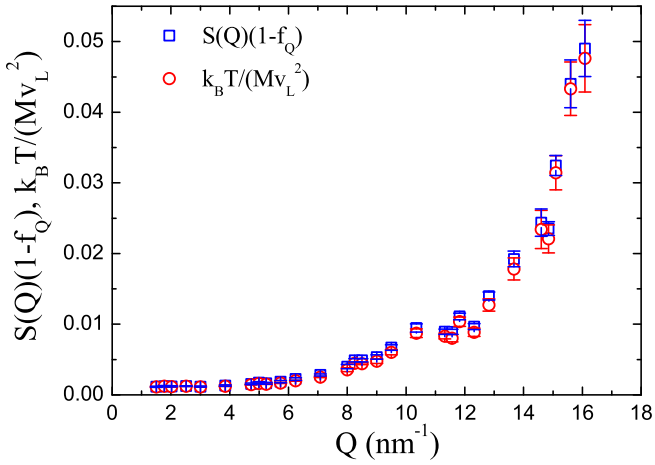

FIGURE 6.8: Check of the validity of relation 4.31 for glassy sulfur measured at T=202 K with IXS.

checked looking at the relation 4.31

$$S(Q)(1 - f_Q) = k_B T/(M v_L^2).$$

Figure 6.8 shows the two sides of relation 4.31 for glassy sulfur at T=202 K. The relation holds in the whole Q range, thus up to the first maximum of the $S(Q)$. This agreement represents moreover a confirmation of the evaluation of the nonergodicity factor.

The static structure factor can be furthermore used to estimate the isothermal compressibility, χ_T^0, of the corresponding supercooled liquid at T_g. In fact as seen in section 4.2.3, χ_T^0 can be obtained from the long wavelength limit of the $S(Q)$ being

$$\chi_T^0(T_g) = \frac{\rho k_B}{M T_g} S(Q \to 0) + M_\infty^{-1}(T_g) - \frac{T}{T_g} M_\infty^{-1}(T). \tag{6.3}$$

This quantity has been calculated as follows: the $S(Q \to 0)$ limit has been estimated using the IXS results on glassy sulfur at T=202 K, the density has been assumed equal to the one measured below T_g ($\rho = 1.92$ g/cm^3) [142] and the values of M_∞^{-1} have been taken from the fully unrelaxed sound velocities v_∞ obtained from the analysis of the low frequency BLS data using the model 6.2. We find $\chi_T^0(T_g) = 0.21 \pm 0.01$ GPa^{-1}.

In the case of glassy sorbitol it has shown that if the data satisfy the relation 4.31 then the long wavelength limit of f_Q is given by relations 4.37 and 4.38.

The nonergodicity factor of sulfur measured at T=202 K is reported in the left panel of Figure 6.9 together with the macroscopic limit given by equation 4.37 and reported in table 6.2. Differently from the case of glassy sorbitol (see Figure 4.18), the f_Q of sulfur is basically flat in the low Q range, up to $Q \sim 7$ nm^{-1} and corresponds to the macroscopic continuum value. This agreement confirms the

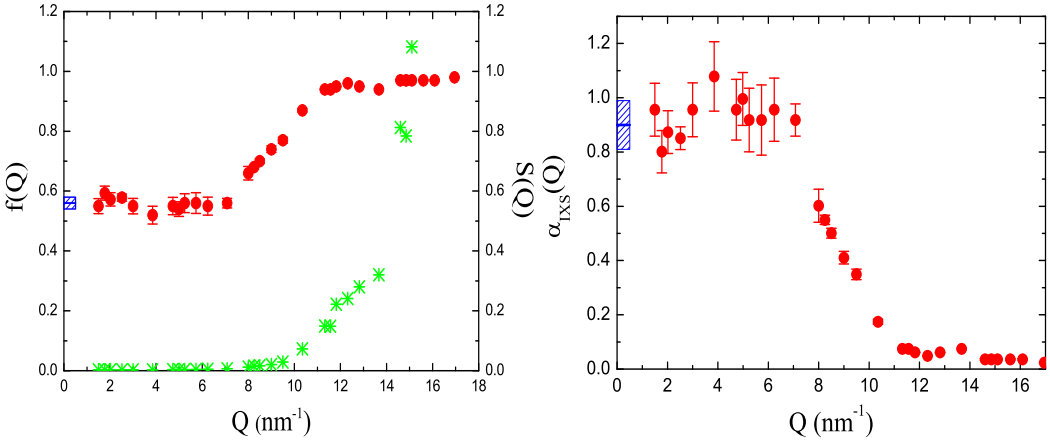

FIGURE 6.9: Left panel: Nonergodicity factor of sulfur measured at T=202 K. The blue square represents the continuum limit given by relations 4.37 and 4.38. The calculated $S(Q)$ is reported as well (green stars). Right panel: Q dependence of the α parameter obtained from relation 4.37. The blue rectangle is the continuum limit obtained through equation 4.38.

validity of both the normalization procedure used for the IXS spectra and of the value obtained for χ_T^0 from relation 6.3. It in fact confirms that it is possible to get information on the isothermal compressibility of a supercooled liquid close to the glass transition through the study of the vibrational dynamics in the corresponding glassy state.
The Q independence of the nonergodicity factor at low wave vectors implies that in the same Q range the shape of the high frequency sound velocity of sulfur is completely described by the Q dependence of the static structure factor. In fact in this range equation 4.31 yields $v_L \propto 1/\sqrt{S(Q)}$ (see Figure 6.10). This relation is not valid in the case of sorbitol due to the marked Q dependence of f_Q in the low Q range (see Figure 4.24).
Equation 4.37, $1/f_Q = 1 + \alpha T/T_g$, can be inverted to obtain the α_{IXS} parameter,

T [K]	$f_{Q,macr.}$	α_χ
202	0.56 ± 0.02	0.90 ± 0.09

TABLE 6.2: Long wavelength limit of the nonergodicity factor and the α_χ parameter obtained from equations 4.37 and 4.38.

shown in the right panel of Figure 6.9, together with the corresponding long wavelength limit α_χ given by equation 4.38 and reported in table 6.2. This quantity can be used to check the validity the correlation $m = 135\alpha$ proposed between the kinetic fragility and the vibrational properties of glasses [3, 4] (see section 2.4). Using the low wave vector value, corresponding to the macroscopic limit, we estimate a kinetic fragility of $m_\chi(T = 202\ K) = 122 \pm 12$. As previously

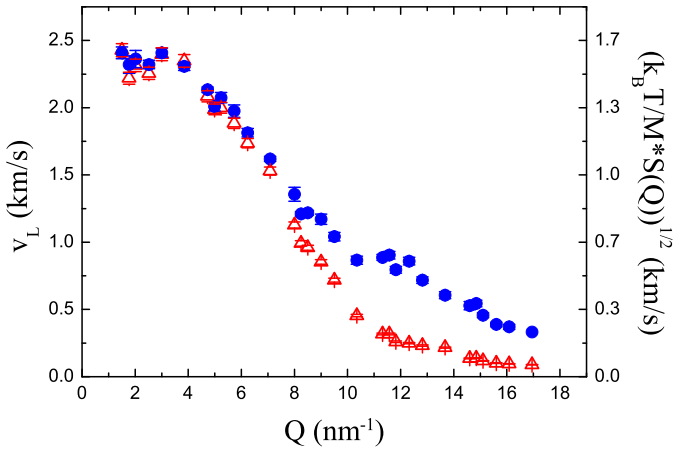

FIGURE 6.10: Wave-vector dependence of the high frequency sound velocity v_L (blue circles, left y axis) and $\sqrt{k_B T/MS(Q)}$ (red triangles, right y axis) of sulfur measured with IXS at T=202 K.

reported, this quantity can be obtained as well from the temperature dependence of the inverse of the nonergodicity factor as a function of the rescaled temperature T/T_g. The corresponding data are reported in Figure 6.11 together with the best fit lineshape. From the slope of the curve we obtain a kinetic fragility of $m_{IXS} = 115 \pm 3$. The two values of the fragility are basically compatible within the experimental errorbars. Albeit their value is slightly higher than the one calculated in the liquid phase ($m_A = 86 \pm 7$, see section 3.4.1), this result seems to confirm the validity of the correlation between fast dynamics in the glassy state and slow dynamics in the supercooled liquid phase in polymeric glassy sulfur. However, as reported in Ref. [29], one should take into account the anharmonic contribution found at low frequency as well (see section 6.2.1). Following the same procedure described in section 4.4.2 for sorbitol (in particular equations 4.42 and 4.44), we find $f_{Q,ana}(T_g) = (13.2 \pm 0.8)10^{-2}$, thus a value almost 10 times higher than that of sorbitol. By using the estimated value $f_{Q,str}(T_g)$ of the nonergodicity factor we find the value $\alpha_{str} = 1.34 \pm 0.12$ for the α parameter related only to the structural relaxation process. Such a value would corresponds to a fragility of $m_{str} = 181 \pm 16$, in clear disagreement with that of the corresponding viscous melt. In reality, the linear relation proposed by Scopigno and coworkers seems to bend at high α values, in agreement with the case of polymeric sulfur. This aspect will be treat more in detail in the next Chapter together with a comparison to other systems.

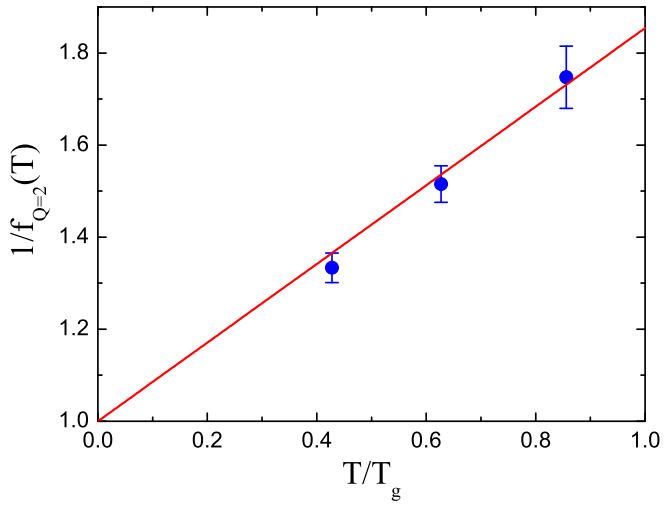

FIGURE 6.11: Inverse of the nonergodicity factor of sulfur for $Q = 2$ nm^{-1} measured at T=101, 148 and 202 K as a function of the rescaled temperature T/T_g. The red line represents the best fit shape obtained from relation $1/f_Q = 1 + \alpha\,(T/T_g)$.

6.3 Glassy sulfur *versus* liquid sulfur

It is interesting to compare the sound velocity measured in the glass at low and high frequency to that corresponding to the liquid phase. Figure 6.12 displays the temperature dependence of the sound velocity measured in the GHz and THz frequency range in the glassy state together with that measured in the MHz [130, 177, 178], GHz [139] and THz [138] frequency ranges in the liquid phase on crossing the λ transition. The differences in the liquid sulfur data corresponding to different frequencies are due to the effect played by the main structural relaxation process. Being present both above and below T_λ, the observed differences in the longitudinal modulus on crossing T_λ are not related to the huge increase in the viscosity during the polymerization transition, as confirmed by the presence of a secondary slow process (see section 3.4) [140].
The structural relaxation process is of course frozen in the glassy phase, and then one should expect that the high-frequency IXS data measured in the polymeric liquid above T_λ and the sound velocity data measured in the glass are strongly related. That this is actually the case is indicated as well in Figure 6.12, where we show that the data in the glass can be extrapolated from the data in the polymeric liquid, and vice versa. This confirms the strict relation between these two states of sulfur, and shows the possibility to get information on the viscoelastic properties of the polymeric liquid phase by studying the elastic properties of the corresponding glass.
In the Figure we added also the point corresponding to the relaxed sound velocity

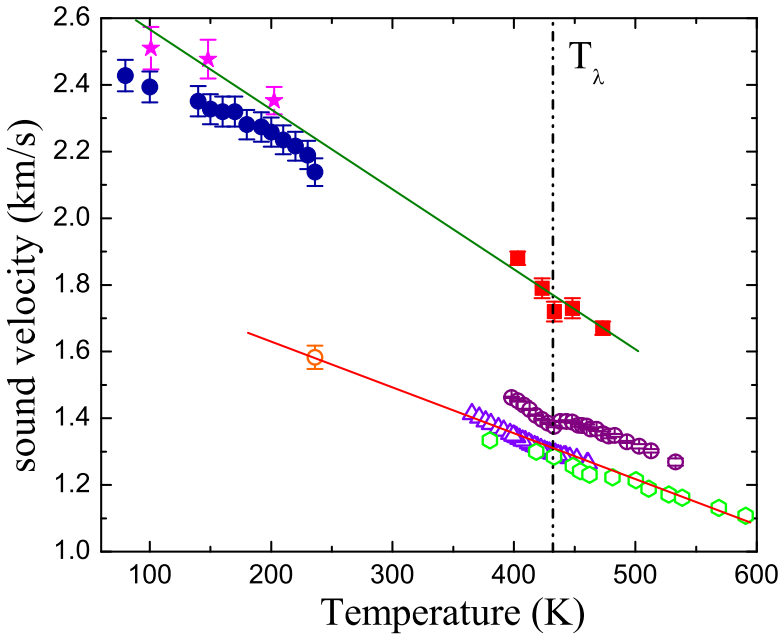

FIGURE 6.12: Temperature dependence of the sound velocity v_l of the longitudinal acoustic excitations. The values measured in the glassy state in the GHz (blue circles) and THz (magenta stars) frequency range are reported together with those measured in the liquid phase in the MHz (empty violet triangles and green hexagons) [130, 177, 178], in the BLS (empty purples circles) [139] and in the IXS (red squares) frequency range. The orange empty circle has been calculated from the relation $v_0(T_g) = 1/\sqrt{\rho(T_g)\chi_T^0(T_g)}$ using the values of $\chi_T^0(T_g)$ obtained from relation 6.3. The dashed black line indicates $T_\lambda = 432$ K. The full green and red lines show that the data in the glass can be obtained by a simple linear extrapolation of the corresponding data in the polymeric liquid phase above T_λ.

$v_0(T_g) = 1/\sqrt{\rho(T_g)\chi_T^0(T_g)}$ estimated from the value of the isothermal compressibility of the liquid at T_g obtained from the analysis of the IXS data (see section 6.2.2). Also in this case the data can be linearly extrapolated from the corresponding ones in the polymeric liquid phase above T_λ.

Résumé du chapitre 7

Dans ce chapitre les principaux résultats de ce travail de thèse sont mis en relation avec le comportement des autres verres. Comme nous l'avons vu dans les chapitres précédents, la rupture de l'approximation du continuum de Debye dans la région mésoscopique semble être une caractéristique universelle des verres et elle se présente toujours avec un fort, genre Rayleigh, régime d'atténuation des excitations acoustiques correspondantes. En outre, ces comportements particuliers peuvent être utilisés pour reproduire quantitativement la forme du BP, en confirmant ainsi la connexion étroite entre BP et les modes acoustiques à haute fréquence. Ce sujet sera traité dans la première partie du chapitre, tandis que dans la deuxième partie, on présentera un résumé des résultats sur les corrélations entre la fragilité des liquides visqueux et les propriétés élastiques des verres. Comme on le montrera même si il existe une indication claire de la présence d'une sorte de relation entre ces deux états de la matière, une corrélation quantitative universelle est toujours manquante. Toutes les relations analysées dans cette thèse sont, en effet, liées à des comportements dépendants du système et, selon le système, leur validité peut être fortement débattue.

Chapter 7

Comparison with other systems

In this Chapter the main results of this Thesis work are discussed in relation with the behavior of other glasses. As anticipated in the previous Chapters the breakdown of the Debye continuum approximation on the mesoscopic spatial range seems to be an universal feature of glasses and comes always with a strong, Rayleigh like, damping of the corresponding acoustic excitations. Furthermore, these peculiar behaviors can be used to quantitatively account for the shape of the boson peak, confirming the strict connection between BP and high frequency acoustic modes. This argument will be treated in the first part of the Chapter, while in the second part, a summary of the results on the correlations between fragility of viscous liquids and elastic properties of glasses will be presented. As it will be shown there, even if there is a clear indication of some sort of relation between these two states of matter, a quantitatively universal correlation is still missing. All of the relations investigated in this Thesis are indeed related to system dependent behaviors and, depending on the system, their validity can be strongly debated.

7.1 Universal behavior of glasses

Figure 7.1 reports the high frequency sound velocity of strong silica [97], intermediate glycerol [96], and fragile sulfur and sorbitol rescaled for the corresponding macroscopic value as a function of E/E_{BP}, in order to compare the different systems. The universal occurrence of the negative dispersion at low Q values is well evident. Moreover it takes place always in the same energy range, below the energy of the corresponding boson peak maximum. As observed in the previous Chapter, polymeric sulfur does not show this universal behavior, being the lowest investigated Q well above E_{BP} and thus above the negative dispersion as well. Moreover the sound velocity of sulfur seems to have already reached the macroscopic limit, suggesting the absence of the negative dispersion in this glass. However, it has been shown that the softening of the modes is responsible for a peak in the reduced

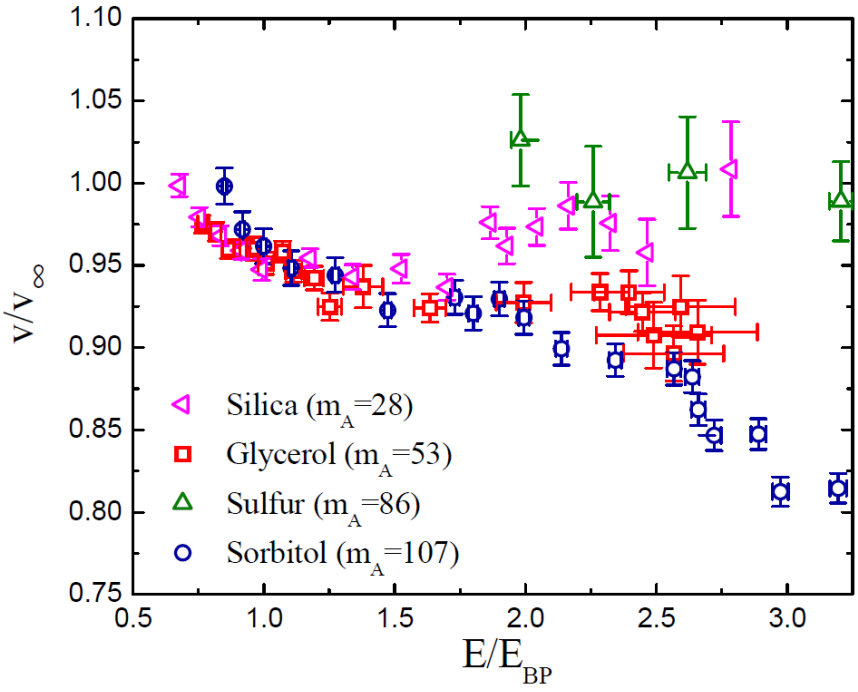

FIGURE 7.1: High frequency sound velocity rescaled by the macroscopic value of silica [97], glycerol [96], sulfur and sorbitol as a function of the energy rescaled to the maximum of the boson peak.

vibrational density of states (see the Figure 5.7 A)). As a consequence, depending on the intensity of the BP we expect to find a more or less evident negative dispersion; in particular the higher is the BP intensity, the larger should be the softening of the sound velocity. As previously reported, the amplitude of the BP is usually lower in fragile systems [60]. Even if we do not have information on the BP intensity of sulfur on an absolute scale, the presence of low elastic moduli, and more precisely of a high bulk to shear moduli ratio ($B'/G' = 7.65 \pm 0.31$, see section 3.5.2) is typical of fragile systems having a BP less intense than glycerol and silica [5, 6, 60]. For this reason, the negative dispersion in sulfur is expected to be smaller than in the other systems, and could be hidden by the large errorbars values (see Figure 7.1).
Different is the situation in the case of sorbitol; it has indeed be shown that despite of the fact that supercooled sorbitol displays a super-Arrhenius behavior on approaching T_g, glassy sorbitol has elastic properties similar to those of strong and intermediate systems, such as high elastic moduli values, and thus a low value of the bulk to shear modulus ratio ($B'/G' = 2.44 \pm 0.07$, see section 3.3.3). In this case in fact, the intensity of the BP is similar to that of intermediate glasses, such as glycerol, with a consequent well evident softening of the sound velocity.

Figure 7.2 shows the high frequency acoustic attenuation as a function of the rescaled energy E/E_{BP} for the same systems reported in Figure 7.1. All the glasses display a strong, Rayleigh-like, behavior of the excitations broadening with the exception of sulfur, whose damping follows a $(\hbar\Omega)^2$ dependence. In particular, as expected from the observations reported in section 6.2, this behavior takes place

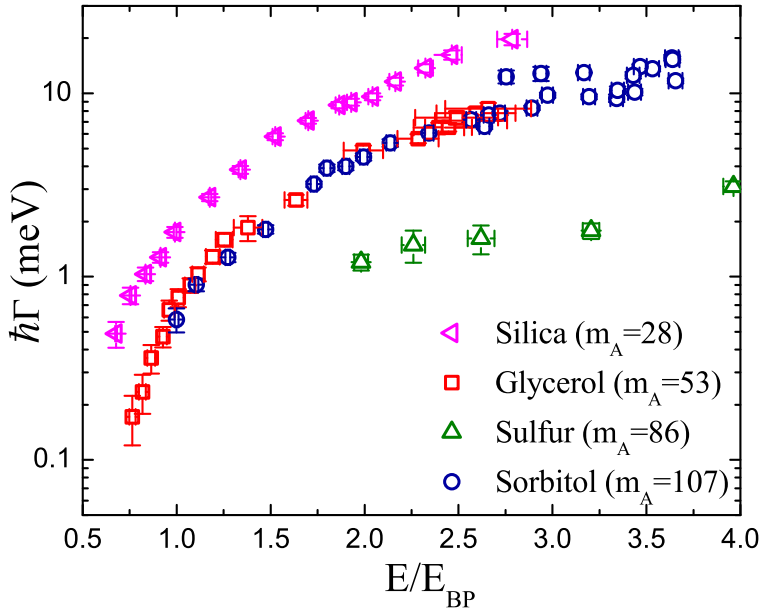

FIGURE 7.2: High frequency sound attenuation of silica [97], glycerol [96], sulfur and sorbitol as a function of the energy rescaled for the maximum of the boson peak.

well above the BP maximum in an energy range where also the other systems exhibit a quadratic dependence of $\hbar\Gamma$ on the excitation energies.
In section 5.3.1 it has shown as the peculiar behavior of the high frequency excitations can be used to quantitatively reproduced the shape of the boson peak. The model equations 5.36 have been successfully applied both for glycerol [96] and sorbitol (see Figure 5.7 B)), while in the case of silica, the model is able to estimate the position of the BP but it underestimates its intensity [179]. Albeit this inconsistency, these results confirm the strict correlation between the BP and the high frequency acoustic modes and should be taken into account to improve the current theoretical models of the vibrational density of states of glasses.

7.1.1 The Ioffe Regel criterion

In section 4.3.3 the Ioffe-Regel criterion has been discussed. We have seen that in the case of sorbitol the upper limit E_{IR} for a description of the acoustic excitations in terms of well defined plane waves takes place at energies higher than that of the boson peak. It is interesting here to compare this result with those of other glasses, and in relation with the elastic anomalies found on the nanometer spatial range. As previously reported, a correlation has been proposed between the boson peak energy and E_{IR}, which is, however, strongly debated [91, 164].

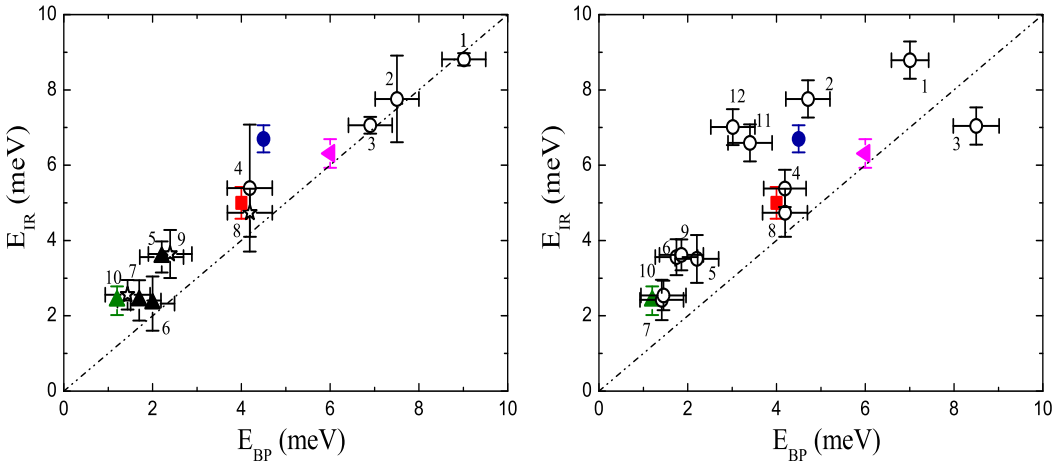

FIGURE 7.3: Left panel: Ioffe-Regel limit *vs* boson peak energy for different glasses. Black symbols are taken from Ref. [91], while the colored symbols correspond respectively to silica (magenta triangle) [97], glycerol (red square) [96], sulfur (green triangle) and sorbitol (blue circle). Right panel: E_{IR} *vs* E_{BP} as in the left panel, but the black symbols are instead taken from Ref. [164].

glass	E_{IR} [meV]	E_{BP} [meV]	E_{IR}/E_{BP}
silica	6.31 ± 0.38	6	1.05 ± 0.06
glycerol	5.00 ± 0.42	4	1.25 ± 0.11
sulfur	2.40 ± 0.38	1.2	2.00 ± 0.32
sorbitol	6.70 ± 0.36	4.5	1.49 ± 0.08

TABLE 7.1: Values of E_{IR} and E_{BP} for silica [97], glycerol [96], sulfur and sorbitol.

Figure 7.3 reports the E_{IR} *vs* E_{BP} plot for various glasses, taken from Ref. [91] (black symbols in the left panel) and from Ref. [164] (black symbols in the right panel). We added the points for silica [97], glycerol [96], sulfur and sorbitol. The corresponding data are reported in table 7.1. Without entering the discussion on the validity of the values used in the two Figures, it is interesting here to note that, in all glasses $E_{IR} \geq E_{BP}$, with the exception of densified silica (number 3 in the right panel). Our data show as well that the Ioffe-Regel limit for the longitudinal modes is larger than the BP energy, as in the case of sorbitol and sulfur. Moreover looking at the elastic anomalies found in silica, glycerol, and sorbitol (see Figures 7.1 and 7.2 and values in table 7.1), it is interesting to note that E_{IR} is also always found close to the upper end of the low Q, Rayleigh like behavior of the acoustic damping (and at the end of the negative dispersion), confirming thus the significance of E_{IR} as a crossover between well-defined acoustic excitations and a more complex pattern of excitations at higher Q. Furthermore, a simple look

at the data reported in table 7.1 shows that it is clearly not possible to find a quantitative relation between the energy of the boson peak and the IR limit: for instance, glassy sorbitol has a higher E_{IR} value than silica but at the same time a lower BP position. Moreover following the definition of the IR limit, $E_{IR} = \pi\hbar\Gamma$, it is clear that this quantity is almost temperature independent while there are systems, such as silica, where E_{BP} is strongly affected by temperature changes [164, 180]. In the previous Chapters we have in fact seen that the excitation energy $\hbar\Omega$ does not display any appreciable temperature dependence (which is only evident in the sound velocity) and that the corresponding high frequency sound attenuation is non dynamic in origin in the low Q range governed by the Rayleigh like regime. Albeit sorbitol is the first glass where this damping mechanism has been measured under temperature changes, being E_{IR} at the crossover between the two different Q regimes for the damping, it is straightforward to imaging a temperature independence of this limit as well. As a consequence, depending on the chosen temperature, several systems can show a worst of better correlation between E_{IR} and the BP energy.

7.2 Fragility of liquids and nonergodicity factor of glasses

In sections 2.4, 4.3.4 and 6.2.2 the relation between slow dynamics in supercooled liquids and fast dynamics in glasses has been largely discussed. The results for sorbitol and sulfur show that in order to properly estimate the nonergodicity factor of glasses, it is necessary to take its macroscopic value, which can be easily obtained from low frequency BLS data and from the knowledge of the isothermal compressibility in the liquid phase at the glass transition temperature (see equations 4.37 and 4.38). In order to properly compare the f_Q with the fragility of liquids, the nonergodicity factor should be related only to the structural relaxation process that is frozen in the glassy state. We have seen that the presence of anharmonic or relaxation contribution can lead to a wrong estimation of the f_Q, and as a consequence of the α parameter to be compared to m_A. It is interesting here to compare the results obtained in sorbitol and sulfur together with those found in other systems.

Figure 7.4 reports the values of the kinetic fragility m_A of supercooled liquids *vs* the values of the α parameter estimated by means of different techniques for several systems [29]. In particular, the Figure shows also new values of the α parameter (blue triangles) obtained for different glasses by considering the presence of an anharmonic or relaxational contribution at very low frequency, as explained in Ref. [29]. The corresponding values for sulfur and sorbitol are also reported. In this case the α parameter has been obtained from the macroscopic limit 4.38 and the Figure reports both the value estimated directly from the measured f_Q (purple circles) than those calculated by considering the anharmonic contribution found in the GHz frequency range through equations 4.42 and 4.44 (magenta circles). Obviously, by removing the anharmonic contribution α shifts toward higher values. It is important to stress that the anharmonic contribution considered in

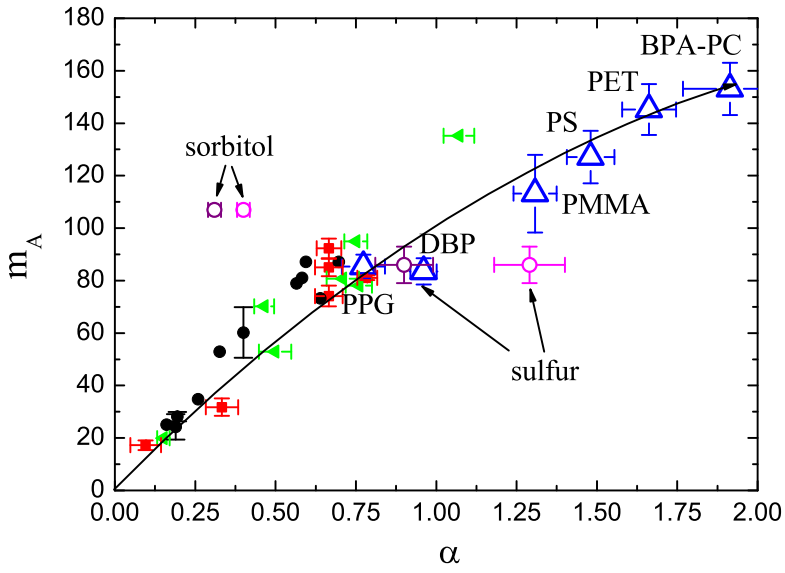

FIGURE 7.4: Correlation between the temperature dependence of the relaxation time (grasped by the kinetic fragility, m_A) and the nonergodicity factor (grasped by the α parameter for several glasses. All the data are taken from Ref. [29] with the exception of sorbitol and sulfur, for which the α parameter has been calculated from relation 4.38 (purple circles) and by considering the anharmonic contribution found in the GHz frequency range (magenta circles). The data without a name are the same as in Figure 2.14.

this Thesis for sorbitol and sulfur is different from that considered in Ref. [29]. Looking at the Figure it is clear than neither sorbitol nor polymeric sulfur fulfill the proposed relation between the kinetic fragility and the nonergodicity factor. In particular, in the case of glassy sulfur the system goes out of the proposed correlation once the anharmonic contribution is taken into account.
These results clearly show the difficulty to find a quantitative relation between α and m_A, in particular once systems with high fragility values are taken into account[1].

The value of the α parameter can be not even always taken as an indication of the fragile character of a system, in the sense that the more fragile the liquid the higher the corresponding α in the glassy state. This is shown by the case for sorbitol (see Figure 7.4) and can be clearly observed looking at Figure 7.5 where the temperature dependence of the inverse of the nonergodicity factor, measured with IXS, is reported as a function of the rescaled temperature T/T_g for several glasses [3].
While for polymeric glassy sulfur the α parameter - and thus the slope of the linear behavior of $1/f_Q$ - is higher than for instance that for OTP in agreement

[1] As previously discussed and shown in Figure 2.14 the relation $m_A = 135\alpha$ seems to be valid for several strong and intermediate glass formers.

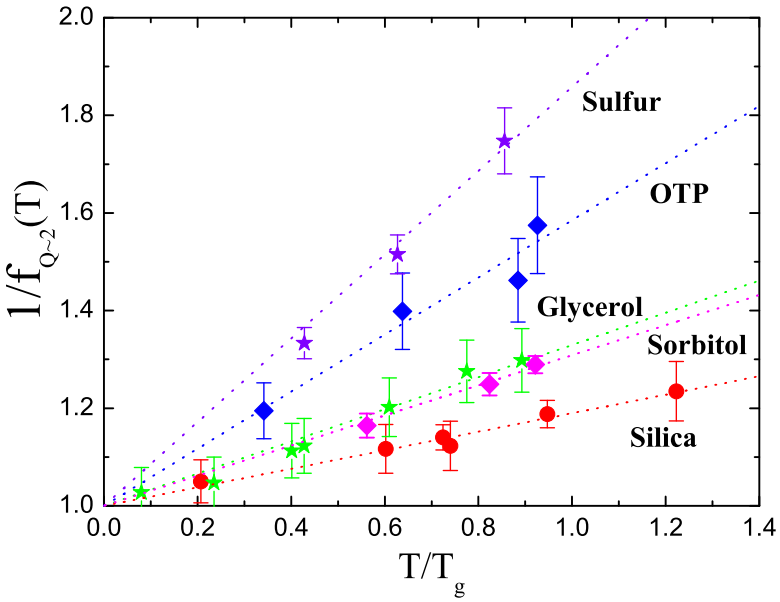

FIGURE 7.5: Temperature dependence of the inverse of the nonergodicity factor as a function of the rescaled temperature T/T_g. The corresponding data for silica, glycerol and OTP are taken from Ref. [3].

with its fragile character, fragile sorbitol exhibits a behavior very close to that of glycerol, and thus of intermediate systems. In Figure 7.5 all the data are reported by assuming the presence of the structural relaxation process alone governing the microscopic dynamics. Anyway, we have seen that in the case of sorbitol, the anharmonic contribution found in the GHz is weak and does not alter the results (see the two values of α in Figure 7.4) which remain in disagreement with any proposed correlation between kinetic fragility and elastic properties of glasses.

Conclusions and perspectives (français)

Au cours de cette thèse nous avons poursuivi l'objectif difficile de clarifier plusieurs aspects concernant les propriétés vibrationelles des verres. Deux thèmes principaux ont été abordé. D'un côté on a largement étudié la relation entre les propriétés élastiques des verres et la bien connue "anomalie" dans la densité réduite des états vibrationnels, donc le BP. De l'autre côté, la connaissance détaillée de la dynamique vibrationnelle des verres dans une grande gamme de fréquences nous a permis de vérifier plusieurs corrélations proposées entre la dynamique rapide dans les verres et la dynamique lente dans les correspondants liquides surfondus.
Cette étude a été soutenue par l'utilisation de la diffusion inélastique de la lumière, de rayons x et de neutrons. La combinaison des résultats trouvés avec ces différentes techniques nous a permis d'effectuer une étude approfondie des propriétés vibrationnelles de deux verres fragiles: sorbitol moléculaire et soufre polymère.
Malgré la structure différente des deux systèmes étudiés, dans les deux cas, les excitations acoustiques à haute fréquence peuvent être décrites avec une bonne approximation dans une approche quasi-harmonique, donc avec une vitesse du son dont la dépendance en température est entièrement régie par les transformations correspondantes du continuum élastique et avec un mécanisme d'atténuation acoustique clairement non dynamique dans son origine. En outre, dans le cas du sorbitol l'excès des modes dans le VDOS à 4,5 meV, par apport à la prédiction du continuum élastique de Debye, est clairement lié à des anomalies observées dans la courbe de dispersion acoustique dans la région mésoscopique de vecteurs d'onde de quelques nm^{-1}. Ces anomalies élastiques se manifestent comme une diminution de la vitesse du son à haute fréquence et en correspondance il y a une forte atténuation gouvernée par un mécanisme genre Rayleigh pour des énergies des excitations proches de celle du maximum du BP. L'étude de la dépendance en température de ces propriétés montre que la connexion avec le BP est maintenue même avec les changements de température. Ces résultats nous permettent de justifier et comprendre la relation déchelle du BP observé avec les paramètres du milieu élastique. Le lien entre BP et les modes acoustiques est d'ailleurs renforcé par la possibilité de reproduire quantitativement sa forme en utilisant la dépendance en Q des excitations collectives à haute fréquence.
Dans le cas du soufre vitreux polymère, les limites actuelles expérimentales de IXS et la valeur basse du maximum du BP ne nous permettent pas d'enquêter le caractère des excitations acoustiques présentes dans la même gamme d'énergie

du BP. Dans cet échantillon, les caractéristiques observées dans le sorbitol sont probablement déplacées vers des énergies plus basses et donc dans une région qui ne peut pas être explorée actuellement. En conséquence, les excitations collectives à haute fréquence du soufre montrent le comportement typique observé dans d'autres verres bien au-dessus de l'énergie du BP. À basses vecteurs d'onde la vitesse du son à haute fréquence du soufre se trouve à être plus élevée par rapport à la limite macroscopique explorée avec BLS. Cet écart peut être expliqué grâce à une contribution anharmonique présente dans la région à basse fréquence.
L'analyse détaillée des propriétés vibrationnelles du soufre polymère et du sorbitol nous a donné la possibilité de vérifier la validité dans ces systèmes de certaines corrélations proposées entre l'état vitreux et la phase liquide correspondante. Nous avons montré que dans les deux systèmes le rapport entre le module de cisaillement instantané et celui de la compressibilité ne suit pas la dépendance linéaire de la fragilité cinétique trouvée pour plusieurs verres par Novikov *et al.* [5, 6]. Bien que les polymères en général violent ce genre de relation, les résultats sur le sorbitol sont plutôt en évident désaccord. Cela est dû à l'étrange caractère de ce système, dont la dynamique est similaire à celle des systèmes forts et intermédiaires dans l'état vitreux et à celle des systèmes très fragiles dans la phase de liquide surfondu.
La relation entre le paramètre de nonergodicité et la fragilité cinétique a été vérifié également en vue de récentes améliorations de la corrélation d'origine proposées par Scopigno et ses collègues [29]. Malgré nous avons utilisé une approche différente par rapport à celle proposée dans Ref. [29], nous constatons que même en considérant la présence des mécanismes de relaxation ou anharmonicité présents à basse fréquence, la relation proposée n'est pas satisfaite ni dans le sorbitol, ni dans le soufre. En outre, le paramètre α qui décrit la dépendance en température du facteur de nonergodicité mesuré avec IXS est strictement lié au comportement des correspondantes excitations collectives à haute fréquence. Une évaluation correcte de ce paramètre, et donc du facteur de nonergodicité, devrait plutôt être effectuée en utilisant son valeur macroscopique. Nous trouvons que cette limite continuum peut être obtenue à partir d'un prolongement naturel dans l'état vitreux de la relation proposée par Buchenau et Wischnewski [4] qui est valable à la température de transition vitreuse.
Ces conclusions nous permettent d'avoir une image raffinée sur des questions fondamentales sur la dynamique vibrationnelle des verres et de nombreux aspects de ce travail de thèse exigeront une enquête plus approfondie. En particulier, les anomalies élastiques universelles trouvées dans des verres à proximité de l'énergie du BP devraient être prises en compte afin d'améliorer les modèles théoriques actuels pour l'excès de modes dans la densité réduite des états. Dans cette perspective, plusieurs autres travaux expérimentaux sont également fondamentaux. Par exemple à l'avenir des études pourraient être effectuées en fonction de la pression dans les verres et en fonction de la température dans la phase liquide surfondu. La comparaison avec les phases cristallines correspondantes devraient être menées, ainsi, afin de clarifier dans quelle mesure les anomalies discutées ici sont vraiment propres à l'état désordonné.
Les résultats sur la corrélation entre les verres et les liquides surfondus posent au contraire beaucoup de doutes sur la possibilité concrète de trouver des relations universelles. Malgré le fait que plusieurs corrélations proposées soient vérifiées

pour un grand nombre de matériaux forts et intermédiaires, les systemes fragiles, tels que le sorbitol moléculaire et le soufre polymère, semblent présenter un comportement plus complexe et dépendant du système.

Conclusions and perspectives

During this Thesis project we pursued the challenging aim to clarify several aspects concerning the vibrational properties of glasses. Two main topics have been tackled. From one side the relation between elastic properties of glasses and the well known "anomaly" in the reduced vibrational density of states, thus the boson peak, has been largely investigated. On the other side, the accurate knowledge of the vibrational dynamics of glasses in a wide frequency range has allowed us to check several proposed correlations between fast dynamics in glasses and slow dynamics in the corresponding supercooled liquids.
This study has been supported by the use of inelastic light (BLS), x-ray (IXS) and neutron (INS) scattering techniques. The combinations of the results found with these different techniques has allowed us to perform a deep investigation of the vibrational properties of two fragile glasses: molecular sorbitol and polymeric sulfur.
Albeit the different structure of the two investigated systems, in both cases the high frequency acoustic excitations can be described to a good approximation in a quasi-harmonic approach, thus with a sound velocity whose temperature dependence is completely governed by the transformation of the corresponding continuum medium and with an acoustic attenuation mechanism clearly non dynamic in its origin. Moreover, in the case of sorbitol the excess in the VDOS at 4.5 meV over the Debye, elastic continuum prediction (boson peak) is found to be clearly related to anomalies observed in the acoustic dispersion curve in the mesoscopic wavenumber range of few nm^{-1}. These elastic anomalies appear as a softening of the high frequency sound velocity and a corresponding strong, thus Rayleigh like, damping mechanism for excitations energies close to that of the boson peak maximum. The study of the temperature dependence of these properties shows that the connection with the BP is kept under temperature changes. These results then lead to a natural frame for justifying and understanding the observed scaling of the boson peak with the parameters of the elastic medium. The link between BP and acoustic modes is moreover strengthen by the possibility to quantitatively reproduce its shape using the Q-dependence of the high frequency collective excitations.
In the case of polymeric glassy sulfur, the current experimental limitations of IXS and the low BP maximum value do not allow the investigation of the character of the acoustic excitations present in the crucial energy range of the BP. In this sample, the features observed in sorbitol are likely shifted toward lower energies and thus in a range that cannot be explored at the current time. As a consequence,

the high frequency collective excitations of sulfur display the typical behavior observed in other glasses well above the BP energy. At low exchanged wavevectors the high frequency sound velocity of sulfur is found to be higher with respect to the macroscopic limit explored with BLS. This discrepancy has be explained in terms of an anharmonic contribution present in the low frequency range.
The detailed analysis of the vibrational properties of sorbitol and polymeric sulfur gave us the possibility to check the validity in these systems of some of the proposed correlations between the glassy state and the corresponding liquid phase. We showed that in both systems the ratio of instantaneous shear to bulk modulus does not follow the linear dependence on the kinetic fragility found for several glasses by Novikov et al. [5, 6]. While polymers usually violate such relation, the results on sorbitol are instead in clear disagreement. This is due to the peculiar character of this glass former, whose dynamics is similar to that of strong and intermediate systems in the glassy state and to very fragile systems in the supercooled liquid phase.
The relation between the nonergodicity parameter and the kinetic fragility has been checked also in view of the recent improvements on the original correlation proposed by Scopigno and coworkers [29]. Albeit we used a different approach with respected to that proposed in Ref. [29], we find that even taking into account the presence of anharmonic or relaxation mechanisms present at low frequencies, the proposed relation is not fulfilled neither in sorbitol nor in sulfur. Moreover the α parameter describing the temperature dependence of the nonergodicity factor measured with IXS is found to be strictly related to the behavior of the corresponding high frequency collective excitations. A correct evaluation of this parameter, and thus of the nonergodicity factor, should be instead performed looking at its macroscopic value. We find that this continuum limit can be obtained from a natural extension in the glassy state of the relation proposed by Buchenau and Wischnewski [4] and valid at the glass transition temperature.
These conclusions allow us to have a refined picture on fundamental questions on the vibrational dynamics of glasses and many aspects of this Thesis work will require further investigation. In particular the universal elastic anomalies found in glasses close to the boson peak energy should be taken into account in order to improve the current theoretical models for the excess of modes in the reduced density of states. In this perspective, several additional experimental works are also fundamental. For instance, studies performed as a function of pressure could be carried out in the future, as well as a function of temperature up to the supercooled liquid phase. The comparison with the corresponding crystalline phases should be carried out as well, in order to clarify to what extent the anomalies discussed here are truly peculiar to the disordered state.
The results on the correlation between glasses and supercooled liquids open instead many doubts on the concrete possibility to find universal relations. Albeit several proposed correlations are verified for many strong and intermediate materials, fragile systems, such as molecular sorbitol and polymeric sulfur, seem to present a more complex and system dependent behavior.

References

- **B. Ruta**, G. Monaco, F. Scarponi and D. Fioretto, *Brillouin light scattering study of glassy sorbitol*. Philosoph. Mag. 88 (2008) 3939.
- G. Baldi, A. Fontana, G. Monaco, L. Orsingher, S. Rols, F. Rossi and **B. Ruta**, *Connection between Boson Peak and Elastic Properties in Silicate Glasses*. Phys. Rev. Lett. 102 (2009) 195502.
- G. Baldi, V. M. Giordano, G. Monaco and **B. Ruta**, *Sound attenuation at terahertz frequencies and the boson peak of vitreous silica*. Phys. Rev. Lett. 104 (2010) 195501.
- **B. Ruta**, G. Baldi, V. M. Giordano, L. Orsingher, F. Scarponi, S. Rols and G. Monaco, *High-frequency acoustic properties and boson peak in glasses: a study of their temperature dependence*. Accepted on J. Chem. Phys.
- G. Baldi, V. M. Giordano, G. Monaco and **B. Ruta**, *High frequency acoustic attenuation of vitreous silica: new insight from inelastic x-ray scattering*. Accepted on J. Non-Cryst. Sol..
- **B. Ruta**, G. Monaco, F. Scarponi, D. Fioretto and K. S. Andrikopoulos, *Brillouin light scattering study of polymeric glassy sulfur*. Submitted to J. Non-Cryst. Sol..

Bibliography

[1] V.K. Malinovsky and A.P. Sokolov. The nature of boson peak in Raman scattering in glasses. *Solid State Commun.*, **57**:757, 1986.

[2] C. A. Angell. Spectroscopy simulation and scattering, and the medium range order problem in glass. *J. Non Cryst. Sol.*, **73**:1, 1985.

[3] T. Scopigno, G. Ruocco, F. Sette, and G. Monaco. Is the Fragility of a Liquid Embedded in the Properties of Its Glass? *Science*, **302**:849, 2003.

[4] U. Buchenau and A. Wischnewski. Fragility and compressibility at the glass transition. *Phys. Rev. B*, **70**:092201, 2004.

[5] V. N. Novikov and A. P. Sokolov. Poissons ratio and the fragility of glass-forming liquids. *Nature*, **431**:961, 2004.

[6] V. N. Novikov, Y. Ding, and A. P. Sokolov. Correlation of fragility of supercooled liquids with elastic properties of glasses. *Phys. Rev. E*, **71**:061501, 2005.

[7] C. A. Angell. Formation of glasses from Liquids and Biopolymers. *Science*, **267**:1924, 1995.

[8] C. M. Roland, S. Hensel-Bielowka, M. Paluch, and R. Casalini. Supercooled dynamics of glass-forming liquids and polymers under hydrostatic pressure. *Rep. Prog. Phys.*, **68**:1405, 2005.

[9] J. C. Dyre. Colloquium: The glass transition and elastic models of glass-forming liquids. *Rev. Mod. Phys.*, **78**:953, 2006.

[10] P. G. Debenedetti and F. H. Stillinger. Supercooled liquids and the glass transition. *Nature*, **410**:259, 2001.

[11] J. Jäckle. Models of the glass transition. *Rep. Prog. Phys.*, **49**:171, 1986.

[12] J. Wong and C. A. Angell. *Glass, Structure by Spectroscopy.* M. Dekker, New York, 1976.

[13] K. Chang. The Nature of Glass Remains Anything but Clear. *The New York Times*, July 29, 2008.

[14] G. Adam and J. H. Gibbs. On the Temperature Dependence of Cooperative Relaxation Properties in Glass-Forming Liquids. *J. Chem. Phys.*, **43**:139, 1965.

[15] M. H. Cohen and D. Turnbull. Molecular Transport in Liquids and Glasses. *J. Chem. Phys.*, **31**:1164, 1964.

[16] M. H. Cohen and D. Turnbull. Metastability of Amorphous Structures. *Nature*, **203**:964, 1964.

[17] D. R. Reichman and P. Charbonneau. Mode-coupling theory. *J. Stat. Mech.*, page P05013, 2005.

[18] M. Goldstein. Viscous Liquids and the Glass Transition: A Potential Energy Barrier Picture. *Phys. Chem.*, **51**:3728, 1969.

[19] A. Cavagna. Supercooled liquids for pedestrians. *Phys. Rep.*, **476**:51, 2009.

[20] F. H. Stillinger. A Topographic View of Supercooled Liquids and Glass Formation. *Science*, **267**:1935, 1995.

[21] M. Paluch, S. Pawlus, S. Hensel-Bielowka, E. Kaminska, D. Prevosto, S. Capaccioli, P. A. Rolla, and K. L. Ngai. Two secondary modes in decahydroisoquinoline: Which one is the true Johari Goldstein process? *J. Chem. Phys.*, **122**:234506, 2005.

[22] G. P. Johari and M. Goldstein. Viscous Liquids and the Glass Transition. II. Secondary Relaxations in Glasses of Rigid Molecules. *J. Chem. Phys.*, **53**:2372, 1970.

[23] G. P. Johari and M. Goldstein. Viscous Liquids and the Glass Transition. III. Secondary Relaxations in Aliphatic Alcohols and Other Nonrigid Molecules. *J. Chem. Phys.*, **55**:4245, 1971.

[24] M. Paluch, C. M. Roland, S. Pawlus, J. Ziolo, and K. L. Ngai. Does the Arrhenius Temperature Dependence of the Johari-Goldstein Relaxation Persist above T_g? *Phys. Rev. Lett.*, **91**:115701, 2003.

[25] S. Capaccioli, K. L. Ngai, and N. Shinyashiki. The Johari-Goldstein β-Relaxation of Water. *Phys. Chem. B*, **111**:8197, 2007.

[26] S. Capaccioli, K. Kessairi, D. Prevosto, M. Lucchesi, and P. A. Rolla. Correlation of structural and Johari-Goldstein relaxations in systems vitrifying along isobaric and isothermal paths. *J. Phys.: Cond. Matt.*, **19**:205133, 2007.

[27] S. Pawlus, M. Paluch, M. Sekula, K. L. Ngai, S. J. Rzoska, and J. Ziolo. Changes in dynamic crossover with temperature and pressure in glass-forming diethyl phthalate. *Phys. Rev. E*, **68**:021503, 2003.

[28] S. Pawlus, R. Casalini, C. M. Roland, M. Paluch, S. J. Rzoska, and J. Ziolo. Temperature and volume effects on the change of dynamics in propylene carbonate. *Phys. Rev. E*, **70**:061501, 2004.

[29] T. Scopigno, D. Cangialosi, and G. Ruocco. Universal relation between viscous flow and fast dynamics in glass-forming materials. *Phys. Rev. B*, **81**:100202, 2010.

[30] W. Götze and L.Sjörgen. Relaxation processes in supercooled liquids. *Rep. Prog. Phys.*, **55**:241, 1992.

[31] W. Kob and H. C. Andersen. Testing mode-coupling theory for a supercooled binary Lennard-Jones mixture. II. Intermediate scattering function and dynamic susceptibility. *Phys. Rev. E*, **52**:4134, 1995.

[32] C. A. Angell, K.L. Ngai, G.B. McKenna, P.F. McMillan, and S.W. Martin. Relaxation in glassforming liquids and amorphous solids. *J. Appl. Phys.*, **88**:3113, 2000.

[33] R. Böhmer, K. L. Ngai, C. A. Angel, and D. J. Plazek. Nonexponential relaxations in strong and fragile glass formers. *J. Chem. Phys.*, **99**:4201, 1993.

[34] M.L. Williams, R.F. Landel, and J.D. Ferry. The Temperature Dependence of Relaxation Mechanisms in Amorphous Polymers and Other Glass-forming Liquids. *J. Am. Chem. Soc.*, **77**:3701, 1955.

[35] R. Richert and C. A. Angell. Dynamics of glass-forming liquids. V. On the link between molecular dynamics and configurational entropy. *J. Chem. Phys.*, **108**:9016, 1998.

[36] L. M. Wang, V. Velikov, and C. A. Angell. Direct determination of kinetic fragility indices of glassforming liquids by differential scanning calorimetry: Kinetic versus thermodynamic fragilities. *J. Chem. Phys.*, **117**:10184, 2002.

[37] G. Ruocco, F. Sciortino, F. Zamponi, C. De Michele, and T. Scopigno. Landscapes and fragilities. *J. Chem. Phys.*, **120**:10666, 2004.

[38] L. M. Martinez and C. A. Angell. A thermodynamic connection to the fragility of glass-forming liquids. *Nature*, **410**:663, 2001.

[39] K. Ito, C. T. Moynihan, and C. A. Angell. Thermodynamic determination of fragility in liquids and a fragile-to-strong liquid transition in water. *Nature*, **398**:492, 1999.

[40] W. Kauzmann. The nature of the glassy state and the behavior of liquids at low temperatures. *Chem. Rev.*, **43**:219, 1948.

[41] S. R. Elliott. *Physics of amorphous materials*. Longaman, 1983.

[42] L. M. Wang, C. A. Angell, and R. Richert. Fragility and thermodynamics in nonpolymeric glass-forming liquids. *J. Chem. Phys.*, **125**:074505, 2006.

[43] L. M. Wang and C. A. Angell. Response to "Comment on 'Direct determination of the fragility indices of glassforming liquids by differential scanning calorimetry: Kinetic versus thermodynamic fragilities". *J. Chem. Phys.*, **118**:10353, 2003.

[44] J. C. Dyre. Heirs of liquid treasures. *Nature Mat.*, **3**:749, 2004.

[45] K. Niss and C. Alba-Simionesco. Effects of density and temperature on correlations between fragility and glassy properties. *Phys. Rev. B*, **74**:024205, 2006.

[46] K. Niss, C. Dalle-Ferrier, V. M. Giordano, G. Monaco, B. Frick, and C. Alba-Simionesco. Glassy properties and viscous slowing down: An analysis of the correlation between nonergodicity factor and fragility. *J. Chem. Phys.*, **129**:194513, 2008.

[47] S. N. Yannopoulos and G. P. Johari. Glass behaviour: Poisson's ratio and liquid's fragility. *Nature*, **442**:E–7, 2006.

[48] R. Richert. Heterogeneous dynamics in liquids: fluctuations in space and time. *J. Phys.: Cond. Matt.*, **14**:R703, 2002.

[49] L. Berthier, G. Biroli, J.-P. Bouchaud, L. Cipelletti, D. El Masri, L' Hôte, F. Ladieu, and M. Pierno. Direct Experimental Evidence of a Growing Length Scale Accompanying the Glass Transition. *Science*, **310**:1797, 2005.

[50] C. Dalle-Ferrier, C. Thibierge, C. Alba-Simionesco, L. Berthier, G. Biroli, J.-P. Bouchaud, F. Ladieu, D. L' Hôte, and G. Tarjus. Spatial correlations in the dynamics of glassforming liquids: Experimental determination of their temperature dependence. *Phys. Rev. E*, **76**:041510, 2007.

[51] R. C. Zeller and R. O. Pohl. Thermal conductivity and specific heat of Noncrystalline solids. *Phys. Rev. B*, **4**:2029, 1971.

[52] L. Landau and E. Lifshitz. *Theory of Elasticity.* Butterworth-Heinemann, London, 1995.

[53] M. A. Ramos. Elasticity theory and Debye model. Student Lectures.

[54] N. W. Ashcroft and N. D. Mermin. *Solid State Physics.* Hartcourt College Publishers, 1976.

[55] C. Kittel. *Introduction to Solid State Physics, 7^{th} Edition.* J. Wiley and Sons Inc., 1996.

[56] U. Buchenau. Amorphous Materials: Low-frequency Vibrations. *Encyclopedia of Materials: Science and Technology*, page 212, 2001.

[57] F. Sette, M. H. Krisch, C. Masciovecchio, G. Ruocco, and G. Monaco. Dynamics of Glasses and Glass-Forming Liquids Studied by Inelastic X-ray Scattering. *Science*, **280**:1550, 1998.

[58] U. Buchenau, N. Ücker, and A. J. Dianoux. Neutron Scattering Study of the Low-Frequency Vibrations in Vitrous Silica. *Phys. Rev. Lett.*, **53**:2316, 1984.

[59] A. I. Chumakov, I. Sergueev, U. van Bürck, W. Schirmacher, T. Asthalter, R. Rüffer, O. Leupold, and W. Petry. Collective Nature of the Boson Peak and Universal Transboson Dynamics of Glasses. *Phys. Rev. Lett.*, **92**:245508, 2004.

[60] A. P. Sokolov, E. Rössler, A. Kisliuk, and D. Quitmann. Dynamics of strong and fragile glass formers: Differences and correlation with low-temperature properties. *Phys. Rev. Lett.*, **71**:2062, 1993.

[61] D. A. Parshin. Soft Potential Model and Universal Properties of Glasses. *Phys. Scr.*, **T49**:180, 1993.

[62] V. L. Gurevich, D. A. Parshin, and H. R. Schober. Anharmonicity, vibrational instability, and the Boson peak in glasses. *Phys. Rev. B*, **67**:094203, 2003.

[63] D. A. Parshin, H. R. Schober, and V. L. Gurevich. Vibrational instability, two-level systems, and the boson peak in glasses. *Phys. Rev. B*, **76**:064206, 2007.

[64] S. N. Taraskin, Y. L. Loh, G. Natarajan, and S. R. Elliott. Origin of the Boson Peak in Systems with Lattice Disorder. *Phys. Rev. Lett.*, **86**:1255, 2001.

[65] T. S. Grigera, V. Martýn-Mayor, G. Parisi, and P. Verrocchio. Phonon interpretation of the boson peak in supercooled liquids. *Nature*, **422**:289, 2003.

[66] G. Parisi. On the origin of the boson peak. *J. Phys.: Condens. Matter*, **15**:S765, 2003.

[67] W. Schirmacher. Thermal conductivity of glassy materials and the boson peak. *Europhys. Lett.*, **73**:892, 2006.

[68] W. Schirmacher, G. Ruocco, and T. Scopigno. Acoustic Attenuation in Glasses and its Relation with the Boson Peak. *Phys. Rev. Lett.*, **98**:025501, 2007.

[69] E. Duval, A. Boukenter, and T. Achibat. Vibrational dynamics and the structure of glasses. *J. Phys.: Cond. Matt.*, **2**:10227, 1990.

[70] E. Duval, A. Mermet, and L. Saviot. Vibrational dynamics and the structure of glasses. *Phys. Rev. B*, **75**:024201, 2007.

[71] B. Rossi, G. Viliani, E. Duval, L. Angelani, and W. Garber. Temperature-dependent vibrational heterogeneities in harmonic glasses. *Europhys. Lett.*, **71**:256, 2005.

[72] A. Tangui, J. P. Wittmer, F. Leonforte, and J.-L. Barrat. Continuum limit of amorphous elastic bodies: A finite-size study of low-frequency harmonic vibrations. *Phys. Rev. B*, **66**:174205, 2002.

[73] F. Leonforte, R. Boissie, A. Tanguy, J. P. Wittmer, and J.-L. Barrat. Continuum limit of amorphous elastic bodies. III. Three-dimensional systems. *Phys. Rev. B*, **72**:224206, 2005.

[74] F. Leonforte, A. Tanguy, J. P. Wittmer, and J.-L. Barrat. Inhomogeneous Elastic Response of Silica Glass. *Phys. Rev. Lett.*, **97**:055501, 2006.

[75] F. Leonforte. *Vibrations et Micromcanique de Matriaux Amorphes Modles*. PhD thesis, Université Claude Bernard - Lyon 1, 2005.

[76] J. P. Boon and S. Yip. *Molecular Hydrodynamics*. Dover Publications, Inc. New York, 1991.

[77] G. S. Grest, S. R. Nagel, and A. Rahman. Longitudinal and Transverse Excitations in a Glass. *Phys. Rev. Lett.*, **49**:1271, 1982.

[78] A. Matic, C. Masciovecchio, D. Engberg, G. Monaco, L. Börjesson, S. C. Santucci, and R. Verbeni. Crystal-Like Nature of Acoustic Excitations in Glassy Ethanol. *Phys. Rev. Lett.*, **93**:145502, 2004.

[79] G. Ruocco and F. Sette. High-frequency vibrational dynamics in glasses. *J. Phys.: Cond. Mat.*, **13**:9141, 2001.

[80] P. Benassi, M. Krisch, C. Masciovecchio, V. Mazzacurati, G. Monaco, G. Ruocco, F. Sette, and R. Verbeni. Evidence of High Frequency Propagating Modes in Vitreous Silica. *Phys. Rev. Lett.*, **77**:3835, 1996.

[81] C. Masciovecchio, A. Mermet, G. Ruocco, and F. Sette. Experimental Evidence of the Acousticlike Character of the High Frequency Excitations in Glasses. *Phys. Rev. Lett.*, **85**:1266, 2000.

[82] O. Pilla, A. Cunsolo, A. Fontana, C. Masciovecchio, G. Monaco, M. Montagna, G. Ruocco, T. Scopigno, and F. Sette. Nature of the Short Wavelength Excitations in Vitreous Silica: An X-Ray Brillouin Scattering Study. *Phys. Rev. Lett.*, **85**:2136, 2000.

[83] M. Foret, R. Vacher, E. Courtens, and G. Monaco. Merging of the acoustic branch with the boson peak in densified silica glass. *Phys. Rev. B*, **66**:024204, 2002.

[84] A. Matic, D. Engberg, C. Masciovecchio, and L. Börjesson. Sound Wave Scattering in Network Glasses. *Phys. Rev. Lett.*, **86**:3803, 2001.

[85] B. Rufflé, M. Foret, E. Courtens, R. Vacher, and G. Monaco. Observation of the Onset of Strong Scattering on High Frequency Acoustic Phonons in Densified Silica Glass. *Phys. Rev. Lett.*, **90**:095502, 2003.

[86] T. Scopigno, E. Pontecorvo, R. Di Leonardo, M. Krisch, G. Monaco, G. Ruocco, B. Ruzicka, and F. Sette. High-frequency transverse dynamics in glasses. *J. Phys.: Cond. Mat.*, **15**:S1269, 2003.

[87] E. Rat, M. Foret, G. Massiera, R. Vialla, M. Arai, R. Vacher, and E. Courtens. Anharmonic versus relaxational sound damping in glasses. I. Brillouin scattering from densified silica. *Phys. Rev. B*, **72**:214204, 2005.

[88] R. Vacher, E. Courtens, and M. Foret. Anharmonic versus relaxational sound damping in glasses. II. Vitreous silica. *Phys. Rev. B*, **72**:214205, 2005.

[89] G. Ruocco, F. Sette, R. Di Leonardo, D. Fioretto, M. Krisch, M. Lorenzen, C. Masciovecchio, G. Monaco, F. Pignon, and T. Scopigno. Nondynamic Origin of the High-Frequency Acoustic Attenuation in Glasses. *Phys. Rev. Lett.*, **83**:5583, 1999.

[90] G. Ruocco, F. Sette, R. Di Leonardo, G. Monaco, M. Sampoli, T. Scopigno, and G. Viliani. Relaxation Processes in Harmonic Glasses? *Phys. Rev. Lett.*, **84**:5788, 2000.

[91] B. Rufflé, G. Guimbretière, E. Courtens, R. Vacher, and G. Monaco. Glass-Specific Behavior in the Damping of Acousticlike Vibrations. *Phys. Rev. Lett.*, **96**:045502, 2006.

[92] U. Buchenau, Yu. M. Galperin, V. L. Gurevich, D. A. Parshin, M. A. Ramos, and H. R. Schober. Interaction of soft modes and sound waves in glasses. *Phys. Rev. B*, **46**:2798, 1992.

[93] W. Schirmacher, G. Diezemann, and C. Ganter. Harmonic Vibrational Excitations in Disordered Solids and the Boson Peak. *Phys. Rev. Lett.*, **81**:136, 1998.

[94] C. Masciovecchio, G. Baldi, S. Caponi, L. Comez, S. Di Fonzo, D. Fioretto, A. Fontana, A. Gessini, S. C. Santucci, F. Sette, G. Viliani, P. Vilmercati, and G. Ruocco. Evidence for a Crossover in the Frequency Dependence of the Acoustic Attenuation in Vitreous Silica. *Phys. Rev. Lett.*, **97**:035501, 2006.

[95] A. Devos, M. Foret, S. Ayrinhac, P. Emery, and B. Rufflé. Hypersound damping in vitreous silica measured by picosecond acoustics. *Phys. Rev. B*, **96**:100201, 2008.

[96] G. Monaco and V. M. Giordano. Breakdown of the Debye approximation for the acoustic modes with nanometric wavelengths in glasses. *Proc. Natl. Acad. Sci. USA*, **106**:3659, 2009.

[97] G. Baldi, V. M. Giordano, G. Monaco, and B. Ruta. Sound Attenuation at Terahertz Frequencies and the Boson Peak of Vitreous Silica. *Phys. Rev. Lett.*, **104**:195501, 2010.

[98] G. Monaco and S. Mossa. Anomalous properties of the acoustic excitations in glasses on the mesoscopic length scale. *Proc. Natl. Acad. Sci. USA*, **106**:16907, 2009.

[99] A. Monaco, A. I. Chumakov, G. Monaco, W. A. Crichton, A. Meyer, L. Comez, D. Fioretto, J. Korecki, and R. Ruffer. Effect of Densification on the Density of Vibrational States of Glasses. *Phys. Rev. Lett.*, **97**:135501, 2006.

[100] K. Niss, B. Begen, B. Frick, J. Ollivier, A. Beraud, A. Sokolov, V. N. Novikov, and C. Alba-Simionesco. Influence of Pressure on the Boson Peak: Stronger than Elastic Medium Transformation. *Phys. Rev. Lett.*, **99**:055502, 2007.

[101] L. Hong, B. Begen, A. Kisliuk, C. Alba-Simionesco, V. N. Novikov, and A. P. Sokolov. Pressure and density dependence of the boson peak in polymers. *Phys. Rev. B*, **78**:134201, 2008.

[102] S. Caponi, A. Fontana, F. Rossi, G. Baldi, and E. Fabiani. Effect of temperature on the vibrational density of states in vitreous SiO2: A Raman study. *Phys. Rev. B*, **76**:092201, 2007.

[103] G. Baldi, A. Fontana, G. Monaco, L. Orsingher, S. Rols, F. Rossi, and B. Ruta. Connection between Boson Peak and Elastic Properties in Silicate Glasses. *Phys. Rev. Lett.*, **102**:195502, 2009.

[104] H. Shintani and H. Tanaka. Universal link between the boson peak and transverse phonons in glass. *Nature Mat.*, **7**:870, 2008.

[105] J. K. Krüger, J. Baller, T. Britz, A. le Coutre, R. Peter, R. Bactavatchalou, and J. Schreiber. Cauchy-like relation between elastic constants in amorphous materials. *Phys. Rev. B*, **66**:012206, 2002.

[106] D. Fioretto, S. Corezzi, S. Caponi, F. Scarponi, G. Monaco, A. Fontana, and L. Palmieri. Cauchy relation in relaxing liquids. *J. Chem. Phys.*, **128**:214502, 2008.

[107] B. Rufflé, S. Ayrinhac, E. Courtens, R. Vacher, M. Foret, A. Wischnewski, and U. Buchenau. Scaling the Temperature-Dependent Boson Peak of Vitreous Silica with the High-Frequency Bulk Modulus Derived from Brillouin Scattering Data. *Phys. Rev. Lett.*, **104**:067402, 2010.

[108] B. J. Berne and R. Pecora. *Dynamic Light Scattering with applications to chemistry, biology and physics*. John Wiley, 1976.

[109] C. Dreyfus, A. Aouadi, R. M. Pick, T. Berger, A. Patkowski, and W. Steffen. Light scattering by transverse waves in supercooled liquids and application to metatoluidine. *Eur. Phys. J. B*, **9**:401, 1999.

[110] G. Monaco, D. Fioretto, L. Comez, and G. Ruocco. Glass transition and density fluctuations in the fragile glass former orthoterphenyl. *Phys. Rev. E*, **63**:061502, 2001.

[111] S. Hensel-Bielowka, M. Paluch, J. Ziolo, and C. M. Roland. Dynamics of Sorbitol at Elevated Pressure. *J. Phys. Chem. B*, **106**:12459, 2002.

[112] A. Barkatt and C.A. Angell. Optical probe studies of relaxation processes in viscous liquids. *J. Chem. Phys.*, **70**:901, 1979.

[113] O. Yamamuro, K. Harabe, T. Matsuo, K. Takeda, I. Tsukushi, and T. Kanaya. Boson peaks of glassy mono- and polyalcohols studied by inelastic neutron scattering. *J. Phys.: Cond. Mat.*, **12**:5143, 2000.

[114] C. Alba Simionesco, C. Dalle Ferrier, and K. Niss. Private communication.

[115] J. Wuttke, W. Petry, G. Coddens, and F. Fujara. Fast dynamics of glass-forming glycerol. *Phys. Rev. E*, **52**:4026, 1995.

[116] A. Döss, M. Paluch, H. Sillescu, and G. Hinze. From Strong to Fragile Glass Formers: Secondary Relaxation in Polyalcohols. *Phys. Rev. Lett.*, **88**:095701, 2002.

[117] M. Naoki, K. Ujitaand, and S. Kashima. Pressure-Volume-Temperature Relations and Configurational Energy of Liquid, Crystal, and Glasses of D-Sorbitol. *J. Phys. Chem.*, **97**:12356, 1993.

[118] S. Shamblin, X. Tango, and L. Chang. Characterization of the Time Scales of Molecular Motion in Pharmaceutically Important Glasses. *J. Phys. Chem. B*, **103**:4113, 1999.

[119] D. Fioretto, G. Carlotti, L. Palmieri, G. Socino, L. Verdini, and A. Livi. Structural relaxation in polymeric films studied by Brillouin light scattering spectroscopy. *Phys. Rev. B*, **47**:15286, 1993.

[120] T. H. K. Barron, J. G. Collins, and G. K. White. Thermal expansion of solids at low temperatures. *Adv. Phys.*, **29**:609, 1980.

[121] J. Fabian and P.B. Allen. Theory of Sound Attenuation in Glasses: The Role of Thermal Vibrations. *Phys. Rev. Lett.*, **82**:1468, 1999.

[122] H. E. Bömmel and K. Dransfeld. Excitations and Attenuation of Hypersonic Waves in Quartz. *Phys. Rev.*, **117**:1245, 1960.

[123] A. Monaco. *Etude de la dynamique vibrationelle des verres*. PhD thesis, Universite Joseph Fourier, Grenoble, France., 2006.

[124] B. Meyer. Elemental Sulfur. *Chem. Rev.*, **76**:367, 1976.

[125] R. Steudel. Liquid Sulfur. *Top. Curr. Chem.*, **230**:81, 2003.

[126] R. F. Bacon and R. Fanelli. The Viscosity of Sulfur. *J. Am. Chem. Soc.*, **65**:639, 1943.

[127] J. Ruiz-Garcia, E. M. Anderson, and S. C. Greer. Shear Viscoslty of Liquid Sutfur near the Polymerization Temperature. *J. Phys. Chem.*, **93**:6980, 1989.

[128] K. M. Zengh and S. C. Greer. The density of liquid sulfur near the polymerization temperature. *J. Chem. Phys.*, **96**:2175, 1992.

[129] S. C. Greer. The dielectric constant of liquid sulfur. *J. Chem. Phys.*, **84**:6984, 1986.

[130] V. F. Kozhenikov, W. B. Payne, J. K. Olson, C. L. Macdonald, and C. E. Inglefield. The dielectric constant of liquid sulfur. *J. Chem. Phys.*, **121**:7379, 2004.

[131] E. D. West. The Heat Capacity of Sulfur from 25 to 450, the Heats and Temperatures of Transition and Fusion. *J. A. Chem. Soc.*, **81**:29, 1959.

[132] S. C. Greer. Physical Chemistry of Equilibrium Polymerization. *J. Phys. Chem. B*, **102**:5431, 1998.

[133] A. V. Tobolsky and A. Eisenberg. Equilibrium Polymerization of Sulfur. *J. Am. Chem. Soc.*, **81**:780, 1959.

[134] J. C. Wheeler, S. J. Kennedy, and P. Pfeuty. Equilibrium Polymerization as a Critical Phenomenon. *Phys. Rev. Lett.*, **45**:1748, 1980.

[135] J. C. Koh and W. Klement Jr. Polymer Content of Sulfur Quenched Rapidly from the Melt. *J. Phys. Chem.*, **20**:4280, 1970.

[136] A. G. Kalampounias, D. Th. Kastrissios, and S. N. Yannopoulos. Structure and vibrational modes of sulfur around the λ-transition and the glass-transition. *J. Non-cryst. Sol.*, **326**:115, 2003.

[137] R. Steudel and B. Eckert. Comment on Probing the sulfur polymerization transition in situ with Raman spectroscopy [J. Chem. Phys. 118, 8460 (2003)]. *J. Chem. Phys.*, **121**:6573, 2004.

[138] G. Monaco, L. Crapanzano, R. Bellisent, W. Crichton, D. Fioretto, M. Mezouar, F. Scarponi, and R. Verbeni. Rubberlike Dynamics in Sulphur above the λ-Transition Temperature. *Phys. Rev. Lett.*, **95**:255502, 2005.

[139] F. Scarponi, D. Fioretto, L. Crapanzano, and G. Monaco. A Brillouin light scattering study of the transition in liquid sulphur. *Philos. Mag.*, **87**:673, 2007.

[140] T. Scopigno, S. N. Yannopoulos, F. Scarponi, K. S. Andrikopoulos, D. Fioretto, and G. Ruocco. Origin of the λ Transition in Liquid Sulfur. *Phys. Rev. Lett.*, **99**:025701, 2007.

[141] A. V. Tobolsky, W. M. MacKnight, R. B. Beevers, and V. D. Gupta. The Glass Transition Temperature of Polymeric Sulfur. *Polymer*, **4**:423, 1963.

[142] W. J. MacKnight and A. V. Tobolsky. *Elemental Sulfur*. 1965.

[143] R. Winter, W. C. Pilgrim, P. A. Egelstaff, P. Chieux, S. Anlauf, and F. Hensel. Neutron Scattering Study on Amorphous Sulphur. *Europhys. Lett.*, **11**:225, 1990.

[144] M. Stoltz, R. Winter, W. S. Howells, R. L. McGreevy, and P. A. Egelstaff. The structural properties of liquid and quenched sulphur II. *J. Phys.: Cond. Matt.*, **6**:3619, 1994.

[145] R. Winter, P. A. Egelstaff, W. C. Pilgrim, and W. S. Howells. The structural properties of liquid, solid and amorphous sulphur. *J. Phys.: Cond. Matt.*, **2**:SA215, 1990.

[146] A. Eisenberg and L.A. Teter. Relaxation Mechanisms in Polymeric Sulfur. *J. Phys. Chem.*, **71**:2332, 1967.

[147] R. F. Bacon and R. Fanelli. Supercooled Sulfur and its Viscosity. *Ind. Eng. Chem.*, **34**:1043, 1942.

[148] R. Sasson and E. T. Arakawa. Temperature dependence of index of refraction, reflection, and extinction coefficient of liquid sulfur in the $0.4-2.0$ μm wavelength range. *Appl. Opt.*, **25**:2575, 1986.

[149] E. Burkel. *Inelastic Scattering of X-Rays with Very High Energy Resolution*. 1991.

[150] E. Burkel. Phonon spectroscopy by inelastic x-ray scattering. *Rep. Prog. Phys.*, **63**:171, 2000.

[151] G. Ruocco and F. Sette. Inelastic X-ray scattering: A new spectroscopy tool to investigate the atomic dynamics in condensed matter. *Synch. Rad.*, **82**:1, 2003.

[152] J. J. Sakurai. *Modern Quantum Mechanics. Revisited edition.* Addison-Wesley Publishing Company, 2004.

[153] L. Van Hove. Correlations in Space and Time and Born Approximation Scattering in Systems of Interacting Particles. *Phys. Rev.*, **95**:249, 1954.

[154] W. Marshall and S. W. Lovesey. *Theory of Thermal Neutron Scattering.* Clarendon Press, Oxford, 1971.

[155] www.esrf.fr/UsersAndScience/Experiments/HRRS/ID16.

[156] R. Verbeni, F. Sette, M. Krisch, U. Bergmanand B. Gorges, C. Halcoussis, K. Martel, C. Masciovecchio, J. F. Ribois, G. Ruocco, and H. Sinn. X-ray Monochromator with $2 \cdot 10^8$ Energy Resolution. *Synch. Rad.*, **3**:62, 1996.

[157] C. Masciovecchio, U. Bergman, M. Krisch, G. Ruocco, F. Sette, and R. Verbeni. A perfect crystal X-ray analyser with meV energy resolution. *Nucl. Instrum. Meth. B*, **111**:181, 1996.

[158] C. Masciovecchio, U. Bergman, M. Krisch, G. Ruocco, F. Sette, and R. Verbeni. A perfect crystal X-ray analyser with 1.5 meV energy resolution. *Nucl. Instrum. Meth. B*, **117**:339, 1996.

[159] A. Bergamin, G. Cavagnero, G. Mana, and G. Zosi. A perfect crystal X-ray analyser with 1.5 meV energy resolution. *J. Appl. Phys.*, **82**:5396, 1997.

[160] N. L. Laberge, V. V. Vasilescu, C. J. Montrose, and P. B. Macedo. Equilibrium Compressibilities and Density Fluctuations in K_2O-S_iO_2 Glasses. *J. Am. Ceram. Soc.*, **56**:506, 1973.

[161] A. C. Wright, R. A. Hulme, and R. N. Sinclair. A small angle neutron scattering study of long range density fluctuations in vitreous silica. *Phys. Chem. Glasses*, **49**:59, 2005.

[162] C. Levelut, R. Le Parc, A. Faivre, R. Brüning, B. Champagnon, V. Martinez, J. Simon, F. Bleyd, and J. Hazemanne. Density fluctuations in oxide glasses investigated by small-angle X-ray scattering. *J. App. Cryst.*, **40**:S512, 2007.

[163] S. N. Taraskin and S. R. Elliott. Low-frequency vibrational excitations in vitreous silica: the IoffeRegel limit. *J. Phys.: Cond. Matt.*, **11**:A219, 1999.

[164] G. Ruocco, A. Matic, T. Scopigno, and S. N. Yannopoulos. Comment on Glass-Specific Behavior in the Damping of Acousticlike Vibrations. *Phys. Rev. Lett.*, **98**:079601, 2007.

[165] S. N. Taraskin and S. R. Elliott. Ioffe-Regel crossover for plane-wave vibrational excitations in vitreous silica. *Phys. Rev. B*, **18**:12031, 2000.

[166] F. Birch. The Velocity and Compressional Waves in Rocks to 10 Kilobars, Part 1. *J. Geophys. Res.*, **65**:1083, 1960.

[167] F. Birch. The Velocity and Compressional Waves in Rocks to 10 Kilobars, Part 2. *J. Geophys. Res.*, **66**:2199, 1961.

[168] J. Jäckle and L.Pichï. Elastic effects of structural relaxation in glasses at low temperatures. *J. Non-Cryst. Solids*, **20**:365, 1976.

[169] S. W. Lovesey. *Theory of neutron scattering from condensed matter*. Clarendon Press, 1984.

[170] G. L. Squires. *Introduction to Thermal Neutron Scattering*. Dover Publications, Inc. New York, 1996.

[171] www.ill.eu/instruments-support/instruments-groups/instruments/in4.

[172] www.ncnr.nist.gov/resources/n-lengths/list.html.

[173] E. Fabiani, A. Fontana, and U. Buchenau. Neutron scattering study of the vibrations in vitreous silica and germania. *J. Chem. Phys.*, **128**:244507, 2008.

[174] H. Schober. Spectroscopie neutronique: un outil idl pour le scientifique des matiaux. *J. Phys. IV France*, **103**:173, 2003.

[175] B. Rufflé, D. A. Parshin, E. Courtens, and R. Vacher. Boson Peak and its Relation to Acoustic Attenuation in Glasses. *Phys. Rev. Lett.*, **100**:015501, 2008.

[176] S. N. Yannopoulos. Private communication.

[177] V. F. Kozhenikov, J. M. Viner, and P. C. Taylor. The dielectric constant of liquid sulfur. *Phys. Rev. B*, **64**:214109, 2001.

[178] M. B. Gitis and I. G. Mikhailov. The dielectric constant of liquid sulfur. *Soviet Phys. Acoust.*, **13**:251, 2001.

[179] G. Baldi. Private communication.

[180] A. Wischnewski, U. Buchenau, A. J. Dianoux, W. A. Kamitakahara, and J. L. Zarestky. Sound-wave scattering in silica. *Phys. Rev. B*, **57**:2663, 1998.

Resumé

Une des questions les plus ambitieuses dans la Physique de la Matière Condensée concerne la compréhension des propriétés vibrationnelles des verres. En particulier, une anomalie présente dans la densité d'états vibrationnels (VDOS) à des énergies de quelques meV a suscité beaucoup d'intérêt en raison de sa présence universelle dans les verres. Cette anomalie, appelée "boson peak" (BP), apparaît comme un pic dans la VDOS réduite par rapport à la prévision du continuum élastique de Debye, dans une région d'énergies où le modèle de Debye fonctionne encore assez bien pour les correspondants cristaux.
Dans ce travail de Thèse on présente les résultats d'une étude expérimentale de la dynamique vibrationelle dans des verres du sorbitol at du soufre, par diffusion inélastique de la lumière, des rayons x et des neutrons. Dans le cas du sorbitol, ces résultats montrent clairement que le BP est lié à des anomalies observées dans la courbe de dispersion acoustique dans la région mésoscopique des vecteurs d'onde de quelques nm^{-1}. En outre, l'étude de la dépendance en température de ces propriétés montre que cette connexion est maintenue même avec les changements de température. Enfin, le comportement des modes à haute fréquence peut être utilisé pour réproduire quantitativement la forme du BP, ce qui suggère une forte relation entre les propriétés acoustiques dans la région mésoscopique et le BP. Ce comportement semble être universel dans les verres. Dans le cas du soufre vitreux le BP est situé à l'extérieur de la fenêtre d'énergies qui peut être sondée par IXS et donc il n'est pas possible expérimentalement d'étudier le caractère des excitations collectives correspondantes.
Mots clés: Boson Peak, diffusion inélastique, dynamique vibrationelle du verres.

Summary

One of the most challenging issue in condensed matter physics concerns the understanding of the vibrational properties of glasses. In particular, an anomaly present in the vibrational density of states (VDOS) at energies of few meV has attracted much interest due to its universal occurrence in glasses. This anomaly, called "boson peak" (BP), appears as a peak in the reduced VDOS over the Debye, elastic continuum prediction in an energy range where the Debye model still works reasonably well for the corresponding crystals.
In this PhD work we present the results of an experimental study of the vibrational dynamics in glassy sorbitol and sulfur by means of inelastic scattering of light, x-ray and neutron. In the case of sorbitol, these results show that the boson peak is clearly related to anomalies observed in the acoustic dispersion curve in the mesoscopic wavenumber range of few nm^{-1}. Moreover, the study of the temperature dependence of these properties shows that this connection is kept under temperature changes. Finally, the behavior of the high frequency modes can be used to quantitatively account for the BP, suggesting a strong connection between acoustic properties in the mesoscopic range and boson peak. This behavior seems to be universal in glasses. In the case of glassy sulfur the BP is located at energies outside the window which can be probed by IXS and it is not possible experimentally to investigate the character of the corresponding collective excitations.
Key words: Boson Peak, inelastic scattering, vibrational dynamics of glasses.